Mechanical properties of steel and concrete under the sequential action of cyclic loading and elevated temperatures

Sina Sinaie

M.Sc. in Structural Engineering

Copyright notice

Abstract

Current design guidelines allow structures to dissipate seismic energy through plastic deformations. As a result, a fire following an earthquake would find a structure in a weaker state than what had been originally assumed during its fire-resistant design. This thesis aims to investigate the potential changes that the mechanical properties of *construction materials* experience under earthquake-then-fire loading sequence.

Earthquake and fire are both extremely random events, so before any attempt to investigate their effects in the material scale, they have to be projected into a more quantifiable form. For this purpose, in the following work, a post-earthquake fire event is replaced by a multi-phase loading history that includes cyclic loading at ambient temperature followed by exposure to high temperatures. In order to make the findings of this research widely applicable to current and future structures, this thesis focuses on two of the most common construction materials: mild steel and normal strength concrete.

The results of this research indicate that a prior history of cyclic loading can significantly affect the ductility and strength of steel and concrete at elevated temperatures. These variations in material properties have great implications when it comes to post-earthquake fire analyses, suggesting that any history of cyclic loading should be included in the post-earthquake fire-resistant design of a structure. Therefore, it is desirable to establish a relationship for each mechanical property, not only as a function of temperature but also the level of damage induced by cyclic loading.

Developing predictive models is a main objective of this thesis. For this purpose, a generic model has been proposed for steel and concrete. This model takes advantage of a special class of functions known as Bézier curves. The proposed model proves to be highly versatile, in the sense that it can successfully take the effect of temperature and pre-induced damage into account. In addition to Bézier curves, more advanced models have also been incorporated in this research. This includes the theory of plasticity for steel and the discrete element method for concrete.

The knowledge gained from this study is not only useful when it comes to designing new structures, but is also suitable for assessing the fire-resistant capacity of structures that have already sustained an earthquake. Moreover, the results of this research can be used to develop fire-resistant guidelines for structures located in earthquake-prone areas.

Declaration

This thesis contains no material which has been accepted for the award of any other degree or diploma at any university or equivalent institution and that, to the best of my knowledge and belief, this thesis contains no material previously published or written by another person, except where due reference is made in the text of the thesis.
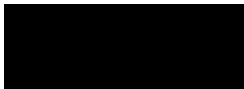
Sina Sinaie
September 2015

Thesis including published works General Declaration

In accordance with Monash University Doctorate Regulation 17.2 Doctor of Philosophy and Research Masters regulations the following declarations are made:

I hereby declare that this thesis contains no material which has been accepted for the award of any other degree or diploma at any university or equivalent institution and that, to the best of my knowledge and belief, this thesis contains no material previously published or written by another person, except where due reference is made in the text of the thesis.

This thesis includes 4 original papers published in peer reviewed journals and 2 other papers currently under review. The core theme of the thesis is structural mechanics. The ideas, development and writing up of all the papers in the thesis were the principal responsibility of myself, the candidate, working within the Department of Civil Engineering under the supervision of Dr. Amin Heidarpour.

(The inclusion of co-authors reflects the fact that the work came from active collaboration between researchers and acknowledges input into team-based research.)
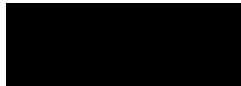
In the case of chapters 2–7 my contribution to the work involved the following:

Ch.	Publication title	Publication status	Nature and extent (%) of student's contributions
2	Mechanical properties of cyclically-damaged structural mild steel at elevated temperatures	Published: Construction and Building Materials (2014)	Establishing methodologies, Experimental work, Data analysis, Write-up and revision 70%
3	Stress-strain-temperature relation for cyclically-damaged structural mild steel	Published: Engineering Structures (2014)	Development of ideas, Development, validation and verification of computer model, Data analysis, Write-up and revision 70%
4	A multi-objective optimisation approach to the parameter determination of constitutive plasticity models for the simulation of multi-phase load histories	Published: Computers and Structures (2014)	Development of ideas, Development, validation and verification of computer model, Data analysis, Write-up and revision 70%

Ch.	Publication title	Publication status	Nature and extent (%) of student's contributions
5	Effect of size on the response of cylindrical concrete samples under cyclic loading	Published: Construction and Building Materials (2015)	Establishing methodologies, Experimental work, Data analysis, Write-up and revision 70%
6	Effect of pre-induced cyclic damage on the mechanical properties of concrete exposed to elevated temperatures	Submitted: Construction and Building Materials	Establishing methodologies, Experimental work, Data analysis, Write-up and revision 70%
7	A micro-mechanical parametric study on the strength degradation of concrete by using a 2-phase discrete element model	Submitted: International Journal of Solids & Structures	Development of ideas, Development, validation and verification of computer model, Data analysis, Write-up and revision 70%

I have renumbered sections of submitted or published papers in order to generate a consistent presentation within the thesis.

Student signature: ▮▮▮▮▮▮▮   **Date:** 24/09/2015

The undersigned hereby certify that the above declaration correctly reflects the nature and extent of the student and co-authors contributions to this work.

Main supervisor signature: ▮▮▮▮▮▮▮   **Date:** 24/09/2015

List of Publications

The following lists the publications resulting from the studies carried out during the candidature. This includes 4 papers published in ISI quarter 1 (Q1) peer reviewed journals in the field of civil engineering and structural mechanics. The list also includes 2 other journal papers that are currently under review and 1 conference paper. The candidate is the lead author in all publication.

Peer reviewed journal papers

Mechanical properties of cyclically-damaged structural mild steel at elevated temperatures
Construction and Building Materials, Volume 52, Pages 465-472
S. Sinaie, A. Heidarpour, X.L. Zhao
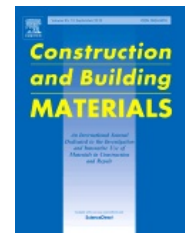
A multi-objective optimization approach to the parameter determination of constitutive plasticity models for the simulation of multi-phase load histories
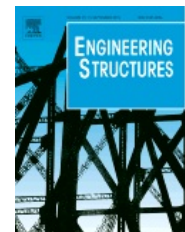*Computers & Structures, Volume 138, Pages 112-132*
S. Sinaie, A. Heidarpour, X.L. Zhao

Stress-strain-temperature relation for cyclically-damaged structural mild steel
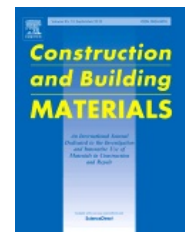*Engineering Structures, Volume 77, Pages 84-94*
S. Sinaie, A. Heidarpour, X.L. Zhao

Effect of size on the response of cylindrical concrete samples under cyclic loading
Construction and Building Materials, Volume 84, Pages 399-408
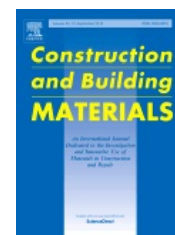S. Sinaie, A. Heidarpour, X.L. Zhao, J.G. Sanjayan

Journal papers currently under review

Effect of pre-induced cyclic damage on the mechanical properties of concrete exposed to elevated temperatures
Submitted to the journal of Construction and Building Materials
S. Sinaie, A. Heidarpour, X.L. Zhao

A micro-mechanical parametric study on the strength degradation of concrete using a 2-phase discrete element model
Submitted to the International Journal of Solids & Structures
S. Sinaie, A. Heidarpour, X.L. Zhao

Conference proceedings

Behaviour of structural steel subjected to post earthquake fire
Proceedings of the 5th international conference on structural engineering, mechanics and computation, SEMC 2013, Pages 2033-2037
S. Sinaie, A. Heidarpour, X.L. Zhao

Acknowledgements

First and foremost, I would like to thank my main supervisor, Dr. Amin Heidarpour, for his continuous support, his patience and his knowledge throughout the entirety of my candidature. His experience not only paved the way for my research, but his support for creative thinking allowed me to explore my research topic by ways of my own interests. I would not have been able to maintain my enthusiasm and motivation without this kind of support.

My gratitude goes to my co-supervisor, Professor Xiao-Ling Zhao, for his involvement, feedback and insight during the period of my candidature. I must also acknowledge the technical staff of the Civil Engineering Laboratory, Mr. Long Goh, Mr. Kevin Nievaart, Mr. Mark Taylor, Mr. Jeff Doddrell, Mr. Zoltan Csaki and Mr Peter Dunbar for their practical advice and help. A very special thanks goes to Mrs. Jenny Manson for her endless support as the research and postgraduate manager in the Civil Engineering Department. Moreover, this research would have not been possible without the financial assistance of the Australian Research Council.

I would also like to thank my family and friends for their encouragement and moral support throughout the years.

Last but not least, my sincerest gratitude goes to all the individuals who selflessly share their knowledge on the internet. Their generosity in expanding the sciences is the very essence of an open-knowledge society, and what I learned from them became an important part of my graduate experience.

Table of Contents

Part II   Concrete

5   Effect of size on the response of cylindrical concrete samples under cyclic loading   119

6   Effect of pre-induced cyclic damage on the mechanical properties of concrete exposed to elevated temperatures   146

List of Tables

List of Figures

CHAPTER 1

Introduction

Contents

1.1   Motivation

Post-earthquake fire (PEF) also known as fire following earthquake (FFE) is cate-gorised as a multi-hazard event. In this thesis, post-earthquake fire refers to a fire acting on a structure that has previously been damaged through seismic loading. Design guidelines allow structures to dissipate seismic energy through plastic defor-mations. Therefore, in cases where an earthquake is followed by fire, the structure can not be assumed to be holding its full fire-resistant capacity. This calls for gaining a better understanding on the high temperature behaviour of construction material after being partially damaged under cyclic loading.

The probability of an earthquake and a fire outbreak are not mutually exclusive. In fact, from a probability point of view, the likelihood of a fire outbreak is amplified through a seismic event. The occurrence of an earthquake can increase the potential of a fire through:

- Damage to utility systems, such as gas lines or electrical lines initiating the fire.
- Malfunction of automated fire extinguishing facilities such as sprinklers.
- Damage to water supply systems, and restricting road access causing difficulty fire-fighter units.

As a result, post-earthquake fires, when they take place, can be a major issue in seismic prone areas. Experience has shown that the conflagrations following an earthquake can possibly result in more damage than the earthquake itself. From a historical point of view, it is important to mention the past occurrences of this extreme event and its casualties. For example, post-earthquake fires accounted for 80% of the total losses in the 1906 San Francisco earthquake [1]. Among the buildings lost during the 1923 earthquake of Tokyo, 77% were due to the fires following the earthquake [2]. The fires that followed the 1906 San Francisco and 1923 Tokyo earthquake are among the largest peacetime urban fires known in history. Although the post-earthquake fires of Loma Prieta (1987), Northridge (1994), Kobe (1995), Tohoku and Kanto (2011) were less severe, they still caused major damage [3, 4].

All of this is compelling evidence that post-earthquake fires should be considered by current design codes. The research presented in this thesis looks at the problem from a structural mechanics standpoint, whereby the aim is to gain the knowledge required to design structures that are fire resistant, even after sustaining seismic

damage. In other words, this research does not attempt to devise strategies to prevent post-earthquake fire, but aims to extend the knowledge on the matter and hence, limit the possible damage it can cause.

1.2 State of the art

Most of the research carried out in the context of post-earthquake fire consists of structural scale simulations. Della Corte et al. [5] demonstrated through case studies that fire resistant capacity is highly affected by the extent of damage sustained by the earthquake. They used a superposition approach to develop a model for the damaged structure. In this model, they considered the residual structural geometry as well as the degradation of mechanical properties of the members (not material) due to plastic deformations. At the same time, the high temperature material properties of steel were determined according to Eurcode 3. By doing this, they showed that a structure designed for the serviceability limit state sustains less reduction in its fire-resistant capacity when compared to a structure that is design for the ultimate limit state. In fact, while the former suffers a reduction of less than 10%, the latter is shown to sustain a significant loss. They concluded that fire-safety guidelines should take into account the seismic activity of the area and advise more stringent requirements for seismic prone regions.

Zaharia and Pintea [6] argue that risk management for post-earthquake fires can be achieved from a local scale (the structure) as well as a global scale (the region). Their study was carried out in the local scale where they evaluated the fire resistance time of structures which were previously damaged through seismic loading. They demonstrated that the time is influenced by the level of damage as well as the type of fire, i.e. standard or natural fires. The most significant difference was observed when the damaged structure suffered a global collapse mechanism rather than a local one. This work also reports that if the structure is over-designed for seismic loading, its remaining resistance after an earthquake can suffice to resist a subsequent fire.

A full-scale test of a partially damaged reinforced concrete frame under fire was carried out by Sharma et al. [7]. In their work, a single story frame consisting of four columns, four beams and a slab was tested. The frame was first subjected to a cyclic lateral load, whereby quasi-seismic damage was induced. Following the cyclic loading, the frame was then exposed to a fire reaching a temperature of 1000°C. The experiment was carried out for three structures with different levels of initial

seismic damage. Numerical simulations of the response were also carried out in this study.

Imani et al. [8] carried out experiments and numerical simulations on the performance of double-skin concrete filled columns under post-earthquake fire. The columns were first subjected to lateral cyclic loads which resulted in residual drifts. This was followed by exposure to a standard fire curve until the columns failed due to local buckling. Three columns with different degrees of initial damage were tested in this program (no damage, moderate and high). They reported that the fire-resistant capacity of the columns were almost the same, whereby the highly damaged sample resisted the fire only 5 minutes less than the undamaged sample (which resisted for 65 minutes).

Memari et al. [4] carried out a series of numerical simulations on the behaviour of low-, medium- and high-rise structures. The structures that they considered were moment resisting frames with reduced beam section connections. Nonlinear time-history analyses were carried out in order to induce seismic damage. The temperature-dependent properties of the material were taken according to Eurocode 3. The damaged structure was then analysed against a time-temperature curve. They reported a series of parameters affecting the global as well as the local response of the structures.

OpenSees is an open source framework for seismic analysis of structures. The code is currently being extended for fire analysis by different researchers. Among this, Khorasani et al. [9] modified the thermal module of OpenSees for post-earthquake fire analysis. Their modification allows a coupled seismic-temperature analysis to be carried out. This itself allows Monte Carlo analyses to be performed based on uncertainties in the fire load density as well as the yield stress and the elastic modulus of steel. They carried out simulations of a 4-bay 9-story 2-dimensional frame for their parametric study.

Song et al. [10] investigated the behaviour of steel beam to column connections through experiments and numerical simulations. The connections were initially subjected to cyclic loads and then exposed to high temperatures. In this word, the temperature variation followed the standard fire curve. During the temperature rise, a constant load was applied to the end of the beam. They reported the significant influence of pre-induced cyclic damage on the subsequent fire-resistant capacity of the connections.

From the aforementioned examples of the research carried out on the topic of post-earthquake fire, it is clear that most researchers have investigated the problem in the structural scale, and mainly through numerical simulations. These simulations usually involve a two-phase loading scheme, whereby the structure is subjected to cyclic loading in the first phase followed by a temperature rise in the second phase. In this fashion, the damage induced by cyclic loading (in the form of residual deformations) is carried over to the second phase. However, in the absence of a true model for the behaviour of the *damaged* material, temperature is the only independent parameter that is used to determine the mechanical properties of the material in the second phase. In other words, it is assumed that the material (not the structure) behaves as though it had never been subjected to cyclic loading. This raises concerns over the accuracy and reliability of the simulations.

1.3 Thesis objectives

Following the available research mentioned in the previous section on the behaviour of structures under post-earthquake fire, the question that needs to be answered is whether the cyclic action of the first phase affects the behaviour of the material under high temperature in the second phase, and if it does, to what extent? Hence, in the search to answer this question, the following objectives have been defined for this thesis.

It is also important to mention that the available research on the individual effects of cyclic loading and high temperatures have been taken into account in designing the methodologies [11–20].

1.3.1 Objective 1: Experimental investigation

Experimentation constitutes an important part of this thesis. An extensive dataset exists in the literature on the mechanical response of construction materials when subjected to the individual action of cyclic loading or high temperature. Using existing research on these individual effects, hypotheses can be made on their combined or sequential action. However, inevitably, actual experiments have to be carried out for the validation and verification of these hypotheses.

As a general rule, standard guidelines have been followed in this research for sample preparation and experimental procedures. However, deviations from standards have been made, where the modifications were necessary for the purpose of the thesis and where they could be justified from a theoretical or practical standpoint.

The results of this study are intended to pertain to both new and existing structures. In addition, in order to make the findings of this research applicable to a wide range of current and future structures, the following materials are considered:

- Structural grade mild steel (300 MPa)
- Normal strength concrete, with a 28-day target strength of 35 MPa

For either of the materials, full stress-strain curves are recorded from the experiments. This allowed for the extraction of the mechanical properties that are required for numerical modelling. It should be noted that the raw data obtained from experiments were always accompanied with random fluctuation of strain values. These fluctuations were carefully filtered out of the measurements to results in clear parametric values, however, without affecting the actual response.

1.3.1.1 Steel experiments

Steel specimens (Fig. 1.1a) used in this study were made of grade 300 mild steel [21], taken from the flange of 200UB22.3 hot rolled sections [22]. Preparation of the samples was consistent with the requirements of ASTM E21-92 [23] and ASTM E606-92 [24]. Samples were loaded through two holes on each end. Loading through two bolts provides more resistance against cyclic buckling, and at the same time, eliminates the need for high strength bolts in the configuration.

High temperature tests on steel can be carried out in two forms: *transient-state*, where the temperature is increased while the sample is under a constant load and *steady-state*, where the load is increased as the temperature is kept constant. Although the transient-state test method is a more realistic reflection of a fire scenario, the steady-state method is commonly used by researchers since it is easier to perform, gives stress-strain curves directly and can be readily used for model calibration. The steady-state test method is therefore used in this research work. All samples are subjected to a two-phase load history involving an ambient-temperature cyclic loading (phase 1), followed by a monotonic tensile load at elevated temperature
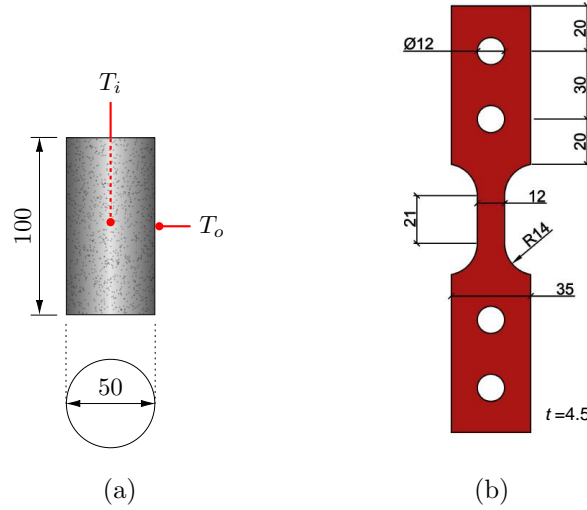
Figure 1.1: Geometry of samples use in high temperature experiments. (a) Steel samples and (b) concrete samples.

(phase 2), in other words:

- **Phase 1**. Induction of cyclic damage.
- **Phase 2**. Determination of mechanical properties at elevated temperature.

The time gap between the two phases was small enough to not allow for any strain aging effect to take place [25]. Hence, when it comes to the analysis of cyclically-damaged steel structures under fire, using the experimental results of this study is limited to scenarios where the fire immediately follows the seismic loading. With the number of cycles and the strain amplitude serving as variables for the cyclic phase, and temperature being the variable for the monotonic phase, their combined influence on subsequent mechanical properties of structural steel at elevated temperatures was examined. Over 120 steel samples were tested in this program. This also includes experiments carried out on control samples which had no pre-induced cyclic damage, and were tested under tension at elevated temperatures. It is worth mentioning that a secondary series of tests were also carried out on steel samples under transient-state testing conditions. These tests were not as comprehensive as the previous tests under steady-state conditions, however, they served as verification to an analytical method proposed for converting the steady-state response to transient-state response.

The experiments carried out in this research gives insight to the behaviour of mild steel under post-earthquake fire conditions. The information can be used for practical design guidelines, as well as more accurate simulations of steel structures under a fire following and earthquake.

1.3.1.2 Concrete experiments

Cylindrical samples of normal strength concrete (28-day target strength of 35 MPa) were cast, cured and tested in this program (Fig. 1.1b). The guidelines of the ASTM standard [26, 27] were considered in the casting and testing of the concrete samples.

When it comes to the effect of high temperature on concrete [28], two main methods can be listed:

- **Hot state**. Stressed/unstressed tests at high temperatures.
- **Cold state**. Tests carried out after cool-down from high temperatures

'Hot' state testing involves concurrent heating and loading on the sample. Stressed and unstressed hot tests are usually carried out in conjunction to one another [29, 30] and differ based on whether the sample is loaded during temperature rise or not. Once the temperature reaches its target value, a monotonic load is applied until failure. The existence of stress during heating leads to complex micro-mechanical interactions. However, the general finding is that stressed samples sustain less strength loss when compared to unstressed ones [28].

In contrast to 'hot' state testing, in a 'cold' state test, the sample is allowed to cool down to room temperature before being subjected to any load [20, 31]. The mechanical properties obtained from a cold-state test are usually referred to as 'residual' properties. The relation between cold-state and hot-state strength varies depending on temperature. It has been reported that up to a temperature of 300-400°C, residual strength is higher than strength at high temperature. However, as the exposure temperature rises beyond this range, the relation becomes reverse and the residual strength is measured to be less than the strength at high temperature.

After careful consideration of the advantages and disadvantages of 'hot' and 'cold' state testing, it was decided to focus this study on the *residual* mechanical properties of cyclically-damaged specimens after being exposed to elevated temperatures ('cold' state testing). The main reasons can be summarised as:

- Lack of a standard method for testing of concrete under high temperature.

- It has been shown that if a generic model was to be established for concrete as a function of temperature, its strength under *cold* conditions is lower than

hot conditions [32]. In fact, Eurocode 4 suggests a further reduction (up to 10%) for *cold* properties as opposed to *hot* properties. Therefore, from a design point of view, *cold* strength can be viewed as a lower limit compared to *hot* strength.

- The same study also shows that *cold* properties involve more data scatter when compared to *hot* properties, therefore, cold state testing is in more need of experimentation. This has been attributed to the additional environmental effects that take place during the cooling regime, such as cooling rate and ambient moisture.

- The occurrence of *delayed failure* is an important issue caused by the reduction of concrete strength as the temperature drops. This is especially important for composite members, and in particular for composite columns, as shown in [32, 33]. Such failure is argued to be more dangerous than a typical failure at high temperature.

- Available literature on *cold* properties are more comprehensive than *hot* properties (over three times more, [32]), allowing the present research to be compared to (and validated against) the work of more researchers.

As a result, the experimental program followed for concrete differs from the one carried out for steel in the sense that it looks into *residual* properties after cooldown rather than properties *at high temperature*. The test program in this part is divided into three separate phases:

- **Phase 1**. Induction of cyclic damaged.
- **Phase 2**. Exposure to elevated temperatures.
- **Phase 3**. Determination of residual properties after cooldown.

More than 140 concrete samples were cast and tested by the end of the study.

The experiments carried out in this research provides the information required for to determine the strength of concrete members and structures after a post-earthquake fire scenario. The information can be used for practical design guidelines, as well as for a more reliable model for concrete structures.

1.3.2 Objective 2: Numerical modelling

Creating numeric models from experimental results is the second main objective of this thesis. In fact, experimental programs were designed based on the needs for creating a numeric model. Note that the models dealt with in this work are in the material scale. In selecting these models, consideration was also given to their possible use in structural scale analyses. This research aims to lay out the foundation for creating models that are suitable for steel, concrete and composite members. This concept has been schematically illustrated in Fig. 1.2.
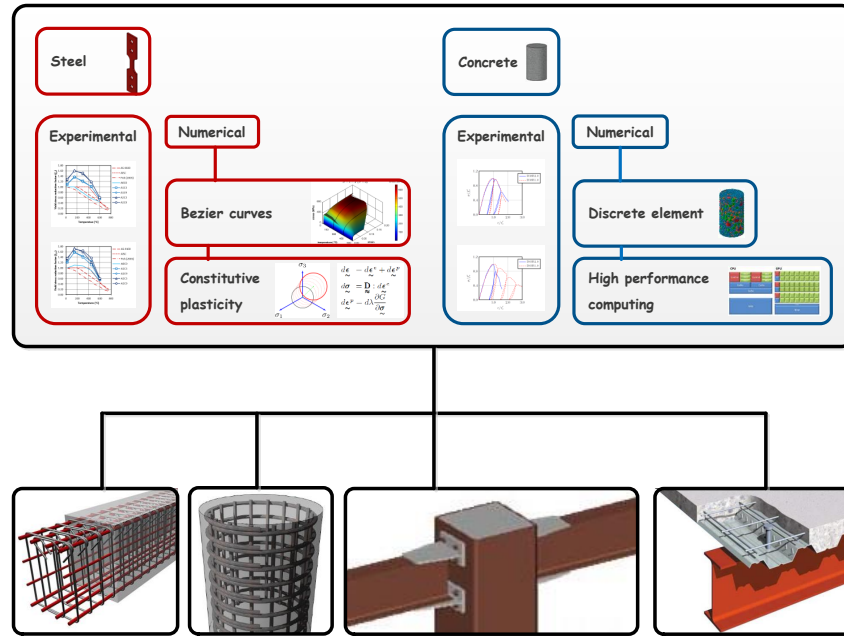
Figure 1.2: Combining studies on steel and concrete for the creation of models for various steel-concrete members.

When it comes to application, material models can be divided into two main categories based on the context that they are meant for:

- Models suitable for engineering purposes.
- Models suitable for research purposes.

Engineering models are usually in the form of empirical equations. These models usually don't have a thermodynamics basis, and are effectively only used to interpolate between experimental results. While the usage of such models is limited, their simplicity is their advantage for engineering design purposes. On the other

hand, for a model to be used for research purposes, it has to have a wider range of applications. Models with this feature are usually based on laws of physics and are hence mathematically more complex than engineering models. Both types of models are dealt with for each of the materials involved in this research.

1.3.2.1   Modelling of Steel

Many empirical stress-strain models exist for steel and stainless steel materials at ambient temperatures. Examples are the models proposed by Ramberg and Osgood [34], Richard and Abbott [35], Rasmussen [36]. Based on these, more complex models have been proposed to represent the behaviour of steel at elevated temperature. An example is the stress-strain-temperature equation developed by Poh [11]. However, such models only treat strain and temperature as independent variables. Whether these models are meant to calculate mechanical properties or stress-strain curves, the temperature variable is 'hard-coded' into these models. Therefore, it is quite difficult to extend them to include additional variables such as the damage parameter sought after in this research. In order to overcome this shortcoming, a generic model was proposed in this thesis based on the Bézier formulation and Bézier curves. By doing this, the inclusion of a damage parameter (or any addition parameter) was drastically simplified.

In addition, constitutive plasticity models were also used in this thesis for research applications. Plasticity models are already well established, however, where they fall short is the lack of a reliable method to determine their intrinsic parameters. Calibrating a material model is the key to accurate simulation, and doing so for a multi-phase response of the material is especially important. This was accomplished in this work using theorems of multi-objective optimisation, whereby the model is calibrated for a tradeoff between its accuracy in simulating monotonic and cyclic behaviour. Moreover, the method is fully automated and does not require any decisions from the operator.

The numerical models developed in this study allow for a more comprehensive stress-strain relationship which takes previous damage and temperature into account. These models can be used to determine the post-earthquake fire-resistant capacity of steel structures.

1.3.2.2 Modelling of concrete

As for an empirical model for concrete, further utilisation of the Bézier formulation was made. Similar to steel, this method was shown to be able to effectively reproduce the changes that mechanical properties of concrete suffer from cyclic damage and temperature exposure.

Although the finite element method has been used in the literature for predicting the behaviour of concrete, it has inherent shortcomings when it comes to simulating discontinuities. Concrete behaviour highly depends on the formation and propagation of cracks, and from a mathematical point of view, cracks can be seen as discontinuities. Therefore, the finite element method will fall short when cracks start to form. On the other hand, the discrete element method can tackle discontinuities quite well. This approach also has the advantage of being able to simulate the interaction between each and every particle. As a result, the discrete element method was selected as a physics based model in this research to simulate the behaviour of concrete at high temperatures. While the model prepared for the means of this thesis is still in early development, it has shown high potential for future applications. Combining the effect of cyclic loading and the effect of elevated temperatures on concrete material is the next step in the development of this model.

As a result of this research, the numerical model developed for concrete can be used to determine the capacity of concrete structures after a post-earthquake fire.

1.4 Thesis Layout

This section describes the layout of the thesis. An overview of the structure is illustrated in Fig. 1.3.

Chapter 1. Introduction	
Part I **Steel**	Chapter 2. Mechanical properties of cyclically-damaged structural mild steel at elevated temperatures
	Chapter 3. Stress-strain-temperature relationship for cyclically-dmaged structural mild steel
	Chapter 4. A multi-objective optimization approach to the parameter determination of constitutive plasticity models
Part II **Concrete**	Chapter 5. Effect of size on the response of cylindrical concrete samples under cyclic loading
	Chapter 6. Effect of temperature on the mechanical properties of concrete under cyclic loading
	Chapter 7. A micro-mechanical parametric study on the strength degredation of concrete using a 2-phase discrete element model
Chapter 8. Conclusions and Future Work	

Figure 1.3: Thesis layout and structure.

Chapter 1: Introduction

This chapter presents an overall view of the thesis. Detailed literature review and comprehensive discussions are given in the chapters that follow. The thesis has been divided into two main parts. Part 1 deals with the work carried out on structural mild steel, while part two involves normal strength concrete. Both parts include experimental and numerical studies, and present the results obtained for each material. With the structure of the thesis being in the form of 'publications', results, discussions and conclusions on the findings have been presented in journal-paper format.

Part 1. Steel

This part of the thesis covers the experimental and numerical works carried out on mild steel. This is presented in the form of three chapters based on three published papers.

Chapter 2: Mechanical properties of cyclically-damaged structural mild steel at elevated temperatures

This article deals with the experimental work carried out to determine the effect of pre-induced damage on the subsequent response of mild steel at elevated tem-

peratures. A literature review is given on cyclic testing and high temperature tests on steel. Based on available evidence, a hypothesis is made on the effect of cyclic loading on the subsequent response at high temperatures. An experimental program is designed and carried out on grade 300 structural mild steel. The variation of mechanical properties are presented as a function of temperature and the level of pre-induced damage. Stress-strain curves at elevated temperatures are also given for cyclically-damaged steel.

Chapter 3. Stress-strain-temperature relation for cyclically-damaged structural mild steel

This study utilises the results of the previous chapter to numerically reconstruct stress-strain curves for any given damage level and temperature value. The model created for this purpose is shown to be robust and versatile. This is accomplished through the use of Bézier formulations and Bézier curves. It is demonstrated that using generic formulations such as Bézier curves eliminates the need for the derivation of complex equations. While the proposed formulation is developed for two independent variables (temperature and damage level), it is possible to further extend it to include addition independent variables. In addition, it is also demonstrated that the Bézier formulation can be used to extrapolate available results to outside the tested range. Aside from that, the proposed model has the advantage of being converted into an inverse relation at no additional computation cost. While most relations given in the literature can only calculate stress as a function of strain, the proposed model is shown to be able to calculate strain as a function of stress, or even strain as a function of stress and temperature. This is arguably the most important feature of the formulation, especially when it comes to analysing full scale structures under fire scenarios, where deformations are to be calculated in terms of the applied loads and a transient temperature.

Chapter 4. A multi-objective optimisation approach to the parameter determination of constitutive plasticity models for the simulation of multiphase load histories

One of the major problems of advanced physical models, such as the theory of plasticity, is the absence of a generic approach for parameter identification. This study develops a general method using established mathematical properties of multi-objective optimisation methods. The stress-strain curves from the previous chapters is used for this purpose. Although using optimisation techniques for parameter determination has been preformed by other researchers in the past, the novelty of the present work is in that it determines the parameters with respect to multiple responses (hence, multi-objective optimisation). In this case, the monotonic response

of the material and its cyclic response are treated at the same time, and while previous researchers have successfully created models that give accurate results for each case individually, this research makes sure that the model has adequate accuracy for both cases at the same time. This is shown by validating the calibrated model against experimental stress-strain curves that were not used in the calibration process.

Part 2. Concrete

The experimental and numerical studies on normal strength concrete is described in this part. This is presented in three chapters based on one published paper and two other papers that are currently under review.

Chapter 5. Effect of size on the response of cylindrical concrete samples under cyclic loading

This study investigates the relationship between sample size and the mechanical properties observed during experimentation. With cylindrical samples being of interest, the diameter and aspect ratio (height-to-diameter) of the samples are taken into account. Doing so gives insight, not only into the variation of monotonic and cyclic properties in terms of size parameters, but also into the reproducibility of the data (data scatter). This can be viewed as a form of sensitivity analysis and the gained knowledge is of value for future experimental work. This work also looks into the damage index as a measure of the induced cyclic damage and compares different definition of this index with one another.

Chapter 6. Effect of pre-induced cyclic damage on the mechanical properties of concrete exposed to elevated temperatures

The effect of temperature on partially damaged samples is investigated in this chapter. The experimental program of this study follows the previous chapter by exposing the cyclically-damaged samples to elevated temperatures. Once the material has been sequentially subjected to the two actions (cyclic loading and high temperature), its residual mechanical properties are determined through compression tests. Bézier curves are used to express the relation between residual properties in terms of temperature and damage level.

Chapter 7. A micro-mechanical parametric study on the strength degradation of concrete by using a 2-phase discrete element model

In this study, a 2-dimensional discrete element model is developed to simulate the effect of high temperature on concrete. With aggregate particles and mortar particles constituting the 2 phases of the model, the effect of high temperature is induced into the virtual sample by two means: thermal incompatibility of the aggregate-paste structure and degradation of the mortar matrix. Temperature is raised to different target values using different values for the coefficient of thermal expansion for the aggregates and the mortar matrix. Mechanical properties are determined under compressive loading. The observations made in this work reveal the effectiveness of the discrete element approach in modelling the behaviour of concrete under the effect of high temperatures. These lay the basis for developing a more comprehensive model for the prediction of the damage caused by subsequent action of cyclic loading and elevated temperatures on concrete.

Chapter 8. Conclusions and future work

The main outcomes of this thesis are summarised in the final chapter. These are either based on experimental results, or numerical simulations. This chapter also gives a list of recommendations for future work on the subject matter. The recommendations are justified through the results of this thesis, and either relate to experimentation or numerical modelling.

References

[1] Charles Scawthorn, Thomas D ORourke, and Frank T Blackburn. The 1906 san francisco earthquake and fireenduring lessons for fire protection and water supply. *Earthquake Spectra*, 22(S2):135–158, 2006.

[2] Beatrice Faggiano, Matteo Esposto, and Federico M Mazzolani. Risk assessment of steel structures under fire. In *14th World Conference on Earthquake Engineering, Beijing, PR of China, paper*, number S19-015, 2008.

[3] Takeyoshi Tanaka. Characteristics and problems of fires following the great east japan earthquake in march 2011. *Fire Safety Journal*, 54:197–202, 2012.

[4] Mehrdad Memari, Hussam Mahmoud, and Bruce Ellingwood. Post-earthquake fire performance of moment resisting frames with reduced beam section connections. *Journal of Constructional Steel Research*, 103:215–229, 2014.

[5] Gaetano Della Corte, Raffaele Landolfo, and Federico M Mazzolani. Post-

earthquake fire resistance of moment resisting steel frames. *Fire Safety Journal*, 38(7):593–612, 2003.

[6] Raul Zaharia and Dan Pintea. Fire after earthquake analysis of steel moment resisting frames. *International Journal of Steel Structures*, 9(4):275–284, 2009.

[7] Umesh Kumar Sharma, Pradeep Bhargava, Bhupinder B Singh, Yogendra Y Singh, Virendra Kumar, Praveen Kamath, Asif Usmani, Jose Torero, Martin Gillie, Pankaj Pankaj, et al. Full-scale testing of a damaged reinforced concrete frame in fire. *Proceedings of the ICE-Structures and Buildings*, 165(7):335–346, 2012.

[8] Reza Imani, Gilberto Mosqueda, and Michel Bruneau. Experimental study on post-earthquake fire resistance of ductile concrete-filled double-skin tube columns. *Journal of Structural Engineering*, page 04014192, 2014.

[9] Negar Elhami Khorasani, Maria EM Garlock, and Spencer E Quiel. Modeling steel structures in opensees: Enhancements for fire and multi-hazard probabilistic analyses. *Computers & Structures*, 157:218–231, 2015.

[10] Qian-Yi Song, Amin Heidarpour, Xiao-Ling Zhao, and Lin-Hai Han. Post-earthquake fire behavior of welded steel i-beam to hollow column connections: An experimental investigation. *Thin-Walled Structures*, 2015.

[11] Weng K Poh. Stress-strain-temperature relationship for structural steel. *Journal of materials in civil engineering*, 13(5):371–379, 2001.

[12] Kristian Dahl Hertz. Concrete strength for fire safety design. *Magazine of Concrete Research*, 57(8):445–453, 2005.

[13] Ju Chen and Ben Young. Stress–strain curves for stainless steel at elevated temperatures. *Engineering Structures*, 28(2):229–239, 2006.

[14] Mohammad Abdel-Karim. An evaluation for several kinematic hardening rules on prediction of multiaxial stress-controlled ratchetting. 26(5):711–730, 2010.

[15] Venkatesh Kodur, Mahmud Dwaikat, and Rustin Fike. High-temperature properties of steel for fire resistance modeling of structures. *Journal of Materials in Civil Engineering*, 22(5):423–434, 2010.

[16] Jiří Chlouba and František Wald. Temperature of a partially embedded connection subjected to fire. *Fire Safety Journal*, 54:121–129, 2012.

[17] Markus Knobloch, Diego Somaini, Jacqueline Pauli, and Mario Fontana. Numerical analysis and comparative study of the cross-sectional capacity of structural steel members in fire. *Journal of Structural Fire Engineering*, 3(1):19–36, 2012.

[18] Markus Knobloch, Jacqueline Pauli, and Mario Fontana. Influence of the strain-rate on the mechanical properties of mild carbon steel at elevated temperatures. *Materials & Design*, 49:553–565, 2013.

[19] Edison Osorio, Jesús M Bairán, and Antonio R Marí. Lateral behavior of concrete under uniaxial compressive cyclic loading. *Materials and structures*, 46(5):709–724, 2013.

[20] Yaopeng Wu and Bo Wu. Residual compressive strength and freeze–thaw resistance of ordinary concrete after high temperature. *Construction and Building Materials*, 54:596–604, 2014.

[21] AS/NZS 3679.1. *Structural steel, Part 1: Hot-rolled bars and sections.* Australian and New Zealand standard, Sydney, NSW, 2010.

[22] BHP. *Hot rolled products.* Broken Hill Proprietary Limited, Melbourne, 1998.

[23] ASTM E21-92. *Standard test methods for elevated temperature tension tests of metallic materials.* Annual book of ASTM standards. American Society of Testing and Materials, Philadelphia, PA, 1998.

[24] ASTM E606-92. *Standard practice for strain-controlled fatigue testing.* Annual book of ASTM standards. American Society of Testing and Materials, Philadelphia, PA, 1998.

[25] Sajjad Hosseini, Amin Heidarpour, Frank Collins, and Christopher R Hutchinson. Effect of strain ageing on the mechanical properties of partially damaged structural mild steel. *Construction and Building Materials*, 77:83–93, 2015.

[26] ASTM C192/C192M-02. *Standard practice for making and curing concrete test specimens in the laboratory.* Annual book of ASTM standards. American Society of Testing and Materials, Philadelphia, PA, 2002.

[27] ASTM C39/C39M-03. *Standard test method for compressive strength of cylindrical concrete specimens.* Annual book of ASTM standards. American Society of Testing and Materials, Philadelphia, PA, 2003.

[28] Qianmin Ma, Rongxin Guo, Zhiman Zhao, Zhiwei Lin, and Kecheng He. Mechanical properties of concrete at high temperaturea review. *Construction and Building Materials*, 93:371–383, 2015.

[29] Long T Phan and Nicholas J Carino. Effects of test conditions and mixture proportions on behavior of high-strength concrete exposed to high temperatures. *ACI Materials Journal*, 99(1), 2002.

[30] Mihail Petkovski. Effects of stress during heating on strength and stiffness of concrete at elevated temperature. *Cement and Concrete Research*, 40(12): 1744–1755, 2010.

[31] Ali Ergün, Gökhan Kürklü, Başpınar M Serhat, and Mohamad Y Mansour. The effect of cement dosage on mechanical properties of concrete exposed to high temperatures. *Fire Safety Journal*, 55:160–167, 2013.

[32] Yi-Hai Li and Jean-Marc Franssen. Test results and model for the residual compressive strength of concrete after a fire. *Journal of Structural Fire Engineering*, 2(1):29–44, 2011.

[33] Mohamed Salah Dimia, Mohamed Guenfoud, Thomas Gernay, and Jean-Marc Franssen. Collapse of concrete columns during and after the cooling phase of a fire. *Journal of Fire Protection Engineering*, page 1042391511423451, 2011.

[34] Walter Ramberg and William R Osgood. Description of stress-strain curves by three parameters. Technical Report 902, National advisory committee for aeronautics, Washington, DC, 1943.

[35] Ralph M Richard and Barry J Abbott. Versatile elastic-plastic stress-strain formula. *Journal of the Engineering Mechanics Division*, 101(4):511–515, 1975.

[36] Kim JR Rasmussen. Full-range stress–strain curves for stainless steel alloys. *Journal of Constructional Steel Research*, 59(1):47–61, 2003.

Part I:

Steel

CHAPTER 2

Mechanical properties of cyclically-damaged structural mild steel at elevated temperatures

Contents

Monash University

Declaration for Thesis Chapter 2

Declaration by candidate

In the case of Chapter 2, the nature and extent of my contribution to the work was the following:

Nature of contribution	Extent of contribution (%)
Establishing methodologies, Experimental work, Data analysis, Write-up and revision	70%

The following authors contributed to the work. If co-authors are students at Monash University, the extent of their contribution in percentage terms must be stated.

Name	Nature of contribution	Extent of contribution (%)
Dr. Amin Heidarpour	Developing ideas Revision Financial support	
Prof. Xiao-Ling Zhao	Revision Financial support	

The undersigned hereby certify that the above declaration correctly reflects the nature and extent of the candidate's and co-authors' contributions to this work.

Candidate's signature: ■   **Date:** 24/09/2015

Main supervisor's signature: ■   **Date:** 24/09/2015

Abstract

The mechanical response of a structural element not only depends on the inherent properties of the materials which constitute the element, but also on the history of any loads it had been previously subjected to. An important instance of this is the response of steel structures under post-earthquake fire. This research aims to investigate the potential changes that the mechanical properties of structural grade mild steel experience under such a loading sequence. The experimental results presented in this paper indicate that a prior history of cyclic loading significantly affects the proceeding ductility and strength of grade 300 steel at high temperatures. This implies that any history of cyclic loading should be included in the post-earthquake fire-resistant design of structures.

2.1   Introduction

In view of the high probability of fires following an earthquake and the extent of the damage associated to them, interest has been shown towards a better understanding of these extreme scenarios. One recent investigation towards this understanding is the work of Tanaka [1] which involves the characterisation and categorization of the different types of fire that followed the 2011 Great East Japan Earthquake.

In the context of structural design, fire is generally considered as an independent event regardless whether it was spontaneous or preceded by an earthquake. However, with design codes being directed towards the performance based design philosophy, distinction should be made between ordinary fire and seismic-induced fire. While seismic-induced fire resistance still remains a single design objective, its relevant guidelines and expressions must constitute elements of the fire as well as the preceding seismic loading. Moreover, one can also argue that even if an earthquake is not succeeded by a fire, appropriate guidelines are still necessary to determine the fire resistance capacity of the structure and to assess the need for fire related rehabilitation of a seismically damaged structure.

One aspect of fire related research involves the assessment of temperature distribution and propagation within structural elements. Such an assessment was carried

out by Ding and Wang [2] for unprotected connections and by Chlouba and Wald [3] for partially embedded connections. The result of such analyses is the temperature profile within a structural element. On the other hand, another aspect of fire related research is the assessment of member capacity degradation at elevated temperatures. This degradation is due to the thermo-mechanical phase changes that structural steel exhibits at elevated temperatures. An example of such research is the work of Ding and Wang [4] on different types of composite connections. This work involved transient state experiments, whereby the connection is subjected to a constant load as the temperature is increased. It was concluded that even the most simple connection types are able to develop substantial catenary action before ultimate failure.

While experiments similar to the one done by Ding and Wang [4] only involve the fire resistance of structural elements, research work has also been carried out on the post-earthquake fire resistance of steel structures and their elements. The post-earthquake fire resistance of plane frames was numerically evaluated by Della Corte et al. [5]. In this work, seismic-induced damage was modelled by decomposing the total damage into a geometrical and a mechanical component. Fire analyses were then carried out on a structure containing the superposition of these damage components. The work of Zaharia and Pintea [6] is another example of research on post-earthquake fire resistance carried out in the structural scale. This work concluded that the level of seismic damage affects the fire resistance time of a structure. As an example for the post-earthquake fire resistance in the structural element scale, one can point to the work of Pucinotti et al. [7], which investigated the seismic-induced fire resistance of composite welded beam-to-column joints.

Regarding the behaviour of structural elements, when comparing the available data on fire resistance as opposed to post-earthquake fire resistance, the former clearly dominates the latter. Similarly, this is also true in the material scale when it comes to the behaviour of structural steel at high temperatures and its post-cyclic behaviour at high temperatures. However, although not much data is available for the material response of structural grade steel under a post-earthquake fire scenario, extensive effort has been made for the understanding of its behaviour at elevated temperatures. For example, the mechanical properties of structural steel at elevated temperatures were investigated by Outinen and Maekelaeinen [8]. This work not only involves the comparison of steady-state and transient-state tests, but also examines the mechanical properties after cool-down. The mechanical properties of high strength structural steel (750 MPa yield strength) at elevated temperatures were compared to those of mild steel (360 MPa yield strength) by Chen et al. [9].

This work concluded that up to temperatures of 500°C the reduction factors concerning the yield strength and elastic modulus are quite similar for the two steel grades. Various high-temperature relationships expressed in American and European standards were compared with respect to experimental data by Kodur et al. [10]. These included mechanical properties such as strength, as well as thermal properties such as specific heat and thermal conductivity. This work also compared the overall fire resistance predicted by different design codes.

In contrast to the above mentioned investigations on the fire resistance of steel, this paper deals with the post-earthquake fire-resistance of this material. It should be noted that when it comes to the definition of post-earthquake fire, this paper incorporates it in the same sense that is defined by Della Corte et al. [5], i.e. the state of high temperatures succeeding a cyclic loading history at ambient temperature. This is in contrast to another definition used by for example Kumar et al. [11], which involves the state of ambient temperature succeeding a cyclic loading history and a heating-cooldown cycle.

In terms of uncertainty, earthquake and fire are both extremely random events. Therefore, before any attempt to investigate their effects, they have to be converted into a more quantifiable form. For this purpose, in this paper, the post-earthquake fire scenario is replaced by a two-phase loading history that includes a cyclic load at ambient temperature followed by a monotonic tensile load at elevated temperature. Three variables have been proposed for consideration in this program: the amplitude of the cyclic load representing the intensity of the structures oscillations during an earthquake, the number of cycles representing the duration of the oscillations, and the temperature of the tensile phase of loading to represent the action of fire. Mechanical properties are then derived under different combinations of these variables and the results are plotted and compared to the ones obtained without a prior history of cyclic loading.

2.2 Experimental program

2.2.1 Test material and specimen

All the specimens used in this study were made of grade 300 mild steel [12], approximately equivalent to ASTM A633A, taken from the flange of 200UB22.3 hot rolled

Table 2.1: Chemical composition of grade 300PLUS steel.

C	Si	Mn	S	P
0.25%	0.50%	1.60%	0.040%	0.040%
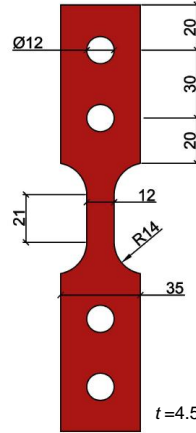
Figure 2.1: Sample geometry (in mm)

sections [13]. The chemical composition of grade 300 steel is given in Table 2.1. Preparation of the samples was consistent with the requirements of ASTM E21-92 [14] and ASTM E606-92 [15]. The specimen geometry is illustrated in Fig. 2.1. Actual dimensions of the cross section of the coupon specimens were measured using a micrometer. Both faces of each specimen were ground to give uniform thickness and a smooth finish across the entire surface. Specimens were restrained by means of two 12 mm high strength bolts at each end.

2.2.2   Test method

There are two major methods of performing elevated temperature tests: transient-state, where the temperature is increased while the sample is under a constant load and steady-state, where the load is increased as the temperature remains constant. While the transient state test method reflects a fire scenario more realistically, the steady-state method is commonly used since it is easier to perform, provides stress-strain curves directly and can be readily used to calibrate models. The steady-state test method is therefore used in this research work.

All samples are subjected to a two-phase load history involving an ambient-temperature cyclic load (phase 1), followed by an elevated temperature monotonic tensile load (phase 2). The test set-up used in this work to perform both phases of loading is

shown in Fig. 2.2. This strain-controlled loading history is illustrated in Fig. 2.3a as a function of time, whereby $\Delta\varepsilon_c$, N_c and T_m act as the test variables. The outcome of this loading history is the variation of stress with time given in Fig. 2.3b. Note that in these figures, the dashed line represents the ambient-temperature cyclic phase of the load history, while the solid line represents the elevated temperature monotonic tensile phase. With all of the samples being of the same material and dimensions, the difference between test cases is in their loading histories. Hence, different test cases are denoted in the form of A□C□_T□, where the blank box (□) in front of A, C and T are respectively filled in by the strain amplitude (in percentage) of the first phase, the number of cycles of the first phase and the temperature (in degrees Celsius) of the second phase. For instance, A1C3_T020 represents a loading history with 3 cycles of 1% strain amplitude followed by tension at room temperature, and A2C9_T600 represents a loading history with 9 cycles of 2% strain amplitude followed by tension at 600°C. Fig. 2.4 illustrates the stress-strain response under the A1C3_T020 load history. Similar to Fig. 2.3, the dashed line in Fig. 2.4 represents the cyclic phase and the solid line represents the tensile phase. It is observed in Fig. 2.4 that peak stresses tend to increase as the strain-controlled cyclic loading progresses. This indicates that the material has cyclic hardening properties. For cyclically hardening material, if loading is carried out in stress-controlled cycles, peak strain values will drop as the cycles progress.

A minimum of two samples were tested for each individual case and their results were averaged. However, if for a specific case, any of the mechanical properties (elastic modulus, yield stress, etc.) had a deviation of more than 5% from the average value, a third sample was also tested and included in the averaging.

2.2.3   Cyclic phase at ambient temperature

For the cyclic phase, a special fixture was designed to prevent the specimens from buckling about the weak axis as they go into compression. This fixture was comprised of two 12 mm plates with aligned holes in order to be fastened by appropriate bolts (Fig. 2.5). The inner faces of these two plates which would be in contact with the specimen were polished and greased to yield minimum friction. Loads were applied by an Instron test machine (model 5982) with a capacity of 100 kN. Axial force values were attained by the machine's built-in transducer, while strains were accumulated by a non-contact MTS laser extensometer (model LX1500). The laser extensometer was targeted towards the thickness of the sample with an effective
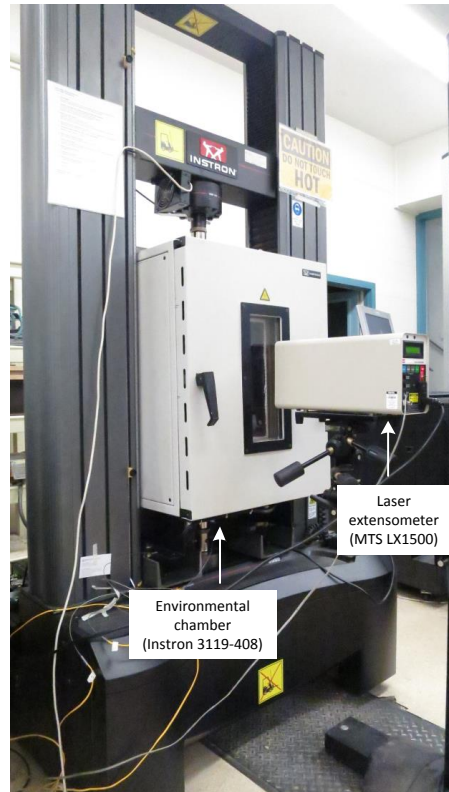
Figure 2.2: Test set-up for the two-phase experimental program.
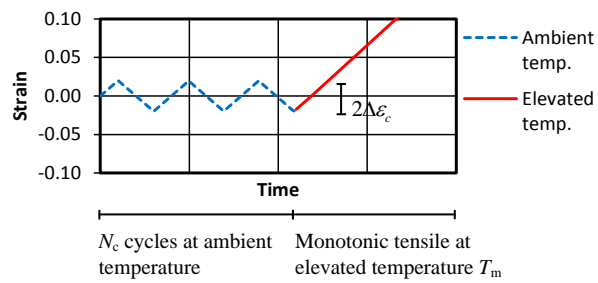
(a)
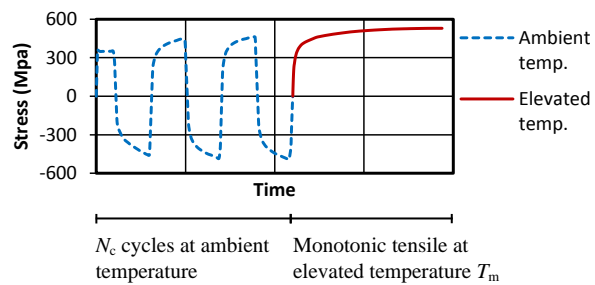
(b)

Figure 2.3: Time variation for the multi-phase loading history (a) Strain variations and (b) Stress variation.
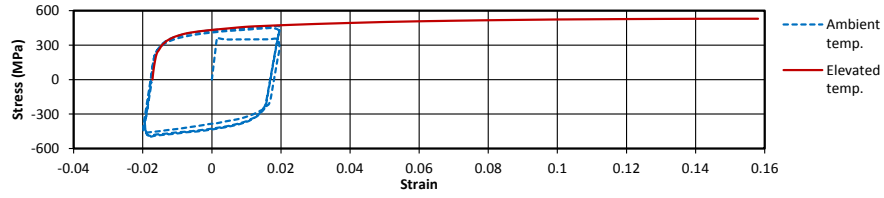
Figure 2.4: Stress-strain hysteresis curve for sample A2C3_T020.
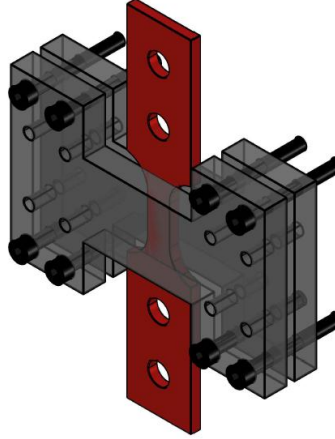
Figure 2.5: Sample placement within the anti-buckling fixture.

gage length equal to 18 mm. Tests were carried out in displacement control, with the displacement being appropriately adjusted for the strain rate at yield to be equal to $10^{-4}\,\mathrm{s}^{-1}$, which is within the $0.005 \pm 0.002\,\mathrm{min}^{-1}$ range specified by ASTM E21-92 [14]. Two different values were used for the strain amplitude ($\Delta\varepsilon_c$), namely 1% and 2%, whereby the 2% strain value coincides with the onset of hardening, and the 1% strain value is midway between initial yield and the onset of stress hardening. These values are considered to be reasonable as means for design as well as for model development. As for the number of cycles, two different values of $N_c = 3$ and $N_c = 9$ were used. These values were selected with respect to cyclic stabilisation of the stress-strain response, which for this material happened at around 6 cycles. Hence, 3 cycles is a state where the material has not yet become cyclically stabilised and 9 cycles is past stabilisation. Note that as shown in Figs. 2.3a and b, the cyclic phase of loading ends at zero-stress and the tensile phase starts from that very same point.
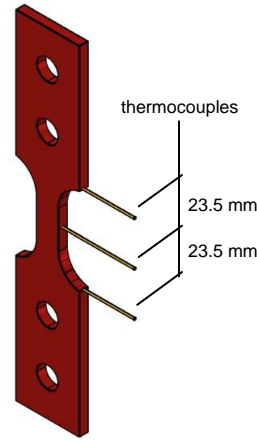
Figure 2.6: Thermocouple placement at three locations on the sample.

2.2.4   Post-cyclic tensile phase at elevated temperature

Tensile tests were carried out as steady-state experiments, i.e. loading at constant temperature. The setup of the experiment was similar to the cyclic stage. However, since there was no need for the anti-buckling fixture, it was removed prior to starting the test in order to have a visual on the initiation of necking. The temperature was raised by means of an Instron environmental chamber (model 3119-408) with a maximum capacity of 600°C. The variable for the monotonic tensile phase is the temperature at which it was performed (T_m in Fig. 2.3). Heating was carried out at a rate of $10°\text{C}\,\text{min}^{-1}$ up to 4 different elevated temperatures, namely 150°C, 300°C, 450°C, 600°C. Thermal expansion was allowed by maintaining a zero load as the temperature increased. During this, the temperature of the sample was logged using three thermocouples attached to three different locations on the sample's surface (Fig. 2.6). Loading was initiated once the temperature of these three points had stabilised with a variance of less than 2% relative to the target temperature. The time duration required to reach this stabilised state varied from 20 minutes for a target temperature of 150°C to 90 minutes for 600°C.

With the loading being in displacement control, the displacement rate was accordingly adjusted for the strain rate to fall within the range of $0.005 \pm 0.002\,\text{min}^{-1}$ specified by ASTM E21-92 [14]. Strain values were accumulated as before using the non-contact laser extensometer. Thermal elongations have been removed from all the strain values reported in this paper. Loading as well as data accumulation was continued at a frequency of 4 Hz until failure. However, only the data attained up to the ultimate strength are presented here, since strain readings after the initiation of necking become significantly inaccurate.

2.3   Results and discussion

The variation of different mechanical properties are derived and discussed in this section. With the properties of the monotonic tensile phase at elevated temperature being of primary interest, Fig. 2.7 is presented to introduce the selected properties. These include the elastic modulus (E), yield stress (f_{pr}, $f_{0.5}$, $f_{1.5}$ and $f_{2.0}$), ultimate stress (f_u), ultimate strain (ε_u, corresponding to f_u) and tangent moduli ($E_{2.0}$, $E_{4.0}$). Results are all given in the form of reduction factors, with the base values being the ones obtained from sample A0C0_T020 which is essentially a standard tensile test are room temperature with no history of cyclic loading.

For the sake of discussion, in regards to the sample codes proposed in the form of A□C□_T□, whenever one of the parameter variables is substituted with a blank box, it should be taken to mean the entire range of values for that parameter. For example, A1C3_T□ is equivalent to saying all of the samples with 1% amplitude and 3-cycle loading history, regardless of the temperature of the second phase.

Another issue worth mentioning at this point is that although it is reasonable to assume that at some point the mechanical transitions caused by high temperatures become dominant over the changes caused by the cyclic history, as it is discussed later, this appears to not happen until the very end of the range covered in this program, i.e. 600°C.

Before presenting the results, it is also worth mentioning that given the chemical composition of the steel used, this material gains hardened properties as the temperature rises up to about 150°C. However, the hardened properties tend to diminish as the temperature approaches 380°C, which afterwards, the material starts to soften. This behaviour was witnessed during testing and is observed in the following results. This behaviour is also reported by Poh [16] on the same steel grade and is discussed in [17].

Figs. 2.9, 2.10, 2.11 and 2.12 illustrate the variation of each of the aforementioned tensile properties as a function of the test parameters, i.e. $\Delta\varepsilon_c$, N_c and T_m. As mentioned before, all values are normalised using the corresponding value for A0C0_T020.
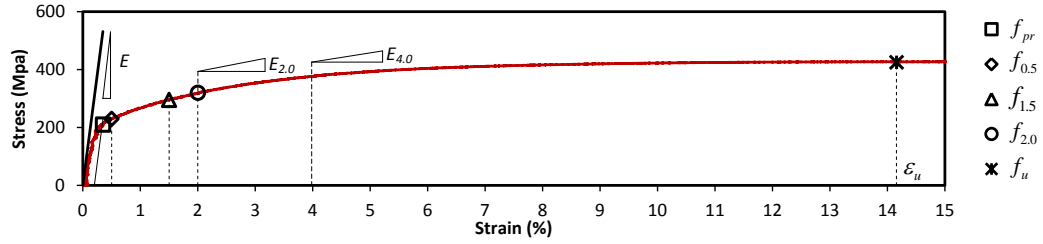
Figure 2.7: Selected mechanical properties relative to the stress-strain curve.

2.3.1 Full stress-strain curves

For comparison reasons, the full range stress-strain curve of samples A0C0_T020, A0C0_T450, A2C9_T020 and A2C9_T450 are presented alongside each other in Fig. 2.8. The changes that stress-strain curves exhibit due to elevated temperature as well as a prior history of cyclic loading is clearly seen in this figure. These changes include, the decrease in yield stress, ultimate stress and ultimate strain caused by heat, as well as the increase in yield stress and decrease in ultimate strain caused by cyclically-induced damage.

Note that all of the following results, specifically strain-based ones, were taken with respect to the original state of zero strain. In other words, all strain values are absolute strains as opposed to being relative to the strain at the beginning of the high temperature tensile phase. Consequently, the strain at the beginning of the high temperature tensile phase is not zero. This can be deduced by observing Fig. 2.8. The reason for this is mainly due to the fact that ending the cyclic phase at zero stress is more feasible than at zero strain. However, this does not raise concern over the strain based parameters, such as the ultimate strain, since it has been long established that even at elevated temperatures, stress-strain curves trace their original paths upon unloading and reloading [18], especially if the unloading is within the elastic region, as is in this case.

2.3.2 Elastic modulus

Fig. 2.9 illustrates the variation of the elastic modulus with temperature in the form of a reduction factor. This reduction factor is defined as the ratio of the elastic modulus at an elevated temperature to its value at ambient temperature. The monotonic decrease of the elastic modulus as the result of increasing temperature
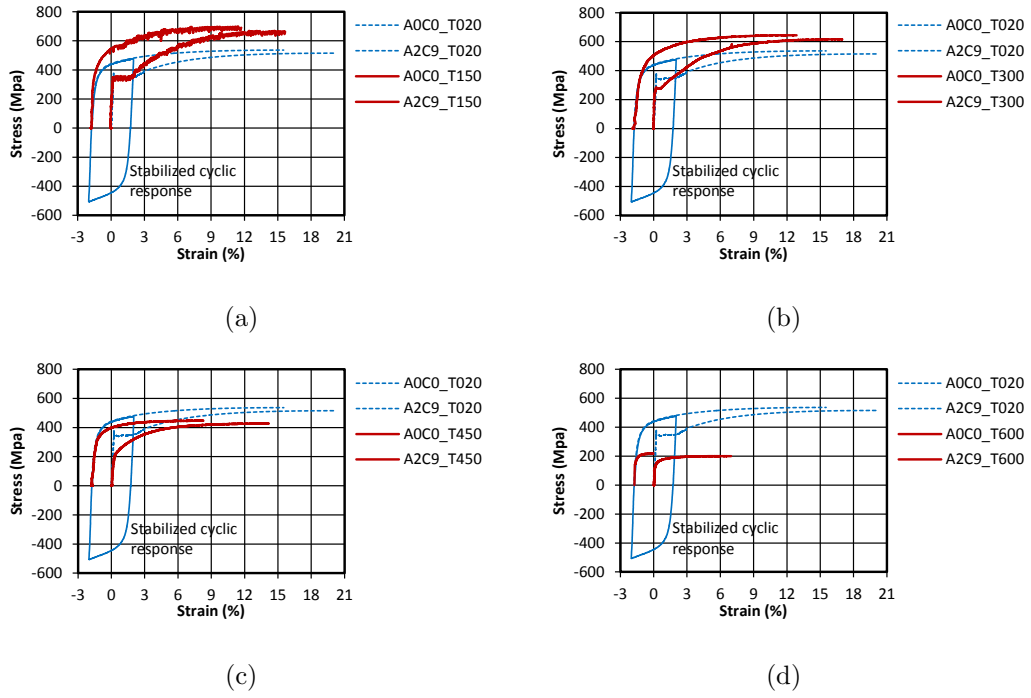
Figure 2.8: Stress strain curves up to ultimate stress and the effect of pre-induced damage. At (a) 150°C, (b) 300°C, (b) 450°C and (d) 600°C.

is the expected behaviour and is observed here. In this figure, the variation of the elastic modulus reduction factor is compared to the expressions given by the AS4100 [19], Eurocode 3 (EC3) [20] and AISC [21] standards, as well as the expression given by Poh [16]. Note that the variations observed in this work are very similar to the variations reported by Poh [16], which is predictable, since both curves are results from testing the same material, i.e. grade 300 steel. However, compared to the AS4100 and EC3 design expressions, the values obtained from this study are higher within the entire tested range $(20 - 600°C)$. Note, that as opposed to other mechanical properties, the existence of a prior history of cyclic loading has no effect on the elastic modulus. This is confirmed in Fig. 2.9 by the small scatter of data points obtained using different levels of pre-induced damage at each temperature value.

2.3.3 Yield stress

In the absence of a uniform definition of yield stress given by different design codes, researchers tend to present and compare stress values at different strain levels, namely the 0.2% proof stress as well as stresses corresponding to 0.5%, 1.5% and 2.0% strain values [22, 23]. These are all defined in Fig. 2.7. The same approach has been taken in this paper, whereby reduction factors for stresses corresponding to
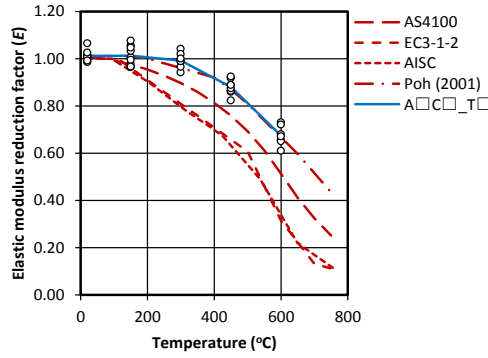
Figure 2.9: Elastic modulus reduction factor.

different strain levels are presented in Figs. 2.10a to d. The 0.2% proof stress (f_{pr}) is defined as the intersection point of the stress-strain curve and the proportional line offset by 0.2% strain. The 0.5%, 1.5% and 2.0% strengths denoted by $f_{0.5}$, $f_{1.5}$ and $f_{2.0}$, correspond to stress values at each specific strain level. The values are all obtained directly from the test results of each specimen and then averaged for each test case. For cases where serration was observed in the stress-strain curve (all the A□C□_T150 test cases) stress values were obtained by averaging the stress over a small vicinity of the desired point. Using this method, a smooth curve was attained for the entire data range, wherein the desired stress value was taken from.

Note that in Fig. 2.10, the solid line with no markers represents test cases without a cyclic history (A0C0_T□). In regards to the A0C0_T□ test cases, it is observed that for f_{pr} and $f_{0.5}$, the reduction factor decreases monotonically as the temperature rises, however, for $f_{1.5}$ and $f_{2.0}$, the reduction factor slightly rises at first and then starts to drop as the temperature further increases. It is also observed that for f_{pr} and $f_{0.5}$, the A0C0_T□ test cases are more consistent with AS4100 [19] and Poh [16], while the data corresponding to $f_{1.5}$ and $f_{2.0}$ seem to follow the EC3 [20] and AISC [21] expressions. As opposed to this, the solid lines with markers represent test cases with a history of cyclic loading. The significance of having a previous history of cyclic loading is clearly observed in Fig. 2.10, whereby f_{pr}, $f_{0.5}$ $f_{1.5}$ and $f_{2.0}$ all exhibit a substantial increase as a result of the prior cyclic history. Moreover, the results also show that within the ranges considered in this study, stress values are more affected by the amplitude of the cyclic phase ($\Delta\varepsilon_c$) than the number of cycles (N_c). For all of these cases, the value of f initially increases as the temperature rises from ambient temperature, reaches its maximum at around 150°C and begins to drop afterwards. This rise and fall of the yield stress is attributed to the hardened properties of mild steel caused by phase changes mentioned before. By comparing to the expressions given by AS4100 [19], EC3 [20], AISC [21] and Poh [16], it is

(a)

(b)

(c)

(d)
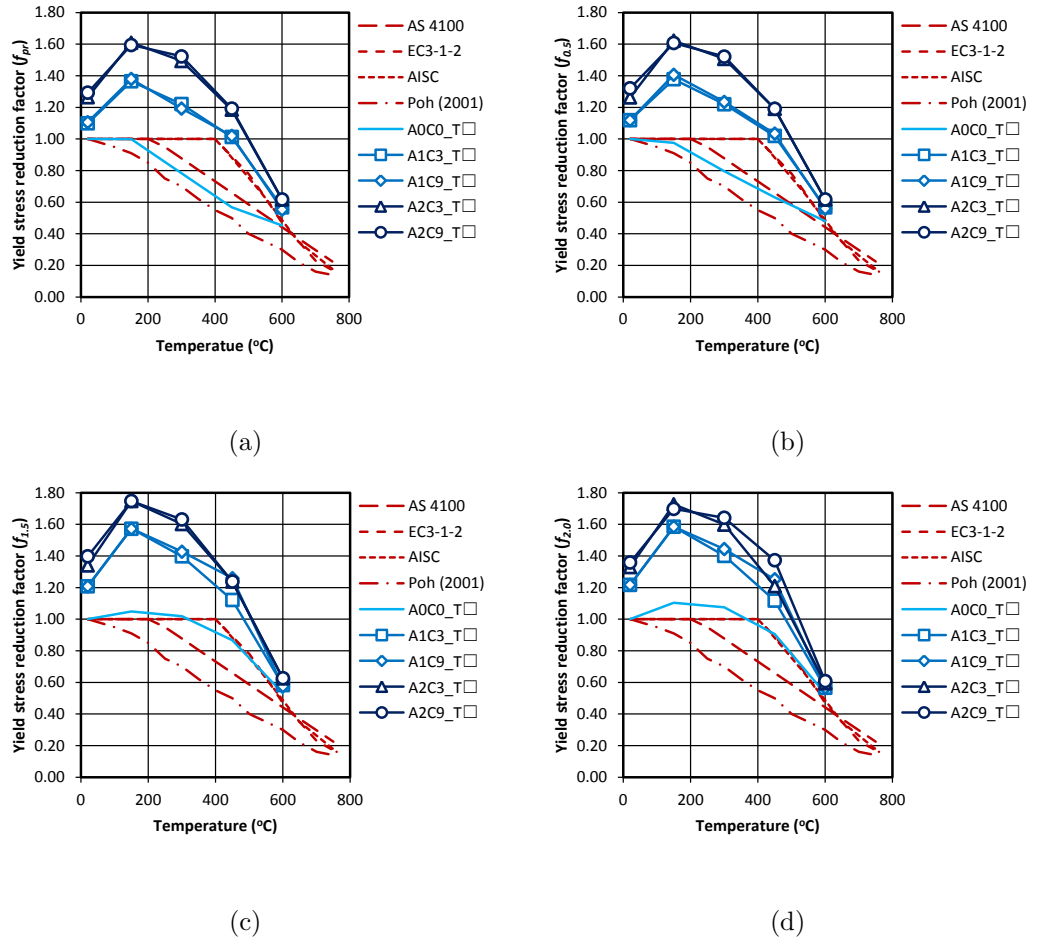
Figure 2.10: Reduction factor for different stress levels. (a) Proof stress f_{pr}, (b) $f_{0.5}$ corresponding to $\varepsilon = 0.5\%$, (c) $f_{1.5}$ corresponding to $\varepsilon = 1.5\%$, (d) $f_{2.0}$ corresponding to $\varepsilon = 2.0\%$.

clearly observed that none of the expressions are suitable for samples with a cyclic history, whereby the test results obtained for these cases can be up to 100% higher than the values predicted by those expressions. As discussed in Section 2.3.2, for the elastic modulus, it was outlined that the variation of the A0C0_T□ curve agrees well with the expression given by Poh [16], which was associated to the fact that the same material was used in both investigations. However, when comparing the same curves, this time for yield strength, the previous agreement is not observed. This can be traced back to the fact that the variation of the yield stress given by Poh [16] is not in fact the variation that was observed in experiments, but the variation of the yield stress that was used in the mathematical expressions used to describe the stress-strain curves.

Another prominent feature of the yield stress variations depicted in Fig. 2.10 is observed at the near end of the temperature range, i.e. 600°C. At this temperature, it appears that all A□C□_T□ curves converge with the A0C0_T□ curve. This implies that at this temperature, having a cyclic history is predominated by the high temperature, and hence the yield strength effectively becomes a function of only one variable which is the temperature.

2.3.4 Ultimate stress

The ultimate stress is an important parameter since it directly affects the ductility and the ultimate capacity of a structure. The variation of ultimate stress, denoted by f_u, is presented in Fig. 2.11a. The most noticeable property of these graphs is the fact that the existence of a cyclic history has negligible effect on the ultimate stress. This is deduced by the fact that all of the data with cyclic history follow the same curve as the one without a cyclic history (A0C0_T□). It has already been mentioned that this type of steel tends to attain hardening properties up to a temperature of 150°C. This is clearly evident in Fig. 2.11 for all of the samples, regardless the existence of a history of cyclic loading or not.

2.3.5 Ultimate strain

As the counterpart for the ultimate stress f_u, the variation of the ultimate strain ε_u with temperature is illustrated in Fig. 2.11b. The ultimate strain is defined as the strain corresponding to the ultimate stress, and is also an important parameter

(a)   (b)
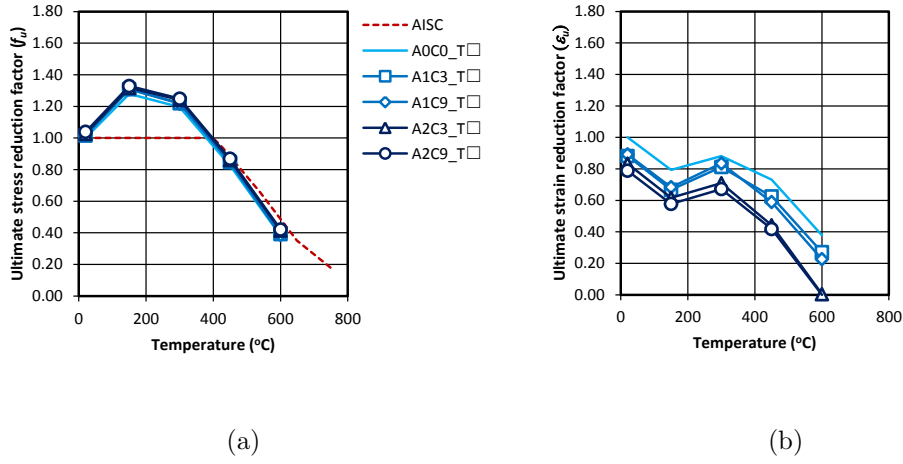
Figure 2.11: Reduction factor for (a) Ultimate stress and (b) Ultimate strain.

when evaluating the ductility of a structure, or in other words, its ability to reach its ultimate capacity. Fig. 2.11b shows a fluctuation of the ultimate strain with rising temperature for sample A0C0_T□ that had no previous cyclic history. With the presence of a cyclic history, the same pattern is followed, however, with a significant reduction in the value of ε_u as the cyclic-phase parameters ($\Delta\varepsilon_c$ and N_c) are increased. While the ultimate stress was observed to not be affected by a previous history of cyclic loading (Fig. 2.11a), the ultimate strain shows to be influenced by such a history (Fig. 2.11b). Moreover, with respect to the variables of the cyclic phase, while the number of cycles (N_c) and the amplitude of the cycles ($\Delta\varepsilon_c$) both affect the ultimate strain, the influence of the latter is more prominent than the former.

The sensitivity of ε_u to the cyclic loading history is due to the movement of dislocations within the crystal structure of the material as the cyclic load goes well into the plastic region and then changes direction [24]. This by itself causes an increase in strength (for cyclically hardening materials) and a decrease in ductility, which eventually leads to the decrease of ultimate strain.

2.3.6   Tangent modulus

Fig. 2.12 presents the tangent modulus of the stress-strain curve at strain levels of $\varepsilon = 2.0\%$ and $\varepsilon = 4.0\%$, respectively denoted by $E_{2.0}$ and $E_{4.0}$, as a function of $\Delta\varepsilon_c$, N_c and T_m. As was the case for other mechanical properties, hardening characteristics can also be seen for both of the tangent moduli at temperatures around 150°C. Another feature observed in Figs. 2.12a and b is that the existence

<div align="center">(a)   (b)</div>
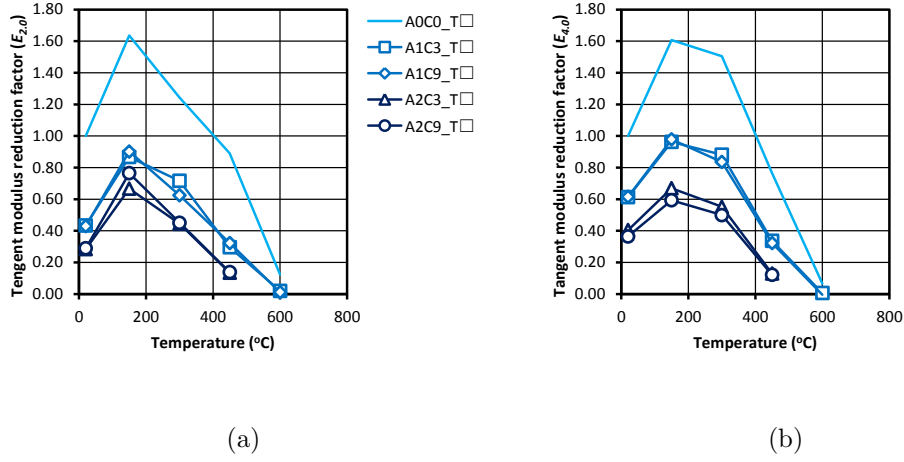
Figure 2.12: Reduction factor for tangent modulus (a) corresponding to $\varepsilon = 2.0\%$ (b) corresponding to $\varepsilon = 4.0\%$.

of a previous history of cyclic loading causes a significant decrease in the tangent modulus. Moreover, both $E_{2.0}$ and $E_{4.0}$ are more affected by the magnitude of the cyclic phase ($\Delta\varepsilon_c$) than the number of cycles (N_c). Note that for A2C3_T□ and A2C9_T□, no value is given for $E_{2.0}$ and $E_{4.0}$ at 600°C, since for these cases, the corresponding strain levels were past the ultimate strength of the material. Tracing the variation of the tangent modulus at specific strain levels allows more accurate analysis deformations. This is especially important when it comes to the local buckling of structural members at high temperatures [25].

2.4 Conclusions

The aim of this research was to gain a fundamental understanding of the effects that a prior history of cyclic loading has on the subsequent monotonic properties of grade 300 structural steel at elevated temperatures. For this purpose, steel specimens were initially subjected to a number of strain-controlled cycles, and then monotonically loaded in tension at different temperatures until failure. With the number of cycles and the strain amplitude serving as variables for the cyclic phase, and temperature being the variable for the monotonic phase, their combined influence on subsequent mechanical properties of structural steel at elevated temperatures was examined. Where admissible, the variations observed in this program were compared to the variations given by design code expressions. The following conclusions can be drawn from the experimental results:

    1. By comparing complete stress-strain curves attained at elevated tempera-

tures without pre-damage to their counterparts that include cyclically-induced pre-damage, it is revealed that high temperature mainly contributes towards strength reduction as well as reduction in ductility, while cyclic-induced damage mainly contributes towards the decrease in ductility. Moreover, both temperature and pre-damage have noticeable effects on stiffness.

2. While both variables of the cyclic loading phase ($\Delta\varepsilon_c$ and N_c) were observed to influence the subsequent tensile properties of steel, it is evident that within the range used in this program, the effect of the amplitude ($\Delta\varepsilon_c$) is more significant than the number of cycles (N_c). In order to generalise this conclusion, further experiments must be performed with higher number of cycles.

3. In view of the variations of f_{pr}, $f_{0.5}$, $f_{1.5}$ and $f_{2.0}$ against temperature and cyclic load variables, it appears that at 600°C, curves with cyclically-induced damage start to converge with the curve without cyclically-induced damage. This implies that at this temperature, the effect of high temperature begins to dominate the effect of pre-damage and hence, the effect of pre-damage on f_{pr}, $f_{0.5}$, $f_{1.5}$ and $f_{2.0}$ becomes insignificant.

4. Regarding the variation of the yield stress with temperature, the difference between design code expressions and the values observed in this research seemingly imply that design code expressions are too conservative when it comes to the post-cyclic behaviour of structural steel. However, when coupled with the loss of ductility due to the decrease in the ultimate strain (ε_u) and the loss of stiffness due to the decrease in the tangent moduli ($E_{2.0}$ and $E_{4.0}$), the combined behaviour becomes much more complex, and not necessarily conservative. This calls for more elaborate design expressions that are not only a function of temperature, but are also a function of the intensity of the previously sustained cyclic loading.

5. As a function of the load variables ($\Delta\varepsilon_c$, N_c and T_m), different mechanical properties display different variational patterns. Hence, for future investigations, different forms of equations must be used to express those patterns or a new unified general equation must be developed that is capable of tracing all forms of the patterns.

Acknowledgement

References

[1] Takeyoshi Tanaka. Characteristics and problems of fires following the great east japan earthquake in march 2011. *Fire Safety Journal*, 2012.

[2] Jian Ding and Yu-Chun Wang. Temperatures in unprotected joints between steel beams and concrete-filled tubular columns in fire. *Fire Safety Journal*, 44 (1):16–32, 2009.

[3] Jiří Chlouba and František Wald. Temperature of a partially embedded connection subjected to fire. *Fire Safety Journal*, 54:121–129, 2012.

[4] J Ding and YC Wang. Experimental study of structural fire behaviour of steel beam to concrete filled tubular column assemblies with different types of joints. *Engineering Structures*, 29(12):3485–3502, 2007.

[5] G Della Corte, R Landolfo, and FM Mazzolani. Post-earthquake fire resistance of moment resisting steel frames. *Fire Safety Journal*, 38(7):593–612, 2003.

[6] Raul Zaharia and Dan Pintea. Fire after earthquake analysis of steel moment resisting frames. *International Journal of Steel Structures*, 9(4):275–284, 2009.

[7] Raffaele Pucinotti, OS Bursi, Jean-Marc Franssen, and Tom Lennon. Seismic-induced fire resistance of composite welded beam-to-column joints with concrete-filled tubes. *Fire Safety Journal*, 46(6):335–347, 2011.

[8] Jyri Outinen and Pentti Maekelaeinen. Mechanical properties of structural steel at elevated temperatures and after cooling down. *Fire and materials*, 28(2-4): 237–251, 2004.

[9] Ju Chen, Ben Young, and Brian Uy. Behavior of high strength structural steel at elevated temperatures. *Journal of Structural Engineering*, 132(12):1948–1954, 2006.

[10] Venkatesh Kodur, Mahmud Dwaikat, and Rustin Fike. High-temperature properties of steel for fire resistance modeling of structures. *Journal of Materials in Civil Engineering*, 22(5):423–434, 2010.

[11] Virendra Kumar, Umesh Kumar Sharma, Bhupinder Singh, and Pradeep Bhargava. Effect of temperature on mechanical properties of pre-damaged steel reinforcing bars. *Construction and Building Materials*, 46:19–27, 2013.

[12] AS/NZS 3679.1. *Structural steel, Part 1: Hot-rolled bars and sections.* Australian and New Zealand standard, Sydney, NSW, 2010.

[13] BHP. *Hot rolled products.* Broken Hill Proprietary Limited, Melbourne, 1998.

[14] ASTM E21-92. *Standard test methods for elevated temperature tension tests of metallic materials.* Annual book of ASTM standards. American Society of Testing and Materials, Philadelphia, PA, 1998.

[15] ASTM E606-92. *Standard practice for strain-controlled fatigue testing.* Annual book of ASTM standards. American Society of Testing and Materials, Philadelphia, PA, 1998.

[16] KW Poh. Stress-strain-temperature relationship for structural steel. *Journal of materials in civil engineering*, 13(5):371–379, 2001.

[17] GME Cooke. An introduction to the mechanical properties of structural steel at elevated temperatures. *Fire safety journal*, 13(1):45–54, 1988.

[18] JA El-Rimawi, IW Burgess, and RJ Plank. The treatment of strain reversal in structural members during the cooling phase of a fire. *Journal of constructional steel research*, 37(2):115–135, 1996.

[19] AS4100-98. *Steel structures.* Australian standard, Sydney, NSW, 1998.

[20] EN 1993-1-2. *Eurocode 3: Design of steel structures - Part 1-2: General rules - Structural fire design.* Annual book of ASTM standards. European commitee for standardization, Brussels, 2005.

[21] AISC. *Specification for structural steel buildings.* American institution of steel construction, Chicago, 2005.

[22] Ju Chen and Ben Young. Experimental investigation of cold-formed steel material at elevated temperatures. *Thin-walled structures*, 45(1):96–110, 2007.

[23] Xuhong Qiang, Frans Bijlaard, and Henk Kolstein. Dependence of mechanical properties of high strength steel S690 on elevated temperatures. *Construction and Building Materials*, 30:73–79, 2012.

[24] K Kitayama, CN Tomé, EF Rauch, JJ Gracio, and F Barlat. A crystallographic dislocation model for describing hardening of polycrystals during strain path changes. application to low carbon steels. *International Journal of Plasticity*, 46:54–69, 2013.

[25] Amin Heidarpour and Mark A Bradford. Local buckling and slenderness limits for flange outstands at elevated temperatures. *Journal of constructional steel research*, 63(5):591–598, 2007.

CHAPTER 3

Stress-strain-temperature relation for cyclically-damaged structural mild steel

Contents

Monash University

Declaration for Thesis Chapter 3

Declaration by candidate

In the case of Chapter 3, the nature and extent of my contribution to the work was the following:

Nature of contribution	Extent of contribution (%)
Development of ideas, Development of original computer model, Model verification and validation, Data analysis, Write-up and revision	70%

The following authors contributed to the work. If co-authors are students at Monash University, the extent of their contribution in percentage terms must be stated.

Name	Nature of contribution	Extent of contribution (%)
Dr. Amin Heidarpour	Developing ideas Revision Financial support	
Prof. Xiao-Ling Zhao	Revision Financial support	

The undersigned hereby certify that the above declaration correctly reflects the nature and extent of the candidate's and co-authors' contributions to this work.

Candidate's signature: ████████ **Date:** 24/09/2015

Main supervisor's signature: ████████ **Date:** 24/09/2015

Abstract

Experimental results suggest that the mechanical properties of mild steel at elevated temperatures are affected by the cyclic load history previously applied to the material. This has great implications when it comes to post-earthquake fire analyzes. Therefore, it is desirable to establish the relationship for each mechanical property, not only as a function of temperature but also the damage induced by the cyclic load history. To achieve this goal, a special class of functions known as Bézier curves have been utilized in this research. These functions are used for the construction of stress-strain curves that depend on temperature and the amplitude of the previously applied strain cycles. Actual experimental results are used throughout the process for calibration and validation purposes. The proposed model proves to be highly versatile in the sense that it can successfully take the effect of temperature and pre-induced strain cycles into account, making it applicable to post-earthquake fire analyzes.

3.1   Introduction

As a result of the importance of fire resistant structural design, the behaviour of different types of steel at elevated temperatures has been the subject of interest for many researchers [1–6]. While one side of the story is extracting behavioural patterns through experiments, the other side is expressing the relationship between stress, strain and temperature. These relationships are developed with the intent of being used either for research or in design guidelines.

Among these relationships, the one given by Ramberg and Osgood [7] is widely accepted. This expression produces a continuous curve commonly used for representing stress-strain responses that don't have distinct yield points. Another continuous curve used for the stress-strain relationship is the one developed by Richard and Abbott [8], which has the capability of tracing the strain softening portion of the response. Both equations given by Ramberg and Osgood [7] and Richard and Abbott [8] involve three parameters; namely the elastic modulus (E), a reference stress (σ_o) and a non-linearity parameter (n) which determines the curvature of the transition between the elastic and plastic parts of the curve.

With the Ramberg-Osgood relation becoming increasingly inaccurate at higher stress levels [9], many modifications have been made to the original equation for its improvement. For example, the advantage of a modified model to trace the stress-strain response of stainless steel, over the original model, is demonstrated in [9]. At the cost of increased complexity, a versatile stress-strain relationship has been presented by Poh [10]. This relation is capable of producing all tangential discontinuities of a complete stress-strain response, including the upper yield point, lower yield point, yield plateau and the initiation of strain hardening. However, the expression requires 10 parameters to trace these features.

As temperature rises, mechanical properties change, even to the point that some parts of the original stress-strain curve vanish, e.g. the upper yield peak and the plastic yield plateau. This calls for a stress-strain-temperature relationship capable of making the transition from ambient temperature to elevated temperatures. To tackle this problem, the expressions given by Rasmussen [9] and Mirambell and Real [11], were used by Chen and Young [12, 13] as the basis of a new equation that is valid up to the ultimate stress. Moreover, the stress-strain relation proposed by Poh [10] was effectively utilised in a subsequent paper [14] to include the effect of temperature on the stress-strain response, hence, producing a stress-strain-temperature relation. Kodur et al. [3] compared Poh's relation [14], along with other high-temperature relationships given by American and European standards, to available experimental data. They also compared the overall fire resistance predicted by different models.

As a next step, if stress-strain-temperature relations are extended further to include the effect of previously applied loads, such an equation can be used to analyse the response of pre-damaged steel structures at elevated temperatures. This can be directly related to a post-earthquake fire scenario, where a cyclically-damaged structure is exposed to a subsequent fire. The experimental results recently presented by Sinaie et al. [15] cover the changes that the mechanical properties of cyclically-damaged structural mild steel exhibit at elevated temperatures. The present paper aims to establish a relationship for those mechanical properties as a function of temperature and the amplitude of the pre-applied strain cycles. The main purpose of this relation is to act as a user-defined material model for finite element packages such as OpenSees [16] and ABAQUS [17] in the analysis of seismically-damaged steel structures under fire. Moreover, such relations can also be used in semi-analytical formulations developed for the analysis of steel structures at elevated temperatures [18–20].

It is worth mentioning that the behaviour of the material under cyclic loading is

not the subject of simulation in this paper. Consequently, the effect of the history of cyclic loading is implemented in the proposed model through a parametric value representing the amplitude of the strain cycles. Simulating the cyclic behaviour of steel requires more advanced models such as the ones based on the constitutive theory of plasticity [21–26]. Due to the importance of the cyclic response of steel in seismic analysis, its numerical simulation has been explicitly dealt with in another paper by the authors [27].

3.2   Experimental background

This section provides a brief description of the experiments carried out by Sinaie et al. [15]. Although only relevant information are presented here, details can be found in the original paper. The experiments involved grade 300 mild steel samples, all of which were subjected to a two-phase load history. The first phase was the damage-induction phase in the form of cyclic loading at ambient temperature. This was followed by the second phase where the remaining strength of the pre-damaged material was evaluated through tensile testing at different temperature levels. The complete strain-controlled loading history is illustrated in Fig. 3.1a as a function of time, whereby $\Delta\epsilon_c$, N_c and T_m act as the test variables denoting the amplitude of the cycles, the number of cycles and the temperature, respectively. The outcome of this loading history is the variation of stress with time given in Fig. 3.1b. Note that in these figures, the dashed line represents the ambient-temperature cyclic phase of the load history (damage induction), while the solid line represents the elevated temperature monotonic tensile phase (strength evaluation). With all of the samples being of the same material and dimensions, the difference between test cases is in their loading histories. Hence, different test cases are denoted in the form of A☐C☐_T☐, where the blank box (☐) in front of A, C and T are respectively filled in by the strain amplitude (in %) of the first phase, the number of cycles of the first phase and the temperature (in °C) of the second phase. Fig. 3.2 illustrates the stress-strain response during the second phase of the load history for a number of test cases. These figures contain the mechanical properties of cyclically-damaged grade 300 mild steel at elevated temperatures. Numerical reproduction of these variations is the goal of the present paper.

It should be mentioned that the variables of the cyclic phase, i.e. N_c and $\Delta\epsilon_c$ in Fig. 3.1 have distinct damaging effects on the material. However, for the ranges of N_c and $\Delta\epsilon_c$ covered in the experiments, the damage caused by the amplitude is
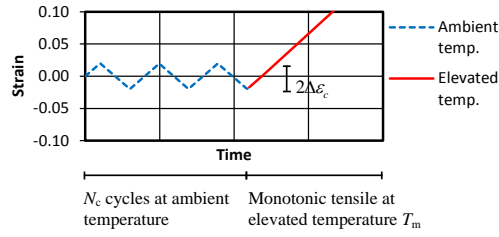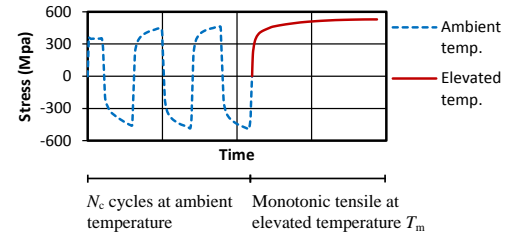
Figure 3.1: Time variation for the multi-phase loading history (a) Strain variations and (b) Stress variation.
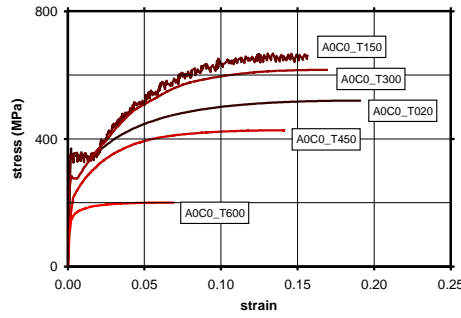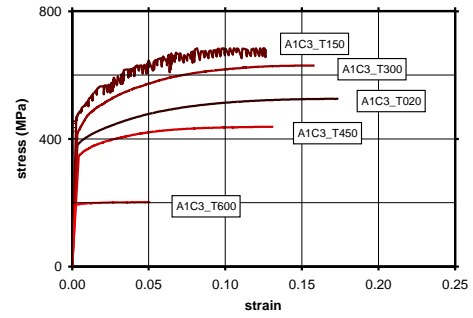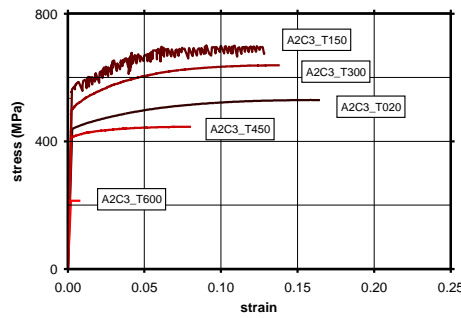
Figure 3.2: Stress-strain curves for different load histories. (a) A0C0, (b) A1C3, (c) A2C3.

more prominent than the number of cycles [15]. Therefore, from this point forward, the effect of N_c is omitted and the level of damage is implied through the strain amplitude of the cyclic phase ($\Delta\epsilon_c$). Although this omission is not necessarily valid for $N_c < 3$, it does not harm the goal of this research, since it has been shown that typical earthquakes have at least 3 effective cycles [28]. However, further tests have to be conducted at higher number of cycles to reach a definite conclusion for values outside the range considered in this research.

It should also be mentioned that in the two-phase experiments conducted by Sinaie et al. [15], the elevated-temperature phase followed the cyclic damage-induction phase within a time gap small enough to not allow for significant strain aging. Hence, when it comes to the analysis of cyclically-damaged steel structures under fire, using the experimental results of [15] is limited to scenarios where the fire immediately follows the seismic loading. The strain aging effect as well as the post-cooling behaviour of the steel material is currently being investigated at Monash University. It is worth noting that the generality of the formulations given in the following sections allows such effects to be easily implemented in the analysis, either by a single overall parameter, or as independent parameters.

3.3   Current stress-strain-temperature relations

In the course of expressing stress as a function of strain and temperature, various explicit relations have been presented by different researchers. Examples of such equations are described and compared to each other by Kodur et al. [3] and Poh [14]. Due to the flexibility and robustness of the equations proposed by Poh [14], a modified version of it is used in this paper for comparative reasons. The original relation involving 10 parameters (β_1-β_{10}) is hereby modified by setting $\beta_6 = 0$. Doing so simplifies the equation by eliminating the upper yield peak from the original model. Note that by setting $\beta_6 = 0$, β_7 also vanishes from the equation. In order to be consistent with their original definitions, the remaining β_i's are not re-indexed here. Hence
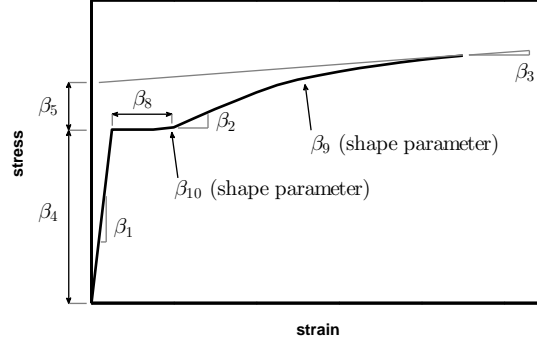
Figure 3.3: Definition of β_i's in Eq. (3.1) for the stress-strain curve [14].

$$\sigma = \frac{\epsilon}{2|\epsilon|} \left[a_1 - |a_2| + B_2 B_3 \right] \tag{3.1a}$$

$$a_1 = \beta_1 |\epsilon| + \beta_4 \tag{3.1b}$$

$$a_2 = \beta_1 |\epsilon| - \beta_4 \tag{3.1c}$$

$$B_2 = \frac{(\beta_2 - \beta_3)b}{\left[1 + \left| \frac{(\beta_2 - \beta_3)b}{\beta_5} \right|^{\beta_9} \right]^{1/\beta_9}} + \beta_3 b \tag{3.1d}$$

$$B_3 = 1 + \frac{|b| - |b - \beta_{10}|}{\beta_{10}} \tag{3.1e}$$

$$b = |\epsilon| - \beta_8 - \frac{\beta_4}{\beta_1} \tag{3.1f}$$

where σ and ϵ denote the values of stress and strain at a given state and the β_i's are parametric values which determine the shape of the stress-strain graph. The definition of the β_i's is illustrated in Fig. 3.3.

Each β_i is by itself a function of temperature, therefore, allowing the stress-strain curve to transform continuously as the temperature rises. For example, the variation of the β_i's can be expressed as [14]

$$\beta_i = \frac{G_1}{G_2} + G_3 \tag{3.2a}$$

$$G_1 = (\gamma_{i2} - \gamma_{i1})(2T - \gamma_{i3} - \gamma_{i4}) \tag{3.2b}$$

$$G_2 = 2\left[1 + \left|\frac{2T - \gamma_{i3} - \gamma_{i4}}{\gamma_{i4} - \gamma_{i3}}\right|^{\gamma_{i6}}\right]^{1/\gamma_{i6}} \tag{3.2c}$$

$$G_3 = \frac{1}{2}(\gamma_{i1} - \gamma_{i2})(\gamma_{i3} - \gamma_{i4}) + \gamma_{i1}T + \gamma_{i5} \tag{3.2d}$$

where the γ_i's are parametric values calibrated against experimental data.

Explicit stress-strain-temperature relations in the form of Eqs. (3.1) and (3.2) are widely accepted and used in research. Being capable of reproducing many characteristics observed in experiments, the above-mentioned equations are very good examples of a robust stress-strain relation. However, they also have shortcomings, which can be summarised as follows:

- They are computationally expensive; having to combine multiple arithmetic operations to be able to reproduce tangential discontinuities in one single relation.

- Some parameters don't necessarily have a physical meaning, and only exist to control the shape of the graph (e.g. β_9 and β_{10}). Such parameters have to be determined by curve fitting techniques.

- Due to the complexity of the equations, they cannot be easily used to calculate strain in terms of stress and temperature. Being able to do so is especially useful when analysing structures under fire conditions.

- It is difficult to introduce new components to an existing equation, for example, to add a damage component to an existing stress-strain-temperature relation.

To overcome these issues, a new type of formulation is presented through the utilisation of 2nd-degree Bézier curves. The proposed method not only shows to be as robust as Eqs. (3.1) and (3.2), but also overcomes the problems pertaining to explicit relations.

3.4   Proposed model

Two approaches can be taken to develop stress-strain relations that are highly representative of actual experimental observations. One approach is to combine different arithmetic operations to produce a single complex equation capable of tracing the stress-strain curve and all of its tangential discontinuities. Eq. (3.1) falls in this category. However, another approach is to maintain simplicity by breaking the entire curve and representing it through a piecewise function. The second approach is the one taken in this paper, with each piece being in the form a 2nd-degree Bézier curve.

3.4.1   Bézier equations

Numerous articles exist regarding the properties of Bézier curves and its applications, especially in relation to computer aided design [29–31]. A brief introduction to Bézier curves and its defining equations is given in the following text.

With $t \in [0, 1]$ being a local coordinate parameter, a two-dimensional Bézier curve of the n-th degree constructed by $n + 1$ control points is given as

$$\vec{\mathbf{B}}(t) = (b_x(t), b_y(t)) = \sum_{i=0}^{n} F_i^n(t)\vec{\mathbf{P}}_i \tag{3.3}$$

where $\vec{\mathbf{P}}_i = (p_{ix}, p_{iy})$ represents the control points and $F_i^n(t)$, known as a Bernstein basis polynomial, is defined as

$$F_i^n(t) = \frac{n!}{i!(n-i)!}t^i(1-t)^{n-i} \tag{3.4}$$

Hence, a 2-dimensional 2nd-degree Bézier curve takes the form

$$b_x(t) = (1-t)^2 p_{0x} + 2t(1-t)p_{1x} + t^2 p_{2x} \tag{3.5}$$

$$b_y(t) = (1-t)^2 p_{0y} + 2t(1-t)p_{1y} + t^2 p_{2y} \tag{3.6}$$
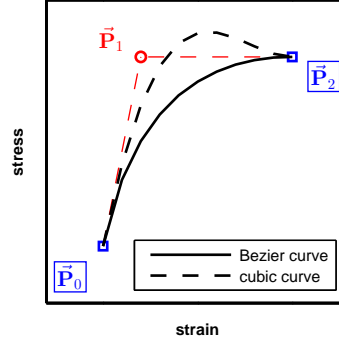
Figure 3.4: 2nd-degree Bézier curve in comparison to 3rd-degree polynomial. The blue squares represent end control points and the red circle is an intermediate control point.

An example of a 2-dimensional 2nd-degree Bézier curve is illustrated in Fig. 3.4. Note that Bézier curves always pass through the end control-points but not necessarily through the intermediate control-points. As seen in Fig. 3.4, the intermediate control point determines the slope of the curve at the two ends. As a result, a unique curve can be established, given the coordinates of the two end points ((x_i, y_i) and (x_j, y_j)), and the desired slope at these two points ($(dy/dx)_i$ and $(dy/dx)_j$). Similarly, a 3rd degree polynomial can also be used to attain a unique curve with the same boundary conditions. However, there are cases where 3rd degree polynomials fail to trace a realistic stress-strain path between two points. An example of this scenario can be seen in Fig. 3.4. The main reason of not using 3rd-degree polynomials for the purpose of this research is to avoid such complications, especially at higher dimensions where in addition to stress and strain, parameters such as temperature and damage also get involved.

Note that Eqs. (3.5) and (3.6) do not give an immediate relation between b_x and b_y. Hence, assuming that the value of b_x is known, Eq. (3.5) can be solved for t. Also note that as a consequence of $p_{0x} \leq p_{1x} \leq p_{2x}$ and $p_{0x} \leq b_x \leq p_{2x}$, one of the two roots of the quadratic equation always lies in the range $0 \leq t \leq 1$. The solved value of t can then be substituted into Eq. (3.6) to yield the corresponding value of b_y. The steps of this process are given in Table 3.1. Alternatively, the same process can be followed to find the value of b_x that corresponds to a given value of b_y. When viewed in the context of a stress-strain relationship, this interchangeability means that this type of formulation not only gives $\sigma = f(\epsilon)$, but at no additional computational cost, also gives $\epsilon = f^{-1}(\sigma)$. This is especially useful when simulating the constant-stress strain-temperature transient response of the material. This property is a prominent

Table 3.1: Algorithm for Bézier interpolation.

```
BezierInterpolation(input x, P̃₀, P̃₁, P̃₂)
```

```
a ← p₀ₓ − 2p₁ₓ + p₂ₓ;

b ← p₁ₓ − p₀ₓ;

c ← p₀ₓ − x;

if(a = 0)

   t ← −0.5c/b;

else

   t ← (−b + √(b² − ac))/a;

y ← (1 − t)²p₀ᵧ + t(1 − t)p₁ᵧ + t²p₂ᵧ;

return(y);
```

advantage of the proposed formulation as opposed to explicit equations available in the literature.

Higher dimension Bézier curves can be readily developed using Eqs. 3.3 and 3.4. For example, a Bézier surface in 3 dimensions can be expressed as

$$\vec{\mathbf{B}}(t_1, t_2) = \sum_{i=0}^{n} \sum_{j=0}^{m} F_i^n(t_1) F_j^m(t_2) \vec{\mathbf{P}}_{ij} \tag{3.7}$$

which maps the unit square of $m+1$ by $n+1$ control points onto a smooth curved surface. Example of a 3-dimensional curve is illustrated in Fig. 3.5. Any property mentioned for the 2-dimensional formulation of the Bézier curve is also valid for the 3-dimensional formulation.

3.4.2 Stress-strain curves

As mentioned before, the approach taken in this paper to reproduce stress-strain curves is to use a piecewise relation. For this purpose, the full-range stress-strain curve of mild steel is divided into 5 pieces. The term full-range refers to the range starting at zero strain and ending at the ultimate strain ϵ_u (corresponding to the ultimate stress). The control points of this division are depicted in Fig. 3.6, with the points p, h and u denoting the proportional limit, the onset of strain hardening and the ultimate state, respectively. The points denoted by $.25u$ and $.50u$ refer to points where the strain is equal to $0.25\epsilon_u$ and $0.50\epsilon_u$, respectively. Note that
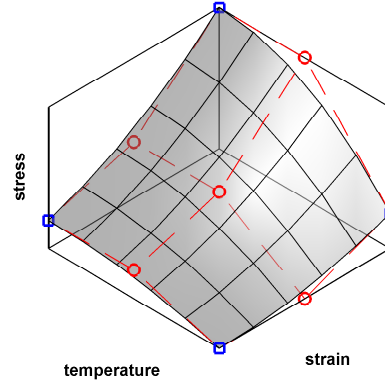
Figure 3.5: 2nd-degree Bézier curve in 3 dimensions. The blue squares represent end control points while the red circles are intermediate control points.
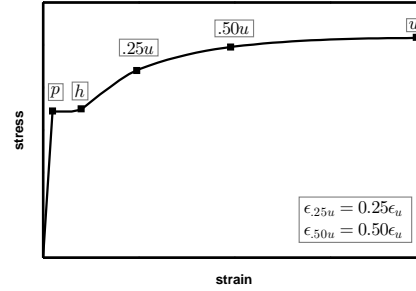
Figure 3.6: Piecewise representation of the stress-strain response of mild steel.

the proportional part of the curve is a straight line, therefore, does not need to be defined by a Bézier curve.

As a result, 12 independent values are used to determine the shape of the full-range stress-strain curve. These are listed in Table 3.2. Note that in Table 3.2, M denotes the slope of the curve ($d\sigma/d\epsilon$). Also note that being in the form of strain, stress or modulus, all of these 12 values have a clear physical meaning.

Each piece of the full-range curve is hereby represented by a 2nd degree Bézier curve, with the division points p, h, $.25u$, $.50u$ and u acting as end points. The

Table 3.2: Independent variables for the proposed stress-strain curve.

location	p	h	$.25u$	$.50u$	u
strain	ϵ_p	ϵ_h	—	—	ϵ_u
stress	σ_p	σ_h	$\sigma_{.25u}$	$\sigma_{.50u}$	σ_u
tangent	M_p	M_h	$M_{.25u}$	$M_{.50u}$	—
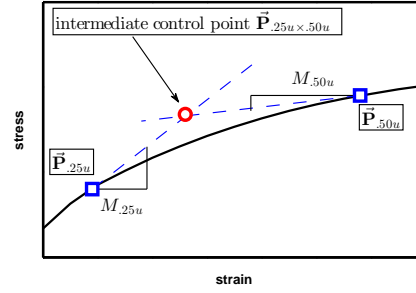
Figure 3.7: Intermediate control point for the curve between $.25u$ to $.50u$.

intermediate control point of each Bézier curve is placed at the intersection of two lines that pass through the end points at an angle defined by the slopes. As an example, the location of the intermediate control point between the $.25u$ and $.50u$ division points is shown in Fig. 3.7.

The process of calculating the piecewise stress-strain curve is given in algorithmic form in Table 3.3. The outcome of using this formulation is illustrated in Section 3.5.

3.4.3   Variation of mechanical properties

Similar to Eq. (3.2) where the β_i's of Eq. (3.1) were expressed as a function of temperature, the variables listed in Table 3.2 should also change as the temperature rises. Therefore, the variation of each mechanical property is determined by a set of control points. As an example, the control points used to determine the variation of the ultimate strain (ϵ_u) against temperature are shown in Fig. 3.8 for a sample with no previous cyclic load history ($\Delta\epsilon_c = 0$). The variation is given in terms of a reduction factor which is the ratio of ϵ_u at elevated temperature to its value at ambient temperature. In this figure, the full temperature range is 20-600°C, whereby it has been divided into four 2nd degree Bézier curves. The end points (in blue) of the Bézier curves are set at 20, 150, 300, 450 and 600°C. These are the temperature levels at which the experiments were carried out [15], hence, setting them as end-points guarantees that the curve passes through them. On the other hand, the intermediate control points (in red) do not necessarily represent a point on the curve, but are rather chosen to determine the slope of the curve at the end-points. Note that although in Fig. 3.8, the intermediate control points are located midway between two adjacent end-points, from a mathematical standpoint, this does not necessarily have to be the case. Similar to any other model, more accurate

Table 3.3: Algorithm for the evaluation of stress as a function of strain ($\vec{\mathbf{P}}_{i\times j}$ denotes the intersection of the tangents that pass through $\vec{\mathbf{P}}_i$ and $\vec{\mathbf{P}}_j$).

```
StressStrain(input ε);
```

$\text{if}(0 \leq \epsilon < \epsilon_{\text{p}})$

    $\tilde{\mathbf{P}}_0 \leftarrow [0\ 0];$

    $\tilde{\mathbf{P}}_1 \leftarrow \tilde{\mathbf{P}}_{\text{o}\times\text{p}};$

    $\tilde{\mathbf{P}}_2 \leftarrow \tilde{\mathbf{P}}_{\text{p}};$

$\text{if}(\epsilon_{\text{p}} \leq \epsilon < \epsilon_{\text{h}})$

    $\tilde{\mathbf{P}}_0 \leftarrow \tilde{\mathbf{P}}_{\text{p}};$

    $\tilde{\mathbf{P}}_1 \leftarrow \tilde{\mathbf{P}}_{\text{p}\times\text{h}};$

    $\tilde{\mathbf{P}}_2 \leftarrow \tilde{\mathbf{P}}_{\text{h}};$

$\text{if}(\epsilon_{\text{h}} \leq \epsilon < \epsilon_{.25\text{u}})$

    $\tilde{\mathbf{P}}_0 \leftarrow \tilde{\mathbf{P}}_{\text{h}};$

    $\tilde{\mathbf{P}}_1 \leftarrow \tilde{\mathbf{P}}_{\text{h}\times.25\text{u}};$

    $\tilde{\mathbf{P}}_2 \leftarrow \tilde{\mathbf{P}}_{.25\text{u}};$

$\text{if}(\epsilon_{.25\text{u}} \leq \epsilon < \epsilon_{.50\text{u}})$

    $\tilde{\mathbf{P}}_0 \leftarrow \tilde{\mathbf{P}}_{.25\text{u}};$

    $\tilde{\mathbf{P}}_1 \leftarrow \tilde{\mathbf{P}}_{.25\text{u}\times.50\text{u}};$

    $\tilde{\mathbf{P}}_2 \leftarrow \tilde{\mathbf{P}}_{.50\text{u}};$

$\text{if}(\epsilon_{.50\text{u}} \leq \epsilon \leq \epsilon_{\text{u}})$

    $\tilde{\mathbf{P}}_0 \leftarrow \tilde{\mathbf{P}}_{.50\text{u}};$

    $\tilde{\mathbf{P}}_1 \leftarrow \tilde{\mathbf{P}}_{.50\text{u}\times\text{u}};$

    $\tilde{\mathbf{P}}_2 \leftarrow \tilde{\mathbf{P}}_{\text{u}};$

$\sigma \leftarrow \texttt{BezierInterpolation}(\epsilon, \tilde{\mathbf{P}}_0, \tilde{\mathbf{P}}_1, \tilde{\mathbf{P}}_2);$

```
return(σ)
```
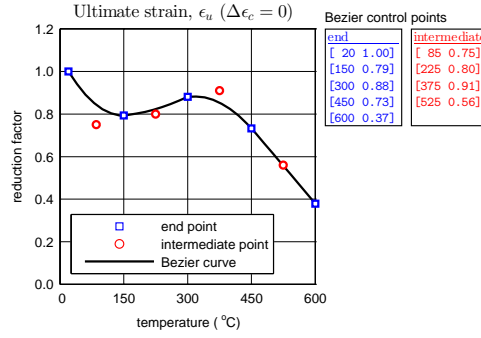
Figure 3.8: Control points for the variation of the ultimate strain (ϵ_u) against temperature for $\Delta\epsilon_c = 0$. (blue points represent end control points, red points are intermediate control points.)

curves can be constructed if more experimental data points are available. Note that mechanical properties are extracted from experimental stress-strain curves resulting from tensile tests.

The step by step process of interpolating these variables is similar to what was described in the previous section for the stress-strain curve. However, with the main difference that here, the independent variable is temperature rather than stress or strain.

Since this research aims to add a new component, representing the effect of pre-applied strain cycles, to the existing stress-strain-temperature relation, the parameters given in Table 3.2 not only have to be a function of temperature, but also the amplitude of the strain cycles ($\Delta\epsilon_c$). Having two independent variables, the 3-dimensional form of the Bézier equations (Eq. (3.7)) is chosen for this purpose. The advantages of using this formulation is discussed in Section 3.5.

3.4.4 Data extrapolation

Although Bézier equations are most effective for interpolating existing data, they can also be used for extrapolation. Taking advantage of this feature, the variation of a mechanical property can be predicted outside the experimented range, which for this program would be $T > 600°C$ and $\Delta\epsilon_c > 2.0$. The procedure for data extrapolation involves the calculation of two control points (one end point and one intermediate point) outside the domain of the existing control points. In other words, a new Bézier curve is constructed from an existing Bézier curve, whereby the two curves

Table 3.4: Algorithm for Bézier extrapolation.

BezierExtrapolation(input $\tilde{\mathbf{P}}_0$, $\tilde{\mathbf{P}}_1$, $\tilde{\mathbf{P}}_2$)
$\tilde{\mathbf{Q}}_0 \leftarrow \tilde{\mathbf{P}}_2$;
$\tilde{\mathbf{Q}}_1 \leftarrow \tilde{\mathbf{P}}_2 + (\tilde{\mathbf{P}}_2 - \tilde{\mathbf{P}}_1)$;
$\tilde{\mathbf{X}} \ \leftarrow \tilde{\mathbf{P}}_1 + (\tilde{\mathbf{P}}_1 - \tilde{\mathbf{P}}_0)$;
$\tilde{\mathbf{Q}}_2 \leftarrow \tilde{\mathbf{X}} \ + (\tilde{\mathbf{P}}_2 - \tilde{\mathbf{X}})$;
return($\tilde{\mathbf{Q}}_0$, $\tilde{\mathbf{Q}}_1$, $\tilde{\mathbf{Q}}_2$);
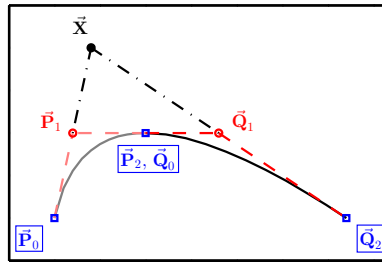
Figure 3.9: Data extrapolation using Bézier equations.

share one single end point and have the same slope at that point. The process is illustrated in Fig. 3.9 and the algorithm is given in Table 3.4. A numerical example of this feature is provided in Section 3.5.4. However, note that similar to many other extrapolation techniques, the result is highly dependent on the variations near the boundary of the existing domain. Hence, just like any other extrapolation method, it cannot predict unexpected behavioural changes.

3.5 Numerical illustration

The model proposed in Section 3.4 is hereby used to numerically reproduce the mechanical response of mild steel as a function of temperature and the amplitude of the previously applied strain cycles ($\Delta \epsilon_c$). The variation of all mechanical properties is acquired from the experimental data given in [15]. Note that where the results are given in terms of reduction factors, they are with respect to an ambient temperature test with no history of previous loading cycles ($T = 20°C$ and $\Delta \epsilon_c = 0$).
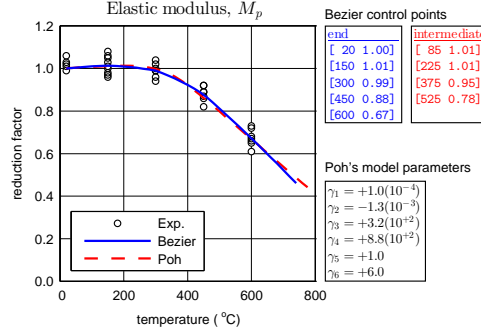
Figure 3.10: Variation of the elastic modulus (M_p) produced by Poh's model and the proposed model.

3.5.1 Mechanical properties

Fig. 3.10 shows the variation of the elastic modulus (M_p) of grade 300 mild steel against temperature as observed in the laboratory [15]. The variation is given in terms of a reduction factor which is the ratio of M_p at elevated temperature to its value at ambient temperature. Note that the elastic modulus is not affected by the previous load history. Also shown in Fig. 3.10 is the result of using Poh's model (Eq. (3.2)) as well as the model proposed in this paper, whereby the parameters used for the former, and the control points used for the latter are also presented. It is observed that both models are quite competent in tracing the experimental variation.

The variation of the proportional stress (σ_p) and ultimate strain (ϵ_u) against temperature is shown in Fig. 3.11 for three different levels of $\Delta\epsilon_c$. This figure clearly shows what is expected of 2-dimensional Bézier curves. The variation of these two parameters are later presented as Bézier surfaces in Figs.3.12a and c.

Fig. 3.12 shows the variation of the yield stress (σ_p), ultimate stress (σ_u), ultimate strain (ϵ_u) and modulus at $\epsilon_{.25u}$ $(M_{.25u})$ against temperature (T) and the amplitude of the previously applied strain cycles $(\Delta\epsilon_c)$ as produced by the proposed model. These 3D illustrations clearly show the separate and combined effects of T and $\Delta\epsilon_c$ on each mechanical property. Such models should first be developed for all of the parameters listed in Table 3.2. Afterwards, they can be used to obtain the stress-strain variation at different values of T with different levels of $\Delta\epsilon_c$. This is carried out in the next section.
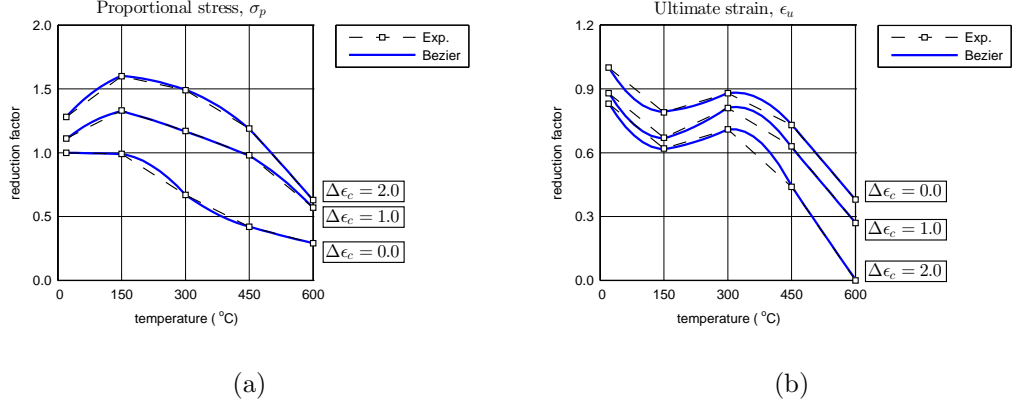
Figure 3.11: Variation of mechanical properties against temperature for different values of $\Delta\epsilon_c$. (a) Proportional stress σ_p and (b) ultimate strain ϵ_u.
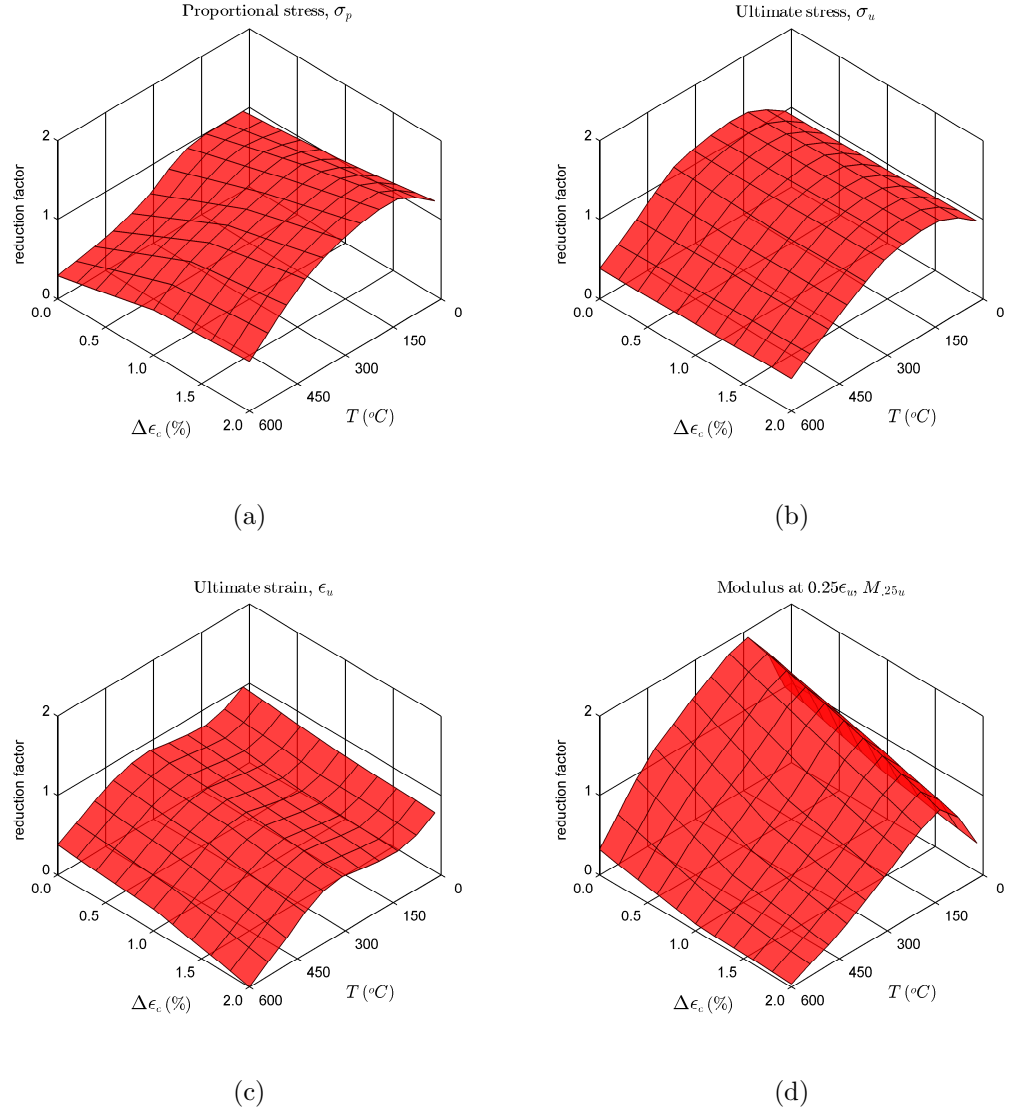
Figure 3.12: Variation of mechanical properties against T and $\Delta\epsilon_c$ as produced by Bézier equations. (a) Proportional stress σ_p, (b) ultimate stress σ_u, (c) ultimate strain ϵ_u and (d) modulus at $\epsilon_{.25u}$ ($M_{.25u}$).
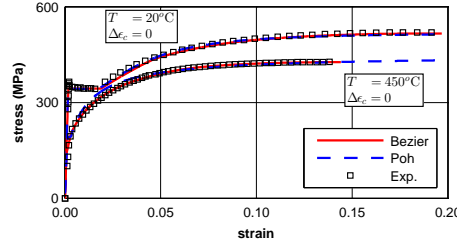
Figure 3.13: Full-range stress-strain curves produced by Poh's equation and the proposed model in comparison to experimental results at 20°C and 450°C.

3.5.2 Full-range σ-ϵ curves

Fig. 3.13 shows the stress-strain response of grade 300 mild steel at 20 and 450°C as observed in the laboratory. Also shown in this figure is the result obtained by Poh's model (Eq. (3.1)) as well as the model developed in this paper. It is observed that both models are capable of effectively tracing the experimental curve at different levels of temperature. Note that Poh's model does not include the ultimate strain (ϵ_u) as a limiting value for strain. This is not problematic, since it can be easily applied to the calculations, however, it should be viewed as an additional parameter to Poh's equation.

Fig. 3.14 illustrates the result of using the proposed model to reproduce the response of a pre-damaged material at different temperatures. This figure shows how well the model can follow the actual experimental curves. Fig. 3.15 illustrates the stress-strain-temperature surface for two different values of $\Delta\epsilon_c$. The surface is produced by taking stress as the dependent variable and calculating it in terms of the independent variables of strain, temperature and the amplitude of the pre-induced strain cycles ($\Delta\epsilon_c$). Notice the transition of the division points as the temperature is increased, and also the reduction in ductility as a result of pre-induced strain cycles.

3.5.3 Constant-stress ϵ-T curves

Fig. 3.16 illustrates ϵ-T contour lines corresponding to different levels of constant stress, with respect to the same stress-strain-temperature surfaces of Fig. 3.15. These curves have been obtained by simply switching strain as the input value in the Bézier interpolation algorithm (Tables 3.1 and 3.3) for stress. In other words, in order to
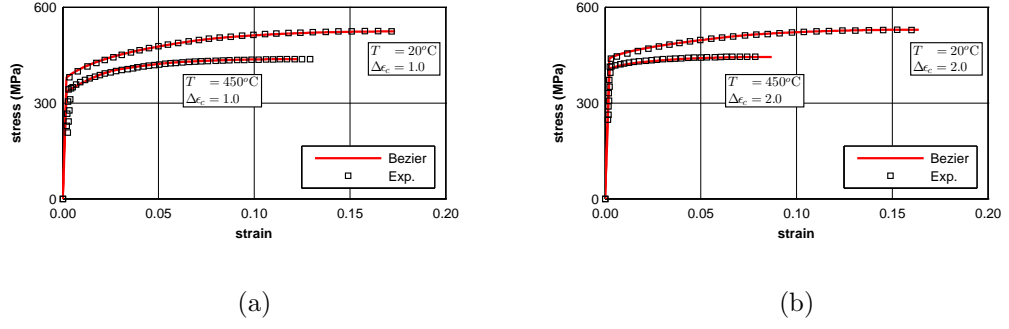
Figure 3.14: Full-range stress-strain curves using the proposed model in comparison to experiment at $T = 20°C$ and $450°C$ for (a) $\Delta\epsilon_c = 1.0$ and (b) $\Delta\epsilon_c = 2.0$.
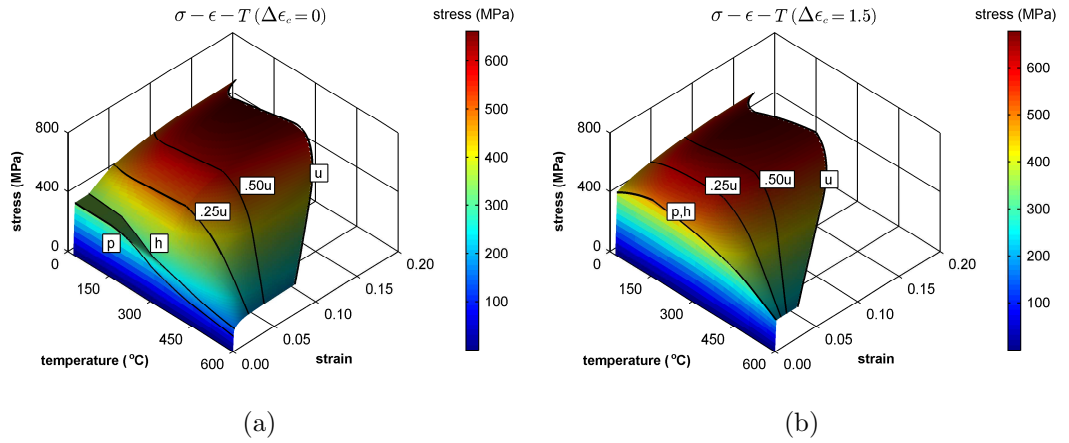
Figure 3.15: Stress-strain-temperature variation for different amplitudes of the pre-induced strain cycles. (a) $\Delta\epsilon_c = 0$ and (b) $\Delta\epsilon_c = 1.5$.
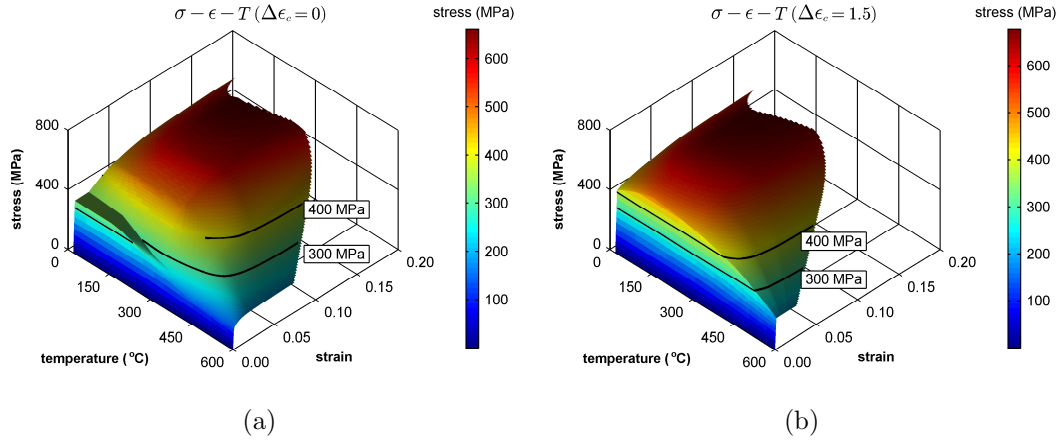
Figure 3.16: Constant-stress contours for different amplitudes of the pre-induced strain cycles. (a) $\Delta\epsilon_c = 0$ and (b) $\Delta\epsilon_c = 1.5$.

obtain these ϵ-T contour lines, strain (ϵ) has been taken as the independent variable and is calculated in terms of the independent variables of σ, T and $\Delta\epsilon_c$. It is an important feature of the proposed method that the user can so easily select the dependent variable and calculate it in terms of the remaining variables. When compared to explicit formulations such as Eqs. (3.1) and (3.2), the ability to obtain ϵ-T curves at the same computational cost of σ-ϵ curves is an added benefit of using Bézier interpolation.

Fig. 3.17 is presented at this point to demonstrate the accuracy of attaining ϵ-T curves through the proposed model. In this figure, the numerically obtained constant-stress ϵ-T curve is compared to experimental data at two stress levels of 300 MPa and 400 MPa with $\Delta\epsilon_c = 0$. Note that in these graphs, thermal elongation has been removed from the experimental response. It is observed that numerical simulation corresponds well with experimental observation for both levels of stress. However, the correspondence is closer at lower stress levels. Higher error at higher stress levels can be related to creep and the fact that it becomes more and more active at higher temperatures and/or stress levels [3, 32, 33].

In order to illustrate the calculation of ϵ-T curves using the proposed model, Figs. 3.18 and 3.19 are presented. Fig. 3.18 shows constant-stress ϵ-T curves at different stress levels for two values of $\Delta\epsilon_c$. Fig. 3.19 shows constant-stress ϵ-T curves for different values of $\Delta\epsilon_c$ at two levels of stress. Note that finding such curves using Poh's formulation, i.e. Eqs (3.1) and (3.2), is not as simple.
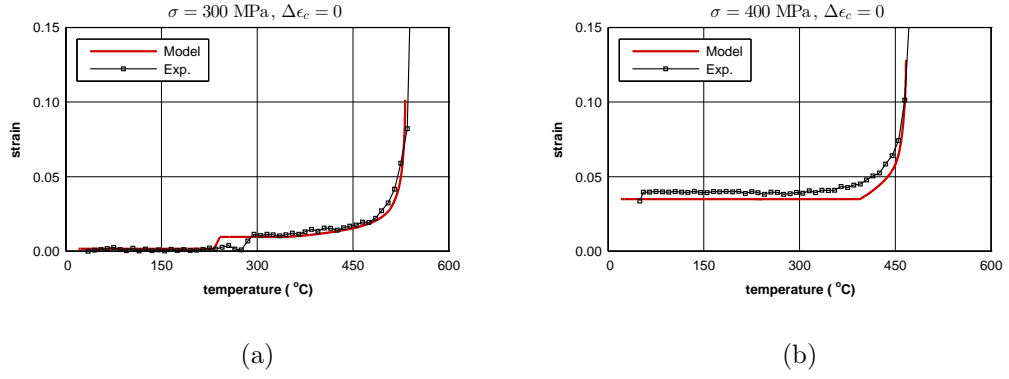
Figure 3.17: Validation of the constant-stress curves against experimental data. (a) Stress of 300 MPa and (b) stress of 400 MPa.
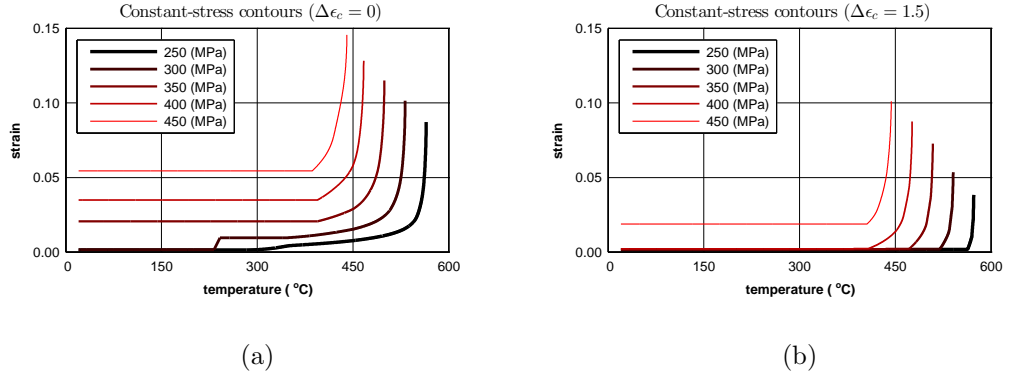
Figure 3.18: Constant-stress ϵ-T response curves predicted by the model for different amplitudes of the pre-induced strain cycles. (a) $\Delta\epsilon_c = 0$ and (b) $\Delta\epsilon_c = 1.5$.
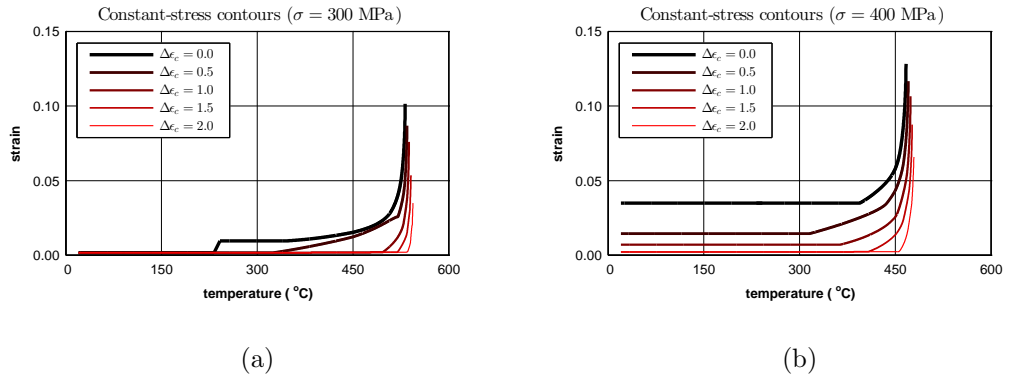
Figure 3.19: Constant-stress curves for different values of the pre-induced cyclic strain amplitude. (a) Under $\sigma = 300$MPa and (b) under $\sigma = 400$MPa.
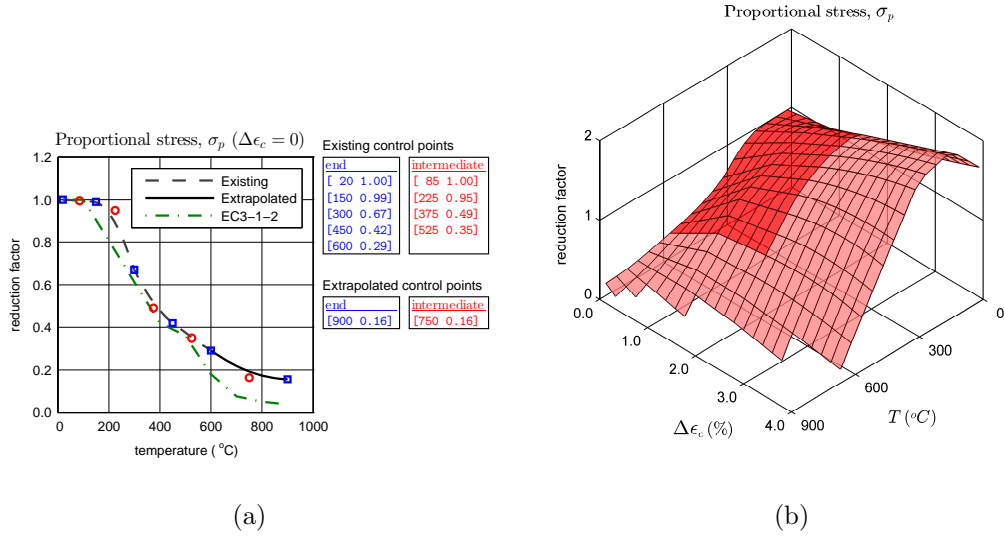
Figure 3.20: Extrapolation of experimental data for the proportional stress (σ_p) with temperatures up to $T = 900°$C and pre-induced strain amplitudes up to $\Delta\epsilon_c = 4.0$. (a) Dashed line represents the original curve while the solid line is the extrapolated data. (b) Darker surface is the original data and the lighter surface represents the extrapolated data.

3.5.4   Data extrapolation

The process of data extrapolation discussed in Section 3.4 is hereby applied to the experimental data points of the proportional stress (σ_p). Given that the experiments in [15] only cover the domain of 20 - 600°C, new control points are calculated here to extend the domain up to 900°C. As indicated in Table 3.4 the procedure requires three existing control points to construct two new control points. Note that the three existing points do not necessarily have to be 3 consecutive control points. In fact, the authors recommend that these points be three points that actually lie on the existing curve. Therefore, for this example, the coordinates of the three end points located at 300°C, 450°C and 600°C are used to construct two new points at 750°C and 900°C. The result is illustrated in Fig. 3.20a, where the coordinates of the new control points are given alongside the original ones. Also shown in this figure for comparison is the variation of the proportional limit as given by Eurocode 3 [34]. Fig. 3.20b shows the result of extrapolating the same parameter (σ_p) along the $\Delta\epsilon_c$ axis, as well as the T axis. Notice that in this figure, the portion of the surface with darker shading represents the original surface, while the portion with lighter shading represents the result of extrapolation.

One has to bear in mind that this method of extrapolation should be used with

caution, especially for mild steel which exhibits crystallographic phase transitions at around 750°C [3]. Further experiments are required to capture the sudden behavioural changes during these phase transitions. Note that for higher accuracy, experiments should be carried out at smaller temperature intervals over these regions, e.g. at $\Delta T = 50$°C instead of 150°C.

3.6 Conclusions

The aim of this research was to construct a relationship between stress, strain, temperature for cyclically-damaged mild steel. Unlike the traditional approach of developing an explicit relationship, this paper established the relation through a class of functions known as Bézier curves. The effectiveness of the proposed formulation was evaluated against actual experimental results, as well as the highly robust explicit relationship proposed by Poh [14]. The following conclusions can be drawn from the results:

1. The proposed model is as effective as an explicit relationship in reproducing full-range stress-strain-temperature curves.

2. Unlike explicit relations, all the parameters used to describe the proposed model are in the form of strain, stress or modulus (ϵ, σ or $d\sigma/d\epsilon$) and therefore, not only have a real physical meaning but can also be directly taken from experimental stress-strain plots.

3. The introduction of a new parameter, representing pre-induced strain cycles, into the relations and hence establishing a relation between σ, ϵ, T and $\Delta\epsilon_c$ is very straightforward.

4. For a given state of T and $\Delta\epsilon_c$, the proposed model is not only capable of calculating stress as a function of strain ($\sigma = f(\epsilon)$), but at no additional cost, it is also capable of calculating strain as a function of stress ($\epsilon = f^{-1}(\sigma)$). Hence, being able to predict the constant-stress strain-temperature response of the material which can be directly used to analyse the transient behaviour of structures under fire conditions.

5. The performance of the model was demonstrated throughout the text within the range of $20 \leq T \leq 600$°C and $0 \leq \Delta\epsilon_c \leq 2.0$, which was the range covered

by experiment. In addition, it was shown that Bézier equations can also be used to extrapolate data points beyond the tested domain. However, the accuracy of these predictions must be evaluated through further experiments.

Acknowledgement

References

[1] Hassan A Saab and David A Nethercot. Modelling steel frame behaviour under fire conditions. *Engineering Structures*, 13(4):371–382, 1991.

[2] Jyri Outinen and Pentti Maekelaeinen. Mechanical properties of structural steel at elevated temperatures and after cooling down. *Fire and materials*, 28(2-4): 237–251, 2004.

[3] Venkatesh Kodur, Mahmud Dwaikat, and Rustin Fike. High-temperature properties of steel for fire resistance modeling of structures. *Journal of Materials in Civil Engineering*, 22(5):423–434, 2010.

[4] Xuhong Qiang, Frans Bijlaard, and Henk Kolstein. Dependence of mechanical properties of high strength steel S690 on elevated temperatures. *Construction and Building Materials*, 30:73–79, 2012.

[5] Jian Jiang and Asif Usmani. Modeling of steel frame structures in fire using opensees. *Computers & Structures*, 118:90–99, 2013.

[6] Amin Heidarpour, Niall S Tofts, Asghar H Korayem, Xiao-Ling Zhao, and Christopher R Hutchinson. Mechanical properties of very high strength steel at elevated temperatures. *Fire Safety Journal*, 64:27–35, 2014.

[7] Walter Ramberg and William R Osgood. Description of stress-strain curves by three parameters. Technical Report 902, National advisory committee for aeronautics, Washington, DC, 1943.

[8] Ralph M Richard and Barry J Abbott. Versatile elastic-plastic stress-strain formula. *Journal of the Engineering Mechanics Division*, 101(4):511–515, 1975.

[9] Kim JR Rasmussen. Full-range stress–strain curves for stainless steel alloys. *Journal of Constructional Steel Research*, 59(1):47–61, 2003.

[10] K. W. Poh. General stress-strain equation. *Journal of materials in civil engineering*, 9(4):214–217, 1997.

[11] Enrique Mirambell and Esther Real. On the calculation of deflections in structural stainless steel beams: an experimental and numerical investigation. *Journal of Constructional Steel Research*, 54(1):109–133, 2000.

[12] Ju Chen and Ben Young. Stress–strain curves for stainless steel at elevated temperatures. *Engineering Structures*, 28(2):229–239, 2006.

[13] Ju Chen and Ben Young. Experimental investigation of cold-formed steel material at elevated temperatures. *Thin-walled structures*, 45(1):96–110, 2007.

[14] K. W. Poh. Stress-strain-temperature relationship for structural steel. *Journal of materials in civil engineering*, 13(5):371–379, 2001.

[15] Sina Sinaie, Amin Heidarpour, and Xiao-Ling Zhao. Mechanical properties of cyclically-damaged structural mild steel at elevated temperatures. *Construction and Building Materials*, 52:465–472, 2014.

[16] Frank McKenna, GL Fenves, MH Scott, et al. Open system for earthquake engineering simulation. *University of California, Berkeley, CA*, 2000.

[17] *ABAQUS, Software package, Version 6.12*. SIMULIA, Providence, RI, 2012.

[18] Amin Heidarpour and Mark A Bradford. Behaviour of a t-stub assembly in steel beam-to-column connections at elevated temperatures. *Engineering Structures*, 30(10):2893–2899, 2008.

[19] Amin Heidarpour and Mark A Bradford. Generic nonlinear modelling of restrained steel beams at elevated temperatures. *Engineering Structures*, 31(11):2787–2796, 2009.

[20] Amin Heidarpour and Mark A Bradford. Non-discretisation formulation for the non-linear analysis of semi-rigid steel frames at elevated temperatures. *Computers & structures*, 88(3):207–222, 2010.

[21] Zi Mroz. On the description of anisotropic workhardening. *Journal of the Mechanics and Physics of Solids*, 15(3):163–175, 1967.

[22] Yannis F Dafalias and Egor P Popov. A model of nonlinearly hardening materials for complex loading. *Acta Mechanica*, 21(3):173–192, 1975.

[23] Chi Shen, Eliji Mizuno, and Tsutomu Usami. A generalized cyclic plasticity model for steels with yield plateau. *Advances in Engineering Plasticity and its Applications*, page 175, 1993.

[24] Kyoosil Choi and Jwo Pan. A generalized anisotropic hardening rule based on the mroz multi-yield-surface model for pressure insensitive and sensitive materials. *International Journal of Plasticity*, 25(7):1325–1358, 2009.

[25] Bahar Ayhan, Pierre Jehel, Delphine Brancherie, and Adnan Ibrahimbegovic. Coupled damage–plasticity model for cyclic loading: Theoretical formulation and numerical implementation. *Engineering Structures*, 50:30–42, 2013.

[26] Dongkeon Kim, Gary F Dargush, and Cemal Basaran. A cyclic two-surface thermoplastic damage model with application to metallic plate dampers. *Engineering Structures*, 52:608–620, 2013.

[27] Sina Sinaie, Amin Heidarpour, and Xiao-Ling Zhao. A multi-objective optimization approach to the parameter determination of constitutive plasticity models for the simulation of multi-phase load histories. *Computers & Structures*, 138:112–132, 2014.

[28] Jonathan Hancock and Julian J Bommer. The effective number of cycles of earthquake ground motion. *Earthquake engineering & structural dynamics*, 34 (6):637–664, 2005.

[29] Jinming Wu. Least squares methods for solving partial differential equations by using bézier control points. *Applied Mathematics and Computation*, 2012.

[30] Licio Hernanes Bezerra. Efficient computation of bézier curves from their bernstein–fourier representation. *Applied Mathematics and Computation*, 220: 235–238, 2013.

[31] Busé Laurent. Implicit matrix representations of rational bézier curves and surfaces. *Computer-Aided Design*, 46:14–24, 2014.

[32] Zhan-Fei Huang, Kang-Hai Tan, and Seng-Kiong Ting. Heating rate and boundary restraint effects on fire resistance of steel columns with creep. *Engineering Structures*, 28(6):805–817, 2006.

[33] Neno Torić, Alen Harapin, and Ivica Boko. Experimental verification of a newly developed implicit creep model for steel structures exposed to fire. *Engineering Structures*, 57:116–124, 2013.

[34] EN 1993-1-2. *Eurocode 3: Design of steel structures - Part 1-2: General rules - Structural fire design.* Annual book of ASTM standards. European commitee for standardization, Brussels, 2005.

CHAPTER 4

A multi-objective optimisation approach to the parameter determination of constitutive plasticity models for the simulation of multi-phase load histories

Contents

Monash University

Declaration for Thesis Chapter 4

Declaration by candidate

In the case of Chapter 4, the nature and extent of my contribution to the work was the following:

Nature of contribution	Extent of contribution (%)
Development of ideas, Development of original computer model, Model verification and validation, Data analysis, Write-up and revision	70%

The following authors contributed to the work. If co-authors are students at Monash University, the extent of their contribution in percentage terms must be stated.

Name	Nature of contribution	Extent of contribution (%)
Dr. Amin Heidarpour	Developing ideas Revision Financial support	
Prof. Xiao-Ling Zhao	Revision Financial support	

The undersigned hereby certify that the above declaration correctly reflects the nature and extent of the candidate's and co-authors' contributions to this work.

Candidate's signature: ██████████ **Date:** 24/09/2015

Main supervisor's signature: ██████████ **Date:** 24/09/2015

Abstract

This work develops a multi-objective optimisation approach to determine the material constants of constitutive plasticity models. The process is implemented using an actual set of experimental results in the form of multi-phase cyclic-monotonic load histories. With the result of a multi-objective approach being a set of solutions (a set of calibrated models), the characteristics of these solutions are examined individually and within the framework of the entire set. Two elements of parameter determination are considered to address the characteristics of the calibrated models in a multi-objective space: The number of material constants, and the load history used to calibrate the models.

Keywords

Multi-objective optimisation, Constitutive plasticity, Parameter determination, Multi-phase loading, Structural steel

4.1   Introduction

Constitutive plasticity models have become more and more complex over the past decades. Researchers have strived to develop more advanced formulations in order to simulate more complex behaviour of material. One main feature of constitutive plasticity models is the existence of a yield surface defined in stress space wherein its location as well as its size can evolve as a result of plastic deformation. The location and size of the yield surface is designated by means of two distinct classes of internal variables whereby each variable evolves according to a pre-defined rule, namely the kinematic and the isotropic hardening rules. As a result, these two internal variables can be viewed as variables which have a memory of the past loading history. While the kinematic variable and kinematic hardening rule are intrinsic to models focusing on cyclic behaviour, inclusion of the isotropic variable and isotropic hardening rule becomes essential for models pertaining to the monotonic or the high amplitude cyclic behaviour of a material.

Each and every available hardening rule has been proposed with the intent to allow a more accurate simulation of the materials response. Among all, the fundamental concept of a multi-component hardening rule proposed by Chaboche [1] has proven to lead to significant improvements [2–4]. On the other hand, the comparison of different models and their accuracy in reproducing specific material responses has also been a topic of interest [5–7].

While more advanced hardening rules provide the means for simulating more complicated behaviour, they have also caused a fundamental problem, which is the increased number of material constants. These constants must be efficiently selected in order to take advantage of the potential of the model. This has given rise to another area of research regarding constitutive modelling, that is the calibration of a model's parameters.

Calibration techniques can be divided into two main categories. The first category includes those methods that are suitable for hand calculations. The methods in this category are developed for a specific model or at best, a specific class of models. Moreover, they are usually based on assumptions for the type of behaviour (monotonic, cyclic, ratcheting, etc.) and initial conditions. Examples of this category of calibration techniques can be found in [5, 6, 8–11].

On the other hand, the second category involves techniques which are primarily developed for computer calculations. These methods provide a general procedure applicable to any model. While the first category is suitable for, and applicable to, models with few material constants, the second category is applicable to any model and suitable for models with higher number of material constants.

When the number of constants incorporated in a model rises, they effectively lose their clear physical meaning. Hence, they must be viewed from a mathematical perspective [12, 13] and selected using mathematical methods, such as optimisation techniques. Mahnken and Stein [14] successfully employed a gradient-based method to develop a parameter determination method for inelastic models. Saleeb et al. [15] used a gradient-based optimisation method in order to minimise the error function and determine optimal material parameters. Also using a gradient-based optimisation method, Desai and Chen [16] demonstrated the advantages of determining material constants through optimisation, as opposed to the simple method of averaging. Simoni and Schrefler [17] implemented a constrained optimisation technique to effectively calibrate generalised plasticity models with a large number of material constants. Furukawa et al. [18] developed an automated parameter determination method for constitutive models using an evolutionary optimisation algorithm. Yoshida et al. [19] employed sequential quadratic programming to perform a multi-point approximation technique and hence minimise the difference between experimental results and numerical simulations. Rahman et al. [20] used a variation of the genetic algorithm method to determine the material properties of their model. Their work was later extended by Krishna et al. [21] to simulate cyclic and monotonic behaviour with one set of material parameters through the imposition

of a number of constraints on the model. Chaparro et al. [22] employed different techniques, namely the genetic algorithm as well as a gradient-based method. They demonstrated that a hybrid of these two methods can be more efficient. Rokonuzzaman and Sakai [23] evaluated different genetic algorithm optimisation techniques for the determination of material parameters. Yun and Shang [24] effectively used the non-gradient-based Nelder-Mead method in their work. De-Carvalho et al. [25] implemented gradient-based as well as evolutionary algorithms to determine the parameters of their constitutive models. They compared the performance of each method and also proposed improved techniques to increase the efficiency and robustness of the parameter determination process.

While the subject of parameter determination has been given attention in the past decades, some of its issues are yet to be addressed. One issue is the absence of a mathematically sound approach to which parameters can be determined with the intention to simultaneously yield suitable results for more than just one type of loading. It has been shown that if a model is calibrated using the response under a specific type of loading, that model will most likely fail to accurately simulate behaviour under other types of loading. This feature has been demonstrated by Bari and Hassan [26], Chen et al. [27], Hassan et al. [28] and Abdel-Karim [11].

In response to the above-mentioned shortcomings, the present work considers the development of an automated method, which based on the concept of multi-objective optimisation, provides a mathematically sound solution to the parameter determination problem. The proposed process falls in the category of computerised calibration techniques, indicating its independence to any specific class of material models. Moreover, since it is based on well-established mathematical theories, the method is inherently robust. These are all demonstrated through its application to an actual set of experimental data obtained from a number of rate-independent, isothermal experiments conducted on grade 300 structural mild steel. The important feature of the experimental program lies in the fact that each test involved a multi-phase loading history, whereby strain-controlled cyclic loading was followed immediately by monotonic tensile loading. Consequently, this requires one single numerical model to be capable of correctly simulating the behaviour under both phases of loading. This work also aims to investigate the process of using optimisation methods to calibrate a constitutive plasticity model to have such capabilities. For this purpose, a yield surface coupled with a multi-component non-linear isotropic/kinematic hardening rule is considered. As for the optimisation method, the gradient-free Nelder-Mead method is employed. This method, otherwise known as the downhill simplex search method, originally developed by Nelder and Mead [29], not only has the advantage

Table 4.1: Basic properties of the steel samples.

E (GPa)	σ_y (MPa)	ε_y (%)	σ_u (MPa)	ε_u (%)
225	330	0.1473	518	19.55
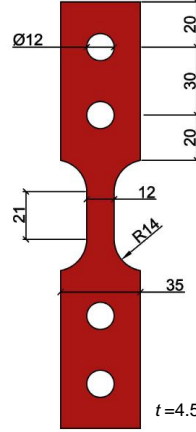
Figure 4.1: Sample geometry (in mm).

of not requiring the derivatives or Hessian of the problem at hand, but also the feasibility of its implementation as a computer code and its high convergence rate.

4.2 Experimental program

4.2.1 Material

All the specimens used in this study were made of grade 300 steel taken from the flange of 200UB22.3 hot rolled sections BHP [30]. The preparation of the samples is consistent with the requirements of ASTM E21-92 [31] and ASTM E606-92 [32]. The specimen geometry is illustrated in Fig. 4.1. Both faces of the specimens were grinded to give uniform thickness and a smooth finish across the entire surface. Specimens were restrained by means of two 12 mm high strength bolts at each end. The mechanical properties of the material are given in Table 4.1, where E is the elastic modulus and σ_y, ε_y, σ_u and ε_u denote the yield stress, yield strain, ultimate stress and ultimate strain (corresponding to the ultimate stress), respectively.

4.2.2 Cyclic loading

For the cyclic phase, a specifically built fixture was used to prevent the specimens from buckling about the weak axis. This fixture was comprised of two 12 mm plates with aligned holes in order to be fastened by appropriate bolts. The inner faces of these two plates, which would be in contact with the specimen, were polished and greased to yield minimum friction. Loads were applied by an Instron test machine (model 5892) with a capacity of 100 kN. Axial force values were attained by the machine's built in transducer, while strains were accumulated by a non-contact MTS laser extensometer (model LX1500). Tests were carried out in displacement control, however, the displacement rates were adjusted such that strain-rates never exceeded $10^{-4}\,\mathrm{s}^{-1}$, which guarantees rate-independent behaviour. Fig. 4.2 illustrates the three different loading histories applied to the samples. Each of these loading histories involves a cyclic phase, followed by a monotonic phase. Figs. 4.2a and b show the loading history for 3 cycles of 2% strain amplitude (denoted by A2C3_T), Figs. 4.2c and d are for 9 cycles of 2% strain amplitude (denoted by A2C9_T) and Figs. 4.2e and f correspond to 9 cycles of random amplitude (denoted by ArC9_T). These figures illustrate strain variations as well as stress variations with respect to a quasi-time variable. The experimental stress-strain response of the material subjected to the A2C3_T loading case is illustrated in Fig. 4.3. It is worth mentioning here that any of these loading histories can be used to calibrate the plasticity model, leaving the other two for verification and validation purposes.

4.2.3 Post-cyclic tensile loading

Tensile tests were carried out with a setup similar to the cyclic stage. However, in order to have a visual on the initiation of necking, the anti-buckling fixture was removed prior to starting the test. Again, the displacement rate was accordingly adjusted to keep strain rates below $10^{-4}\,\mathrm{s}^{-1}$. Loading as well as data accumulation was continued until failure.
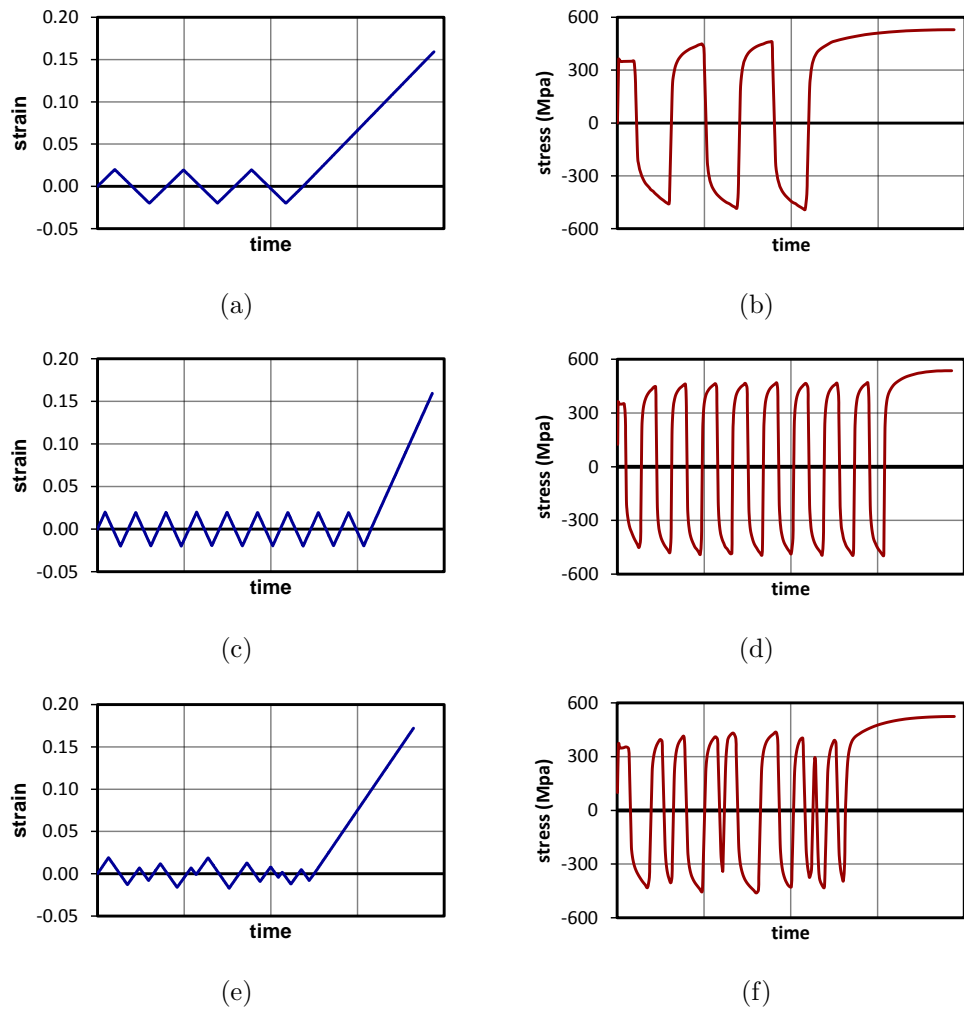
Figure 4.2: Load histories consisting of strain-controlled cyclic loading followed by a monotonic tensile loading (a,b) for A2C3_T, (c,d) for A2C9_T and (e,f) for ArC9_T.
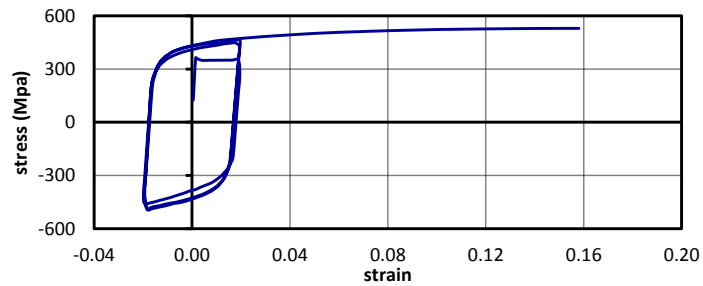
Figure 4.3: Stress-strain response of grade 300 mild steel under the A2C3_T load history.

4.3 Constitutive plasticity

4.3.1 Fundamentals of plasticity models

While the application of the proposed parameter determination process is not confined to any particular plasticity model, in this work, it is only examined using a specific case. The model used here involves the von Mises yield surface, coupled with a mixed isotropic-kinematic hardening rule and the assumption of an associated plastic flow. The constitutive relations of this model are presented in the following. The fundamental assumption of classical plasticity (stress-space plasticity) is the decomposition of the total strain increment into elastic and plastic components

$$d\underset{\sim}{\boldsymbol{\epsilon}} = d\underset{\sim}{\boldsymbol{\epsilon}}^e + d\underset{\sim}{\boldsymbol{\epsilon}}^p \tag{4.1}$$

$$d\underset{\sim}{\boldsymbol{\epsilon}}^e = \frac{1+\nu}{E}d\underset{\sim}{\boldsymbol{\sigma}} - \frac{\nu}{E}tr(d\underset{\sim}{\boldsymbol{\sigma}})\underset{\sim}{\mathbf{I}} \tag{4.2}$$

$$d\underset{\sim}{\boldsymbol{\epsilon}}^p = d\lambda\frac{\partial F}{\partial \underset{\sim}{\boldsymbol{\sigma}}} \tag{4.3}$$

where $d\underset{\sim}{\boldsymbol{\sigma}}$, $d\underset{\sim}{\boldsymbol{\epsilon}}$, $d\underset{\sim}{\boldsymbol{\epsilon}}^e$ and $d\underset{\sim}{\boldsymbol{\epsilon}}^p$ are second order tensors denoting increments in stress, total strain, elastic strain and plastic strain, respectively. In Eq. (4.2), E is the elastic modulus, ν denotes Poisson's ratio, $tr()$ represents the trace operator (i.e. $tr(\underset{\sim}{\mathbf{A}}) = A_{ii}$) and $\underset{\sim}{\mathbf{I}}$ is the second order unit tensor. In Eq. (4.3), $d\lambda$ is a non-negative scalar quantity known as the plastic multiplier. The function $F()$ is called the yield surface and plays two roles in an associated plasticity model. First, its gradient in stress space $(\partial F/\partial d\underset{\sim}{\boldsymbol{\sigma}})$ determines the direction of plastic flow, which is expressed by Eq. (4.3). Second, the yield surface designates the elastic domain. The von Mises yield surface only consists of one material constant, i.e. the uniaxial yield stress σ_y, and is written in the following form

$$F(\underset{\sim}{\boldsymbol{\sigma}},\underset{\sim}{\mathbf{X}}, R) = \sqrt{2J_2(\underset{\sim}{\boldsymbol{\sigma}} - \underset{\sim}{\mathbf{X}})} - R - \sqrt{3/2}\sigma_y < 0 \tag{4.4}$$

with

$$2J_2(\underset{\sim}{\boldsymbol{\sigma}} - \underset{\sim}{\mathbf{X}}) = (\underset{\sim}{\boldsymbol{\sigma}}' - \underset{\sim}{\mathbf{X}}') : (\underset{\sim}{\boldsymbol{\sigma}}' - \underset{\sim}{\mathbf{X}}') \tag{4.5}$$

where $J_2()$ denotes the second deviatoric invariant function and R is a scalar quantity representing the size change of the yield surface. In addition, the second order tensors $\underset{\sim}{\mathbf{X}}$, $\underset{\sim}{\mathbf{X}}'$ and $\underset{\sim}{\boldsymbol{\sigma}}'$ denote backstress, deviatoric backstress and deviatoric stress, respectively. The symbol ":" designates the product contracted twice, i.e. $\underset{\sim}{\mathbf{A}} : \underset{\sim}{\mathbf{B}} = A_{ij}B_{ij}$ with Einstein's summation convention (as opposed to "·" denoting

the product contracted once, i.e. $\underset{\sim}{\mathbf{A}} \cdot \underset{\sim}{\mathbf{B}} = A_{ik}B_{kj}$). For convenience in upcoming formulations, $\underset{\sim}{\boldsymbol{\sigma}}' - \underset{\sim}{\mathbf{X}}'$ is denoted by $\underset{\sim}{\boldsymbol{\rho}}$

The non-negative scalar $d\lambda$ presented in Eq. (4.3) can be determined through the loading-unloading condition expressed in the Kuhn-Tucker form

$$\begin{cases} d\lambda \geq 0 \\ F(\underset{\sim}{\boldsymbol{\sigma}}, \underset{\sim}{\mathbf{X}}, R) \leq 0 \\ d\lambda F(\underset{\sim}{\boldsymbol{\sigma}}, \underset{\sim}{\mathbf{X}}, R) = 0 \end{cases} \tag{4.6}$$

Hardening characteristics of a model are described by differential relations on R and $\underset{\sim}{\mathbf{X}}$. In common terminology, a change in R is known as isotropic hardening, while a change in the backstress $\underset{\sim}{\mathbf{X}}$ is called kinematic hardening. For multi-components hardening rules

$$dR = \sum_{j=1}^{M} dR_j \tag{4.7}$$

$$d\underset{\sim}{\mathbf{X}} = \sum_{j=1}^{K} d\underset{\sim}{\mathbf{X}}_j \tag{4.8}$$

where in this paper, the following expressions are used for the components

$$dR_j = b_j(Q_j - R_j)dp \tag{4.9}$$

$$d\underset{\sim}{\mathbf{X}}_j = \frac{2}{3}B_j d\underset{\sim}{\boldsymbol{\epsilon}}^p - \gamma_j \underset{\sim}{\mathbf{X}}_j dp \tag{4.10}$$

$$dp = \sqrt{\frac{2}{3}d\underset{\sim}{\boldsymbol{\epsilon}}^p : d\underset{\sim}{\boldsymbol{\epsilon}}^p} \tag{4.11}$$

In Eqs. (4.7) to (4.8), I and K denote the number of isotropic and kinematic components, respectively. Moreover, b, Q, B and γ are material constants which are to be determined from experimental data. Eq. (4.9) corresponds to a non-linear isotropic hardening rule, while Eq. (4.10) represents a common non-linear kinematic hardening rule. In this work, the isotropic rule is coupled with the kinematic rule to yield a mixed hardening model.

4.3.2 Integration of rate equations

In order to use the constitutive equations described by Eqs. (4.1) to (4.11), the following method is implemented. For the von Mises yield surface defined by Eq. (4.4), the following relations can be deduced

$$\frac{\partial F}{\partial \underset{\sim}{\boldsymbol{\sigma}}} = -\frac{\partial F}{\partial \underset{\sim}{\mathbf{X}}} = \frac{\underset{\sim}{\boldsymbol{\rho}}'}{\sqrt{2J(\underset{\sim}{\boldsymbol{\rho}}')}} \tag{4.12}$$

$$\frac{\partial F}{\partial R} = -1 \tag{4.13}$$

Moreover, using Eqs. (4.1) to (4.3), one can attain

$$\Delta \underset{\sim}{\boldsymbol{\sigma}} = \underset{\approx}{\mathbf{D}} : (\Delta \underset{\sim}{\boldsymbol{\epsilon}} - \Delta \underset{\sim}{\boldsymbol{\epsilon}}^p) = \underset{\approx}{\mathbf{D}} : (\Delta \underset{\sim}{\boldsymbol{\epsilon}} - \Delta \frac{\partial F}{\partial \underset{\sim}{\boldsymbol{\sigma}}}) \tag{4.14}$$

where $\Delta \underset{\sim}{\boldsymbol{\epsilon}}$ denotes the total strain increment which the constitutive equations are to be integrated over. Noting that

$$\underset{\approx}{\mathbf{D}} = \frac{E}{1+\nu} \underset{\approx}{\mathbf{I}} + \frac{E\nu}{(1+\nu)(1-2\nu)} (\underset{\sim}{\mathbf{I}} \otimes \underset{\sim}{\mathbf{I}}) \tag{4.15}$$

where $\underset{\sim}{\mathbf{I}}$ and $\underset{\approx}{\mathbf{I}}$ denote second and forth order unit tensors and '$\otimes$' represents tensor multiplication, and therefore, the following equations are valid

$$\frac{\partial F}{\partial \underset{\sim}{\boldsymbol{\sigma}}} : \underset{\approx}{\mathbf{D}} = \frac{E}{1+\nu} \frac{\underset{\sim}{\boldsymbol{\rho}'}}{\sqrt{2J(\underset{\sim}{\boldsymbol{\rho}'})}} \tag{4.16}$$

$$\frac{\partial F}{\partial \underset{\sim}{\boldsymbol{\sigma}}} : \underset{\approx}{\mathbf{D}} : \frac{\partial F}{\partial \underset{\sim}{\boldsymbol{\sigma}}} = \frac{E}{1+\nu} \tag{4.17}$$

Assuming a loading condition (i.e. $d\lambda > 0$ in Eq. (4.6)), the consistency condition dictates that the stress state must lie on the yield surface, so that

$$F(\underset{\sim}{\boldsymbol{\sigma}} + \Delta \underset{\sim}{\boldsymbol{\sigma}}, \underset{\sim}{\mathbf{X}} + \Delta \underset{\sim}{\mathbf{X}}, R + \Delta R) = 0 \tag{4.18}$$

In order to use Newton's iterative method of solving non-linear problems, the first two terms of Taylor's expansion are extracted from Eq. (4.18), hence

$$F(\underset{\sim}{\boldsymbol{\sigma}}, \underset{\sim}{\mathbf{X}}, R) + \frac{\partial F}{\partial \underset{\sim}{\boldsymbol{\sigma}}} : \Delta \underset{\sim}{\boldsymbol{\sigma}} + \frac{\partial F}{\partial \underset{\sim}{\mathbf{X}}} : \Delta \underset{\sim}{\mathbf{X}} + \frac{\partial F}{\partial R} \Delta R = 0 \tag{4.19}$$

Substituting Eqs. (4.3),(4.7) and (4.8) into Eq. (4.19) and using Eqs. (4.12) to (4.18) results in

$$\Delta \lambda = \frac{\dfrac{\partial F}{\partial \underset{\sim}{\boldsymbol{\sigma}}} : \underset{\approx}{\mathbf{D}} : \Delta \underset{\sim}{\boldsymbol{\epsilon}}}{\dfrac{\partial F}{\partial \underset{\sim}{\boldsymbol{\sigma}}} : \underset{\approx}{\mathbf{D}} : \dfrac{\partial F}{\partial \underset{\sim}{\boldsymbol{\sigma}}} + H_k + H_i}$$

$$= \frac{1}{1 + \dfrac{(1+\nu)}{E}(H_k + H_i)} \frac{(\underset{\sim}{\boldsymbol{\rho}'} : \Delta \underset{\sim}{\boldsymbol{\epsilon}})}{\sqrt{2J(\underset{\sim}{\boldsymbol{\rho}'})}} \tag{4.20}$$

$$H_k = \sum_{j=1}^{K} \left[\frac{2}{3} B_j - \gamma_j \frac{\underset{\sim}{\boldsymbol{\rho}'} : \underset{\sim}{\mathbf{X}}_j}{\sqrt{2J(\underset{\sim}{\boldsymbol{\rho}'})}} \sqrt{\frac{2}{3}} \right] \tag{4.21}$$

$$H_i = \sum_{j=1}^{M} b_j (Q_j - R_j) \tag{4.22}$$

Eqs. (4.1) to (4.3) are then used to attain $\Delta\underset{\sim}{\boldsymbol{\epsilon}}^p$, $\Delta\underset{\sim}{\boldsymbol{\epsilon}}^e$ and $\Delta\underset{\sim}{\boldsymbol{\sigma}}$ consecutively. It is worth mentioning that when using the von Mises model, the described approach only needs to be performed once to maintain the stress state in the yield surface. However, this is accomplished by linearisation of the constitutive equations. In order to capture the non-linear variation of stress and produce more accurate results, it is recommended that from the onset of plastic flow, the total strain increment ($\Delta\underset{\sim}{\boldsymbol{\epsilon}}$) be divided into a number of substeps [33]. For cases where the initial stress is inside the yield surface (the elastic domain), the point at which the stress path reaches the yield surface is calculated using the following scalar

$$\alpha = \frac{-F(\underset{\sim}{\boldsymbol{\sigma}}, \underset{\sim}{\mathbf{X}}, R)}{F(\underset{\sim}{\boldsymbol{\sigma}} + \underset{\approx}{\mathbf{D}} : \Delta\underset{\sim}{\boldsymbol{\epsilon}}, \underset{\sim}{\mathbf{X}}, R) - F(\underset{\sim}{\boldsymbol{\sigma}}, \underset{\sim}{\mathbf{X}}, R)} \tag{4.23}$$

For cases where $\alpha > 0$, the intersection point is determined by $\underset{\sim}{\boldsymbol{\sigma}}_{\text{int}} = \underset{\sim}{\boldsymbol{\sigma}}_{\text{o}} + \alpha(\underset{\approx}{\mathbf{D}} : \Delta\underset{\sim}{\boldsymbol{\epsilon}})$, where $\underset{\sim}{\boldsymbol{\sigma}}_{\text{o}}$ is the original stress state. On the other hand, a value of $\alpha \leq 0$ indicates that the stress path never crosses the yield surface and therefore, the increment is entirely elastic. From an algorithmic viewpoint, Eq. (4.23) can be used prior to any other calculation to determine whether plastic flow ever takes place during a strain increment.

4.4 Multi-objective optimisation

4.4.1 General

The aim is to determine the material constants of a constitutive model with the intention of reproducing the response observed in an actual experiment. If a set of material constants are suggested in the process, the degree of success of this set in simulating that specific experimental response can be quantified by means of a function $f(\vec{\mathbf{x}})$, where $\vec{\mathbf{x}} = [x_1 \quad x_2 \quad \cdots \quad x_n]$ is the vector of material constants, and the return value of $f()$ represents the discrepancy between the analytical response and the experimental observation. Therefore, the problem can now be rephrased in mathematical terms as an unconstrained optimisation problem

$$\min_{\vec{\mathbf{x}}} f(\vec{\mathbf{x}}) \tag{4.24}$$

where $\vec{\mathbf{x}} \in S$ is the n-dimensional decision variable vector, and $S \subset \mathbb{R}^n$ is called the feasible region. The feasible region contains all possible $\vec{\mathbf{x}}$ that can be used to evaluate $f(\vec{\mathbf{x}})$. In common terminology, $f()$ is known as the fitness function

or the objective function. For the purpose of determining material constants of a constitutive model, objective functions are usually defined in the form of an error function acting on the entire domain of a measured variable [24, 34], similar to the following equation

$$f(\vec{\mathbf{x}}) = \frac{1}{K} \sum_{i=1}^{K} \left| p_i^{\text{sim}}(\vec{\mathbf{x}}) - p_i^{\text{exp}} \right| \tag{4.25}$$

where p_i^{sim} and p_i^{exp} are the simulated and experimental values of the same variable (e.g. stress)at a given instant i, and K is the total number of instances. In addition, $||$ represent the absolute value.

In the context of parameter determination, the aforementioned representation has two shortcomings. First, it places fixed emphasis on the entire duration of the response. This is not always desirable, since there are situations where different parts of the load history differ in terms of importance (e.g. in multi-phase load histories) and the aim is to determine the material constants accordingly. Second, it does not provide the mathematical tools required to obtain one single set of material constants, suitable for simultaneously simulating the behaviour under two or more types of loading. Hence, as a more general solution, the objective function used in the current paper is defined in a more primitive form, such that

$$\begin{aligned} f_i(\vec{\mathbf{x}}) &= f(\vec{\mathbf{x}}, t_i, t_{i+1}) \\ &= \frac{1}{t_{i+1} - t_i} \int_{t=t_i}^{t_{i+1}} \left| p_i^{\text{sim}}(\vec{\mathbf{x}}, t) - p_i^{\text{exp}}(t) \right| dt \end{aligned} \tag{4.26}$$

This representation gives the ability to arbitrarily slice an entire time span into two or more segments, and therefore, define a unique objective function for each part of the response. With the availability of a number of objective functions, the initial single-objective optimisation problem can be converted to a multi-objective one. In addition, within the context of multi-objective optimisation, any number of load histories can be processed simultaneously. One of the benefits of using multi-objective optimisation is the amount of control it grants over the management of the objectives. This means more control over the simulation of each loading phase; individually and in relation to all other phases. The proceeding text describes the basic concepts of multi-objective optimisation, and addresses the issues that arise for such problems.

4.4.2   Definitions

The following definitions are used henceforth to describe multi-objective concepts [35]:

Definition 1: Multi-objective optimisation
An unconstrained multi-objective optimisation problem is defined as

$$\min_{\vec{\mathbf{x}}} \vec{\mathbf{F}}(\vec{\mathbf{x}}) = [f_1(\vec{\mathbf{x}}), \ldots, f_M(\vec{\mathbf{x}}))] \tag{4.27}$$

While by previous definitions, the feasible region contains all possible $\vec{\mathbf{x}}$ that can be used to evaluate $\vec{\mathbf{F}}(\vec{\mathbf{x}})$, the admissible region contains all $\vec{\mathbf{F}}(\vec{\mathbf{x}})$ that can be attained by all possible $\vec{\mathbf{x}}$.

Definition 2: Pareto dominance
The vector $\vec{\mathbf{u}} = (u_1, \ldots, u_M)$ is said to dominate the vector $\vec{\mathbf{v}} = (v_1, \ldots, v_M)$, if and only if $\vec{\mathbf{u}}$ is partially less than $\vec{\mathbf{v}}$ (i.e. $\forall i \in \{1, \ldots, M\} : u_i \leq v_i$ and $\exists i \in \{1, \ldots, M\} : u_i < v_i$). This is denoted by $\vec{\mathbf{u}} \preceq \vec{\mathbf{v}}$.

Definition 3: Pareto optimality
In a multi-objective framework, in general, no single $\vec{\mathbf{x}} \in S$ simultaneously gives the least possible values for all f_i. Therefore, for these problems, the concept of *Pareto optimality* becomes useful. A solution $\vec{\mathbf{x}} \in S$ is said to be Pareto optimal with respect to the feasible region Ω, if and only if $\nexists \vec{\mathbf{x}}' \in S : \vec{\mathbf{F}}(\vec{\mathbf{x}}') \preceq \vec{\mathbf{F}}(\vec{\mathbf{x}})$. This means that if $\vec{\mathbf{x}} \in S$ is Pareto optimal, there does not exist another feasible vector which would decrease some objective without causing a simultaneous increase in at least one other objective.

Definition 4: Pareto optimal set
For a specific multi-objective optimisation problem, the *Pareto optimal set* is the set of all Pareto optimal solutions, and is defined as $P^* = \{\vec{\mathbf{x}} \in S | \nexists \vec{\mathbf{x}}' \in S : \vec{\mathbf{F}}'(\vec{\mathbf{x}}) \preceq \vec{\mathbf{F}}(\vec{\mathbf{x}})\}$. In other words, the Pareto optimal set constitutes the solutions for which any attempt to decrease one objective value would result in an increase in the value of one or more other objectives. Hence, the Pareto set can be considered as such a compromise between the solutions of an optimisation problem.

Definition 5: Pareto front
For a specific multi-objective optimisation problem with a Pareto optimal set P^*, the Pareto front is defined as $PF^* = \{\vec{\mathbf{u}} = \vec{\mathbf{F}}(\vec{\mathbf{x}}) | \vec{\mathbf{x}} \in P^*\}$. In contrast to a single-
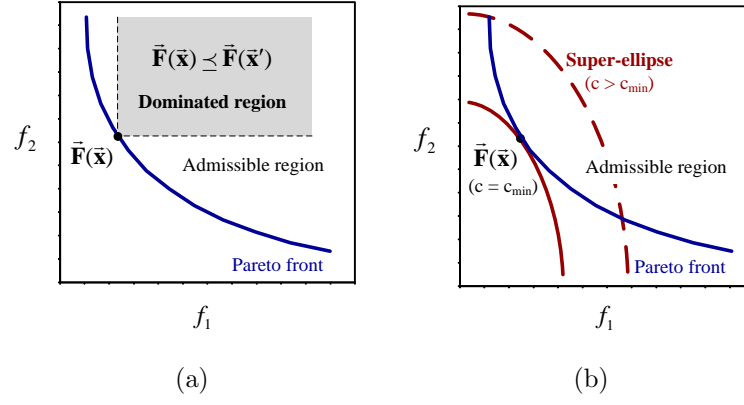
Figure 4.4: Pareto front. (a) Admissible region and the dominated region. (b) Super-ellipse and capturing Pareto optimal solutions.

objective problem, a multi-objective optimisation problem does not have a single unique optimal solution, but rather a set of solutions. The main goal of a multi-objective problem is to find this set known as the Pareto optimal set. For an unbiased problem, any of the solutions constituting the Pareto set are equally acceptable.

The definition of the Pareto front and its properties are used as the basis for finding the Pareto optimal set. In what follows, the solution process is discussed in the context of a minimisation problem, and for the sake of simplicity, is exemplified for a bi-objective case ($M = 2$). For the Pareto front, the following properties can be deduced from the aforementioned definitions 1-5:

- The Pareto front constitutes the edge of the admissible region.

- In terms of f_1 and f_2, the Pareto front takes the form of a monotonically decreasing function.

These two properties are illustrated in Fig. 4.4.

For the purpose of finding the points on the Pareto front, a super-ellipse (Lamé curve) in (f_1, f_2) space with its centre at the origin of the coordinate system is expressed such that

$$[w_1 [f_1]^p + w_2 [f_2]^p]^{\frac{1}{p}} = c \tag{4.28}$$

where c is a constant, and assuming that the value of c is large enough, a portion of the super ellipse will lie within the admissible region. By decreasing the value of c, the overlapping portion becomes smaller and smaller, until at a specific value ($c = c_{min}$), the overlapped portion becomes a single point (Fig. 4.4). Note that a super-ellipse with a value of $c < c_{min}$, has no point inside the admissible region.

Using this feature, one can define

$$G(\vec{\mathbf{x}}) = [w_1 \, [f_1(\vec{\mathbf{x}})]^p + w_2 \, [f_2(\vec{\mathbf{x}})]^p]^{\frac{1}{p}} \tag{4.29}$$

and seek the solution to

$$\min_{\vec{\mathbf{x}}} G(\vec{\mathbf{x}}) \tag{4.30}$$

Knowing that the minimum value only corresponds to points on the Pareto front, the multi-objective optimisation problem has now been reduced to a single-objective one. As expected, different combinations of w_1 and w_2 yield different members of the Pareto optimal set and hence, different points on the Pareto front. More details on the properties of this and other aggregation methods have been discussed by Marler and Arora [36].

4.4.3 Preference preservation

There are always two stages to a parameter determination problem; one is the calibration of the model, and the other is the validation of that calibrated model. Hence, after the parameters of a model are determined by minimising a specific objective function, the same parameters must then be used to validate the model under other error functions. One method of validation is the evaluation of the calibrated model by using secondary objective functions and ensuring that the resulting error is smaller than a predefined value. This is effectively illustrated by Desai and Chen [16] where a model with 13 parameters is first optimised for least error against a series of test results and then validated using a different set of experimental data. This kind of validation is of great importance and necessary for any parameter determination problem, regardless of the number of objective functions.

However, when multiple objectives are present, an additional validation criterion can be introduced. The basis of this additional validation is, in this paper, referred to as the *preservation of preferences*. In order to understand the concept of preference preservation, one can look into Eq. (4.29) and Fig. 4.5. Two specific points are marked in Fig. 4.5a. The first point corresponding to $\vec{\mathbf{x}}_1$ and being the result of only including f_1 in Eq. (4.29) ($w_2 \approx 0$) and the second point corresponding to $\vec{\mathbf{x}}_2$ and being the result of only including f_2 in Eq. (4.29) ($w_1 \approx 0$). Notice that the point on the Pareto front corresponding to $\vec{\mathbf{x}}_1$ has the lowest value of f_1 among all other points, while the point corresponding to $\vec{\mathbf{x}}_2$ has the lowest value of f_2. Consequentially, any other combination of w_1 and w_2 results in a Pareto optimal solution ($\vec{\mathbf{x}}$) which
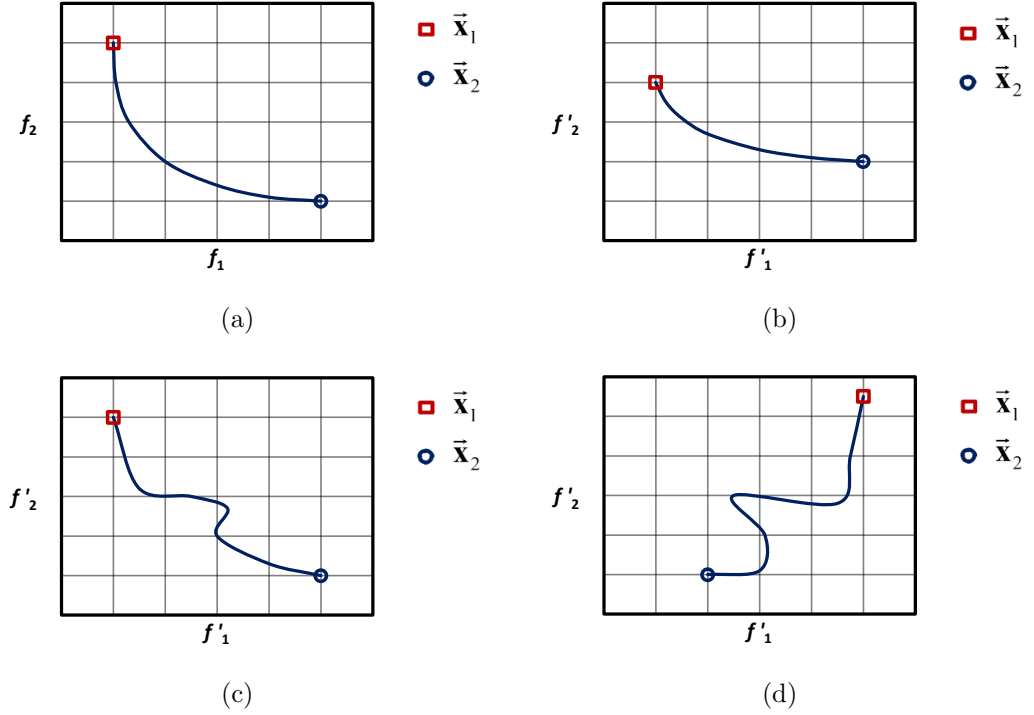
Figure 4.5: Pareto front in (f_1, f_2) space and its mapped counterparts in (f'_1, f'_2) space. (a) Original Pareto front. (b) Prefect preference preservation. (c and d) Partial preference preservation.

corresponds to a point somewhere between the two ends of the Pareto front. An operator selects a specific $\vec{\mathbf{x}}$ over all the other Pareto optimal solutions, based on his/her preferences for the respective values of f_1 and f_2. However, the question is whether the selected model preserves those preferences under another set of error functions.

In order to validate the Pareto optimal solutions for preference preservation, two new error functions f'_1 and f'_2 are presented. It is reasonable to assume that in terms of the type of response, f'_1 is in the same class as f_1, and f'_2 is in the same class as f_2. For example, in the context of material behaviour, f_1 and f'_1 can both be cyclic responses, but under different load amplitudes, and f_2 and f'_2 can both be thermal responses, but under different temperature gradients. If each and every Pareto optimal solution (calibrated model) of Fig. 4.5a is used to evaluate f'_1 and f'_2, the result would be a curve in (f'_1, f'_2) space. This new curve is a mapped counterpart of the original Pareto front from (f_1, f_2) to (f'_1, f'_2). Figs. 4.5b-d are examples of how the mapped curve might look like.

With N being the number of Pareto optimal solutions used to construct the Pareto front, the Pareto optimal set is arranged as $f_1(\vec{\mathbf{x}}_1) \leq \ldots \leq f_1(\vec{\mathbf{x}}_N)$. Note that accord-

ing to the second deduced property of the Pareto front, the condition $f_1(\vec{\mathbf{x}}_i) \leq f_1(\vec{\mathbf{x}}_j)$ immediately concludes that $f_2(\vec{\mathbf{x}}_i) \geq f_2(\vec{\mathbf{x}}_j)$. This allows the following definition for the preference preservation criterion

$$\forall i \in \{1, \ldots, N-1\}:$$
$$f_1'(\vec{\mathbf{x}}_i) \leq f_1'(\vec{\mathbf{x}}_{i+1}) \wedge f_2'(\vec{\mathbf{x}}_i) \geq f_2'(\vec{\mathbf{x}}_{i+1}) \tag{4.31}$$

With this definition, it is observed that the mapped counterpart of Fig. 4.5b satisfies the criterion, while Figs. 4.5c and d do not.

The condition given in Eq. (4.31) is very strict, only being satisfied when the mapped counterpart is a monotonically decreasing function. If a model passes such a strict condition, it can be considered a perfect preference preserving model. However, it is more common for a model to only partially pass the preservation condition, i.e. monotonically decrease over some parts but not the entire domain. In such cases, a preference preservation index (k_p) can be defined as follows

$$k_p = L_p/L_t \tag{4.32}$$

where L_p and L_t are defined as

$$L_p = \sum_{i=1}^{N-1} \Bigg[\|\vec{\mathbf{x}}_{i+1} - \vec{\mathbf{x}}_i\|$$
$$\times H(f_1'(\vec{\mathbf{x}}_{i+1}) - f_1'(\vec{\mathbf{x}}_i))$$
$$\times H(f_2'(\vec{\mathbf{x}}_i) - f_2'(\vec{\mathbf{x}}_{i+1})) \Bigg] \tag{4.33}$$

and

$$L_t = \sum_{i=1}^{N-1} \|\vec{\mathbf{x}}_{i+1} - \vec{\mathbf{x}}_i\| \tag{4.34}$$

In the above equations, $H()$ is the Heaviside step function ($H(x) = 1$ for $x \geq 0$ and $H(x) = 0$ for $x < 0$) and $\|\vec{\mathbf{x}}\|$ denotes the norm of $\vec{\mathbf{x}}$. Based on the definition of L_p and L_t, the value of k_p is in the range of $0 < k_p < 1$. Note that Eq. (4.33) only involves non-principal objectives where preference preservation characteristics are sought. This preference preservation parameter is used in the subsequent section to compare the response of different models.

4.5   Numerical illustration

As mentioned in the previous sections, the tests conducted in the present work involved two stages of loading; an initial cyclic load, followed immediately by a

monotonic tensile load (Fig. 4.2). It has also been mentioned that these tests were part of a more extensive experimental program planned to be conducted in the future for the investigation of the behaviour of structural elements under post-cyclic scenarios. The purpose of the initial tests is to determine a set of material properties which is capable of producing reasonable results for both phases of loading. It is imperative for the future part of the work that the selected material constants produce valid results, for both the cyclic loading phase and the monotonic tensile loading phase.

The uniaxial time variations of stress and strain under cyclic loading, succeeded by tensile loading are illustrated in Fig. 4.2. The loading is strain-controlled, therefore in what follows, stress values are considered as the output values for the tests as well as the numerical calculations.

The constitutive model selected for the numerical simulation is based on the descriptions given in Section 3. In this work, each isotropic hardening component is paired with a kinematic hardening component. Therefore, the decision vector is in the form of

$$\vec{\mathbf{x}} = \begin{bmatrix} \vec{\mathbf{x}}_1 & \vec{\mathbf{x}}_2 & \cdots & \vec{\mathbf{x}}_N \end{bmatrix} \tag{4.35}$$

with $\vec{\mathbf{x}}_i = \begin{bmatrix} b_i & Q_i & B_i & \gamma_i \end{bmatrix}$ and N being the total number of isotropic-kinematic pairs. This work uses three different settings of N equal to 1, 2 and 3 corresponding to 4, 8 and 12 material constants, respectively.

It should be mentioned that the elastic modulus and the uniaxial yield stress are directly derived from the stress-strain curve and are set to be $E = 250\text{GPa}$ and $\sigma_y = 330\text{MPa}$. It should also be mentioned that all material constants are only allowed to attain positive values. Enforcing a decision variable to stay within the positive range is achieved by programming the objective function to return a very large number when it encounters a decision variable with a negative value. However, for models with $N \geq 2$, an exception is made and Q_1 is allowed to take negative values. Doing so leads to a great improvement in simulating the yield plateau of the stress-strain curve. A negative Q means softening behaviour, consequently implying that during an increment, previously stored plastic work as well as the instantaneous change in plastic work is allowed to dissipate [7]. In the realm of classic plasticity (stress space plasticity), when softening behaviour is to be modelled, it is crucial to implement a highly accurate integration method. Using the integration method formulated in Section 4.3 alongside a substepping scheme has proven to be adequately accurate.

The parameter determination process utilised here is according to the concepts developed in section 4. The two objective functions used for the optimisation process are

$$
\begin{aligned}
f_c(\vec{\mathbf{x}}) &= f(\vec{\mathbf{x}}, t_o, t_c) \\
&= \frac{1}{t_c - t_o} \int_{t=t_o}^{t_c} \left| \sigma^{\text{sim}}(\vec{\mathbf{x}}, t) - \sigma^{\text{exp}}(t) \right| dt
\end{aligned}
\tag{4.36}
$$

$$
\begin{aligned}
f_m(\vec{\mathbf{x}}) &= f(\vec{\mathbf{x}}, t_c, t_m) \\
&= \frac{1}{t_m - t_c} \int_{t=t_c}^{t_m} \left| \sigma^{\text{sim}}(\vec{\mathbf{x}}, t) - \sigma^{\text{exp}}(t) \right| dt
\end{aligned}
\tag{4.37}
$$

These objective functions are in the form of error functions which describe the difference between simulation and experimental results as an average stress value. As can be seen, the two functions are of the same form, but only differ in the time spans which they apply to. Given that t_o, t_c and t_m respectively correspond to the onset of loading, the end of the cyclic loading and the end of the monotonic loading, it is clear that Eq. (4.36) acts on the duration of the cyclic phase of the response while Eq. (4.37) acts on the monotonic tensile phase.

As mentioned in Section 4.4.2, one way of dealing with a multi-objective optimisation problem is to aggregate the objectives into a single-objective problem using Eq. (4.29), hence

$$
G(\vec{\mathbf{x}}) = \left[w \left[f_c(\vec{\mathbf{x}}) \right]^p + (1 - w) \left[f_m(\vec{\mathbf{x}}) \right]^p \right]^{\frac{1}{p}}
\tag{4.38}
$$

Considering two special cases with $w = 1$ and $w = 0$, it can be said that the former exclusively favours the cyclic phase, while the latter exclusively favours the monotonic phase. Any value of w between these two special cases is an intermediate scenario favouring each of the two phases to some extent. This function is minimised using the Nelder-Mead method described in the appendix. The initial values for the decision variables at one vertex of the simplex are all set to zero. The other n vertices are attained by substituting zero with an arbitrary value for each decision variable. Minimisation steps are continued until the deviation in the form of Eq. (4.45) became smaller than 1.0×10^{-6}. With a continuous variation of w between $0 < w < 1$, the result is a number of Pareto optimal solutions and corresponding to those solutions is a Pareto front similar to what is shown in Fig. 4.6. This figure illustrates the tradeoff between the accuracy in which the cyclic and monotonic phases can be simulated. Note that in an unbiased problem, all the Pareto optimal solutions are equally acceptable.

A model can be calibrated using any one of the loading histories given in Fig. 4.2, and then evaluated against the remaining two load histories. In the proceeding
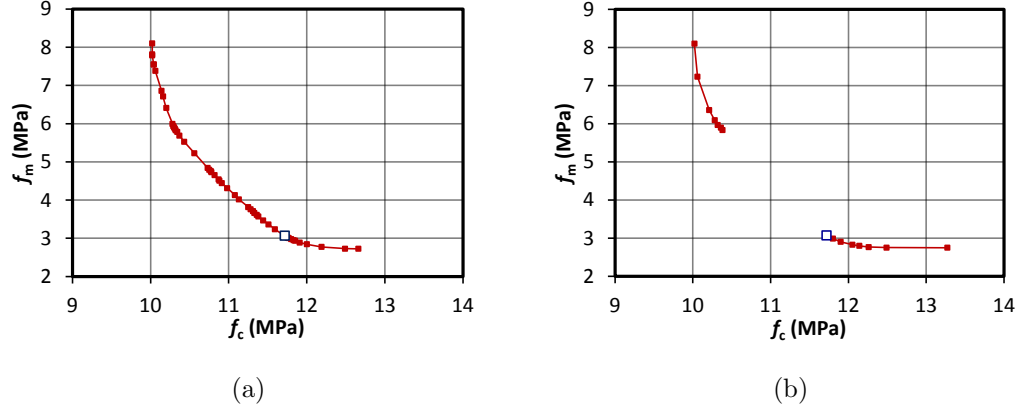
Figure 4.6: Pareto front in (f_c, f_m) space using (a) $p = 8$ and (b) $p = 1$, along with the single-objective optimisation solution indicated with a hollow marker.

text, the load history used to calibrate the model is referred to as the *principal* load history, while the load histories that are only used to evaluate a calibrated model are called the *non-principal* load histories.

An issue regarding Eq. (4.38), is the value of p, with higher values being required when the Pareto front is non-convex. In order to demonstrate this requirement, the overall analysis was carried out, once for $p = 1$ and again for $p = 8$ and the resulting Pareto fronts are presented in Fig. 4.6. Note that these two analyses were performed using A2C3_T as the principal load history (Fig. 4.2a and b) and a constitutive model with $N = 2$ (Eq. (4.35)). It is observed that the entire curve is successfully attained when $p = 8$ is used (Fig. 4.6a). However, in the case where $p = 1$, the process fails to capture the non-convex portion of the Pareto front (Fig. 4.6b). Also shown in Fig. 4.6, by a hollow marker, is the solution which is obtained if the problem is taken as a simple single-objective one, i.e. the entire load history is taken as one objective function.

Table 4.2 presents the calibrated material constants corresponding to different values of w used to obtain Fig. 4.6a. Also given in this table, are the return values of each objective function (f_c and f_m) as well as the aggregated objective function (G). These solutions are only a limited number of points out of the entire range of solutions which constitute the Pareto front given in Fig. 4.6a.

The evolution of the objective values at 5-iteration intervals is illustrated in Figs. 4.7a and b for the special case of $w = 10^{-2}$. In addition, Fig. 4.8 presents the simulated stress response at iterations 0, 10 and 20 along with the final simulation for the same case. This figure not only illustrates the high convergence rate of the optimisation method, but also the accuracy of the final simulation.

Table 4.2: Pareto optimal solutions for different values of w with $p = 8$ and A2C3_T as the principal load history.

w	f_c (MPa)	f_m (MPa)	G (MPa)	b_1	Q_1 (MPa)	B_1 (MPa)	γ_1	b_2	Q_2 (MPa)	B_2 (MPa)	γ_2
1	10.02	8.102	10.02	316.245	-220.379	72346.0	705.377	26.9984	149.242	3310.73	44.5690
10^{-1}	10.28	5.994	7.818	228.265	-209.771	44403.3	515.513	32.1015	166.409	2702.42	36.8014
10^{-2}	10.73	4.845	6.156	217.768	-204.695	38301.5	447.650	32.0772	165.528	2333.53	32.4033
10^{-3}	11.25	3.818	4.841	191.360	-215.202	33972.5	403.726	35.0878	180.460	2025.55	28.2181
10^{-4}	11.72	3.062	3.798	191.702	-205.232	30878.2	363.941	33.4792	172.920	1764.10	24.8997
10^{-5}	12.19	2.774	3.093	169.026	-198.588	24490.7	312.395	33.8057	179.979	1584.26	22.9317
10^{-6}	12.49	2.730	2.789	170.463	-196.307	24299.4	304.942	32.6793	178.428	1501.39	22.2052
10^{-7}	12.66	2.726	2.733	175.770	-196.081	24297.0	303.594	33.8007	178.274	1483.04	22.0393

(a) (b)
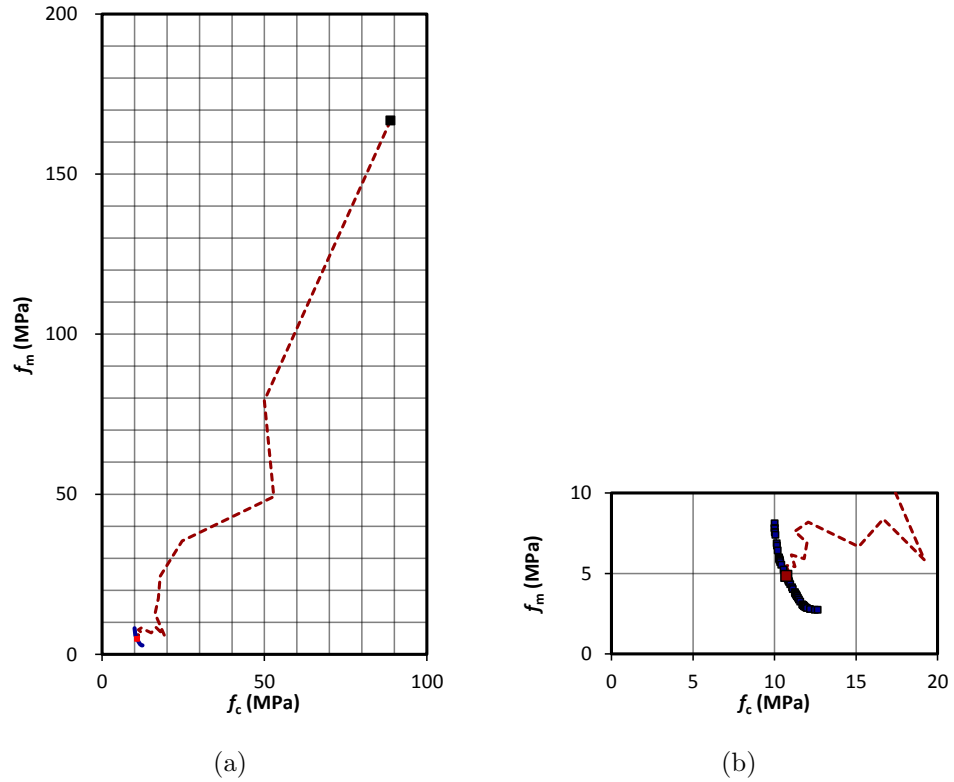
Figure 4.7: Performance evolution of the constitutive model in multi-objective space for (a) the entire range and (b) the near-solution range.
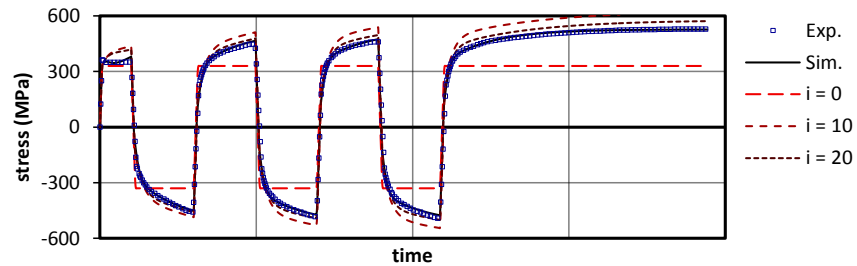
Figure 4.8: Simulation of the experimental response at the beginning and end of the optimisation process as well as iterations 10 and 20.

(a)

(b)

(c)
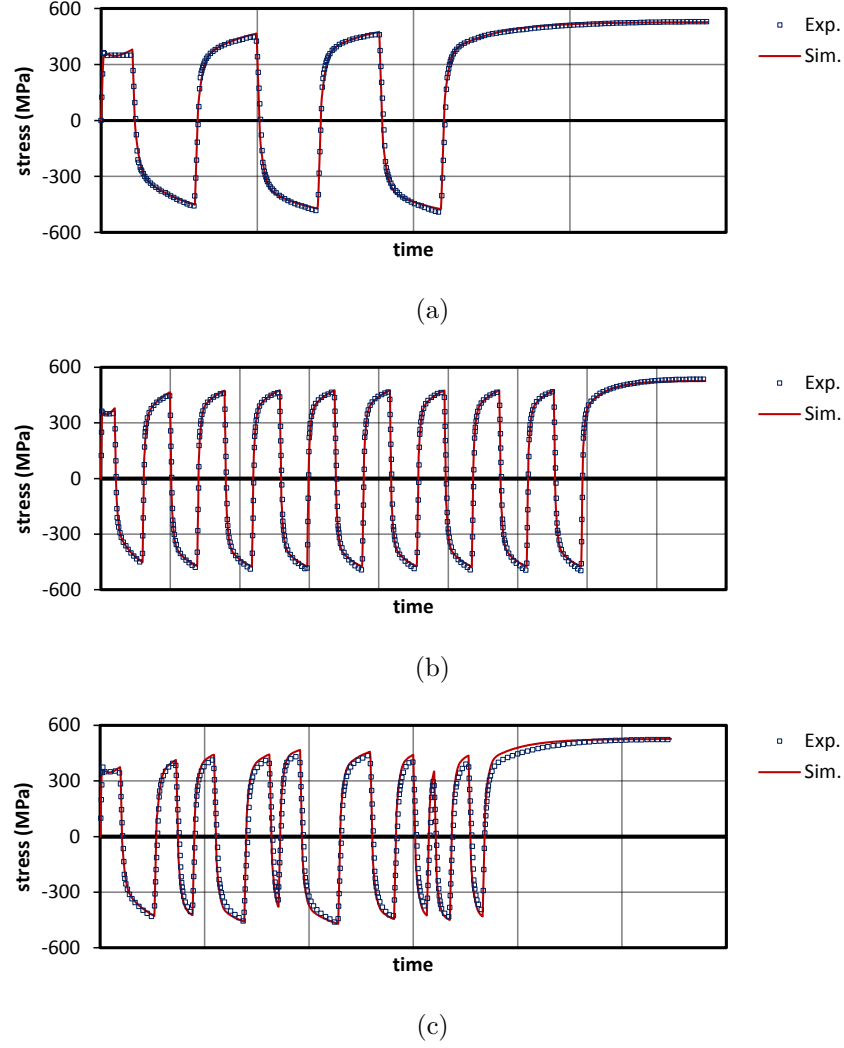
Figure 4.9: Comparison of experimental results with numerical simulations based on the solution obtained with $w = 10^{-2}$. (a) A2C3_Tload history. (b) A2C9_Tload history. (c) ArC9_Tload history.

Using the material constants of $w = 10^{-2}$ given in Table 4.2, the stress variations resulting from the loading histories of Fig. 4.2 are obtained. These are compared to the experimental variations in Fig 4.9. Note that the material constants are calibrated with respect to the A2C3_T load history (Fig. 4.2a and b), and then evaluated using the A2C9_T and ArC9_T load histories (Figs. 4.2c to f). In other words, A2C3_T is the principal load history, while A2C9_T and ArC9_T are non-principal load histories. The fact that the obtained model accurately simulates the experimental response of the principal load history (A2C3_T) was somewhat expected, since the model was calibrated against that load history. However, the capability of that same model to reasonably simulate non-principal load histories (A2C9_T and ArC9_T) demonstrates the effectiveness of the entire calibration process.

This paper also uses the concept of preference preservation (as described in Sec-
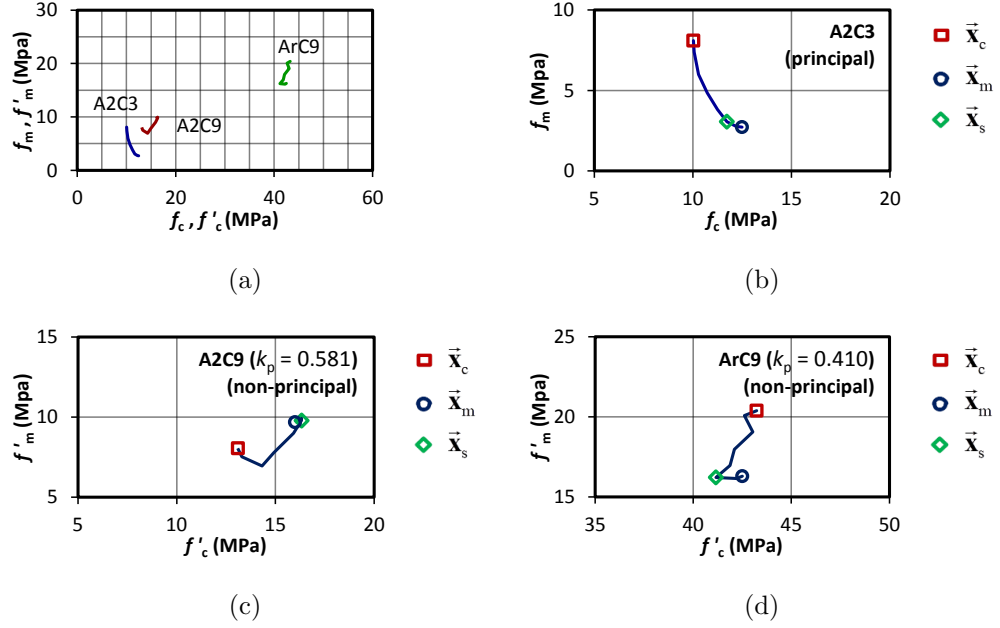
Figure 4.10: Pareto front for $N = 2$ and the A2C3_T load history alongside its A2C9_T and ArC9_T mapped counterparts. (a) With respect to each other. Detailed view for (b) A2C3_T, (c) A2C9_T and (d) ArC9_T.

tion 4.4.3) as another method to evaluate a calibrated model. Based on the definition given previously, the load history used to calibrate a model is referred to as the principal load history. Therefore, a Pareto front corresponds to the principal load history. When a Pareto optimal solution is obtained by relatively favouring one phase of the principal loading history over the other (through the value of w in Eq. (4.38)) that solution has a preference of simulating that phase of the principal load history more accurately than the other phase. However, it is also desirable for that solution to show the same relative preference when it comes to simulating load histories other than the principal one. In order to simplify the discussions, this feature is referred to as *preference preservation*. Henceforth, in order to examine whether a calibrated model preserves its preferences, the set of solutions represented by the Pareto front are mapped from the (f_c, f_m) space to the (f'_c, f'_m) space using the non-principal load histories. This is illustrated in Fig. 4.10 for the solution set discussed so far.

In Fig. 4.10 (and all other figures that follow) the point corresponding to $\vec{x}_c$ is the Pareto optimal solution obtained by setting $w \approx 1$ in Eq. (4.26) while $\vec{x}_m$ is the result of setting $w \approx 0$. In addition, the point corresponding to $\vec{x}_s$ is the result of a single-objective problem where the entire load history is used for a single error function.

(a)

(b)

Figure 4.11: Experimental result and numerical simulation ($N = 2$) of the A2C3_T test case. With A2C3_T as the principal and non-principal load history. (a) Stress-time variation. (b) The difference between experimental and numerical stress values (absolute error).

The result of using $\vec{\mathbf{x}}_c$ and $\vec{\mathbf{x}}_m$ as material constants for the numerical simulation of the principal load history A2C3_T is shown in Fig. 4.11a. As is observed from this figure, both $\vec{\mathbf{x}}_c$ and $\vec{\mathbf{x}}_m$ produce results that accurately simulate the experimental data. However, if the variation of the absolute error is plotted as in Fig. 4.11b, the tradeoff of using $\vec{\mathbf{x}}_c$ or $\vec{\mathbf{x}}_m$ can be readily observed. The fact that $\vec{\mathbf{x}}_c$ produces better results than $\vec{\mathbf{x}}_m$ during the cyclic phase of the load history is evident in Fig. 4.11b. Similarly, it is also seen that $\vec{\mathbf{x}}_m$ produces better results than $\vec{\mathbf{x}}_c$ during the monotonic phase. Note that the absolute error presented Fig. 4.11b is equal to the absolute value of the difference between the experimental and simulation data points.

Figs. 4.12 and 4.13 show the variation of stress and its absolute error over time when $\vec{\mathbf{x}}_c$ and $\vec{\mathbf{x}}_m$ are used to simulate the non-principal load histories A2C9_T and ArC9_T. Looking into Fig. 4.12b, there is no indication of $\vec{\mathbf{x}}_m$ producing better results than $\vec{\mathbf{x}}_c$ during the monotonic phase. Similarly, Fig. 4.13b shows that $\vec{\mathbf{x}}_c$ is not more accurate that $\vec{\mathbf{x}}_m$ during the cyclic phase. This change in preferences is observed in Fig. 4.10, where the relative position of $\vec{\mathbf{x}}_c$ and $\vec{\mathbf{x}}_m$ with respect to each other, before and after being mapped, indicates that these two models do not preserve their preferences. In fact, this can be generalised to all of the Pareto optimal solutions of Fig. 4.10b as they are mapped to Figs. 4.10c and d, henceforth, leading

(a)

(b)

Figure 4.12: Experimental result and numerical simulation ($N = 2$) of the A2C9_T test case. With A2C3_T as the principal and A2C9_T as the non-principal load history. (a) Stress-time variation. (b) The difference between experimental and numerical stress values (absolute error).

to the conclusion that even if a Pareto optimal solution is obtained by favouring one phase of the principal load history (through the value of w in Eq. (4.38)), that solution does not necessarily tend to preserve its preferences under a non-principal load history. Defined by Eqs. (4.33) and (4.34) the preference preservation index for these mapped counterparts are calculated and included in Figs. 4.10c and d.

Reiterating that the main objective of this work is to calibrate a constitutive model in a way for it to be suitable for multi-phase loading histories, it is therefore desirable to find a solution set that does not fail to preserve its intended multi-phase preferences. In the following sections, two elements of the concept of parameter determination are considered to investigate this issue: The number of parameters, i.e. the number of hardening components in the constitutive model and the choice of the principal load history.

4.5.1 Number of hardening components

This section examines the effect that the number of hardening components has on the characteristics of the calibrated model. The A2C3_T load history and the

(a)

(b)

Figure 4.13: Experimental result and numerical simulation ($N = 2$) of the ArC9_T test case. With A2C3_T as the principal and ArC9_T as the non-principal load history. (a) Stress-time variation. (b) The difference between experimental and numerical stress values (absolute error).

corresponding stress variation (Fig. 4.2a and b) are used for calibration purposes of this section, whereas the A2C9_T and ArC9_T load cases are used to evaluate the calibrated model. In other words, A2C3_T is the principal load history, while A2C9_T and ArC9_T are the non-principal load histories.

Fig. 4.14 shows the attained Pareto front for three different values of N in Eq. (4.35). While Fig. 4.14a shows the overall positioning of the three Pareto fronts in (f_c, f_m) space, Figs. 4.14b, c and d use a larger scale to show the details of each Pareto front. The location of $\vec{\mathbf{x}}_c$, $\vec{\mathbf{x}}_m$ and $\vec{\mathbf{x}}_s$ are indicated by markers. As before, the point corresponding to $\vec{\mathbf{x}}_c$ is the Pareto optimal solution obtained by setting $w \approx 1$ in Eq. (4.26) while $\vec{\mathbf{x}}_m$ is the result of setting $w \approx 0$. It is clearly observed that as the number of hardening components increases, numerical simulations become more accurate. However, the improvement gained by increasing the number of hardening components becomes less prominent as the number of components increases. These properties can also be deduced from Figs. 4.15, 4.11 and 4.16 where the variation of stress and its absolute error is shown against time as the A2C3_T load history is being simulated.

If the Pareto fronts given in Fig. 4.14 are mapped using the non-principal A2C9_T

(a)

(b)

(c)

(d)
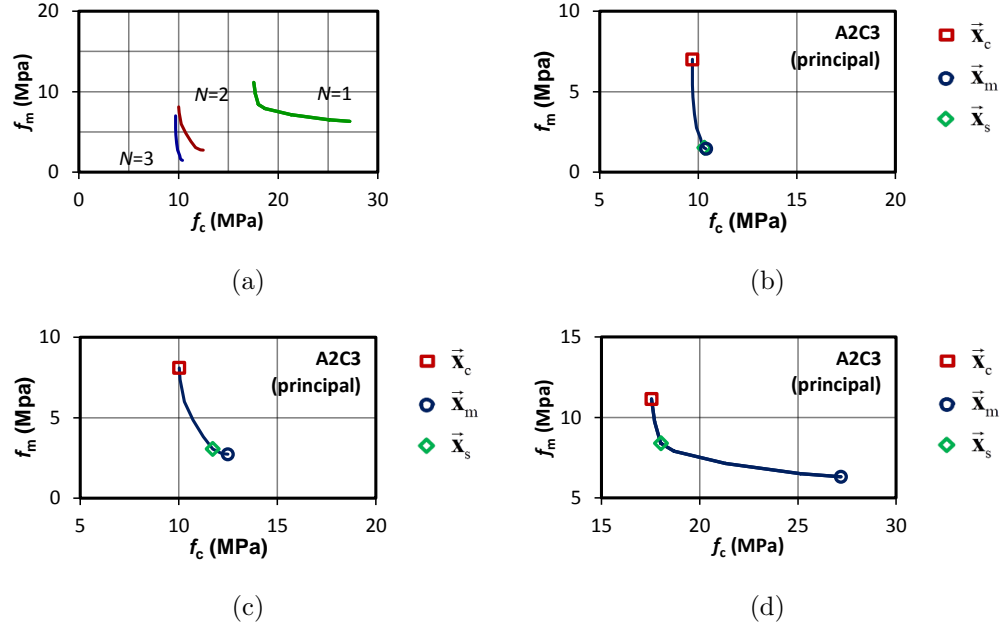
Figure 4.14: Pareto front for $N = 1, 2, 3$ and the A2C3_T load history. (a) For all three values of N with respect to each other. Detailed view for (b) $N = 3$, (c) $N = 2$ and (d) $N = 1$.

(a)

(b)
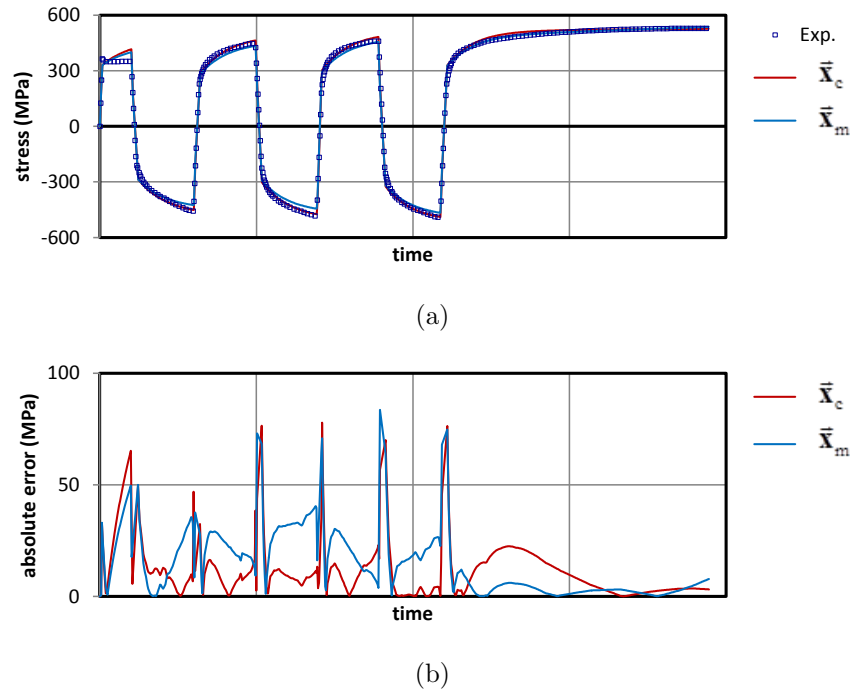
Figure 4.15: Experimental result and numerical simulation ($N = 1$) of the A2C3_T test case. With A2C3_T as the principal and non-principal load history. (a) Stress-time variation. (b) The difference between experimental and numerical stress values (absolute error).

(a)

(b)
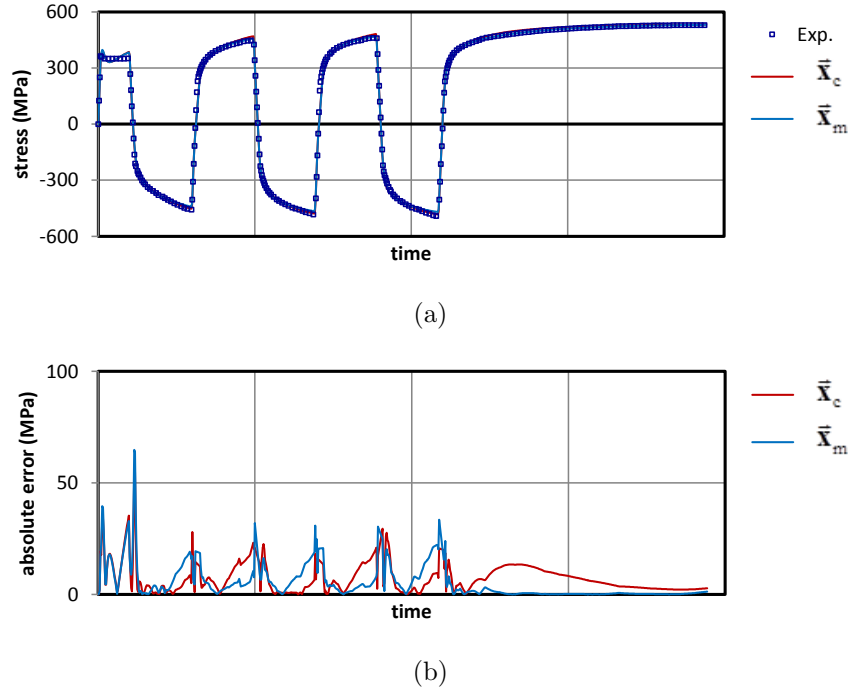
Figure 4.16: Experimental result and numerical simulation ($N = 3$) of the A2C3_T test case. With A2C3_T as the principal and non-principal load history. (a) Stress-time variation. (b) The difference between experimental and numerical stress values (absolute error).

load history, the result would be the curves shown in Fig. 4.17 with the time variation graphs given in Figs. 4.18, 4.12 and 4.19. The most important fact deduced from these figures is the major improvement of using $N \geq 2$ as opposed to $N = 1$. Also note that increasing the number of hardening components does not preserve the intended multi-phase preferences. This is clearly seen when considering the position of $\vec{\mathbf{x}}_c$ and $\vec{\mathbf{x}}_m$ within the Pareto front (Fig. 4.14) and within the mapped curves of Fig. 4.17.

Similar statements can also be made for the case where the Pareto front curves of Fig. 4.14 are mapped using the ArC9_T non-principal load history. The result of such mapping is shown in Fig. 4.20 with relevant time variation graphs given in Figs. 4.21, 4.13 and 4.22.

Figs. 4.17 and 4.20 both illustrate the fact that when A2C3_T is used as the principal load history, the Pareto optimal solution set does not preserve its intended multi-phase preferences when mapped from (f_c, f_m) space to (f'_c, f'_m) space using A2C9_T and ArC9_T as non-principal load histories. Relevant values for the preference preservation index (Eqs. (4.33) and (4.34)) are also provided in these figures for comparison.
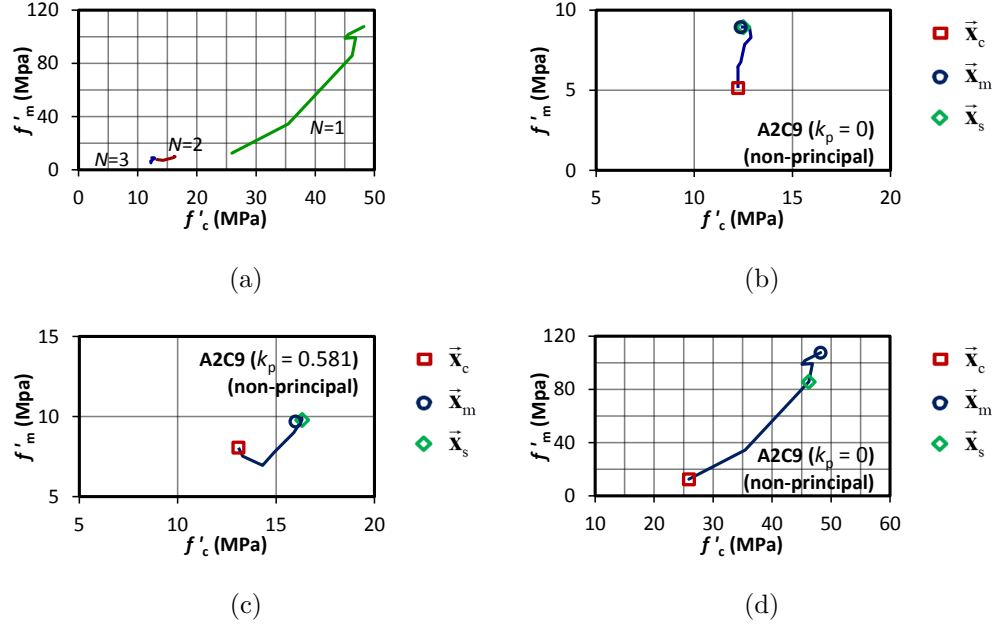
Figure 4.17: Mapped counterparts of the Pareto front for $N = 1, 2, 3$ and the A2C9_T load history. (a) For all three values of N with respect to each other. Detailed view for (b) $N = 3$, (c) $N = 2$.
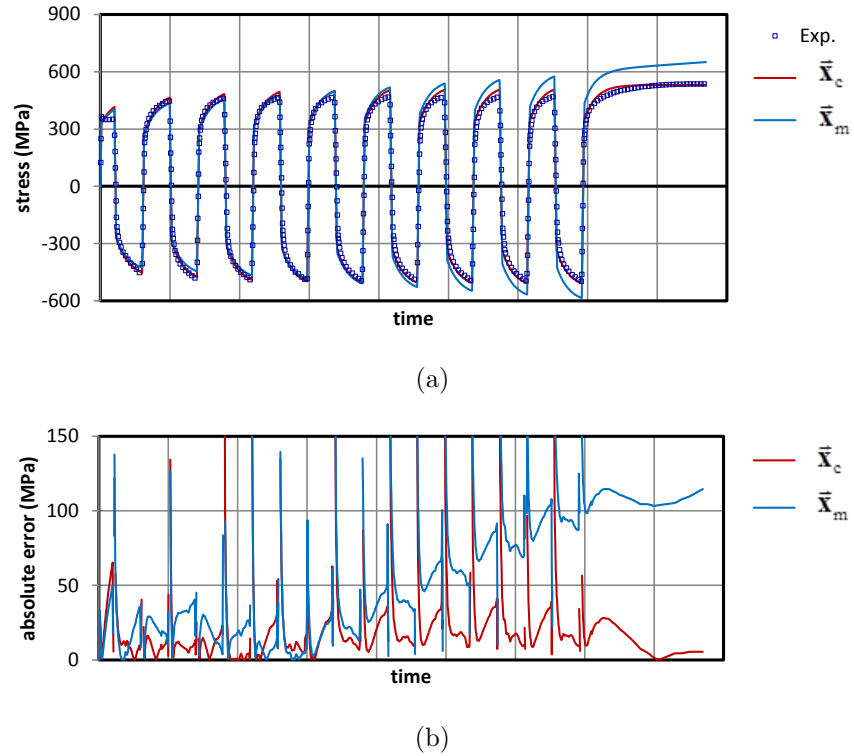
Figure 4.18: Experimental result and numerical simulation ($N = 1$) of the A2C3_T test case. With A2C3_T as the principal and non-principal load history. (a) Stress-time variation. (b) The difference between experimental and numerical stress values (absolute error).

(a)

(b)
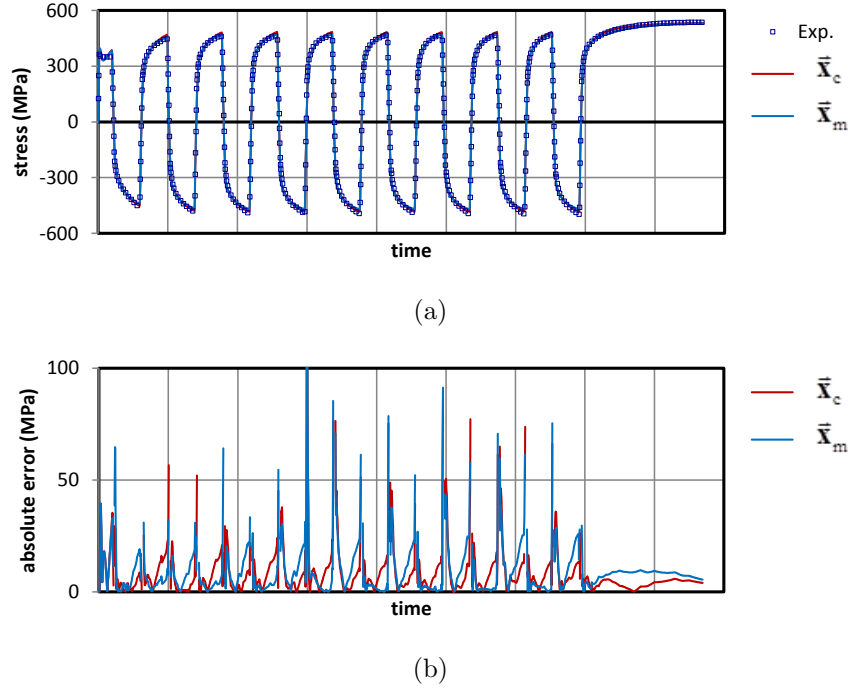
Figure 4.19: Experimental result and numerical simulation ($N = 3$) of the A2C3_T test case. With A2C3_T as the principal and non-principal load history. (a) Stress-time variation. (b) The difference between experimental and numerical stress values (absolute error).

(a)

(b)

(c)

(d)
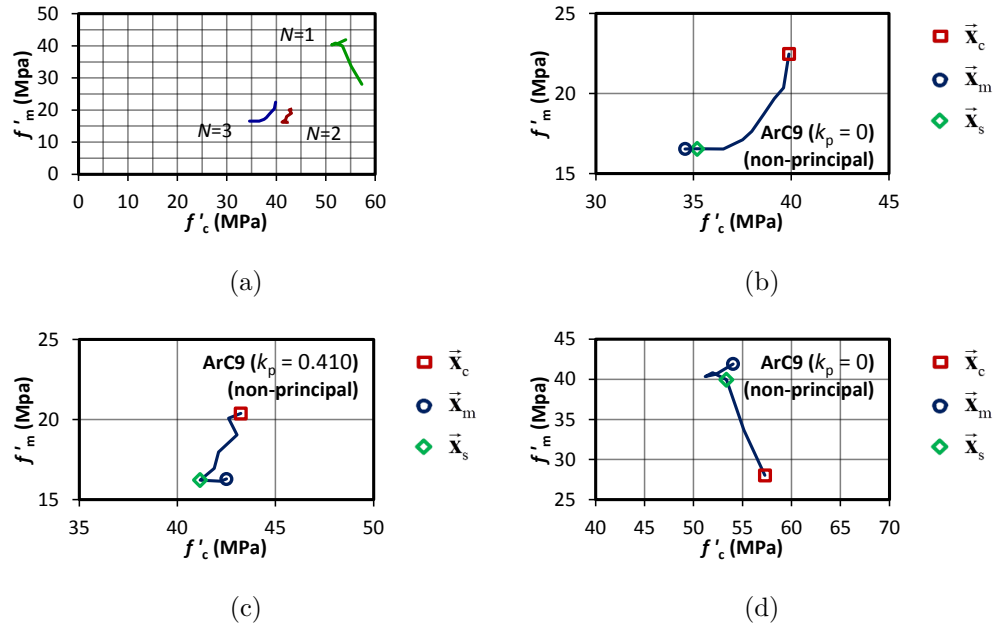
Figure 4.20: Mapped counterparts of the Pareto front for $N = 1, 2, 3$ and the ArC9_T load history. (a) For all three values of N with respect to each other. Detailed view for (b) $N = 3$, (c) $N = 2$ and (d) $N = 1$.
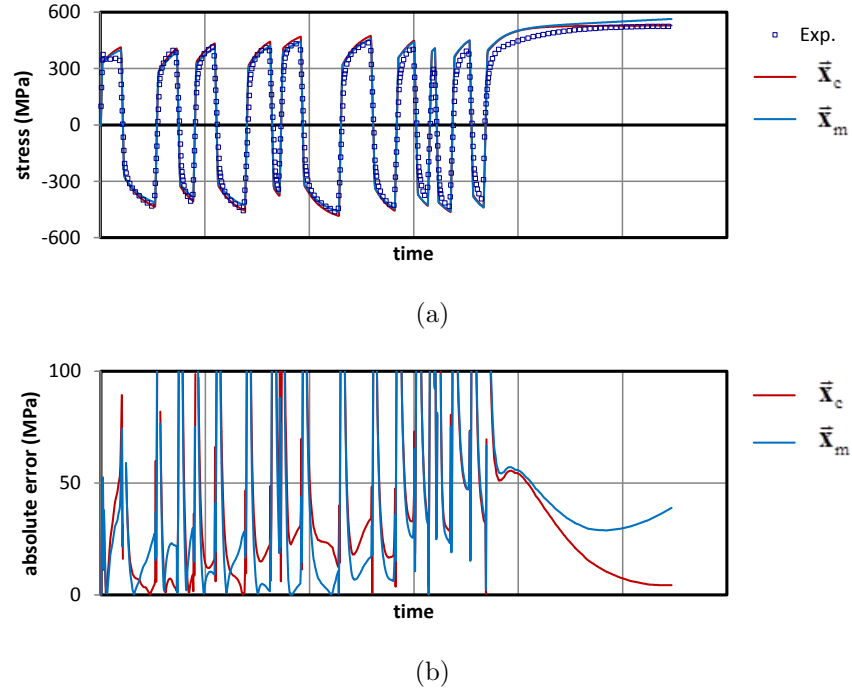
Figure 4.21: Experimental result and numerical simulation ($N = 1$) of the A2C3_T test case. With A2C3_T as the principal and non-principal load history. (a) Stress-time variation. (b) The difference between experimental and numerical stress values (absolute error).
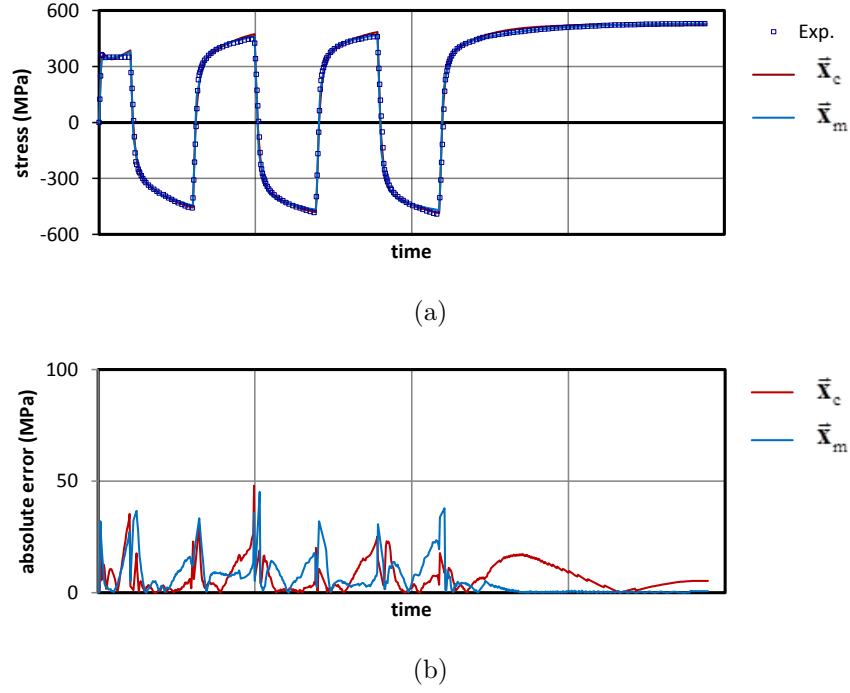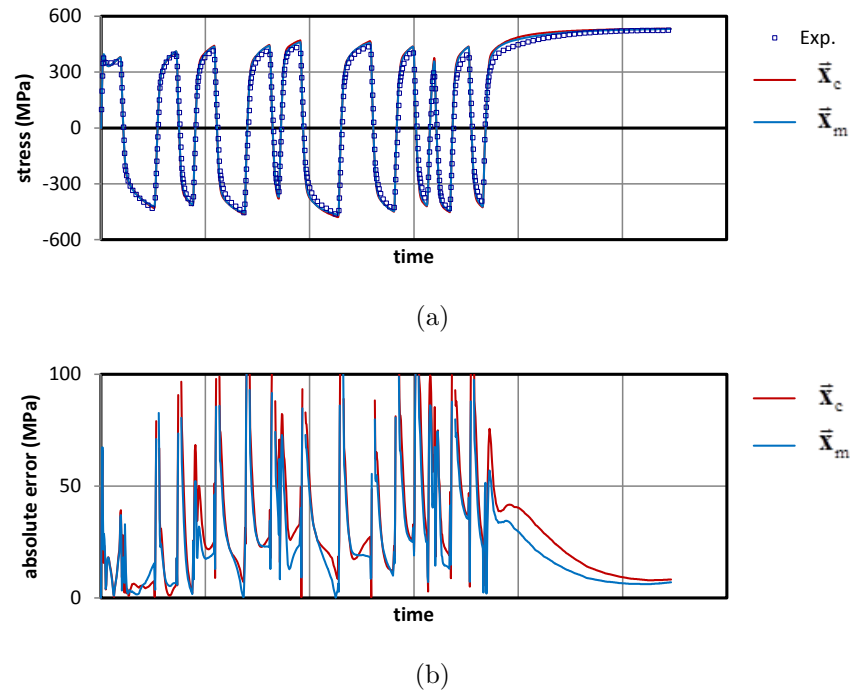

Figure 4.22: Experimental result and numerical simulation ($N = 1$) of the A2C3_T test case. With A2C3_T as the principal and non-principal load history. (a) Stress-time variation. (b) The difference between experimental and numerical stress values (absolute error).

In the next section, the issue of preference preservation is further investigated and solved by replacing A2C3_T with A2C9_T as the principal load history.

4.5.2   Principal load history

As previously mentioned, in this section A2C9_T is opted as the principal load history, whereas A2C3_T and ArC9_T are considered the non-principal load histories. The numerical analyses of this section are all carried out with $N = 2$, hence, the results presented here should be compared to those given in Fig. 4.10. The new Pareto front obtained by using the new principal load history (A2C9_T) is illustrated in Fig. 4.23. As before, stress-time variations as well as their corresponding error variations are also evaluated for $\vec{\mathbf{x}}_c$ and $\vec{\mathbf{x}}_m$, and are presented in Figs. 4.24, 4.25 and 4.26. Also shown in this figure are the mapped curves corresponding to the non-principal (A2C3_T and ArC9_T) load histories along with their preference preservation indices. When comparing the curves in Fig. 4.23 with the ones in Fig. 4.10, it is seen that although the error values have changed, the overall accuracy is somewhat the same. However, a closer look at Fig. 4.23 reveals the fact that when the A2C9_T load history is used to calibrate a model, that model tends to preserve its intended multi-phase preferences. Note that the position of $\vec{\mathbf{x}}_c$ and $\vec{\mathbf{x}}_m$ with respect to each other and with respect to the entire Pareto front (Fig. 4.23b) is maintained after mapping (Fig. 4.23c).

When mapping with the ArC9_T load history (Fig. 4.23d), it is observed that the multi-phase preferences are being preserved, but not as strongly as they were when mapping with the A2C3_T load history (Fig. 4.23c). This is confirmed by their respective preference preservation indices.

As a result, when it comes to preserving the multi-phase favouritism, using A2C9_T as the principal load history is preferred to using the A2C3_T load history. This is clearly evident by comparing Figs. 4.10 and 4.23. When compared to the A2C3_T load history, the only downside of A2C9_T is that it takes longer to carry it out in the laboratory.
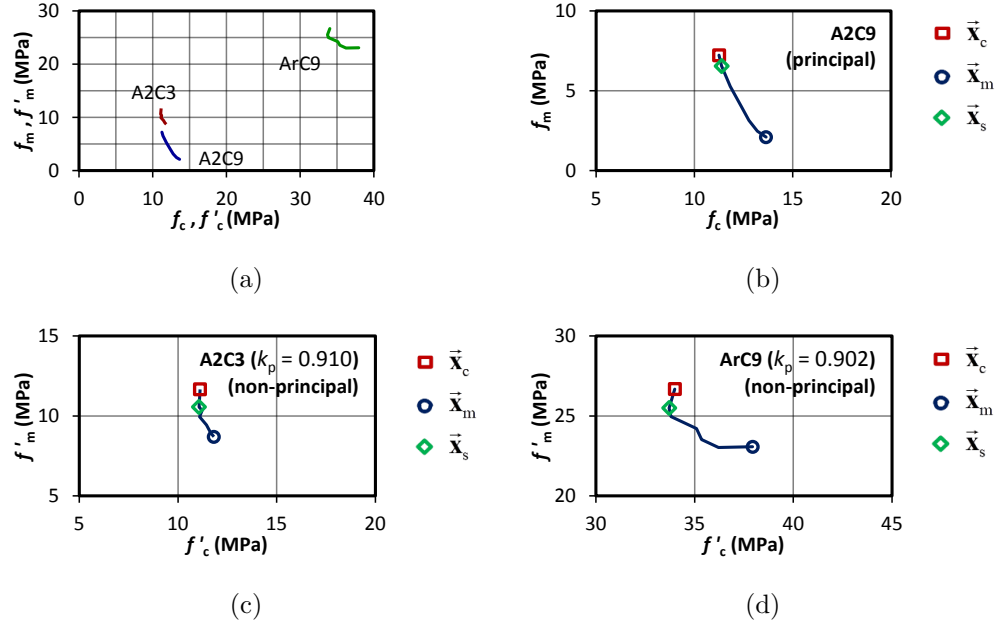
Figure 4.23: Pareto front for $N = 2$ and the A2C9_T load history alongside its A2C3_T and ArC9_T mapped counterparts. (a) With respect to each other. Detailed view for (b) A2C9_T,(c) A2C3_T and (d) ArC9_T.
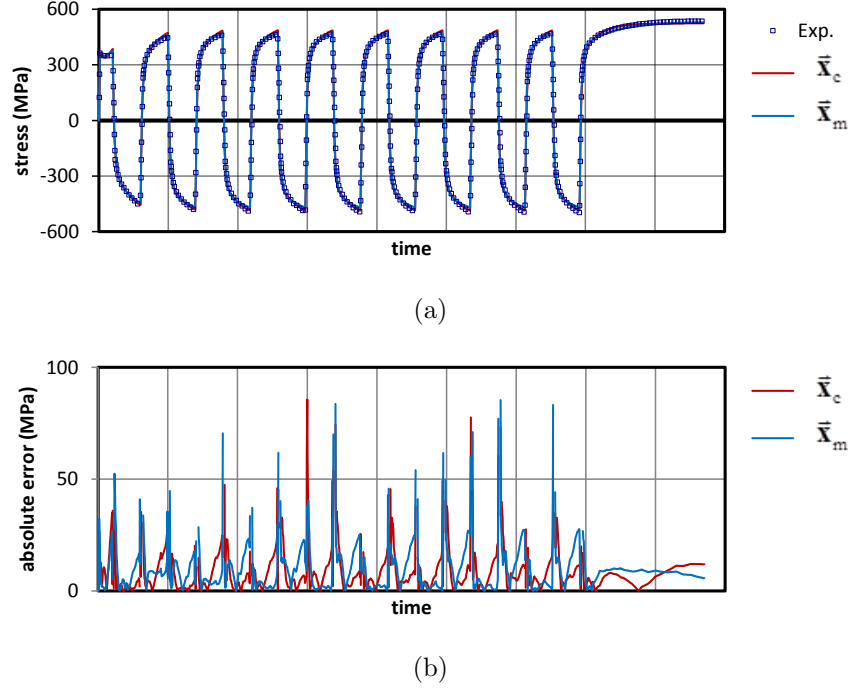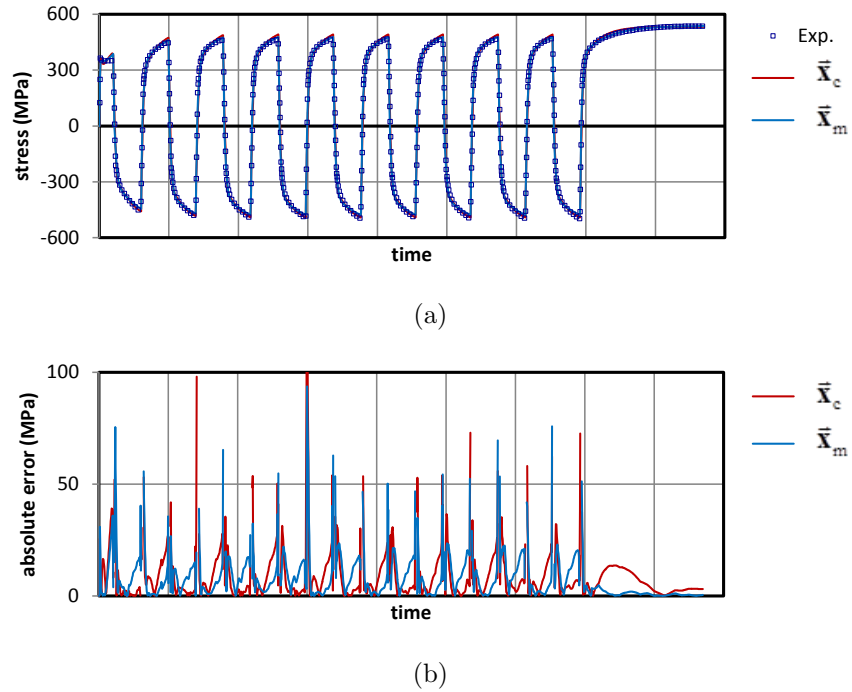

Figure 4.24: Experimental result and numerical simulation ($N = 1$) of the A2C3_T test case. With A2C3_T as the principal and non-principal load history. (a) Stress-time variation. (b) The difference between experimental and numerical stress values (absolute error).

(a)

(b)
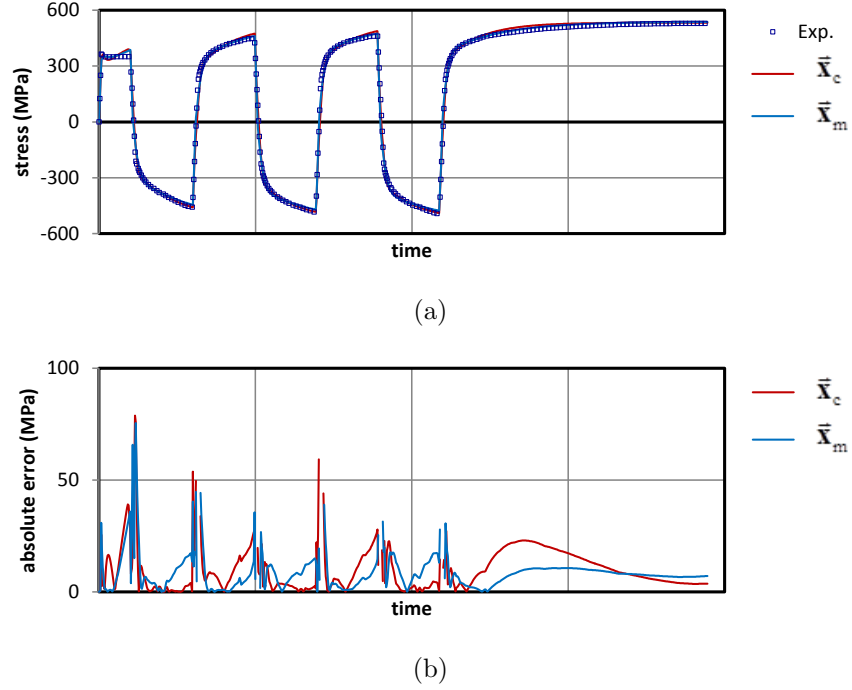
Figure 4.25: Experimental result and numerical simulation ($N = 1$) of the A2C3_T test case. With A2C3_T as the principal and non-principal load history. (a) Stress-time variation. (b) The difference between experimental and numerical stress values (absolute error).
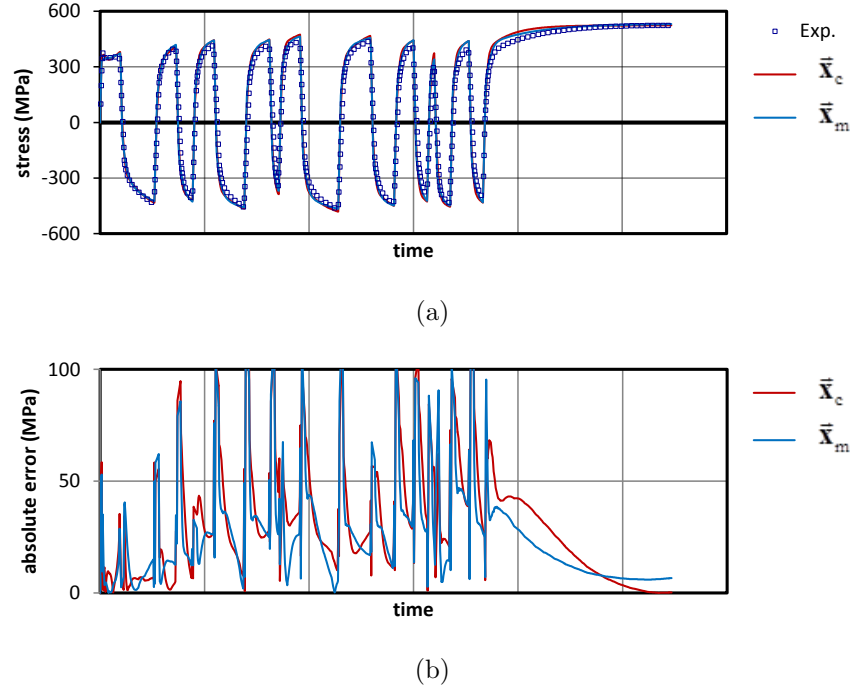

(a)

(b)
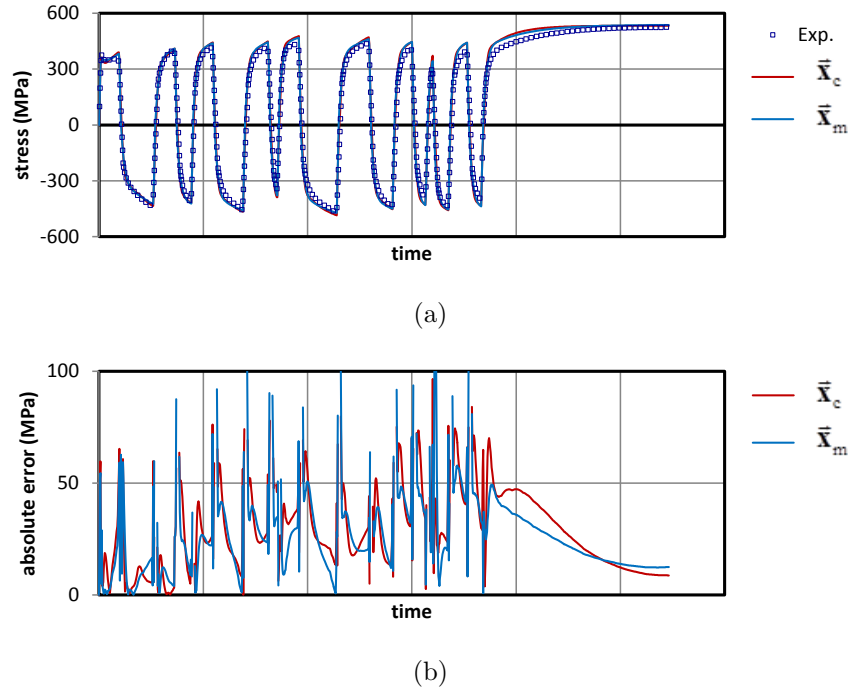
Figure 4.26: Experimental result and numerical simulation ($N = 1$) of the A2C3_T test case. With A2C3_T as the principal and non-principal load history. (a) Stress-time variation. (b) The difference between experimental and numerical stress values (absolute error).
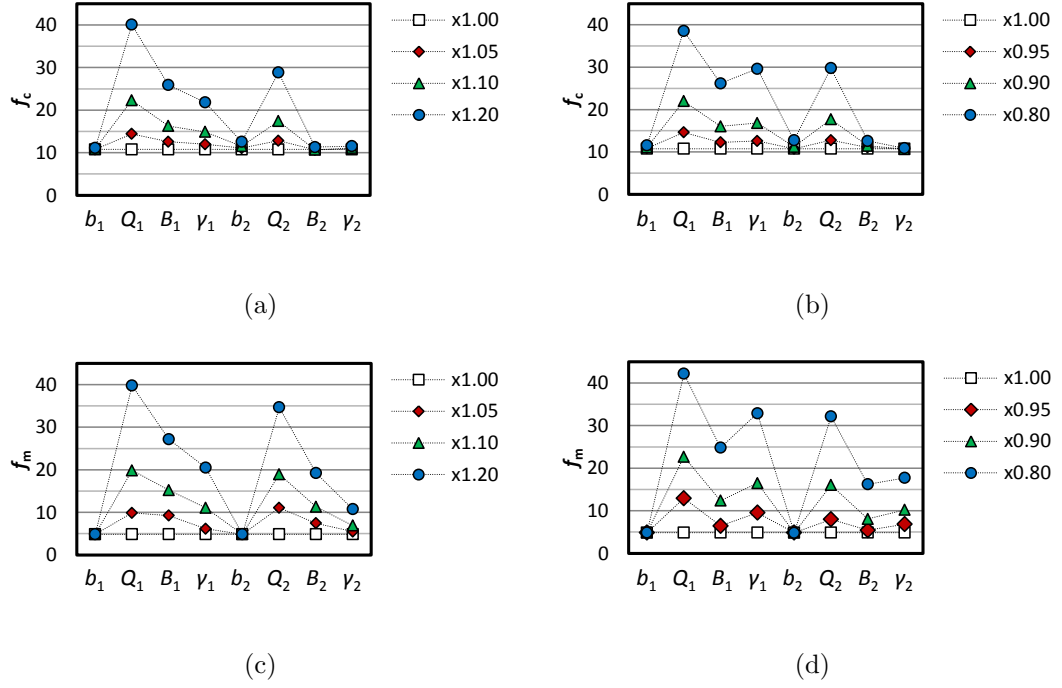
Figure 4.27: Error accumulation when only one material parameter is scaled. (a) f_c subjected to up-scaling, (b) f_c subjected to down-scaling, (c) f_m subjected to up-scaling and (d) f_m subjected to down-scaling.

4.5.3   Sensitivity analysis

The sensitivity of f_c and f_m to the material constants are evaluated in this section. For this purpose, the parametric values corresponding to $w = 10^{-2}$ in Table 4.2 are considered as the basis. This represents a model with 8 independent hardening parameters ($N = 2$). New models are created by scaling any given parameter and leaving the remaining 7 parameters constant. With the scaling factors being selected as 1.20, 1.10, 1.05, 0.95, 0.90 and 0.80, a total of $8 \times 6 = 48$ new models are created and then analysed. The analyses are carried out through the A2C3_T test case, and the corresponding values of f_c and f_m are attained according to Eqs. 4.36 and 4.37. For each material parameter, the variation of f_c and f_m is plotted in Fig. 4.27 with respect to the scaling factor.

It is observed from Fig. 4.27 that the sensitivity of f_c and f_m to material parameters is different. While f_c and f_m both seem to have the least sensitivity to b_1 and b_2, the former also has very low sensitivity to B_2 and γ_2. On the other hand, having the highest sensitivity towards Q_1, B_1, γ_1 and Q_2 is common between f_c and f_m, however, with the later also being sensitive to B_2 and γ_2.

4.5.4 Multi-objective solution vs. single-objective solution

Throughout this paper, material constants have been determined as a set of Pareto optimal solutions, meaning that there are multiple equally acceptable solutions to a single parameter determination problem. Having multiple solutions is the result of have a multi-objective problem, which itself is the result of splitting the load histories of Fig. 4.2 into two distinct phases of loading.

On the other hand, if the problem was to be solved as a single objective optimisation problem, the result would be a single unique solution that would minimise the difference between experimental and numerical data points (Eq. (4.26)) over the entire duration of a load history. Denoted by $\vec{\mathbf{x}}_s$, this solution vector is referred to as the single-objective solution.

Note that similar to $\vec{\mathbf{x}}_c$ and $\vec{\mathbf{x}}_m$, $\vec{\mathbf{x}}_s$ is also a member of the Pareto optimal set and therefore, also corresponds to a specific point on the Pareto front of a multi-objective problem. This has been illustrated in Figs. 4.6, 4.10, 4.14, 4.17, 4.20 and 4.23. Referring to these figures, one can see that after being mapped from (f_c, f_m) to (f'_c, f'_m), Pareto optimal solutions are no longer equally acceptable, since many of them lead to higher values for both error functions in the mapped (f'_c, f'_m) space, i.e. compared to the other Pareto optimal solutions. The single-objective solution $(\vec{\mathbf{x}}_s)$ can also be one of these high-error solutions and hence, not be the best choice for the material parameters of a model (for example, Fig. 4.17d).

Now considering the fact that a single objective problem has the benefit of being solved much faster than a multi-objective one, either method has its own merits when selected as a parameter determination technique.

4.6 Conclusions

In this paper, the concept of multi-objective optimisation was used to determine the material constants of a J_2 plasticity model. The calibration process was developed by first, briefly stating the required mathematical bases of multi-objective optimisation and then, implementing these concepts to an actual problem involving a set of multi-phase cyclic-monotonic load histories. The approach used in this work falls in the category of *a priori* techniques, and hence, enables the development of a fully

automated process.

After calibrating the first constitutive model using the chosen principal load history (A2C3_T), the stress-time variations under all load histories were simulated using that model. The results indicated that the calibrated model not only accurately traces the stress variation of the load history it was calibrated against, but is also capable of tracing other load histories.

In order to gain a deeper understanding of the characteristics of the calibration process, especially from a multi-objective viewpoint, another method of validation was also employed. This type of validation was mathematically described and referred to as *preference preservation*. This involved obtaining all the Pareto optimal solutions and the corresponding Pareto front with respect to the principal load history and then mapping the Pareto front using the remaining non-principal load histories. By implementing this approach, the results of the previously calibrated model revealed that Pareto optimal solutions do not necessarily preserve their intended multi-phase preferences when subjected to non-principal load histories.

The number of hardening components was investigated, whereby the results show that a model produces more accurate simulations as the number of its components is increased. However, the results also pointed to the fact that the degree of improvement declines as the number of components is increased. Moreover, the number of components didn't show any sign of improving the preference preservation index.

As for the choice of the principal load history, the initial choice of A2C3_T was replaced with A2C9_T. By comparing the results of the former with the latter, it was observed that although the error values of the Pareto front and its mapped counterparts are different for the two scenarios, the overall accuracy of the results experiences no significant change. However, the new principal load history (A2C9_T) had led to a Pareto optimal set with a much higher preference preservation index, indicating that these models preserve their preferences after being mapped under non-principal load histories.

The above-mentioned results conclude that the performance of a calibrated model not only depends on the constitution of the model itself (number of hardening components), but also on the load history that is used to calibrated the model. The fact that selecting A2C9_T over A2C3_T led to the advantage, implies that calibrating a model using *a more restrictive load history* can lead to improved preference preserving properties of the calibrated model. What is meant by a more restrictive load

history is one that requires the model to trace a more complex response path, which in this case, was in the form of having more instances of load reversals. While this is immediately implied by the results presented in this paper, further investigations must be carried out in order to reach a definite conclusion.

Within a Pareto optimal set, there exists a Pareto optimal solution which is the same solution that is obtained if the entire load history is taken as a single objective function. The location of this single-objective optimisation problem is marked in all Pareto front curves presented in this paper. This specific point indicates the error that a single-objective solution produces during the cyclic and monotonic phases of loading. By comparing the location of the single-objective solution to all the other solutions, and its translation as the Pareto front is mapped through non-principal load histories, one can conclude that the single-objective solution, in general, does not lead to the least error. This is in addition to the fact that in a multi-objective problem, the operator has the power to enforce preferences into the solution. Hence, giving a multi-objective approach advantages that are not available through a single-objective method. Using a multi-objective approach, however, comes at the cost of more computational time compared to a single-objective one.

4.7   The Nelder-Mead optimisation algorithm (Appendix)

The Nelder and Mead [29] method is used in this paper to minimise the aggregated objective function defined by Eq. (4.29). A description of the Nelder-Mead optimisation algorithm is given in what follows.

The search begins by setting up an initial simplex in $\mathbb{R}^n$, where n is the number of variables of the optimisation problem. By definition, a simplex in $\mathbb{R}^n$ is a set of $n+1$ points which do not lie in a hyper-plane. The $n+1$ vertices of the simplex are then indexed as $\vec{\mathbf{v}}_i (i = 0, 1, \ldots, n)$ based on their function values, so that $f(\vec{\mathbf{v}}_0) \leq f(\vec{\mathbf{v}}_1) \leq \ldots \leq f(\vec{\mathbf{v}}_n)$. The algorithm of the Nelder-Mead search method is based on generating trial points and evaluating the function value at these trial points. There are three different types of trial points in this method, whereby each one is generated for a specific purpose. These are known as 'reflection points', 'expansion points' and 'contraction points' [37]. The generation of a trial point is followed by the evaluation of the function value at that point, which is then used to make
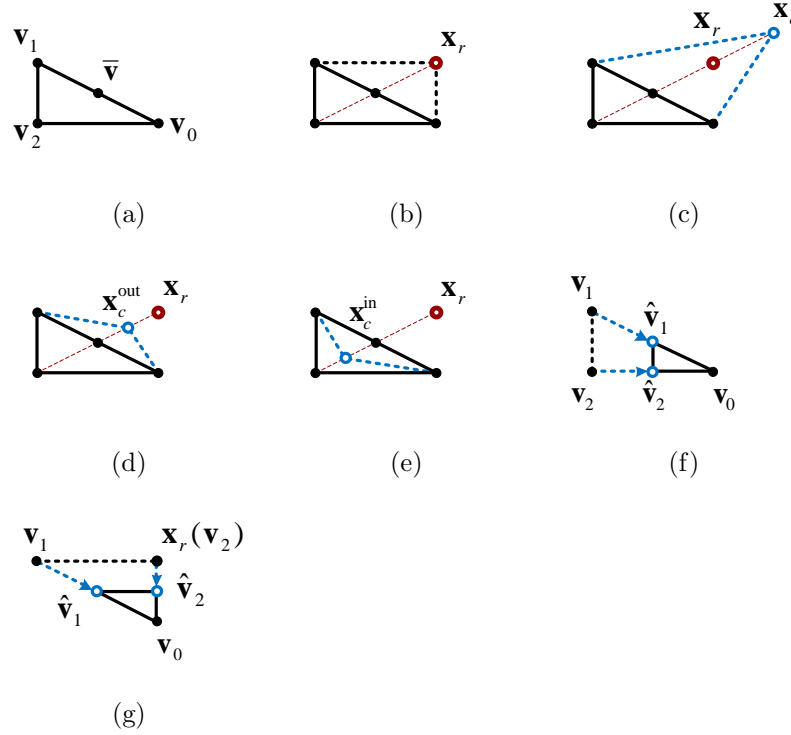
Figure 4.28: The Nelder-Mead algorithm. (a) Initial configuration. (b) Reflection trial point. (c) Expansion trial point. (d) Outside contraction point. (e) Inside contraction point. (f) Shrink when $f(\vec{\mathbf{x}}_r) \geq f(\vec{\mathbf{v}}_n)$. (g) Shrink when $f(\vec{\mathbf{v}}_{n-1}) < f(\vec{\mathbf{x}}_r) < f(\vec{\mathbf{v}}_n)$.

a decision for the next step. These trial points are generated with respect to the midpoint ($\vec{\mathbf{v}}_m$) of all vertices excluding the worst vertex, therefore

$$\vec{\bar{\mathbf{v}}} = \frac{1}{n} \sum_{i=0}^{n-1} \vec{\mathbf{v}}_i \tag{4.39}$$

With Fig. 4.28 illustrating the concept for $n = 2$, the configuration of the simplex at the start of an iteration is depicted in Fig. 4.28a.

1. Reflection: The first trial of any iteration constitutes the reflection point $\vec{\mathbf{x}}_r$ generated using the reflection coefficient $\mu_r > 0$ (Fig. 4.28b).. The term 'reflection' refers to the fact that this trial point is the reflection of the current worst point, through the midpoint of the rest of the vertices, that is

$$\vec{\mathbf{x}}_r = \vec{\bar{\mathbf{v}}} + \mu_r(\vec{\bar{\mathbf{v}}} - \vec{\mathbf{v}}_n) \tag{4.40}$$

Decision on reflection trial involves:

- If $f(\vec{\mathbf{v}}_0) \leq f(\vec{\mathbf{x}}_r) \leq f(\vec{\mathbf{v}}_{n-1})$, replace the current worst vertex $\vec{\mathbf{v}}_n$ with the reflection point $\vec{\mathbf{x}}_r$;

- If $f(\vec{\mathbf{x}}_r) < f(\vec{\mathbf{v}}_0)$, perform an expansion trial;

- If $f(\vec{\mathbf{x}}_r) > f(\vec{\mathbf{v}}_{n-1})$, perform a contraction trial;

2. Expansion: When the function value of the reflection point is even better (smaller in a minimisation problem) than the best vertex, an opportunity arises to take advantage of the direction with which the reflection point was created. This opportunity is considered through the expansion point $\vec{\mathbf{x}}_e$ generated using the expansion coefficient $\mu_e > 1$ (Fig. 4.28c)

$$\vec{\mathbf{x}}_e = \vec{\overline{\mathbf{v}}} + \mu_e(\vec{\mathbf{x}}_r - \vec{\overline{\mathbf{v}}}) \qquad (4.41)$$

Decision on expansion trial involves:

- If $f(\vec{\mathbf{x}}_e) < f(\vec{\mathbf{v}}_0)$, replace the current worst vertex $\vec{\mathbf{v}}_n$ with the expansion point $\vec{\mathbf{x}}_e$;

- If $f(\vec{\mathbf{x}}_e) \geq f(\vec{\mathbf{v}}_0)$, replace the current worst vertex $\vec{\mathbf{v}}_n$ with the reflection point $\vec{\mathbf{x}}_r$;

3. Contraction: If reflection does not lead to any practical improvements, contraction is considered using the contraction coefficient $0 < \mu_c < 1$. Contraction trial points come in two types: inside contraction points and outside contraction points illustrated in Figs. 4.28d and e, respectively. The type of contraction is chosen based on a comparison between the reflection point $\vec{\mathbf{x}}_r$ and the current worst vertex $\vec{\mathbf{v}}_n$. So, if $f(\vec{\mathbf{x}}_r) > f(\vec{\mathbf{v}}_n)$ then an inside contraction point $\vec{\mathbf{x}}_c^{\text{in}}$ is generated by using

$$\vec{\mathbf{x}}_c^{\text{in}} = \vec{\overline{\mathbf{v}}} + \mu_c(\vec{\mathbf{v}}_n - \vec{\overline{\mathbf{v}}}) \qquad (4.42)$$

and if $f(\vec{\mathbf{x}}_r) \leq f(\vec{\mathbf{v}}_n)$ then an outside contraction point $\vec{\mathbf{x}}_c^{\text{out}}$ is generated such that

$$\vec{\mathbf{x}}_c^{\text{out}} = \vec{\overline{\mathbf{v}}} + \mu_c(\vec{\mathbf{x}}_r - \vec{\overline{\mathbf{v}}}) \qquad (4.43)$$

Decision on contraction trial involves:

- If $f(\vec{\mathbf{x}}_c) \leq f(\vec{\mathbf{v}}_n)$, replace the worst vertex $\vec{\mathbf{v}}_n$ with the contraction point $\vec{\mathbf{x}}_c$;

- If $f(\vec{\mathbf{x}}_c) > f(\vec{\mathbf{v}}_n)$, perform a shrink operation;

4. Shrink: If all three types of trial points fail to make an improvement to the current simplex, the simplex is then subjected to a 'shrink' modification (reduction in size). The shrink operation is performed by relocating all vertices closer to the best vertex $\vec{\mathbf{v}}_0$ (Figs. 4.28f and g).

$$\hat{\vec{\mathbf{v}}}_i = \vec{\mathbf{v}}_0 + \mu_s(\vec{\mathbf{v}}_i - \vec{\mathbf{v}}_0) \qquad (4.44)$$

In this equation, $\hat{\vec{\mathbf{v}}}_i$ is the new substitute for each current vertex $\vec{\mathbf{v}}_i$, and $0 < \mu_s < 1$ is known as the shrink coefficient.

In the present work, the coefficients μ_r, μ_e, μ_c and μ_s of the Nelder-Mead method are set to 1.0, 2.0, 0.5 and 0.5, respectively. These vales have been commonly used in the literature [24, 38].

The stopping criterion of this method is defined as

$$\sqrt{\frac{1}{1+n} \sum_{i=0}^{n} \left[f(\vec{\mathbf{v}}) - \bar{f} \right]} < \rho \qquad (4.45)$$

where $\bar{f}$ is the average function value over all the vertices of the simplex, such that $\bar{f} = \sum f(\vec{\mathbf{v}}_i)/(n+1)$ and ρ is a pre-set termination value. The process of the Nelder-Mead simplex search method is depicted as a flowchart in Fig. 4.29.
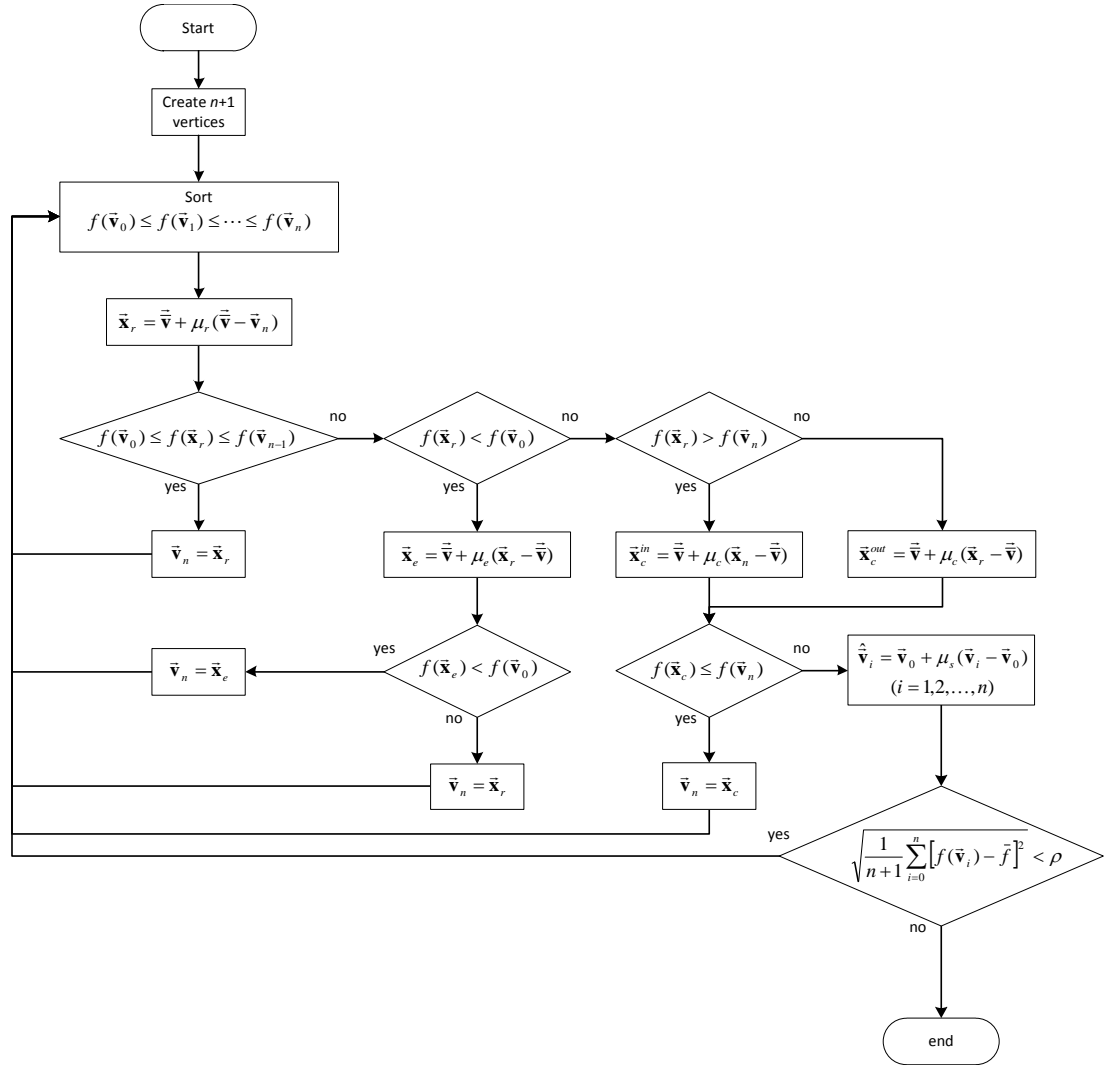
Figure 4.29: Flowchart of the Nelder-Mead algorithm.

Acknowledgement

References

[1] Jean-Louis Chaboche. Time-independent constitutive theories for cyclic plasticity. 2(2):149–188, 1986.

[2] Mohammad Abdel-Karim. Modified kinematic hardening rules for simulations of ratchetting. 25(8):1560–1587, 2009.

[3] Yannis F Dafalias and Heidi P Feigenbaum. Biaxial ratchetting with novel variations of kinematic hardening. 27(4):479–491, 2011.

[4] Dunji Yu, Gang Chen, Weiwei Yu, Duomin Li, and Xu Chen. Visco-plastic constitutive modeling on ohno–wang kinematic hardening rule for uniaxial ratcheting behavior of z2cnd18. 12n steel. 28(1):88–101, 2012.

[5] Shafiqul Bari and Tasnim Hassan. Anatomy of coupled constitutive models for ratcheting simulation. 16(3):381–409, 2000.

[6] Mohammad Abdel-Karim. An evaluation for several kinematic hardening rules on prediction of multiaxial stress-controlled ratchetting. 26(5):711–730, 2010.

[7] Yuzhong Xiao, Jun Chen, and Jian Cao. A generalized thermodynamic approach for modeling nonlinear hardening behaviors. 2012.

[8] Guozheng Kang and Qianhua Kan. Constitutive modeling for uniaxial time-dependent ratcheting of ss304 stainless steel. 39(5):488–499, 2007.

[9] Mohamad Rezaiee-Pajand and Sina Sinaie. On the calibration of the chaboche hardening model and a modified hardening rule for uniaxial ratcheting prediction. 46(16):3009–3017, 2009.

[10] Mohamad Rezaiee-Pajand and Sina Sinaie. Calibration of hardening rules for cyclic plasticity. 26(4):351–364, 2012.

[11] Mohammad Abdel-Karim. An extension for the ohno–wang kinematic hardening rules to incorporate isotropic hardening. 87(4):170–176, 2010.

[12] Junhong Li, Ruifeng Ding, and Yi Yang. Iterative parameter identification methods for nonlinear functions. 36(6):2739–2750, 2012.

[13] Feng Ding. Combined state and least squares parameter estimation algorithms for dynamic systems. 2013.

[14] Rolf Mahnken and Erwin Stein. A unified approach for parameter identification of inelastic material models in the frame of the finite element method. 136(3): 225–258, 1996.

[15] Atef F Saleeb, Atef S Gendy, and Thomas E Wilt. Parameter-estimation algorithms for characterizing a class of isotropic and anisotropic viscoplastic material models. 6(4):323–361, 2002.

[16] Chandra S Desai and Joseph Y Chen. Parameter optimization and sensitivity analysis for disturbed state constitutive model. 6(2):75–88, 2006.

[17] L Simoni and BA Schrefler. Parameter identification for a suction-dependent plasticity model. 25(3):273–288, 2001.

[18] Tomonari Furukawa, Tomohiro Sugata, Shinobu Yoshimura, and Mark Hoffman. An automated system for simulation and parameter identification of inelastic constitutive models. 191(21):2235–2260, 2002.

[19] Fusahito Yoshida, Masaki Urabe, Ryutaro Hino, and Vassili V Toropov. Inverse approach to identification of material parameters of cyclic elasto-plasticity for component layers of a bimetallic sheet. 19(12):2149–2170, 2003.

[20] Syed M Rahman, Tasnim Hassan, and S Ranji Ranjithan. Automated parameter determination of advanced constitutive models. ASME, 2005.

[21] Shree Krishna, Tasnim Hassan, Ilyes Ben Naceur, Kacem Saï, and Georges Cailletaud. Macro versus micro-scale constitutive models in simulating proportional and nonproportional cyclic and ratcheting responses of stainless steel 304. 25(10):1910–1949, 2009.

[22] Bruno M Chaparro, Sandrine Thuillier, Lus F Menezes, Pierre-Yves Manach, and Jos V Fernandes. Material parameters identification: Gradient-based, genetic and hybrid optimization algorithms. 44(2):339–346, 2008.

[23] Mohammad Rokonuzzaman and Toshinori Sakai. Calibration of the parameters for a hardening–softening constitutive model using genetic algorithms. 37(4): 573–579, 2010.

[24] Gun Jin Yun and Shen Shang. A self-optimizing inverse analysis method for estimation of cyclic elasto-plasticity model parameters. 27(4):576–595, 2011.

[25] Ricardo De-Carvalho, Robertt AF Valente, and Antnio Andrade-Campos. Optimization strategies for non-linear material parameters identification in metal forming problems. 89(1):246–255, 2011.

[26] Shafiqul Bari and Tasnim Hassan. An advancement in cyclic plasticity modeling for multiaxial ratcheting simulation. 18(7):873–894, 2002.

[27] Xu Chen, Rong Jiao, and Kwang Soo Kim. On the ohno–wang kinematic hardening rules for multiaxial ratcheting modeling of medium carbon steel. 21 (1):161–184, 2005.

[28] Tasnim Hassan, Lakhdar Taleb, and Shree Krishna. Influence of non-proportional loading on ratcheting responses and simulations by two recent cyclic plasticity models. 24(10):1863–1889, 2008.

[29] John A Nelder and Roger Mead. A simplex method for function minimization. 7(4):308–313, 1965.

[30] BHP. *Hot rolled products*. Broken Hill Proprietary Limited, Melbourne, 1998.

[31] ASTM E21-92. *Standard test methods for elevated temperature tension tests of metallic materials*. Annual book of ASTM standards. American Society of Testing and Materials, Philadelphia, PA, 1998.

[32] ASTM E606-92. *Standard practice for strain-controlled fatigue testing*. Annual book of ASTM standards. American Society of Testing and Materials, Philadelphia, PA, 1998.

[33] Michael A Crisfield. *Non-linear finite element analysis of solids and structures: Advanced topics*. John Wiley & Sons, Inc., 1997.

[34] Bernd Kleuter, Andreas Menzel, and Paul Steinmann. Generalized parameter identification for finite viscoelasticity. 196(35):3315–3334, 2007.

[35] Carlos A Coello Coello, Gary B Lamont, and David A Van Veldhuizen. *Evolutionary algorithms for solving multi-objective problems*. Springer, 2007.

[36] R Timothy Marler and Jasbir S Arora. Survey of multi-objective optimization methods for engineering. 26(6):369–395, 2004.

[37] Marco A Luersen and Rodolphe Le Riche. Globalized nelder–mead method for engineering optimization. 82(23):2251–2260, 2004.

[38] Shu-Kai S Fan and Erwie Zahara. A hybrid simplex search and particle swarm optimization for unconstrained optimization. 181(2):527–548, 2007.

PART II:

CONCRETE

Effect of size on the response of cylindrical concrete samples under cyclic loading

Contents

Monash University

Declaration for Thesis Chapter 5

Declaration by candidate

In the case of Chapter 5, the nature and extent of my contribution to the work was the following:

Nature of contribution	Extent of contribution (%)
Establishing methodologies, Experimental work, Data analysis, Write-up and revision	70%

The following authors contributed to the work. If co-authors are students at Monash University, the extent of their contribution in percentage terms must be stated.

Name	Nature of contribution	Extent of contribution (%)
Dr. Amin Heidarpour	Developing ideas Revision Financial support	
Prof. Xiao-Ling Zhao	Revision Financial support	
Prof. Jay Sanjayan	Revision	

The undersigned hereby certify that the above declaration correctly reflects the nature and extent of the candidate's and co-authors' contributions to this work.

Candidate's signature: ██████ **Date:** 24/09/2015

Main supervisor's signature: ██████ **Date:** 24/09/2015

Abstract

An experimental program is carried out to investigate the relation between size and the cyclic response of cylindrical concrete samples. For this purpose, normal strength concrete samples are cast in 9 different sizes and tested under strain-controlled cyclic loads. With the 9 sizes forming an array of samples with different diameters and aspect ratios, the effect of size on peak stress and peak strain is determined. Normalised cyclic stress-strain curves are then used to evaluate the variation of cyclic parameters in terms of the diameter and aspect ratio of the sample. The results of this study show that the diameter and the aspect ratio of the sample have the most influence on the reloading strength and reloading tangent of the cyclic response. Moreover, a key feature deduced from the results is that as the diameter of a sample becomes smaller, the effect of aspect ratio on the post-peak response diminishes. Finally, cyclic parameters are plotted against three different definitions of the damage index. With these definitions being based on strain, strength and dissipated energy, the results imply that the degradation of different cyclic properties might be originating from different damage mechanics.

Keywords

Concrete; Mechanical properties; Size effect; Cyclic loading

5.1 Introduction

Having a deep understanding of the cyclic characteristics of structural materials is a key step in creating models which reliably predict the response of structural systems under cyclic loading. With the widespread use of concrete as a construction material, any study that increases the understanding of its response under cyclic loading is beneficial to a wide range of engineering structures. This not only refers to the design of new structures, but also to the performance evaluation of current ones.

One of the earlier works dealing with the fundamental characteristics of the cyclic response of plain concrete is the work carried out by Bahn and Hsu [1]. An important observation made in their work is the fact that the monotonic stress-strain response of concrete envelopes the cyclic curves. Although this correlation between the monotonic and cyclic behaviour of concrete had also been reported in previous studies, a prominent feature that distinguishes the work of Bahn and Hsu [1] is the emphasis on random-amplitude cycles. With the intention of developing a

cyclic model suitable for any general loading history, they not only took constant-amplitude cyclic loading into account, but also considered random-amplitude cycles in their experiments. Further work in this area has been carried out by other researchers [2–11]. The more recent study by Osorio et al. [9] aims at establishing a fundamental understanding of the behaviour of confined concrete under cyclic loading by examining lateral and longitudinal strains during the load cycles. The experiments conducted by Lam et al. [7], involve monotonic and cyclic loading tests at elevated temperatures. A key observation made in their experiments is that, even at high temperatures, the monotonic stress-strain curve of concrete envelopes the cyclic response.

On the other hand, it has been well established that in concrete testing, the observed response depends on the size, the shape and the boundary conditions of the specimen being tested. While such dependencies have been widely investigated with the main focus on strength (f'_c) [12–16], few studies have considered the effect of size on peak strain (ϵ'_c) or other parameters that depend on strain, such as the tangent modulus (E_o). Through their experiments, Choi et al. [17] investigated the relation between the peak strain (ϵ'_c) and the aspect ratio (height-to-diameter ratio, $R = H/D$) of the sample, reporting an inverse relation between the two. It can also be concluded from their experimental data that this correlation becomes less pronounced as the aspect ratio becomes larger, especially for $R > 2$. Chin et al. [18] evaluated the effect of sample size on strength, initial tangent modulus and peak strain. Their experiments involved prismatic specimens with lateral dimensions down to 75 mm, whereby they concluded that the size of the specimen does not have a significant effect on the initial tangent or the peak strain. However, with lateral dimensions ranging from 400 mm to as small as 50 mm, the results reported by Sim et al. [19] indicate a clear increase in the peak strain (ϵ'_c) as the size of the sample decreases.

From another perspective, the use of smaller concrete samples can be advantageous when it comes to material testing. This is mainly due to the fact that their casting becomes more feasible, they require less storage space during curing, and that they can be tested using loading machines with less capacity. Note that ASTM provisions [20] allow cylindrical samples with diameters as small as 50 mm and an aspect ratio of $R = 2$ to be used for the determination of compressive strength and elastic modulus. Consequently, when it comes to the effect of size on basic mechanical parameters (f'_c, ϵ'_c and E_0), this lower range of sample dimensions has been covered in the literature. However, the effect of size on the observed cyclic characteristics of concrete is yet to be determined. Therefore, with the focus on small samples ($38 \leq D \leq 63$ mm), the present work aims to determine the relationship between
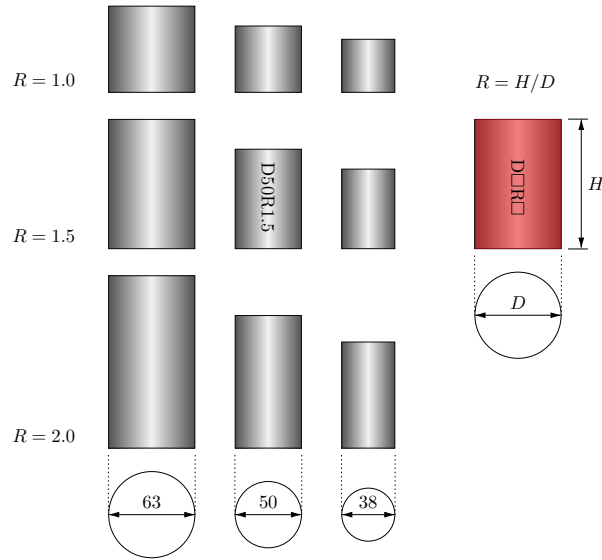
Figure 5.1: Concrete sample geometry (in mm).

sample size and cyclic behaviour. Through the experimental program of this work, the effect of size on strength (f_c') and strain-related parameters $(\epsilon_c'$ and $E_o)$ is first determined. Cyclic stress-strain curves are then normalised by f_c' and ϵ_c', whereby the effect of size on cyclic parameters is studied.

The results obtained from this program lay out the foundation for future experimental and numerical studies of concrete under cyclic loading. An example is the effect of temperature on cyclically-damaged concrete, currently being carried out at Monash University. It is worth mentioning that these studies fall under a broader research program to determine the response of structures under post-earthquake fire conditions [21–23].

5.2   Experimental program

Cylindrical samples of normal strength concrete were cast, cured and tested in this program. These samples consisted of nine different sizes varying in diameter (D) and aspect ratio $(R = H/D)$. With diameters of 38, 50 and 63 mm and aspect ratios of 1.0, 1.5 and 2.0, an array of samples depicted in Fig. 5.1 were prepared. Also given in this figure is the naming convention of the samples. This is in the form of A☐C☐_T, where the blank boxes (☐) next to the letters D and R are respectively filled in by the diameter and the aspect ratio of the sample. For example, the sample with a 50-mm diameter and an aspect ratio of 1.5 is hereby denoted by A50C1.5_T.

Table 5.1: Mix design for 1 m^3 of concrete.

General purpose cement (kg/m^3)	364
Coarse aggregates (max diameter 8 mm, kg/m^3)	1170
Fine aggregate (kg/m^3)	687
Water (kg/m^3)	200

5.2.1 Material

All specimens were made using the same concrete mix with a 28-day target strength of 35 MPa. With a maximum diameter of $d_a = 8$ mm, the coarse aggregates used in this study were small enough to avoid the wall effect [20, 24]. The specific gravity of coarse aggregates was equal to 2.69 at a saturated surface-dry condition whilst fine aggregates were comprised of silica-based sand with a fineness modulus of 2.10. General purpose cement (type I Portland cement) was used as the only cementitious component of the concrete mix, while the water-to-cement ration was selected as 0.55. Table 5.1 provides the material proportions of the concrete mixture used in this study.

5.2.2 Sample preparation

Samples were cast into plastic moulds. They were removed from their moulds after 24 hours and placed inside a curing tank where they would rest in lime-saturated water at a temperature of approximately 23°C. On day-7, samples were removed from the tank and were allowed to cure further in free air at room temperature until testing day. On approximately day-10, the two ends of the samples were ground for a smooth and parallel finish. All samples were tested on day-28, except for the samples that were used to monitor the development of strength over time. Note that not all samples that were tested in this program were made from the same concrete batch. Therefore, in order to ensure consistency between different batches, sample A50C1.5_T was taken as the control sample and six samples of this size were always cast from each individual batch of concrete. The mechanical properties obtained from testing these control samples not only served as a reference to evaluate the consistency between different batches, but they were also used to normalise the results of other sample sizes within each individual batch (Section 5.3.1).

5.2.3   Testing scheme

The machine used for testing was a Shimadzu AG-X with a load capacity of 300 kN. Samples were loaded at a constant displacement rate of 0.1 mm/min which results in strain rates lower than $\dot{\epsilon} = 10^{-4}$ s^{-1} for all sample sizes. Displacements were recorded using a non-contact MTS laser extensometer (model LX1500) with a resolution of $1\,\mu$m. Fig. 5.2 illustrates the schematics and the actual laboratory view of the test setup used in this program. The relative displacement of the two hardened-steel platens was used to determine the overall longitudinal strain of the sample. This was achieved by targeting the laser extensometer towards the two retro-reflective tapes that were attached to the front of the platens (Fig. 5.2). It is generally understood that strains are not necessarily uniform along the sample height and that near the boundaries, strains are affected by the stiffness of the platens as well as the friction between the platens and the concrete surface. However, attaining reasonable strain values within the post-peak region was only possible when strains were calculated from the overall sample deformation [1, 7, 9]. Therefore, relative platen displacement was used to capture strains throughout the entire response. However, it should be mentioned that true strains may still be obtained by using a correction technique such as the one described by Mansur et al. [25].

The load history applied to the concrete samples involved multiple cycles of controlled straining up to specific values, followed by full unloading to near-zero stresses. Stress and strain values were constantly logged and monitored during the experiments, and load reversals were administered using real-time measurements. The maximum induced strain value was increased with each cycle, causing additional damage to the sample as the cycles progressed. Cyclic loading was continued until the reloading strength (f_r in Fig. 5.4) of the sample had reduced to half of the peak stress ($f_r < 0.5f_c'$). However, for samples where the reloading strength reduced rapidly, load cycles were continued until the unloading strain (ϵ_u in Fig. 5.4) was at least as twice as the peak strain ($\epsilon_u > 2\epsilon_c'$). Examples of stress-strain curves corresponding to this load history can be seen in Figs. 5.3 and 5.12. It is important to point out that Fig. 5.3b is produced by normalising the plot in Fig. 5.3a with respect to f_c' and ϵ_c'. Note that in most of the following figures, stresses and strains have been normalised by the value of the peak stress f_c' and the value of the peak strain ϵ_c', respectively. Each of the 9 individual sample sizes was cast and tested a minimum of 6 times in order to attain reliable statistical values. However, additional experiments were carried out when required.
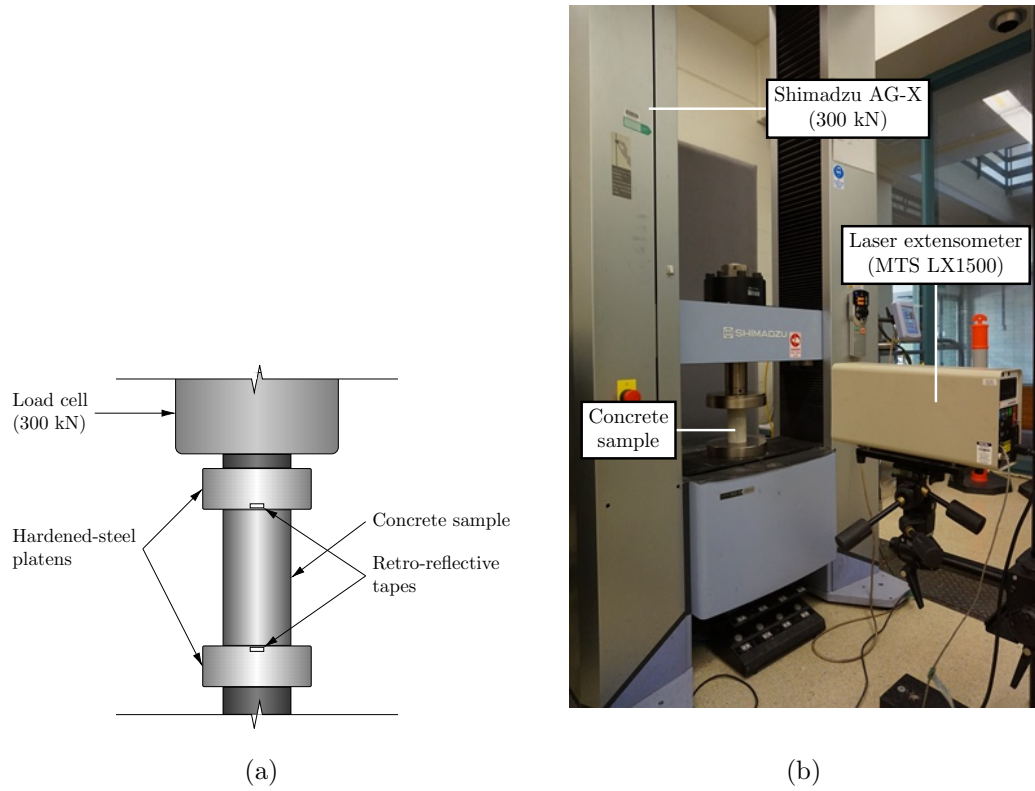
Figure 5.2: Test setup with the gauge length being the distance between the retro-reflective tapes. (a) Schematic diagram. (b) Laboratory view.
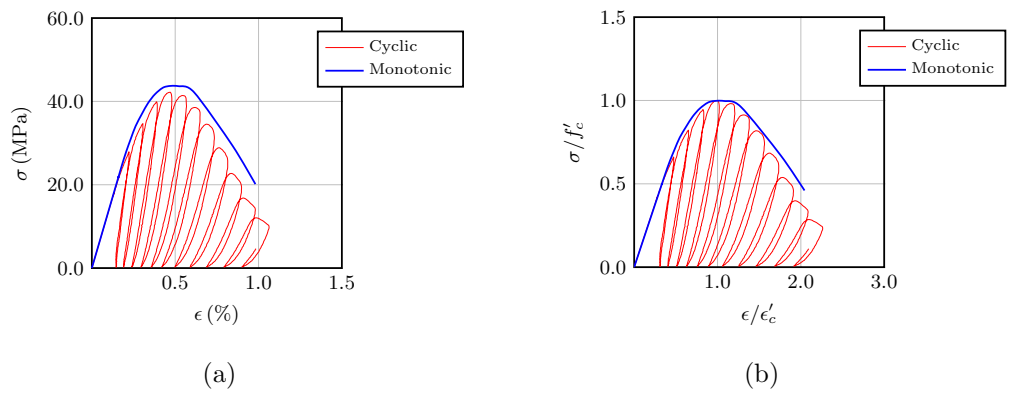
Figure 5.3: Cyclic response and the monotonic envelope curve for sample A50C1.5_T. (a) Original curves and (b) Normalised curves.
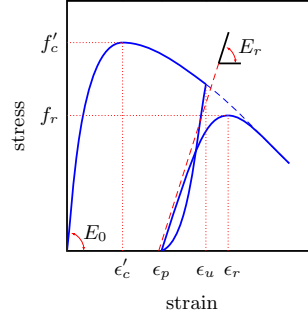
Figure 5.4: Parameter definitions for the cyclic response of concrete.

5.3 Results and discussion

The variation of mechanical properties are derived and presented in this section. The properties considered in this paper are depicted in Fig. 5.4, and are referred to as either basic parameters or cyclic parameters in the following discussions. Basic parameters include the peak stress f'_c, peak strain ϵ'_c and initial tangent modulus E_0. On the other hand, cyclic parameters are the parameters related to the cyclic response of the material and are defined as the unloading strain ϵ_u, plastic strain ϵ_p, reloading strain ϵ_r, reloading stress f_r, and reloading tangent modulus E_r. These parameters are commonly used for the numerical simulation of concrete behaviour under cyclic loading [1, 26].

Fig. 5.5 shows the development of strength over time for sample A50C1.5_T (sample with a 50-mm diameter and height to diameter ratio of 1.5). Also given in this figure, are the values of peak stress, peak strain and initial tangent modulus at an age of 28 days for this sample. These specific values are hereby denoted by $\bar{\epsilon}'_c$, $\bar{f}'_c$ and $\bar{E}_0$ and are used as base values for comparing the basic properties of samples with different dimensions.

Before going into the presentation of test results, it is important to understand how the aspect ratio and diameter influence the failure mechanics of cylindrical samples. The two underlying phenomena that affect the failure mechanics of concrete samples are schematically illustrated in Figs. 5.6 and 5.7. Fig. 5.6 shows the distribution of lateral stresses for samples with different aspect ratios. These lateral stresses are caused by the frictional forces appearing between the sample and the loading platens. With the lateral stresses acting in compression, these regions can be viewed as confined zones where the strength of the material can attain values higher than
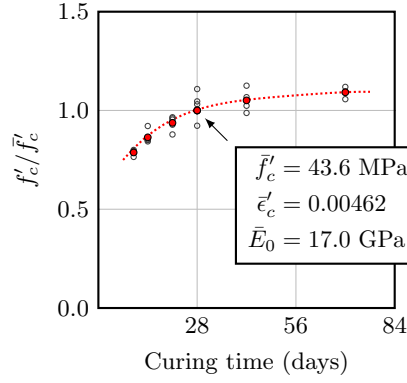
Figure 5.5: Development of strength as a function of curing time.
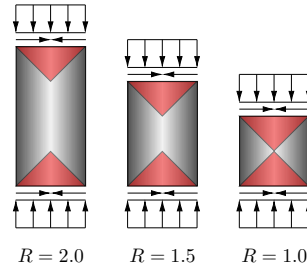
Figure 5.6: Lateral stresses and the confined zone for samples with different aspect ratios.

those for unconfined concrete. Hence, as the aspect ratio of the sample decreases, a larger portion of the sample experiences confinement, which in turn leads to the higher strength and higher ductility of the sample [27]. On the other hand, when it comes to the lateral dimension of the sample, it is not the diameter alone that influences the failure of the sample, but the maximum aggregate size to diameter ratio (d_a/D). This has been shown by the work of Sim et al. [19], where size effect experiments were carried out by using samples with different diameters and aspect ratios, as well as concrete mixes with different maximum aggregate sizes $(d_a = 8 - 19$ mm). It is deduced that as d_a/D increases, the length of the cracks that develop around the aggregates increase, hence, increasing the energy required to form the cracks (Fig. 5.7). However, since the maximum aggregate size of the concrete mix used in the present program is the same for all samples, the following results are presented in terms of D for simplicity.

Fig. 5.8 illustrates the crack patterns observed for four of the sample sizes used in this program. Further examination of the failed samples indicated that all cracks were formed in the concrete paste. In addition, the cracks were observed to be more dense for samples with smaller aspect ratios, leading to a more ductile failure.
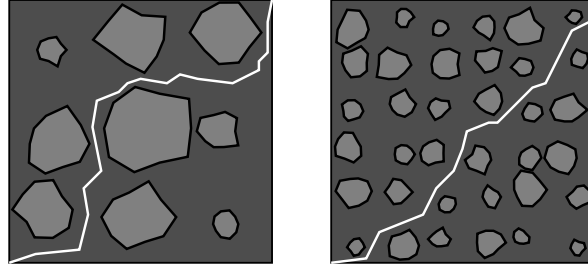
Figure 5.7: Crack propagation in concrete for different ratios of d_a/D.
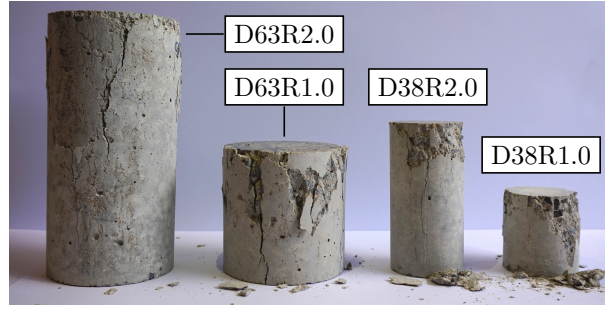
Figure 5.8: Crack patterns for samples A63C2.0_T, A63C1.0_T, A38C2.0_Tand A38C1.0_T.

5.3.1 Basic properties

This section deals with the basic properties of concrete under monotonic loading and the test results obtained from samples with different dimensions. These properties include the peak stress f'_c, peak strain ϵ'_c and the initial tangent modulus E_0 and are the minimum requirements for the reconstruction of compressive stress-strain curves [26]. Figs. 5.9, 5.10 and 5.11 respectively show the variation of f'_c, ϵ'_c and E_0 in terms of sample diameter D and aspect ratio R. The values given in these figures are averaged test results that have been normalised by the values of the control sample A50C1.5_T. The logic behind using sample A50C1.5_T as the control sample was discussed in Section 5.2.2. In addition to normalised averaged results, also shown in Figs. 5.9, 5.10 and 5.11 is the standard deviation of each parameter by the utilisation of error bars. These error bars help give insight towards the degree of certainty of each parameter.

5.3.1.1 Peak stress

The peak stress f'_c represents the strength of the material and is the maximum stress observed in the stress-strain curve. It can be seen from Fig. 5.9 that for any
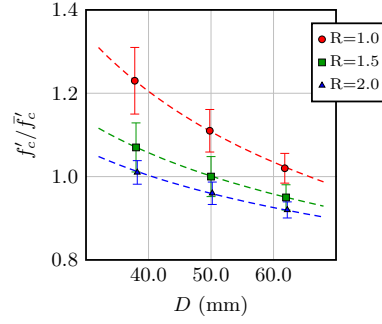
Figure 5.9: Variation of peak stress f'_c with sample diameter and aspect ratio.

given diameter, f'_c increases as the aspect ratio decreases. Moreover, f'_c also tends to increase as the diameter of the sample becomes smaller. Another observation made from Fig. 5.9 is that as samples become smaller in diameter or aspect ratio, test data become more dispersed and hence lead to a higher standard deviation. This is in agreement with the general understanding that due to higher heterogeneity, smaller samples tend to produce more scattered results [12].

5.3.1.2   Peak strain

The peak strain ϵ'_c is defined as the strain value that corresponds to the peak stress f'_c. Fig. 5.10 indicates that for any given diameter, the peak strain ϵ'_c tends to increase as the aspect ratio of the sample decreases. Similarly, for any given aspect ratio, the peak strain ϵ'_c increases as the diameter of the sample becomes smaller. Among the two parameters, the aspect ratio appears to have a more prominent effect on peak strain. This can be directly related to the effect of the confined zone (Fig. 5.6), whereby samples with lower aspect ratios experience multi-axial compressive stress states over a larger portion of their volume and therefore, increased ductility [17]. On the other hand, it is observed that if the diameter is kept constant, lower aspect ratios lead to higher values of the standard deviation. However, for samples with the same aspect ratio, the diameter of the sample does not appear to affect the standard deviation. By comparing the standard deviation of the peak strain ϵ'_c to the ones obtained for the peak stress f'_c, it can be concluded that in general, strain values exhibit more scatter.
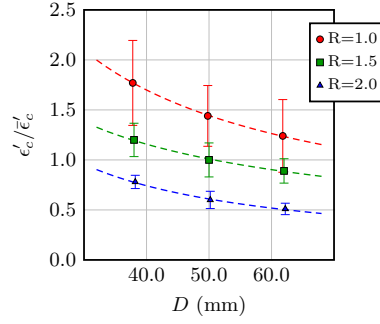
Figure 5.10: Variation of peak strain ϵ_c' with sample diameter and aspect ratio.
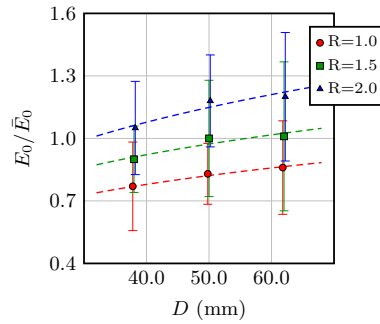
Figure 5.11: Variation of initial tangent modulus E_0 with sample diameter and aspect ratio.

5.3.1.3 Initial tangent modulus

The initial tangent modulus E_0 is the stiffness that a non-damaged material exhibits before its response becomes non-linear. While similar patterns were observed for the variation of peak stress f_c' and peak strain ϵ_c', the initial tangent modulus E_0 appears to be completely different. From Fig. 5.11 it is observed that for any given diameter, the initial tangent E_0 decreases as the aspect ratio of the sample decreases. In addition, for any given aspect ratio, the initial tangent E_0 decreases as the diameter of the sample becomes smaller. The standard deviation of the initial tangent E_0 is seen to have higher values than the ones attained for peak stress f_c' and peak strain ϵ_c'. However, unlike the peak stress f_c' and peak strain ϵ_c', it also appears that the standard deviation of the initial tangent E_0 is not affected by the diameter or the aspect ratio of the sample. It is worth noting that although the variation of the average values given in Fig. 5.11 show evident trends, due to the high scatter of data, no conclusive result can be drawn for the initial tangent until a more comprehensive set of experiments are carried out.
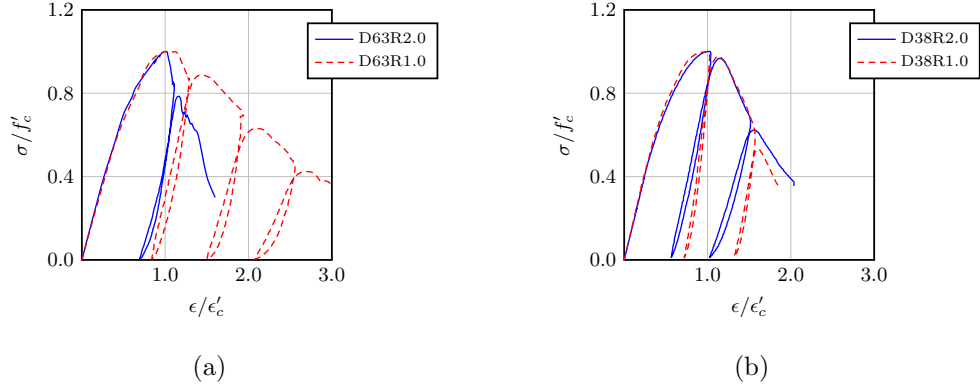
Figure 5.12: Normalised stress-strain curves for samples (a) A63C2.0_T and A63C1.0_T and (b) A38C2.0_T and A38C1.0_T.

5.3.2 Cyclic properties

This section presents the cyclic properties of samples in terms of their diameter and aspect ratio. The parameters under discussion here are defined in Fig. 5.4. Note that although only one cycle of loading has been shown in Fig. 5.4, when a sample is subjected to multiple cycles, the point at which the sample is unloaded from ($\epsilon < \epsilon_u$) is defined as the beginning of a single cycle. Hence, the values of ϵ_p, f_r, ϵ_r and E_r attained from each cycle are always correlated to the unloading point that initiated the cycle.

5.3.2.1 Cyclic stress-strain curves

In order to directly examine the effect that the dimensions of a sample have on the shape of the cyclic stress-strain curves, each individual curve is first normalised by its own f'_c and ϵ'_c. Fig. 5.12 shows normalised stress-strain curves for four different samples. Qualitatively speaking, it is observed from this figure that the pre-peak region of the stress-strain curve ($\epsilon/\epsilon'_c < 1.0$) is not affected by the dimensions of the sample. On the other hand, the post-peak region of the curve ($\epsilon/\epsilon'_c > 1.0$) exhibits increased ductility as the diameter or the aspect ratio of the sample decreases. While higher ductility is a well known characteristic of smaller samples [19, 27], an additional key feature that is revealed by comparing Figs. 5.12a and b is that the effect of aspect ratio on ductility diminishes as the diameter of the sample decreases.

Based on the observations made by Bahn and Hsu [1] and later by Lam et al. [7], the following assumptions are made for the extraction and the interpretation of the
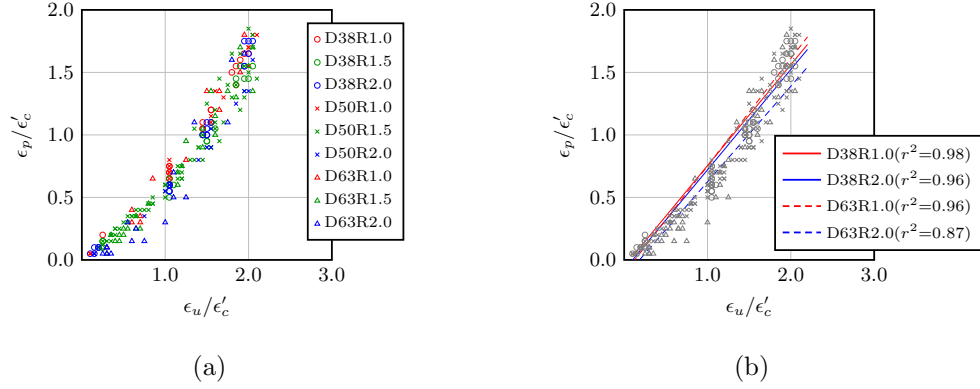
Figure 5.13: Variation of ϵ_p with ϵ_u. (a) Scatter data and (b) best fit lines.

cyclic parameters:

- Full-range monotonic stress-strain curves are viewed as upper bounds for the cyclic response; and

- The unloading strain ϵ_u is considered as the primary independent variable that dictates the subsequent reloading parameters.

The consequence of adhering to these two assumptions is the construction of Figs. 5.13, 5.14, 5.15 and 5.16 showing the variation of each cyclic parameter as a function of the unloading strain ϵ_u. As mentioned before, in order to obtain the data presented in these figure, each experimental stress-strain curve was first normalised by its f'_c and ϵ'_c and the value of the parameters were then taken from the normalised curve. These graphs show the scatter data for all sample sizes. In addition, they also include best fit lines which help understand the individual effects of sample diameter and aspect ratio. These best fit lines are obtained using linear regression and the least-squares estimation. The reasoning behind the utilisation of best fit lines rather than best fit curves is that best fit lines allow a more direct comparison of the relationship between degradation of cyclic properties and different definitions of the damage index. Such comparison is carried out later in Section 5.3.3.

5.3.2.2 Plastic strain, ϵ_p

The plastic strain ϵ_p is the accumulated residual strain that the material exhibits upon the completion of each unloading sequence. Fig. 5.13 shows the variation of the plastic strain ϵ_p with unloading strain ϵ_u. While the original scatter data
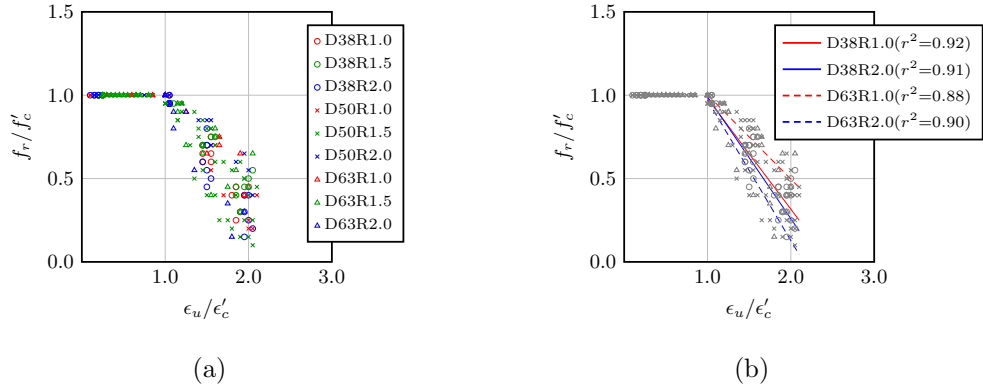
Figure 5.14: Variation of f_r with ϵ_u. (a) Scatter data and (b) best fit lines.
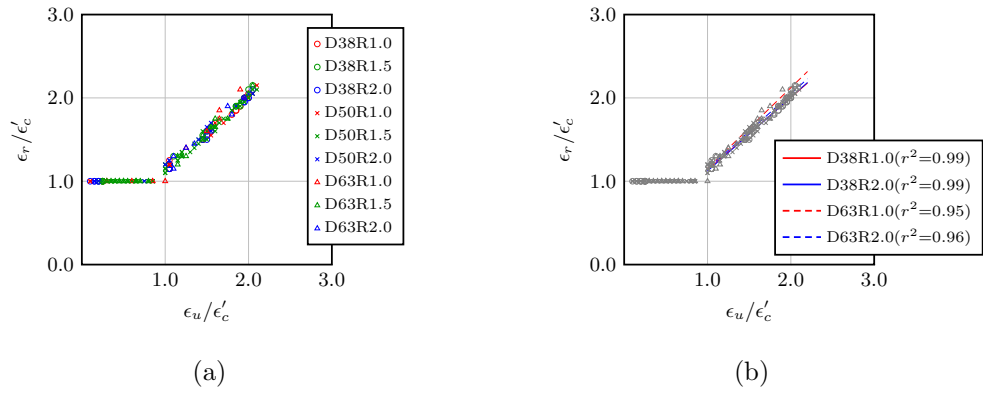
Figure 5.15: Variation of ϵ_r with ϵ_u. (a) Scatter data and (b) best fit lines.
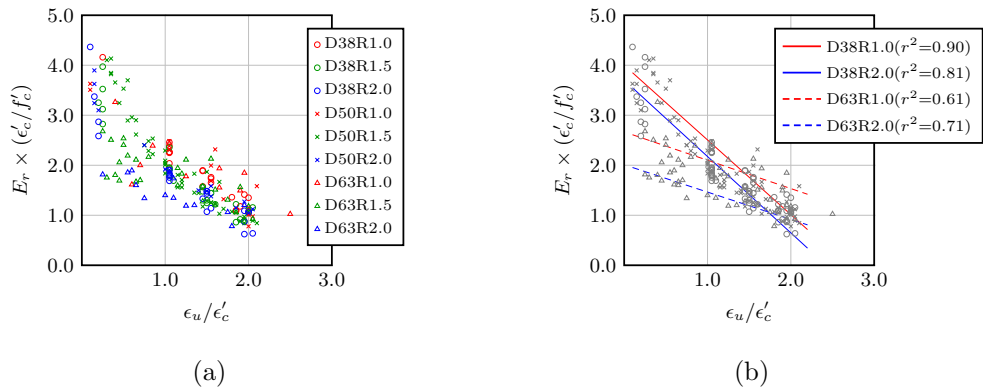
Figure 5.16: Variation of E_r with ϵ_u. (a) Scatter data and (b) best fit lines.

have been plotted in Fig. 5.13a, best fit lines for samples A38C1.0_T, A38C2.0_T, A63C1.0_T and A63C2.0_T are introduced in Fig. 5.13b. It is observed from the best fit lines that the dimensions of the sample have no significant effect on the relationship between ϵ_p and ϵ_u.

5.3.2.3 Reload strength, f_r

The reloading strength f_r is the maximum stress value that the damaged material can undergo upon reloading. The variation of the reloading strength f_r with unloading strain ϵ_u is presented in Fig. 5.14. The best fit lines given for $\epsilon_u/\epsilon_c' > 1.0$ in Fig. 5.14b indicate that the negative slope of $\epsilon_u - f_r$ lines becomes less steep as one dimension is reduced while the other dimension is kept constant. This is a direct result of increased ductility for samples with smaller dimensions, which was discussed in Section 5.3.2.1. Therefore, it is not surprising to also see that the effect of aspect ratio on the slope of the $\epsilon_u - f_r$ line diminishes for samples with a smaller diameter, and hence, the best fit lines corresponding to samples A38C1.0_T and A38C2.0_T being almost identical.

5.3.2.4 Reload strain, ϵ_r

The reloading strain ϵ_r is the strain value that corresponds to the reloading strength f_r of the damaged material. Fig. 5.15 shows the variation of the reloading strain ϵ_r with unloading strain ϵ_u. The best fit lines given in Fig. 5.13b for samples A38C1.0_T, A38C2.0_T, A63C1.0_T and A63C2.0_T indicate that the relationship between ϵ_r and ϵ_u is not affected by the dimensions of the sample.

5.3.2.5 Reload tangent, E_r

The reloading tangent E_r is defined as the stiffness of the damaged material upon reloading from a zero stress state. The cyclic parameter that is most affected by the dimensions of the sample is the reloading tangent. Fig. 5.16 shows the scatter data and the best fit lines for the variation of the reloading tangent E_r against unloading strain ϵ_u. The best fit lines of Fig. 5.16b indicate that for a given sample diameter and for a specific ϵ_u, the value of E_r is always higher for samples with lower aspect ratios. In addition, for a constant value of the aspect ratio, the slope of the $\epsilon_u - E_r$

line increases as the diameter of the sample becomes smaller. Lastly, note that the diameter of the sample highly influences the pre-peak ($\epsilon_u/\epsilon_c' < 1$) region of the $\epsilon_u - E_r$ curve.

5.3.3 Damage index

In Section 5.3.2, cyclic parameters were plotted in terms of the unloading strain ϵ_u. In other words, the unloading strain ϵ_u was taken as the damage index governing the behaviour of the material upon unloading and subsequent reloading. However, it has been argued that using ϵ_u as the damage index and taking it as the independent variable that determines unloading and reloading paths is not a valid choice [26]. This section introduces two additional definitions of the damage index and compares them to the unloading strain. The first damage index is based on the idea of strength degradation [26] and is defined as:

$$\delta_d = 1 - \frac{\sigma}{E_0 \epsilon} \tag{5.1}$$

and the second damage index takes into account the ratio of dissipated energy per unit volume [28], defined by:

$$\delta_e = \frac{\displaystyle\int_{\epsilon=0}^{\epsilon_p} \sigma d\epsilon}{\displaystyle\int_{\epsilon=0}^{\epsilon_f} \sigma d\epsilon} \tag{5.2}$$

where ϵ_f is the strain at which the material is completely damaged and $\epsilon = \epsilon_p$ refers to the state where the sample is about to be reloaded (Fig. 5.4).

In Eqs. (5.1) and (5.2), δ_d and δ_e are damage indices based on strength degradation and energy dissipation, respectively. Both indices vary between 0 (no material damage) and 1.0 (fully damaged material). In these equations, σ and ϵ are corresponding stress and strain values from the monotonic compressive response of the material. This means that in order to quantify the damage index, a general stress-strain relationship must first be assumed for the monotonic compressive response. The stress-strain relationship proposed by Yang et al. [29] is hereby chosen for this purpose. This relationship is defined as:

Table 5.2: Variables used for Eq. (5.3)

sample	$E_0 \times \left(\frac{\epsilon'_c}{f'_c}\right)$	$\frac{\epsilon_{0.5}}{\epsilon'_c}$	$\beta_1 \, (\epsilon \leq \epsilon'_c)$	$\beta_1 \, (\epsilon > \epsilon'_c)$
A38C1.0_T	2.114	1.76	0.803	3.464
A38C2.0_T	1.408	1.69	2.403	3.741
A63C1.0_T	1.708	1.98	1.330	2.537
A63C2.0_T	1.438	1.54	2.230	4.931

$$\sigma = \frac{(\beta_1 + 1)\left(\frac{\epsilon}{\epsilon'_c}\right)}{\left(\frac{\epsilon}{\epsilon'_c}\right)^{\beta_1+1} + \beta_1} f'_c \tag{5.3}$$

where the value of β_1 is attained by solving the following equation:

$$\begin{cases} 0.4(X_a)^{\beta_1+1} + (0.4 - X_a)\beta_1 - X_a = 0 & , \epsilon \leq \epsilon'_c \\ (X_d)^{\beta_1+1} + (1 - 2X_d)\beta_1 - sX_d = 0 & , \epsilon > \epsilon'_c \end{cases} \tag{5.4}$$

with $X_a = 0.4f'_c/E_0\epsilon'_c$ and $X_d = \epsilon_{0.5}/\epsilon'_c$. All parameters have been described previously, except for $\epsilon_{0.5}$ which denotes the post-peak strain value corresponding to a stress state of $0.5f'_c$. Table 5.2 gives the values of the parameters of Eq. (5.3) used for samples A38C1.0_T, A38C2.0_T, A63C1.0_T and A63C2.0_T. Fig. 5.17 shows the stress-strain curves developed by these parametric values. Substituting these stress-strain relationships into Eqs. (5.1) and (5.2), one can obtain the variation of each damage index in terms of compressive strain. The result of this substitution is the variation of δ_d and δ_e with ϵ, as illustrated in Fig. 5.18.

Cyclic properties which were introduced in Section 5.3.2 are now plotted against the damage index δ_d in Fig. 5.19. The plots in this figure cover samples A38C1.0_T, A38C2.0_T, A63C1.0_T and A63C2.0_T, whereby for each sample, the best fit line with its corresponding coefficient of determination r^2 is also given. The same cyclic properties are plotted against δ_e in Fig. 5.20.

Comparing Figs. 5.19 and 5.20 with Figs. 5.13, 5.14, 5.15 and 5.16 indicate the difference that the definition of the damage index makes when it comes to the description of cyclic parameters. The utilisation of best fit lines rather than best fit
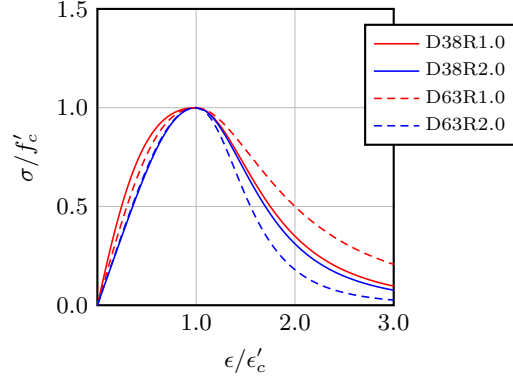
Figure 5.17: Stress-strain curves produced by Eq. (5.3) proposed by Yang et al. [29].

(a)

(b)
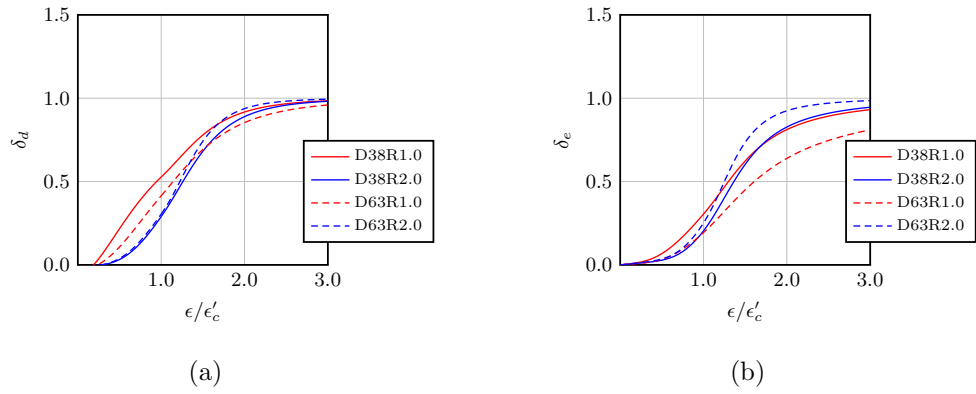
Figure 5.18: Variation of the damage index with strain based on (a) strength degradation Eq. (5.1) and (b) dissipated energy Eq. (5.2).
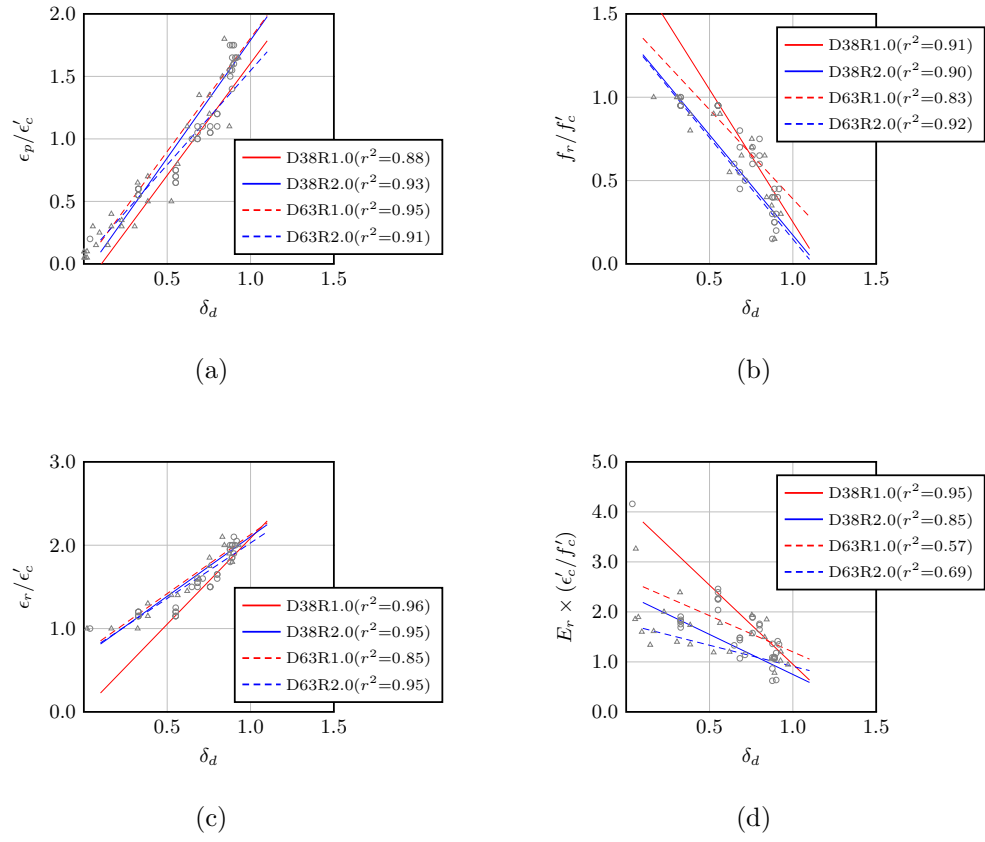
Figure 5.19: Variation of cyclic parameters against damage index δ_d given by Eq. (5.1). (a) Plastic strain ϵ_p, (b) reload strength f_r, (c) reload strain ϵ_r and (d) reload tangent modulus E_r.
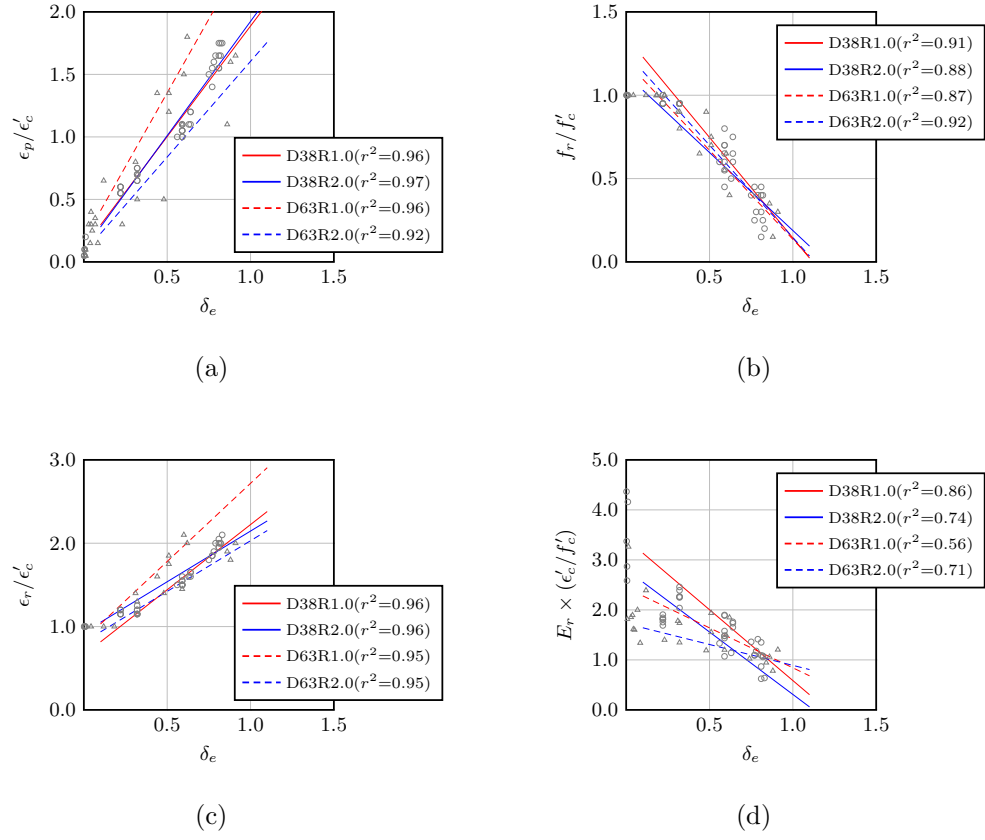
Figure 5.20: Variation of cyclic parameters against damage index δ_e given by Eq. (5.2). (a) Plastic strain ϵ_p, (b) reload strength f_r, (c) reload strain ϵ_r and (d) reload tangent modulus E_r.

curves allows for the identification of any direct relationship between each damage index and cyclic parameters. It is observed from these figures that using the unloading strain ϵ_u as the damage index agrees well with the variational patterns of the reloading strain ϵ_r and the reloading strength f_r. This is deduced by comparing the r^2 values resulting from the three damage indices. On the other hand, the strength based damage index δ_d is best suited for the reloading tangent E_r, and the energy based damage index δ_e gives the best correspondence for the plastic strain ϵ_p.

Although more experiments have to be carried out before a definite conclusion can be made, but these observations imply that the variation of different cyclic properties may be due to different damage mechanisms within the material.

5.4 Conclusions

The aim of this research was to determine the effect of size on the cyclic response of concrete samples. For this purpose, cylindrical samples of 9 different sizes were cast and tested. These samples consisted of an array of different diameters (D) and different aspect ratios (R). The effect of size on peak stress (f'_c), peak strain (ϵ'_c) and initial tangent (E_o) was first determined. Cyclic stress-strain curves were then normalised by the individual values of f'_c and ϵ'_c for each sample, and cyclic parameters were determined from the normalised curves. These cyclic parameters were initially interpreted in terms of their variation with the unloading strain (ϵ_u), but were later also examined against a strength based damage index (δ_d) and an energy based damage index (δ_e). The following conclusions can be drawn from the results:

1. Peak stress (f'_c) and peak strain (ϵ'_c) values are shown to increase as the diameter (D) and the aspect ratio (R) decrease.

2. The initial tangent (E_o) tends to decrease as the diameter (D) and the aspect ratio (R) decrease.

3. The post-peak ductility of the samples increases as the diameter (D) and the aspect ratio (R) decrease. However, this correlation diminishes as the diameter (D) decreases.

4. As a result of increased ductility with smaller diameters (D) and smaller aspect

ratios (R), the negative slope of the $\epsilon_u - f_r$ line tends to become less steep as the diameter (D) and the aspect ratio (R) of the sample decrease. However, similar to ductility, this dependency diminishes as the diameter (D) becomes smaller.

5. The variations of plastic strain and reloading strain with unloading strain ($\epsilon_u - \epsilon_p$ and $\epsilon_u - \epsilon_r$) are independent of sample size.

6. The reloading tangent (E_r) tends to have higher values for smaller values of diameter (D) and aspect ratio (R), while at the same time, the slope of the $\epsilon_u - E_r$ line becomes more steep as the diameter of the sample decreases.

7. When comparing the unloading strain (ϵ_u) as a damage index with the strength based damage index (δ_d) and the energy based damage index (δ_e), it is observed that the variation of the reloading strength (f_r) and reloading strain (ϵ_r) are best described with the unloading strain (ϵ_u). On the other hand, the variation of the reloading tangent (E_r) and plastic strain (ϵ_p) are best described by δ_d and δ_e, respectively.

8. A deeper understanding of the underlying damage mechanisms which result in the dependencies pointed out in the previous item can be gained through further experiments. However, the authors believe that performing numerical simulations using the discrete element approach can also lead to further insight on the subject.

Acknowledgement

References

[1] Byong Youl Bahn and Cheng-Tzu Thomas Hsu. Stress-strain behavior of concrete under cyclic loading. *ACI Materials Journal*, 95(2), 1998.

[2] Pietro Bocca and Matteo Crotti. Variations in the mechanical properties and temperature of concrete subjected to cyclic loads, including high loads. *Materials and structures*, 36(1):40–45, 2003.

[3] Weena P Lokuge, Jay G Sanjayan, and Sujeeva Setunge. Triaxial test results of high-strength concrete subjected to cyclic loading. *Magazine of Concrete Research*, 55(4):321–329, 2003.

[4] Weena P Lokuge, Jay G Sanjayan, and Sujeeva Setunge. Constitutive model for confined high strength concrete subjected to cyclic loading. *Journal of materials in Civil Engineering*, 16(4):297–305, 2004.

[5] Lik Lam, Jinguang Teng, Chihang Cheung, and Yan Xiao. Frp-confined concrete under axial cyclic compression. *Cement and Concrete composites*, 28(10): 949–958, 2006.

[6] Junichi Sakai and Kazuhiko Kawashima. Unloading and reloading stress–strain model for confined concrete. *Journal of Structural Engineering*, 132(1):112–122, 2006.

[7] Eddie Siu-Shu Lam, Bo Wu, Qun Liu, and Ivy Fung-Yuen Ho. Monotonic and cyclic behavior of high-strength concrete with polypropylene fibers at high temperature. *ACI Materials Journal*, 109(3), 2012.

[8] Reza Abbasnia, Farid Hosseinpour, Maziar Rostamian, and Hassan Ziaadiny. Cyclic and monotonic behavior of frp confined concrete rectangular prisms with different aspect ratios. *Construction and Building Materials*, 40:118–125, 2013.

[9] Edison Osorio, Jesús M Bairán, and Antonio R Marí. Lateral behavior of concrete under uniaxial compressive cyclic loading. *Materials and structures*, 46(5):709–724, 2013.

[10] Eunsoo Choi, Baik-Soon Cho, Wonseok Chung, and David Hui. Monotonic and cyclic behavior of densely confined concrete using stainless steel rings. *KSCE Journal of Civil Engineering*, 17(6):1403–1412, 2013.

[11] Hamoon Fathi and Kianoosh Farhang. Effect of cyclic loadings on heated self-compacting concrete. *Construction and Building Materials*, 69:26–31, 2014.

[12] Adam M Neville. The influence of size of concrete test cubes on mean strength and standard deviation. *Magazine of Concrete Research*, 8(23):101–110, 1956.

[13] Robert L Day and Naseer Haque. Correlation between strength of small-and standard-size concrete cylinders. *ACI Materials Journal*, 90(5), 1993.

[14] Javier R Del Viso, Jacinto R Carmona, and Gonzalo Ruiz. Shape and size effects on the compressive strength of high-strength concrete. *Cement and Concrete Research*, 38(3):386–395, 2008.

[15] Michelle R Roddenberry, Raphael Kampmann, Marcus H Ansley, Nicholas Bouchard, and W Virgil Ping. Failure behavior of concrete cylinders under different end conditions. *ACI Materials Journal*, 108(1), 2011.

[16] Raphael Kampmann, Michelle Roddenberry, and W Virgil Ping. Contribution of specimen surface friction to size effect and rupture behavior of concrete. *ACI Materials Journal*, 110(2), 2013.

[17] Sokhwan Choi, Karl C Thienel, and Surendra P Shah. Strain softening of concrete in compression under different end constraints. *Magazine of Concrete Research*, 48(175):103–115, 1996.

[18] MS Chin, Mohammad A Mansur, and Tionghuan Wee. Effects of shape, size, and casting direction of specimens on stress-strain curves of high-strength concrete. *ACI materials journal*, 94(3), 1997.

[19] Jae-Il Sim, Keun-Hyeok Yang, and Joong-Kyu Jeon. Influence of aggregate size on the compressive size effect according to different concrete types. *Construction and Building Materials*, 44:716–725, 2013.

[20] ASTM C192/C192M-02. *Standard practice for making and curing concrete test specimens in the laboratory*. Annual book of ASTM standards. American Society of Testing and Materials, Philadelphia, PA, 2002.

[21] Sina Sinaie, Amin Heidarpour, and Xiao-Ling Zhao. Mechanical properties of cyclically-damaged structural mild steel at elevated temperatures. *Construction and Building Materials*, 52:465–472, 2014.

[22] Sina Sinaie, Amin Heidarpour, and Xiao-Ling Zhao. A multi-objective optimization approach to the parameter determination of constitutive plasticity models for the simulation of multi-phase load histories. *Computers & Structures*, 138:112–132, 2014.

[23] Sina Sinaie, Amin Heidarpour, and Xiao-Ling Zhao. Stress–strain–temperature relation for cyclically-damaged structural mild steel. *Engineering Structures*, 77:84–94, 2014.

[24] Adam M Neville. *Properties Of Concrete, 5/E*. Pearson Education, 2011.

[25] Mohammad Mansur, Tionghuan Wee, and MS Chin. Derivation of the complete stress–strain curves for concrete in compression. *Magazine of Concrete Research*, 47(173):285–290, 1995.

[26] Jose Fernando Sima, Pere Roca, and Climent Molins. Cyclic constitutive model for concrete. *Engineering structures*, 30(3):695–706, 2008.

[27] Jan GM Van Mier, Surendra P Shah, M Arnaud, JP Balayssac, A Bascoul, S Choi, D Dasenbrock, G Ferrara, C French, ME Gobbi, et al. Strain-softening of concrete in uniaxial compression. *Materials and Structures*, 30(4):195–209, 1997.

[28] Daniel C Jansen and Surendra P Shah. Effect of length on compressive strain softening of concrete. *Journal of Engineering Mechanics*, 123(1):25–35, 1997.

[29] Keun-Hyeok Yang, Ju-Hyun Mun, Myung-Sug Cho, and Thomas H-K Kang. Stress-strain model for various unconfined concretes in compression. *ACI Structural Journal*, 111(1-6), 2014.

CHAPTER **6**

Effect of pre-induced cyclic damage on the mechanical properties of concrete exposed to elevated temperatures

Contents

Monash University

Declaration for Thesis Chapter 6

Declaration by candidate

In the case of Chapter 6, the nature and extent of my contribution to the work was the following:

Nature of contribution	Extent of contribution (%)
Establishing methodologies, Experimental work, Data analysis, Write-up and revision	70%

The following authors contributed to the work. If co-authors are students at Monash University, the extent of their contribution in percentage terms must be stated.

Name	Nature of contribution	Extent of contribution (%)
Dr. Amin Heidarpour	Developing ideas Revision Financial support	
Prof. Xiao-Ling Zhao	Revision Financial support	

The undersigned hereby certify that the above declaration correctly reflects the nature and extent of the candidate's and co-authors' contributions to this work.

Candidate's signature: ███████ **Date:** 24/09/2015

Main supervisor's signature: ███████ **Date:** 24/09/2015

Abstract

This research aims to investigate the effect of high temperature on concrete samples which have been previously damaged under cyclic loading. For this purpose, normal strength concrete samples are initially subjected to strain-controlled load cycles and then exposed to elevated temperatures. Residual mechanical properties of the samples are measured after allowing them to slowly cool down to room temperature. These properties are expressed in terms of two independent parameters, i.e. the level of damage induced by cyclic loading as well as the exposure temperature. It is shown that the variation of residual properties is simultaneously affected by both parameters, however, the influence of pre-induced damage diminishes as the exposure temperature increases. In addition, an effective approach is described for the numerical reproduction of stress-strain curves for any given level of damage and temperature.

6.1   Introduction

In view of the devastating outcomes of extreme events such as post-earthquake fires [1, 2], the importance of having a model for the fire-resistant capacity of a seismically-damaged structure becomes evident. Creating such models requires research in the structural scale [3–6] as well as the material scale [7–9].

Due to its popularity as a construction material, the study of concrete is a vibrant topic and extensive research has been carried out on its behaviour under cyclic loading [10–12] as well as high temperature [13–20]. However, there is a lack of experimental data when it comes to the changes that high temperature inflicts on a specimen that has already sustained cyclically-induced damage. At increasing temperatures, concrete undergoes changes in its chemical composition and physical structure. The chemical and mechanical changes that concrete experiences at high temperatures have been outlined by several researchers [15–17]. Exposure to high temperature affects the strength and durability of concrete members, and while some changes are instantaneous (e.g. stresses due to thermal incompatibility), others take place over time (e.g. dehydration of chemically bound water). Hence, the complex interaction of physical, chemical and mechanical changes becomes a time-dependent process.

Zhai et al. [21] investigated the properties of concrete samples after being exposed to high temperatures (up to 1200°C). Their results show that the changes take place in both the cement paste and the aggregates. It also shows that these changes are of different nature at different levels of temperature. At the same time, the experiments conducted by Wu and Wu [19] imply that up to a temperature of 600°C and over a duration of 1-6 hours, the extent of strength degradation is almost independent of the duration of exposure.

Arioz [17] studied the effect of high temperature on the residual compressive strength of concrete specimens. Also included in this study, was the influence of aggregate type and water-cement ratio on the relative strength reduction. Attributed to the mineral structure, it was concluded that concrete made from river gravel experiences higher strength reductions when compared to crushed limestone. However, the results indicate that the water-cement ratio has negligible effect on the relative strength reduction.

Thermal incompatibility of the cement paste and aggregates is considered a main factor causing degradation at elevated temperatures [15, 17, 20]. Therefore, strength degradation of concrete is not only a result of the decomposition of cement hydration products, but is also influenced by the micro-cracks which develop due the difference between the thermal expansion of the paste and that of the aggregates.

Despite the importance of multi-phase load histories such as post-earthquake fire or post-impact fire, not much attention has been given to the understanding of such sequential load histories and their effect on construction material [7, 22–24]. A recent investigation by Sinaie et al. [7] involved the behaviour of cyclically-damaged mild steel at elevated temperatures. A similar problem is treated in the present paper for normal strength concrete. In other words, this research investigates the changes that material properties undergo when concrete samples are first subjected to cyclic loading and then exposed to elevated temperatures. This study is part of a series of investigations currently being carried out at Monash University on extreme events and resilient structures [7, 22–26].

6.2   Experimental program

When it comes to the effect of high temperature on concrete, three methods of testing are carried out by researchers [27]:

- Stressed tests at high temperature

- Unstressed tests at high temperature

- Residual tests after exposure to high temperature

Stressed tests at high temperature involve concurrent heating and loading on the sample. In these tests, samples are loaded up to a fraction of their nominal strength and then heated while the load is kept constant. Once the temperature reaches its target value, the existing load is increased until failure. *Unstressed tests at high temperature* are similar to stressed tests, but without the initial load. Stressed and unstressed tests are usually carried out in conjunction to one another [28]. While the existence of stress during heating leads to complex micro-mechanical interactions, results indicate that in general, stressed samples sustain less strength loss when compared to unstressed ones.

In contrast to stressed and unstressed tests at high temperature, for *residual tests after exposure to high temperature*, the sample is allowed to cool down to room temperature before being subjected to loading [19]. The relation between residual strength and high temperature strength varies depending on temperature. It has been reported that up to a temperature of 400°C, residual strength is higher than strength at high temperature. However, as the exposure temperature rises beyond 400°C, the residual strength is measured to be less than the strength at high temperature. This has been attributed to the decomposition of calcium hydroxide into calcium oxide and water which takes place at around 400°C. While this decomposition causes strength loss at high temperature, it is reversible and as the calcium oxide absorbs water during cooling, the new calcium hydroxide crystals cause the existing cracks to open further and lead to additional strength loss [15].

This study aims to determine the *residual* mechanical properties of cyclically-damaged specimens after being exposed to elevated temperatures. For this purpose, the test program was divided into three separate phases:

- **Phase 1**. Induction of cyclic damaged.

- **Phase 2**. Exposure to elevated temperature.

- **Phase 3**. Determination of residual properties.
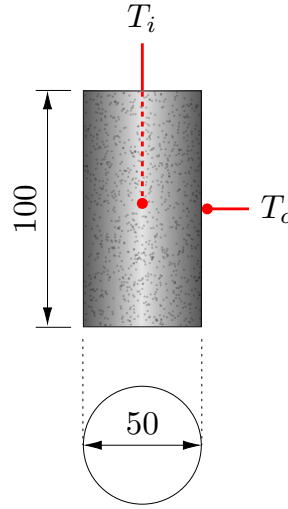
Figure 6.1: Concrete sample geometry (in mm) and thermocouple placement.

In the first phase, undamaged samples were taken and subjected to cyclic loading. This resulted in samples that were in a state of partial damage. In the second phase, the partially-damaged samples were exposed to different levels of temperature. After being cooled down to room temperature, samples were tested under compression in the third and final phase. A detailed description of each phase is given in Section 6.2.3.

6.2.1 Material

One major concern of this research was to induce a state of uniform damage throughout a single concrete sample. With the damage being of mechanical and thermal origin, the dimensions of the samples should be selected as to accompany uniform damage caused by both phenomena.

In regards to cyclic damage, the results reported by Sinaie et al. [12] were taken into consideration. On the other hand, to avoid size-related thermal damage, especially in the form of spalling, the findings of other researchers were taken into account [15, 29]. As a result, samples of 50-mm diameter and 100-mm height were used in this program (Fig. 6.1). This sample size has shown to produce reliable results in terms of reproducibility of data (less scatter within the test results) under monotonic as well as cyclic loading [12]. At the same time, with the cross section being of cylindrical shape and the diameter of the sample being 50 mm (smaller than the commonly used 100- or 150-mm diameter), the process of attaining uniform temperature is simplified.

Table 6.1: Mix design for 1 m^3 of concrete.

General purpose cement (kg/m^3)	364
Coarse aggregates (max diameter 8 mm, kg/m^3)	1170
Fine aggregate (kg/m^3)	687
Water (kg/m^3)	200

The results of this study were intended to pertain to both new and existing structures. Therefore, with normal strength concrete being the most common class of concrete in both categories, the mix design used in this program was based on normal strength concrete with no special additives. All specimens were made using the same concrete mix with a 28-day target strength of 35 MPa. With a maximum diameter of $d_a = 8$ mm, the coarse aggregates used in this study were small enough to avoid the wall effect. The specific gravity of coarse aggregates was equal to 2.69 at a saturated surface-dry condition and the fine aggregates were comprised of silica-based sand with a fineness modulus of 2.10. General purpose cement (type I Portland cement) was used as the only cementitious component of the concrete mix, while the water-to-cement ratio was selected as 0.55. Table 6.1 provides the material proportions of the concrete mixture used in this study.

6.2.2   Sample preparation

Samples were cast into plastic moulds. They were removed from their moulds after 24 hours and placed inside a curing tank where they would rest in lime-saturated water at a temperature of approximately 23°C. On day-7, samples were removed from the tank and were allowed to cure further in free air at room temperature until testing day. On approximately day-10, the two ends of the samples were ground for a smooth and parallel finish. Note that not all samples tested in this program were made from the same batch. Therefore, in order to ensure consistency between different batches, three samples were taken as control samples from each individual batch of concrete and tested simultaneously with the rest of the batch. The mechanical properties obtained from testing these control samples served as a reference to evaluate the consistency between different batches. They were also used to normalise the results of the rest of the batch.
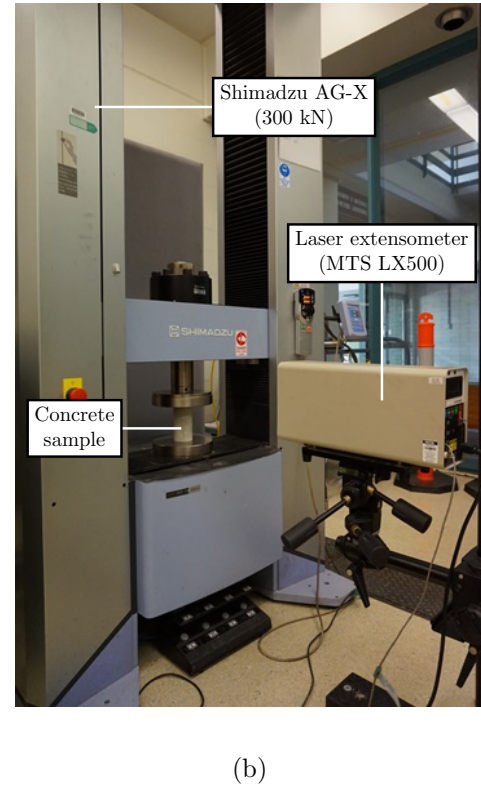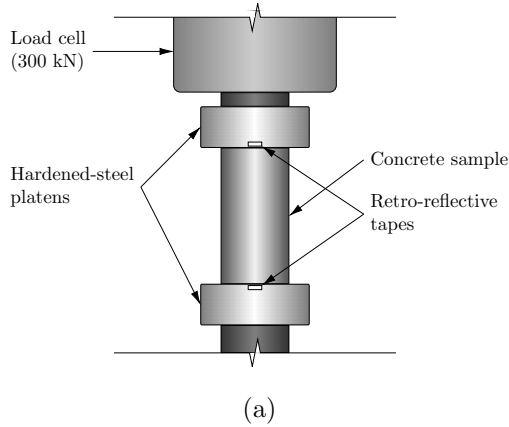
Figure 6.2: Test setup and the location of the retro-reflective tapes. (a) Schematics and (b) Laboratory setup.

6.2.3   Testing scheme

Samples were tested after 90 days of casting, whereby each test was repeated 4 times. A total of 144 samples were cast and tested by the end of the study.

The machine used for testing was a Shimadzu AG-X with a load capacity of 300 kN. Samples were loaded at a constant cross-head displacement rate of 0.1 mm/min which results in strain rates lower than $\dot{\epsilon} = 10^{-4}$ s^{-1}. Strains were recorded using a non-contact MTS laser extensometer (model LX500) with a resolution of $1 \, \mu$m.

Fig. 6.2 illustrates the schematics of the test setup used in this program. The relative displacement of the two hardened-steel platens was used to determine the overall longitudinal strain of the sample. This was achieved by targeting the laser extensometer towards the two retro-reflective tapes that were attached to the front of the platens (Fig. 6.2).

6.2.3.1   Phase 1. Induction of cyclic damage

In the first phase of the test, samples were subjected to cyclic loading in the same manner described by Sinaie et al. [12]. Loading was carried out in a displacement-controlled configuration, whereby the amplitude of the cycles was based on strain. It is pointed out later in Section 6.3 that the maximum strain experienced by the sample in this phase is taken as the measure of the level of cyclically-induced damage. The load history applied to the concrete samples involved 3 cycles of controlled straining up to a certain level of damage, followed by full unloading to near-zero stress. Stress and strain values were constantly logged and monitored during the experiments, and load reversals were administered using real-time measurements. Note that choosing the number of applied cycles to be equal to 3 was based on preliminary results and the effect of number of cycles is later discussed in Section 6.3.4.

6.2.3.2   Phase 2. Exposure to elevated temperature

In the second phase of the test, samples were exposed to elevated temperatures. Special care was taken in this stage so that the damage induced by temperature be more representative of the material itself and not depend on the size and shape of the sample. Therefore, it was important to achieve a state of uniform temperature within the volume of the sample, and at the same time, avoid any form of spalling.

Spalling can be due to many factors including high moisture and/or temperature gradients caused by rapid heating [29, 30]. Limiting these factors allows the damage to mainly be caused by chemical reactions and the thermal incompatibility of the mortar-aggregate structure. This was accomplished by taking the following measures:

- Selecting cylindrical specimens over cubic ones for uniform circumferential heat exposer and penetration.

- Using samples of 50-mm diameter to reduce the thermal gradient in the radial direction, without having to reduce the heating rate to very small values.

- Avoiding a rapid heating rate, as well as rapid cooling.

- Testing the samples after 90 days of casting for low moisture content.

(a) (b)

Figure 6.3: Laboratory setup for temperature exposure. (a) Environmental chamber and (b) placement of samples in groups of 7 inside the chamber.

As a result, spalling was not observed in any of the samples tested in this program.

Samples were exposed to elevated temperatures by means of an Instron environmental chamber (model 3119-408) with a maximum capacity of 600°C (Fig. 6.3). Target temperatures were 200, 300, 400, 500 and 600°C, while the heating rate was set to 10°C min^{-1}. Samples were placed inside the chamber in groups of 7, where one of the samples was used to monitor the inner and outer temperature (Fig. 6.4). Once the inner temperature of the sample (not the chamber) reached the target value, the temperature was kept constant for 60 minutes (Fig. 6.5). This 1 hour duration is usually used by researchers as a lower limit for the exposure time [19]. This seems reasonable given the uncertainties of a real fire and the duration of exposure before being extinguished. On the other hand, it has been shown by Wu and Wu [19] that for normal strength concrete, exposure durations above 1 hour have negligible effect on strength reduction. Therefore, a 60-minute exposure duration was selected in this program. After this 60-minute period, the heater was turned off and to avoid any thermal shock, the samples were allowed to slowly cool down to room temperature before opening the chamber. During this time, the temperature of the sample was logged by thermocouples on the surface and inside the specimen (Fig. 6.1).

It is worth pointing to Fig. 6.4 which shows the variation of temperature with time recorded from the two thermocouples depicted in Fig. 6.1. One thermocouple mea-
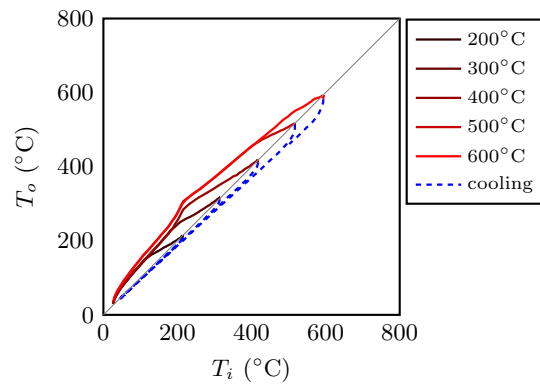
Figure 6.4: Centre temperature against surface temperature recorded by the thermocouples placed inside (T_i) and on the surface (T_o) of the sample.
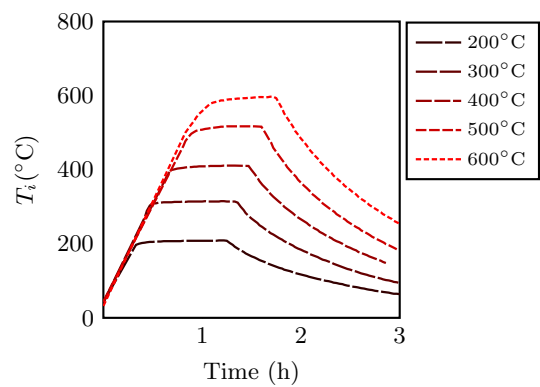
Figure 6.5: Variation of temperature with time.

sured the temperature on the surface of the sample, while the other was embedded inside the sample and measured the temperature at the centre.

6.2.3.3   Phase 3. Determination of residual properties

Residual mechanical properties of cooled-down samples were measured in this phase. This is accomplished by testing the samples under compression and recording the entire stress-strain response until failure. Loading was carried out under a constant rate of 0.1 mm/min which resulted in strain rates lower than $\dot{\epsilon} = 10^{-4}\,\mathrm{s}^{-1}$. Force values were directly accumulated from the machine, while strain values were recorded using the non-contact laser extensometer (MTS LX500) at a resolution of $1\,\mu\mathrm{m}$. Loading as well as data accumulation was continued at a frequency of 4 Hz until failure.

6.3   Results and discussion

The variation of mechanical properties are derived and presented in this section. The properties considered in this paper are depicted in Fig. 6.6, and are referred to as residual properties in the following discussions. These are denoted by the superscript r and include the residual peak stress f_c^r, peak strain ϵ_c^r, initial modulus E_c^r and $\epsilon_{0.5}^r$ which represents the post-peak strain at 50% peak stress $(0.5f_c')$. Also depicted in Fig. 6.6 is ϵ_u which is referred to as the unloading strain and represents the strain value at which loading is reversed. Note that results are presented in dimensionless form after being normalised by either f_c', ϵ_c' or E_c.

6.3.1   Effect of cyclic loading

Fig. 6.7 illustrates the typical response of concrete samples under cyclic loading. It has been argued that the unloading strain ϵ_u defined in Fig. 6.6 might not be the best choice as the independent damage index [10]. However, it has been shown by Sinaie et al. [12] that converting this definition of the damage index into other forms is possible and is simply a mathematical problem. Therefore, for the remainder of this study, the value of $\Delta\epsilon_c = \epsilon_u/\epsilon_c'$ is taken as the independent variable representing the level of cyclic damage that the material has sustained. When viewed as a two-
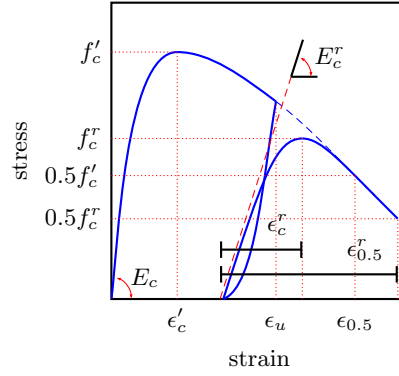
Figure 6.6: Definition of base and residual properties.
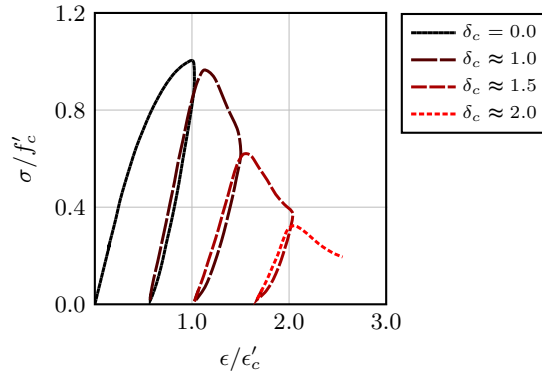
Figure 6.7: Typical cyclic response of concrete (strain and stress values have been normalised by ϵ_c' and f_c', respectively).

phase testing scheme, at any given state of the material, all the cycles leading to that state can be identified as the damage induction phase, while the subsequent response is viewed as the phase where residual properties are observed. This is illustrated in Fig. 6.7 and is also incorporated into Fig. 6.6 for the definition of mechanical properties.

Note that while cyclic loading is an integral part of the process, it is important to understand that cyclic parameters are not sought after in this study. The parameters that are of interest are those constituting the residual response of the material after it has been subjected to cyclic loading and elevated temperature. These include the residual values for peak stress f_c^r, peak strain ϵ_c^r, initial modulus E_c^r and the post-peak strain $\epsilon_{0.5}^r$ at 50% peak stress $0.5f_c^r$, all of which are depicted in Fig. 6.6. Note that in this figure, the values of ϵ_c^r and $\epsilon_{0.5}^r$ are measured from the onset of the residual response. Doing this establishes a direct correspondence between base properties and residual properties and hence, allows us to utilise the same stress-

strain equation with different parametric values for both cases.

In regards to the micro-mechanical development of damage in concrete samples under quasi-static loading [31], the process of crack formation and crack propagation is summarise in the following. This summary is later used to interpret the experimental observations in subsequent sections.

- At zero load conditions, micro cracks exist within the material, especially at the interfacial transition zone (ITZ).

- Up to $0.3f_c$, ITZ micro-cracks are stable.

- Up to $0.7 - 0.9f'_c$, ITZ cracks increase in length, width and number. Over this range of loading, cracks also begin to form in the mortar, bridging the ITZ cracks together.

- Over $0.7 - 0.9f'_c$ (close to the peak load), cracks propagate at a faster rate and are unstable. At this point, failure can occur, even if the load is maintained at a constant value.

Fig. 6.8 shows the variation of the residual properties as a function of $\Delta\epsilon_c = \epsilon_u/\epsilon'_c$ at room temperature.

It is seen from Fig. 6.8a that the residual peak stress f^r_c does not show any significant change as long as $\Delta\epsilon_c < 1.0$, but tends to drop as the damage level increases beyond $\Delta\epsilon_c \geq 1.0$. This can be explained by the fact that for $\Delta\epsilon_c < 1.0$, micro-cracking is mostly at the ITZ and in a stable state (below $0.7 - 0.9f'_c$). Studies have shown that ITZ cracks are not a defining factor in the compressive strength of concrete samples [31]. Therefore, it is reasonable to say that f^r_c is not influenced by the level of damage while $\Delta\epsilon_c < 1.0$.

On the other hand, the propagation of cracks, either through ITZ or the mortar matrix, directly affects the stiffness of the material. This explains the reduction of the residual modulus E^r_c starting at $\Delta\epsilon_c \approx 0.7$, where initial micro-cracks start to increase in length and number. As damage passes the peak state ($\Delta\epsilon_c > 1.0$), cracks propagate at a faster rate and so the residual modulus drops at a higher rate (Fig. 6.8b).

The value of the residual peak strain ϵ^r_c depends on the residual strength f^r_c and

Figure 6.8: Variation of residual properties against damage level without exposure to elevated temperatures. (a) Residual strength, (b) initial modulus, (c) peak strain and (d) post-peak strain at 50% peak stress.

modulus E_c^r. Therefore, it also starts to drop before $\Delta\epsilon_c = 1$ and continues to drop as the damage level progresses. This is observed in Fig. 6.8c.

Finally, the post-peak strain $\epsilon_{0.5}^r$ at 50% peak stress $0.5 f_c^r$ is an indication of the level of post-peak localisation in the specimen. It is stated in the literature that the softening part of the stress-strain curve is a structural property, meaning that it is highly dependent on the size, the shape and the boundary conditions of the sample being tested [32]. Since the size, shape and end conditions of samples do not change for different levels of damage, the $\epsilon_{0.5}^r/\epsilon_c^r$ ratio tends to remain constant over the entire range of $\Delta\epsilon_c$ (Fig. 6.8d).

6.3.2 Effect of temperature exposure

Fig. 6.9 shows the variation of residual properties against temperature. Note that this figure shows the results from samples that have not been subjected to any cyclic loading. The values are measured after an original sample has been exposed to a target temperature for 60 minutes and then allowed to slowly cool down to room temperature (Fig. 6.5). The results are in agreement with those reported by other researchers, for example [16].

Among different factors, heating rate and peak temperature are the two which have a significant influence on the residual properties. From the literature [15–17], the progression of damage caused by temperature can be summarised as:

- Starting at around 110°C, the paste begins to dehydrate where the chemically bound water is released from the calcium silicate hydrate (CSH). At the same time, the thermal incompatibility of cement paste and aggregate causes internal stresses to take form.

- Once the temperature passes 300°C, micro-cracks begin to form at the ITZ causing degradation of strength and stiffness. From this stage on, strength loss is irreversible.

- In the range of $400 - 800$°C, calcium hydroxide decomposes into calcium oxide and water, causing major strength reduction. If the material is allowed to cool down from this state, calcium oxide will absorb water, whereby the expansion will cause the already formed cracks to open further and lead to additional
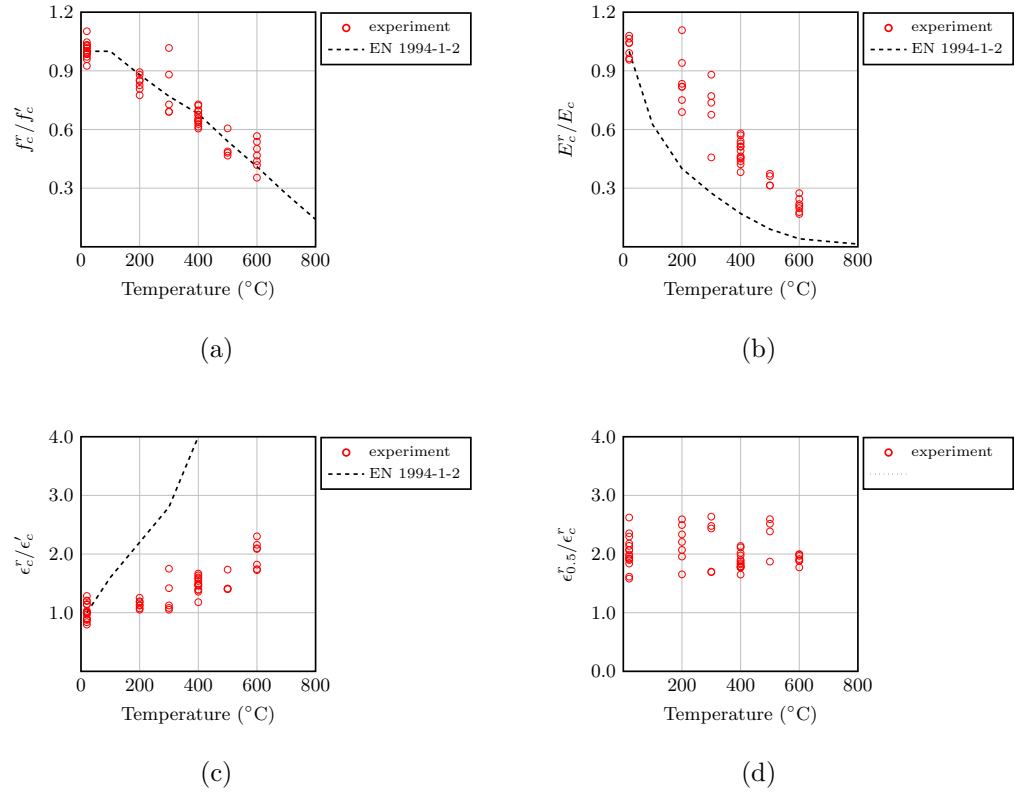
Figure 6.9: Variation of residual properties against temperature. (a) Residual strength, (b) initial modulus, (c) peak strain and (d) post-peak strain at 50% peak stress.

strength loss.

Fig. 6.9a shows that the residual strength f_c^r tends to drop as the temperature rises. The reduction is observed to start from the very beginning of temperature rise and therefore, can be attributed to the dehydration of the cement paste as well as cracks caused by thermal incompatibility of the paste/aggregate structure. Also shown in this figure is the variation of the residual strength given by EN 1994-1-2 [33].

The residual modulus E_c^r also tends to decrease as the temperature rises (Fig. 6.9b). Moreover, the reduction seems to take place at a higher rate, as the temperature passes $200-300°$C. As mentioned before, the stiffness of concrete is highly influenced by existing micro-cracks. Therefore, the formation of micro-cracks at temperatures above $300°$C can account for the increasing rate of reduction at this temperature (Fig. 6.9b). This figure also compares the experiments results with the values derived from EN 1994-1-2 [33].

It is observed from Fig. 6.9c that the residual peak strain ϵ_c^r increases as the temperature rises. This can be justified by correlating the variation of ϵ_c^r with the rate at which residual strength f_c^r and residual modulus E_c^r decrease. With the value of E_c^r dropping at a higher rate than f_c^r, the residual peak strain ϵ_c^r has the tendency to increase. This figure shows a significant difference between test results and the values suggested by EN 1994-1-2 [33]. Such difference has been reported by other researchers as well [16].

Fig. 6.9d shows that the $\epsilon_{0.5}^r/\epsilon_c^r$ ratio tends to remain constant as the temperature rises. This means $\epsilon_{0.5}^r$ changes at the same rate as ϵ_c^r. As before, this can be justified by the fact that $\epsilon_{0.5}^r/\epsilon_c^r$ is a result of the size, shape and end conditions of the samples, and therefore, does not show significant variation as long as the experimental setup is the same.

6.3.3   Effect of temperature exposure on cyclically-damaged samples

This section deals with the residual properties of samples that have been subjected to cyclic damage before being exposed to elevated temperatures. The results are shown in Fig. 6.10 where the variation of residual properties is presented in terms of the damage level $\Delta\epsilon_c$ and the target temperature T. These variations are discussed
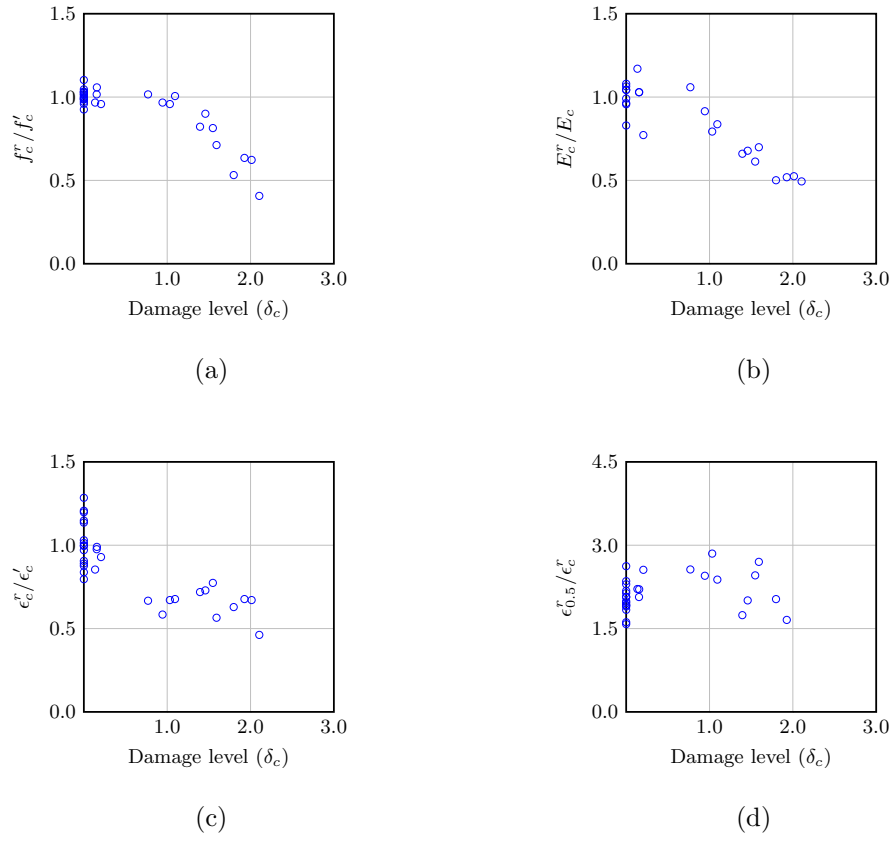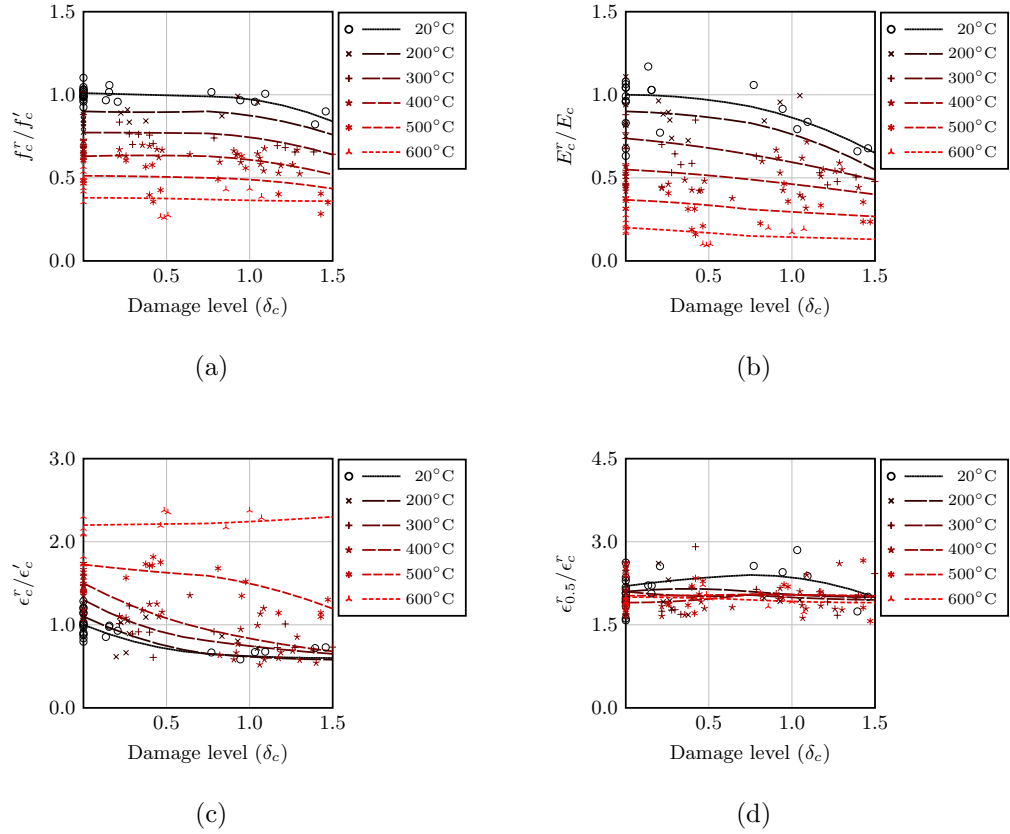
Figure 6.10: Variation of residual properties against damage level $\Delta\epsilon_c$ and temperature T. (a) Residual strength, (b) initial modulus, (c) peak strain and (d) post-peak strain at 50% peak stress.

in terms of the damage progression summarised in the previous sections.

Fig. 6.10a shows the variation of the residual strength against $\Delta\epsilon_c$ and T. Regardless of temperature, reduction in strength appears to take place only when the damage index is greater than 1.0. However, at higher values of T, the effect of $\Delta\epsilon_c$ on the residual strength diminishes. As a result, at a temperature of 600°C, residual strength f_c^r seems to remain constant over the entire range of $\Delta\epsilon_c$. It can be concluded that for any given level of damage $\Delta\epsilon_c$, there exists a certain temperature whereby the strength reduction caused by dehydration of the paste and internal thermal cracks surpasses the previously induced cyclic damage.

The variation of the residual modulus E_c^r against $\Delta\epsilon_c$ and T is presented in Fig. 6.10b. These results indicate that the stiffness of the material tends to drop as the cyclically-induced damage level $\Delta\epsilon_c$ and/or temperature T increase. Considering the origins of mechanical and thermal damage, the results indicate that material degradation due to temperature exposure accumulates with cyclically induced damage, resulting in an accumulation of stiffness reduction. However, similar to the variation of the

residual strength f_c^r, the effect of $\Delta\epsilon_c$ on E_c^r diminishes as higher temperature are reached.

Fig. 6.10c shows the variation of residual peak strain ϵ_c^r against $\Delta\epsilon_c$ and T. The individual effect of cyclic damage $\Delta\epsilon_c$ (Fig. 6.8c) and temperature T on the residual peak strain ϵ_c^r (Fig. 6.9c) act in opposite directions, with the former having a direct relation and the latter having an inverse relation. This results in a non-uniform trend in the variation of ϵ_c^r. Therefore, for any given temperature below 500°C, the residual peak strain decreases as the damage index $\Delta\epsilon_c$ attains higher values. On the other hand, at a temperature of 600°C, the residual peak strain increases as the damage level $\Delta\epsilon_c$ increases. However, more importantly, in view of the sequence of the events acting on the material (temperature exposure being after cyclic loading), it can be concluded that once the level of damage $\Delta\epsilon_c$ is ascertained, the residual peak strain monotonically increases as the temperature T increases.

The variation of the post-peak strain $\epsilon_{0.5}^r$ against $\Delta\epsilon_c$ and T is illustrated in Fig. 6.10d. The results given in this figure imply that the damage level $\Delta\epsilon_c$ and temperature T have no significant effect on $\epsilon_{0.5}^r$. This is reasonable given the fact that the individual effects of $\Delta\epsilon_c$ and T on $\epsilon_{0.5}^r$ were also insignificant (Figs. 6.8d and 6.9d).

6.3.4 Effect of number of cycles

It was pointed out in Section 6.2.3.1 that samples were subjected to 3 cycles of controlled straining during the first phase of the experiment. In order to determine the effect of number of cycles on the residual properties, a preliminary study was carried out where the variable was the number of cycles. The number of cycles were taken to be $n = 1$, 3 and 9 which cover the range expected from typical structures under earthquake loading [34]. In addition, the damage level was selected as $\Delta\epsilon_c = 1.0$ and the temperature was set to $T = 400$°C. Table 6.2 shows the results obtained from these tests. While there seems to be a slight decrease in residual properties as the number of cycles increases, the variation is negligible compared to the effect of $\Delta\epsilon_c$ and T. These tests were carried out prior to the main experiments. With this knowledge, the number of cycles was not studied any further and the main tests only involved 3 cycles of loading ($n = 3$).

Table 6.2: Effect of number of cycles ($n = 1, 3, 9$) on residual properties. Values correspond to $\Delta\epsilon_c = 1.0$ and $T = 400°C$.

n	f_c^r/f_c'	E_c^r/E_c	ϵ_c^r/ϵ_c'	$\epsilon_{0.5}^r/\epsilon_{0.5}$
1	0.603	0.467	0.823	2.175
3	0.609	0.463	0.806	2.044
9	0.591	0.448	0.783	1.952

6.3.5 Numerical representation of residual properties as a function of $\Delta\epsilon_c$ and T

In order to use the results of this study (Section 6.3.3) in a structural model, a numerical expression is required to calculate the value of each residual mechanical property for any given value of the damage level $\Delta\epsilon_c$ and temperature T. In a previous paper, the authors demonstrated the advantages of using Bézier formulations to represent the variation of mechanical properties of mild steel as a function of temperature and damage [8]. The same methodology is implemented for this study. Numerous articles exist regarding the properties of Bézier curves and its applications, especially in relation to computer aided design [35]. Therefore, only the fundamentals are presented here.

A three-dimensional Bézier curve can be expressed by:

$$\vec{\mathbf{B}}(t_1, t_2) = \sum_{i=0}^{n} \sum_{j=0}^{m} F_i^n(t_1) F_j^m(t_2) \vec{\mathbf{P}}_{ij} \tag{6.1}$$

which maps the unit square of $m+1$ by $n+1$ control points onto a smooth curved surface. In Eq. (6.1), $t_1, t_2 \in [0, 1]$ are local coordinates and $\vec{\mathbf{P}}_i = (p_{ix}, p_{iy})$ represents the control points. In addition, $F_k^n(t)$ is known as a Bernstein basis polynomial and is defined as:

$$F_k^n(t) = \frac{n!}{k!(n-k)!} t^k (1-t)^{n-k} \tag{6.2}$$

An example of a 3-dimensional curve is illustrated in Fig. 6.11. In this figure, the control points are either *end*-type control points (blue cubes), or *intermediate*-type
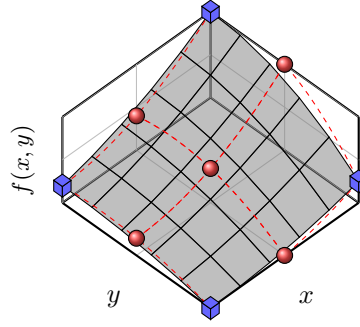
Figure 6.11: A 3 by 3 Bézier curve in 3D space. Blue cubes represent end-type control points while red spheres are intermediate-type control points.

control points (red spheres). End control points dictate where the curve passes, while intermediate control points determine the slope of the cure. If control points are equally spaced as in Fig. 6.11, the local coordinates t_1 and t_2 of Eq. (6.1) simplify to the following values in their corresponding range of damage $\Delta\epsilon_c$ and temperature T.

$$t_1 = \frac{(\Delta\epsilon_c)_{i+1} - (\Delta\epsilon_c)}{(\Delta\epsilon_c)_{i+1} - (\Delta\epsilon_c)_i} \quad \text{and} \quad t_2 = \frac{(T)_{i+1} - (T)}{(T)_{i+1} - (T)_i} \tag{6.3}$$

Further details regarding the usage of Eq. (6.1) and the actual interpolation algorithms can be found in [8] and will not be repeated here. Once the underlying algorithms are established, one only needs to define the control points representing the curve. Table 6.3 contains the control points used for the residual strength f_c^r. These control points have been used alongside Eq. (6.1) to produce the three-dimensional plot of f_c^r against $\Delta\epsilon_c$ and T shown in Fig. 6.12a.

Using the same approach, the variation of the remaining residual mechanical properties are calculated and given in Figs. 6.12b–d. It should be noted that the trend-lines previously illustrated in Fig. 6.10 were derived from the three dimensional curves of Fig. 6.12. Those trend-lines are simply iso-temperature curves extracted from Eq. (6.1) by setting the temperature variable equal to 20, 200, 300, 400, 500 and 600°C.

Table 6.3: Control points used for f_c^r/f_c'. *End*-type control points (in bold) have the coordinates $T = 20, 200, 400, 600°C$ and $\Delta\epsilon_c = 0.0, 0.5, 1.0, 1.5$. The remaining control points are of *intermediate* type.

$T(°C)$	$\Delta\epsilon_c$						
	0.00	0.25	0.50	0.75	1.00	1.25	1.50
20	**1.00**	1.00	**0.99**	0.98	**0.97**	0.97	**0.96**
110	0.98	0.99	0.99	0.97	0.95	0.93	0.91
200	**0.97**	0.97	**0.96**	0.95	**0.93**	0.92	**0.90**
300	0.80	0.79	0.77	0.75	0.73	0.72	0.71
400	**0.65**	0.65	**0.64**	0.64	**0.63**	0.62	**0.61**
500	0.52	0.52	0.51	0.50	0.48	0.44	0.40
600	**0.50**	0.46	**0.36**	0.36	**0.37**	0.38	**0.38**

(a)

(b)

(c)

(d)
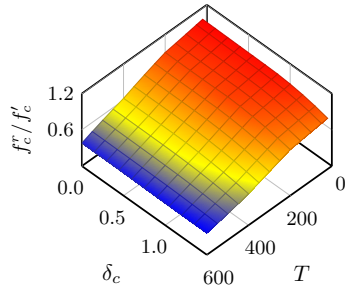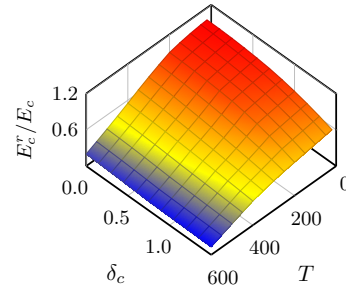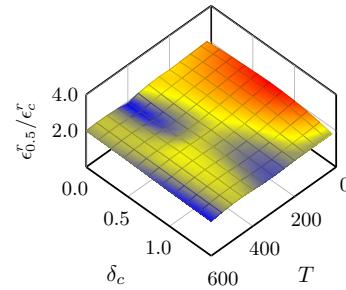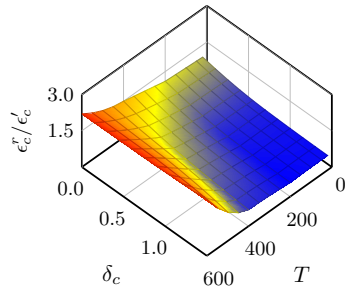
Figure 6.12: Bézier curves for the representation of residual mechanical properties against damage level $\Delta\epsilon_c$ and temperature T. (a) Residual strength, (b) initial modulus, (c) peak strain and (d) post-peak strain at 50% peak stress.

Table 6.4: Variables in Eq. (6.4) for damage level $\Delta\epsilon_c = 0.0$ (Fig. (6.13a)).

$T(°C)$	$E_c \times \left(\dfrac{\epsilon'_c}{f'_c}\right)$	$\dfrac{\epsilon_{0.5}}{\epsilon'_c}$	$\beta_1\,(\epsilon \le \epsilon'_c)$	$\beta_1\,(\epsilon > \epsilon'_c)$
20	3.216	2.3	0.367	1.942
200	2.894	2.4	0.343	2.318
400	1.739	2.8	0.280	2.538
600	0.643	4.2	0.457	2.808

6.3.6 Residual stress-strain curves

The stress-strain relationship proposed by Yang et al. [36] is used for the means of this study. This relationship is defined as:

$$\sigma = \frac{(\beta_1 + 1)\left(\dfrac{\epsilon}{\epsilon'_c}\right)}{\left(\dfrac{\epsilon}{\epsilon'_c}\right)^{\beta_1+1} + \beta_1} f'_c \tag{6.4}$$

where the value of β_1 is attained by solving the following equation:

$$\begin{cases} 0.4(X_a)^{\beta_1+1} + (0.4 - X_a)\beta_1 - X_a = 0 & ,\epsilon \le \epsilon'_c \\ (X_d)^{\beta_1+1} + (1 - 2X_d)\beta_1 - sX_d = 0 & ,\epsilon > \epsilon'_c \end{cases} \tag{6.5}$$

with $X_a = 0.4f'_c/E_0\epsilon'_c$ and $X_d = \epsilon_{0.5}/\epsilon'_c$.

Table 6.4 gives the values of the parameters of Eq. (6.4) used for the calculation of the stress-strain curves shown in Fig. 6.13a. This figure (Fig. 6.13a) illustrates the calculated stress-strain variations in comparison to those obtained from experiment for a damage level of $\Delta\epsilon_c = 0.0$ and temperatures of 20, 200, 400 and 600°C. Similarly, Figs. 6.13b–d show the stress-strain curve for damage levels of $\Delta\epsilon_c = 0.5$, 1.0 and 1.5. The close agreement between numerically evaluated stress-strain curves and experimental ones indicates the effectiveness of Eq. (6.4) in simulating the response, once the mechanical properties are evaluated through the utilisation of Bézier curves.
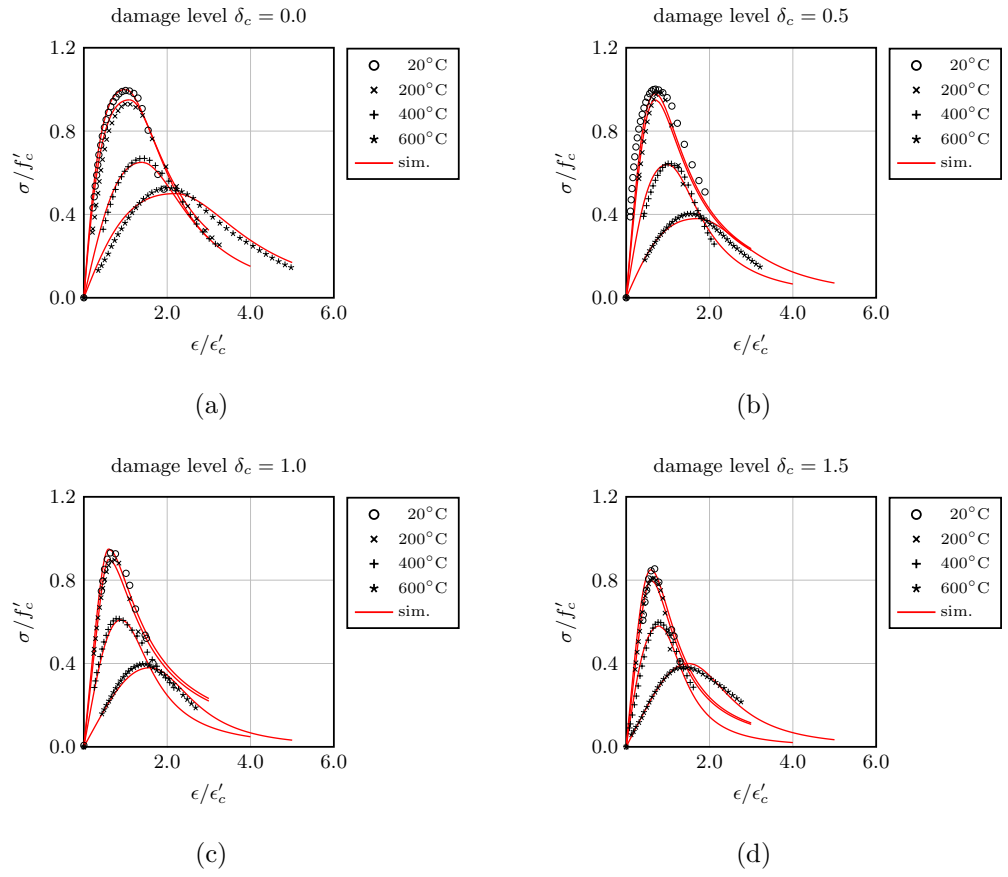
Figure 6.13: Numerical simulation of stress-strain curves using residual properties calculated by Bézier formulation as input values for Eq. 6.4.

6.4 Conclusions

This research investigates the effect of temperature exposure on concrete samples that have previously been subjected to cyclic loading. For this purpose, cylindrical samples were cast and tested over a 3-phase program. Phase 1 comprised of subjecting samples to cyclic loading. In phase 2, damaged samples were exposed to a target temperature for 60 minutes and then allowed to slowly cool down. Phase 3 was the final phase, where the residual properties of the damaged samples were attained through compression tests. The following conclusions can be drawn from the results:

1. Under cyclic loading alone, all residual properties decrease in value except for $\epsilon_{0.5}^r$ which remains constant. The variations are explained in the text through the progression of cracks and micro-cracks under mechanical loading.

2. Under temperature exposure alone, f_c^r and E_c^r deteriorate, while ϵ_c^r increases in value and $\epsilon_{0.5}^r$ remains constant. These variations can be explained by available knowledge on chemical degradation and thermal stresses caused by high temperature.

3. When the two events (cyclic loading and temperature exposure) act in sequence, the variation of the residual properties becomes a function of both parameters ($\Delta\epsilon_c$ and T). However, these variations can still be explained in the context of each individual event.

4. Given the sequence of events (cyclic damage and then temperature exposure), it is interesting to note that once the level of damage is determined, under increasing temperature, f_c^r and E_c^r degrade, while ϵ_c^r increases and $\epsilon_{0.5}^r$ has negligible variation.

5. As the temperature attains higher values, its effect begins to dominate over the effect of pre-induced damage.

6. Bézier formulations are demonstrated to be capable of evaluating residual properties in terms of the two independent variables $\Delta\epsilon_c$ and T.

7. The stress-strain equation developed by Yang et al. [36], when combined with Bézier formulations, is shown to produce accurate results for any given $\Delta\epsilon_c$

and T in the tested range.

8. While the present study allows for a qualitative and quantitative understanding of the subject matter, carrying out experiments under hot conditions (without cooldown) will extend this understanding and is recommended for future research. Investigating the effect of higher temperatures (above 600°C) as well as heating and cooling rates can also give more insight into the subject.

9. In addition to further experimental investigations, the authors also believe that a better understanding on the subject can be attained through numerical discrete element simulations.

Acknowledgement

References

[1] Shahab Mousavi, Ashutosh Bagchi, and Venkatesh KR Kodur. Review of post-earthquake fire hazard to building structures. *Canadian Journal of Civil Engineering*, 35(7):689–698, 2008.

[2] Takeyoshi Tanaka. Characteristics and problems of fires following the great east japan earthquake in march 2011. *Fire Safety Journal*, 54:197–202, 2012.

[3] Raul Zaharia and Dan Pintea. Fire after earthquake analysis of steel moment resisting frames. *International Journal of Steel Structures*, 9(4):275–284, 2009.

[4] R Imani, G Mosqueda, and M Bruneau. Experimental study on post-earthquake fire resistance of ductile concrete-filled double-skin tube columns. *Journal of Structural Engineering*, page 04014192, 2014.

[5] Mehrdad Memari, Hussam Mahmoud, and Bruce Ellingwood. Post-earthquake fire performance of moment resisting frames with reduced beam section connections. *Journal of Constructional Steel Research*, 103:215–229, 2014.

[6] Qian-Yi Song, Amin Heidarpour, Xiao-Ling Zhao, and Lin-Hai Han. Post-earthquake fire behavior of welded steel I-beam to hollow column connections: An experimental investigation. *Thin-Walled Structures*, 2015. doi: 10.1016/j.tws.2015.03.032.

[7] Sina Sinaie, Amin Heidarpour, and Xiao-Ling Zhao. Mechanical properties of cyclically-damaged structural mild steel at elevated temperatures. *Construction and Building Materials*, 52:465–472, 2014.

[8] Sina Sinaie, Amin Heidarpour, and Xiao-Ling Zhao. Stress–strain–temperature relation for cyclically-damaged structural mild steel. *Engineering Structures*, 77:84–94, 2014.

[9] Sina Sinaie, Amin Heidarpour, and Xiao-Ling Zhao. A multi-objective optimization approach to the parameter determination of constitutive plasticity models for the simulation of multi-phase load histories. *Computers & Structures*, 138:112–132, 2014.

[10] Jose Fernando Sima, Pere Roca, and Climent Molins. Cyclic constitutive model for concrete. *Engineering Structures*, 30(3):695–706, 2008.

[11] Edison Osorio, Jesús M Bairán, and Antonio R Marí. Lateral behavior of concrete under uniaxial compressive cyclic loading. *Materials and structures*, 46(5):709–724, 2013.

[12] Sina Sinaie, Amin Heidarpour, Xiao-Ling Zhao, and Jay G Sanjayan. Effect of size on the response of cylindrical concrete samples under cyclic loading. *Construction and Building Materials*, 84:399–408, 2015.

[13] W Nechnech, Fkri Meftah, and Jean M Reynouard. An elasto-plastic damage model for plain concrete subjected to high temperatures. *Engineering structures*, 24(5):597–611, 2002.

[14] Bibiana M Luccioni, MI Figueroa, and Rodolfo F Danesi. Thermo-mechanic model for concrete exposed to elevated temperatures. *Engineering Structures*, 25(6):729–742, 2003.

[15] Kristian Dahl Hertz. Concrete strength for fire safety design. *Magazine of Concrete Research*, 57(8):445–453, 2005.

[16] Yun-Fei Chang, Yih-Houng Chen, Maw-Shyong Sheu, and George C Yao. Residual stress–strain relationship for concrete after exposure to high temperatures. *Cement and Concrete Research*, 36(10):1999–2005, 2006.

[17] Omer Arioz. Effects of elevated temperatures on properties of concrete. *Fire Safety Journal*, 42(8):516–522, 2007.

[18] MA Youssef and M Moftah. General stress–strain relationship for concrete at elevated temperatures. *Engineering structures*, 29(10):2618–2634, 2007.

[19] Yaopeng Wu and Bo Wu. Residual compressive strength and freeze–thaw resistance of ordinary concrete after high temperature. *Construction and Building Materials*, 54:596–604, 2014.

[20] Minho Yoon, Gyuyong Kim, Gyeong Choel Choe, Youngwook Lee, and Taegyu Lee. Effect of coarse aggregate type and loading level on the high temperature properties of concrete. *Construction and Building Materials*, 78:26–33, 2015.

[21] Yue Zhai, Zichen Deng, Nan Li, and Rui Xu. Study on compressive mechanical capabilities of concrete after high temperature exposure and thermo-damage constitutive model. *Construction and Building Materials*, 68:777–782, 2014.

[22] Mahsa Mirmomeni, Amin Heidarpour, Xiao-Ling Zhao, Christopher R Hutchinson, Jeffrey A Packer, and Chengqing Wu. Mechanical properties of partially damaged structural steel induced by high strain rate loading at elevated temperatures–an experimental investigation. *International Journal of Impact Engineering*, 76:178–188, 2015.

[23] Sajjad Hosseini, Amin Heidarpour, Frank Collins, and Christopher R Hutchinson. Effect of strain ageing on the mechanical properties of partially damaged structural mild steel. *Construction and Building Materials*, 77:83–93, 2015.

[24] Fatemeh Azhari, Amin Heidarpour, Xiao-Ling Zhao, and Christopher R Hutchinson. Mechanical properties of ultra-high strength (grade 1200) steel tubes under cooling phase of a fire: An experimental investigation. *Construction and Building Materials*, 2015.

[25] Fatemeh Javidan, Amin Heidarpour, Xiao-Ling Zhao, and Jussi Minkkinen. Performance of innovative fabricated long hollow columns under axial compression. *Journal of Constructional Steel Research*, 106:99–109, 2015.

[26] Mohammad Nassirnia, Amin Heidarpour, Xiao-Ling Zhao, and Jussi Minkkinen. Innovative hollow corrugated columns: A fundamental study. *Engineering Structures*, 94:43–53, 2015.

[27] Qianmin Ma, Rongxin Guo, Zhiman Zhao, Zhiwei Lin, and Kecheng He. Mechanical properties of concrete at high temperaturea review. *Construction and Building Materials*, 93:371–383, 2015.

[28] Mihail Petkovski. Effects of stress during heating on strength and stiffness of concrete at elevated temperature. *Cement and Concrete Research*, 40(12): 1744–1755, 2010.

[29] Grard Debicki, R Haniche, and Fabien Delhomme. An experimental method for assessing the spalling sensitivity of concrete mixture submitted to high temperature. *Cement and Concrete Composites*, 34(8):958–963, 2012.

[30] Kristian Dahl Hertz. Limits of spalling of fire-exposed concrete. *Fire Safety Journal*, 38(2):103–116, 2003.

[31] Tülin Akçaoğlu, Mustafa Tokyay, and Tahir Çelik. Effect of coarse aggregate size and matrix quality on itz and failure behavior of concrete under uniaxial compression. *Cement and Concrete Composites*, 26(6):633–638, 2004.

[32] Jan GM Van Mier, Surendra P Shah, M Arnaud, JP Balayssac, A Bascoul, S Choi, D Dasenbrock, G Ferrara, C French, ME Gobbi, et al. Strain-softening of concrete in uniaxial compression. *Materials and Structures*, 30(4):195–209, 1997.

[33] *Eurocode 4: Design of composite steel and concrete structures Part 1-2: General rules - Structural fire design, EN 1994-1-2.* European committee for Standardization, 2005.

[34] Tony F Zahrah and William J Hall. Earthquake energy absorption in sdof structures. *Journal of structural Engineering*, 110(8):1757–1772, 1984.

[35] Przemysław Gospodarczyk. Degree reduction of bézier curves with restricted control points area. *Computer-Aided Design*, 62:143–151, 2015.

[36] Keun-Hyeok Yang, Ju-Hyun Mun, Myung-Sug Cho, and Thomas H-K Kang. Stress-strain model for various unconfined concretes in compression. *ACI Structural Journal*, 111(1-6), 2014.

A micro-mechanical parametric study on the strength degradation of concrete using a 2-phase discrete element model

Contents

Monash University

Declaration for Thesis Chapter 7

Declaration by candidate

In the case of Chapter 7, the nature and extent of my contribution to the work was the following:

Nature of contribution	Extent of contribution (%)
Development of ideas, Development of original computer model, Model verification and validation, Data analysis, Write-up and revision	70%

The following authors contributed to the work. If co-authors are students at Monash University, the extent of their contribution in percentage terms must be stated.

Name	Nature of contribution	Extent of contribution (%)
Dr. Amin Heidarpour	Developing ideas Revision Financial support	
Prof. Xiao-Ling Zhao	Revision Financial support	

The undersigned hereby certify that the above declaration correctly reflects the nature and extent of the candidate's and co-authors' contributions to this work.

Candidate's signature: ■■■■■ **Date:** 24/09/2015

Main supervisor's signature: ■■■■■ **Date:** 24/09/2015

Abstract

The present paper investigates the extent of damage caused by temperature on concrete samples. This is accomplished by a parametric approach using a 2-phase discrete element model which incorporates temperature as a global variable. Two main factors of concrete degradation have been focused on in this study: the thermal incompatibility of the aggregates-mortar composite and the degradation of the bonds between the particles. The base models of this parametric study are created using concrete specimens tested in the laboratory after been exposed to elevated temperatures. Using these base models, the coefficient of thermal expansion (CTE) of aggregate and mortar particles are varied independently and the assembly is subjected to an increasing temperature. The residual strength of the thermally-cracked assembly is then determined under compressive loading. The results of 72 different combinations of the CTE show the extent of damage that can be induced due to the thermal incompatibility of the particles. The variation of residual strength and residual stiffness are discussed in terms of the number of inter-particle bonds that break under rising temperature.

Keywords

Concrete; Discrete element; 2-phase model; Temperature; Thermal incompatibility

7.1 Introduction

The mechanical changes that concrete experiences under increasing temperatures have been investigated by many researchers. Zhai et al. [1] investigated the properties of concrete samples after being exposed to high temperatures (up to 1200°C). Their results show that chemical and physical changes take place in both the cement paste and the aggregates and that the changes are of different nature at different levels of temperature. At the same time, the experiments conducted by Wu and Wu [2] imply that up to a temperature of 600°C and over a duration of 1-6 hours, the extent of strength degradation is almost independent of the duration of exposure. Ergun et al. [3] have reported that strength reduction caused by high temperature is independent of the cement dosage used in the mix design.

Arioz [4] also reported that the water-cement ratio has negligible effect on the relative strength reduction. However, the results show that the extent of degradation is affected by the type of aggregate used in the concrete mix. This can be the result of the mineral structure of the aggregates as well as the thermal expansion of the

aggregates. In fact, thermal incompatibility of the cement paste and aggregates is considered a main factor causing degradation at elevated temperatures [5, 6]. The experiments carried out by Yoon et al. [6] indicate that the strength degradation of concrete made from lightweight aggregate is less than that of normal aggregate. This has been attributed to the fact that normal aggregate has a higher thermal expansion coefficient compared to light-weight aggregate. Therefore, strength degradation of concrete is not only a result of the decomposition of cement hydration products, but is also influenced by the micro-cracks which develop due to the difference between the coefficient of thermal expansion (CTE) of the paste and that of the aggregates. Fu et al. [7] investigated the variations of CTE for cement and mortar samples as the temperature increases from room temperature to 500°C. Their results show that the CTE of mortar samples is rather constant over this range. At the same time, the tests conducted by Odelson et al. [8] on cement paste indicate that stiffness degradation primarily occurs before the temperature reaches 200°C, whereby they concluded that the primary mechanism of this reduction is microcracking. They suggested that this microcracking is a product of water expansion and evaporation and that the effect of chemical degradation is insignificant once these micro-cracks have formed.

When it comes to simulating the effect of temperature on concrete material, various models have been proposed, each focusing on different aspects of temperature effects. Tenchev and Purnell [9] developed a damage constitute model to simulate the behaviour of concrete at high temperatures. Their model incorporated the effect of transient creep, heat transfer and pore pressure in the simulations. Gernay et al. [10] created a 3-dimensional thermomechanical model for concrete by coupling plasticity and damage theories. Gawin et al. [11, 12] studied the importance of different parameters in the simulation of a concrete wall exposed to high temperatures. Xotta et al. [13] used the finite element method to create a meso-scale model of the interactions between aggregates and the hydrated cement paste. They used their model to study the damage evolution of concrete under high temperatures.

Over the last decade, with the increasing processing power of computers, the discrete element method has been extensively used to predict the macro-scale properties of concrete which originate from micro-scale interactions. Nitka and Tejchman [14] utilised the discrete element method to simulate the response of concrete under compression and tension. They investigated many aspects of this method, including the effect of minimum particle size, the relation between 2D and 3D assemblies and the advantages of multi-phase models over single-phase models. Javidan et al. [15] use a lattice discrete particle model to simulate the failure of concrete blocks under

different loading scenarios. Onate et al. [16] also implemented the discrete element method to simulate concrete behaviour. Using experimental results, they carried out simulations on cement and concrete samples. They also demonstrated the advantage of parallel computing in reducing the analysis time of large particle assemblies. Tran et al. [17] applied the discrete element method to model concrete samples under triaxial loading. Azevedo et al. [18] carried out discrete element simulations on 2D models in tension and compression. They used a two-phase interaction model between aggregate particles and cement matrix particles. They concluded that aggregate deformability, ductile tensile rupture and pure friction under compression cause the fracture energy to increase and therefore, allow a more accurate simulation of concrete behaviour, especially over the post-peak range. Rojek et al. [19] studied the difference of using localised interaction parameters for pairing particles as opposed to a global set of parameters applying to all the particles in the assembly. They demonstrated that as the heterogeneity of the material increases, a global set of parameters cannot be used for all of the particles, and the interaction parameters between two particles should be set according to the geometry of the two particles that are being paired.

Many researchers have pointed to the importance of the coefficient of thermal expansion in relation to strength degradation of concrete under high temperatures [4–6, 13]. However, there still exists a lack of knowledge on the extent of damage caused by what is called 'thermal incompatibility' between the different components of concrete material. The present study looks into the thermal incompatibility of the constituents of concrete and its effect on the evolution of damage as the temperature increases. This damage is simultaneously coupled with the damage induced in the material by chemical dehydration, whereby the residual mechanical properties of the concrete sample is determined after cooldown. To perform these simulations, a discrete element program is developed based on a 2-phase model which distinguishes between particles representing the aggregates and the ones that represent the mortar matrix. This study is part of a series of investigations currently being carried out at Monash University on extreme events involving fire effects on civil structures [20–24].

7.2   Two-phase discrete element model

In contrast to single-phase models [16, 17] where all particles are taken to be of the same material, this study makes a distinction between particles representing aggre-

gates and those representing the mortar matrix. This 2-phase representation is an essential component of this study, allowing different thermo-mechanical properties to be associated to the particles. Henceforth, properties associated to aggregate particles and mortar particles are differentiated by subscripts of 'a' and 'm' in the remaining text.

The interaction between any two particles is categorised as either *contact* interactions or *cohesive bond* interactions. Each category is described in the following sections.

7.2.1 Kinematics of cohesive bond interactions

When two particles are close enough at the beginning of the analysis (Fig. 7.1), and at least one of the particles is of mortar type, a cohesive bond is assumed to exist between them. These cohesive bonds are created only at the beginning of the analysis, and although existing bonds can break during the analysis, additional bonds are never created. Moreover, cohesive bonds are assumed to be in a state of zero stress when they are created and they can carry normal forces (in compression and tension) as well as shear.

The condition for establishing a bond between two particles i and j is:

$$\frac{|\vec{\mathbf{d}}_{ij}|}{r_i + r_j} \leq 1 + \gamma \tag{7.1}$$

where $\gamma > 1.0$ is a parameter allowing a bond interaction to be established between two particles that are not perfectly in contact. A value of $\gamma = 0.1$ is used in this study. This value is selected so that the average number of interactions per particle is approximately $5 \sim 6$, and to keep them limited to the nearest neighbour. Moreover, in Eq. (7.1), $\vec{\mathbf{d}}_{ij} = \vec{\mathbf{x}}_j - \vec{\mathbf{x}}_i$ is the distance between the centroids of particles i and j.

As illustrated in Fig. 7.1, the distance between the centroid of particle i and the contact point c is denoted by the vector $\vec{\mathbf{d}}_{ci}$ and is equal to:

$$\vec{\mathbf{d}}_{ci} = \vec{\mathbf{d}}_{ij} \left(\frac{r_i}{r_i + r_j} \right) \tag{7.2}$$

(a)

(b)

(c)
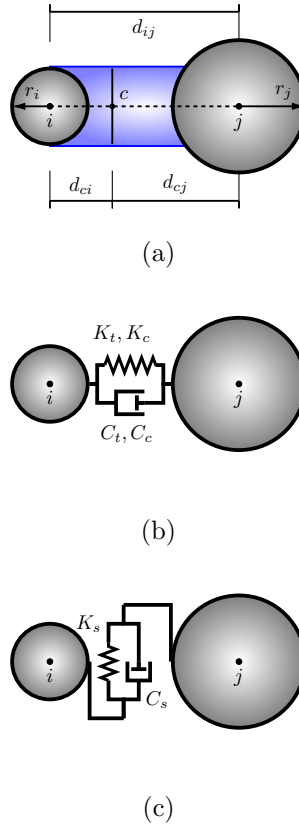
Figure 7.1: Cohesive bond mechanism. (a) Interaction interface, (b) normal (tensile and compressive) mechanism and (c) shear mechanism.

At the same time, for a 2D model of unit thickness, the bond area is assumed to be:

$$A_{ij} = \pi[\min(r_i, r_j)] \tag{7.3}$$

Once a cohesive bond interaction is created, the initial position ($\vec{\mathbf{x}}_0$) and orientation ($\vec{\boldsymbol{\theta}}_0$) of the two particles is saved into memory and utilised over the entire analysis. Using these stored values, the displacement and rotation of each particle up to time t relative to its initial state become $\Delta\vec{\mathbf{x}} = \vec{\mathbf{x}}_t - \vec{\mathbf{x}}_0$ and $\Delta\vec{\boldsymbol{\theta}} = \vec{\boldsymbol{\theta}}_t - \vec{\boldsymbol{\theta}}_0$.

Therefore, the displacement of the contact point on particle i is:

$$\Delta\vec{\mathbf{x}}_{ci} = \Delta\vec{\mathbf{x}}_i + (\vec{\mathbf{d}}_{ci} \times \Delta\vec{\boldsymbol{\theta}}) \tag{7.4}$$

and the relative displacement between the contact points on the two particles becomes $\Delta\vec{\mathbf{x}}_{c,rel} = \Delta\vec{\mathbf{x}}_{cj} - \Delta\vec{\mathbf{x}}_{ci}$.

Finally, the unit normal vector of a cohesive bond is defined as:

$$\hat{\mathbf{n}}_{ij} = \vec{\mathbf{d}}_{ij}/|\vec{\mathbf{d}}_{ij}| \tag{7.5}$$

and the unit shear vector is:

$$\hat{\mathbf{s}}_{ij} = \frac{\dot{\vec{\mathbf{x}}}_{c,rel} - (\dot{\vec{\mathbf{x}}}_{c,rel} \cdot \hat{\mathbf{n}}_{ij})\hat{\mathbf{n}}_{ij}}{|\dot{\vec{\mathbf{x}}}_{c,rel} - (\dot{\vec{\mathbf{x}}}_{c,rel} \cdot \hat{\mathbf{n}}_{ij})\hat{\mathbf{n}}_{ij}|} \tag{7.6}$$

7.2.2 Force-displacement formulation of cohesive bond interactions

It is worth mentioning at this point that the formulation presented here contains a number of damage parameters (η, λ, δ). Section 7.2.3 has been dedicated to describing these parameters. However, is it important to mention that the concept of damage is categorised as either mechanical (λ and δ) or thermal (η). Moreover, while some damage parameters are related to stiffness (η_k and λ), others relate to strength (η_f and δ). The value of all damage parameters is set to 1.0 (no degradation) at the beginning of the analysis, whereby a value of 0.0 represents fully damaged.

Using the unit vectors defined in Eqs. (7.5) and (7.6), the force acting between two interacting particles (Fig. 7.1) is decomposed into normal and shear components:

$$\vec{\mathbf{F}} = F_n\hat{\mathbf{n}}_{ij} + F_s\hat{\mathbf{s}}_{ij} \tag{7.7}$$

where F_n and F_s are the magnitudes of the normal and shear components and are calculated using:

$$\begin{cases} F_n = \lambda_t K_n u_n & \text{(if } u_n \geq 0.0) \\ F_n = \lambda_c K_n u_n & \text{(if } u_n < 0.0) \\ F_s = K_s u_s \end{cases} \tag{7.8}$$

A graphical representation of these relationships is illustrated in Figs. 7.2. In Eq. (7.8), the reduction factors λ_t and λ_c represent the level of *mechanical* damage in relation to tensile and compressive stiffness and are described in Section 7.2.3. Moreover, stiffness in the normal (K_n) and shear (K_s) directions appearing in Eq. (7.8) are determined by:

$$
\begin{cases}
K_n = \eta_k \dfrac{K_i K_j}{K_i + K_j}, \ K_i = \dfrac{E_i A_{ij}}{|\vec{\mathbf{d}}_{ci}|} \\[2ex]
K_s = \xi K_n
\end{cases}
\tag{7.9}
$$

where E_i is the elastic modulus of the material and η_k represents the *thermal* degradation of stiffness. Normal stiffness and shear stiffness are related through the parameter ξ. With damage parameters included in the model, force-deformation relations in the normal direction take the form illustrated in Fig. 7.2. Note that the normal and shear deformations $(u_n$ and $u_s)$ appearing in Eq. (7.8) are determined using:

$$
\begin{cases}
u_n = \Delta\vec{\mathbf{x}}_{c,rel} \cdot \hat{\mathbf{n}} \\[1ex]
u_s = \Delta\vec{\mathbf{x}}_{c,rel} \cdot \hat{\mathbf{s}}
\end{cases}
\tag{7.10}
$$

7.2.3   Damage model

Once the interactive bond forces between two particles have been determined using Eq. (7.8), their values have to be checked to fall into the admissible region. This admissible region is shown in Fig. 7.3 and is defined as:

$$
\begin{cases}
|F_n| \leq \delta_t \bar{F}_t \quad (\text{if } u_n \geq 0.0) \\[1ex]
|F_n| \leq \delta_c \bar{F}_c \quad (\text{if } u_n < 0.0) \\[1ex]
\ \ F_s \leq \delta_s \bar{F}_s
\end{cases}
\tag{7.11}
$$

where $\bar{F}_t$, $\bar{F}_c$ and $\bar{F}_s$ are the limiting forces in the tensile, compressive and shear directions, respectively, and:
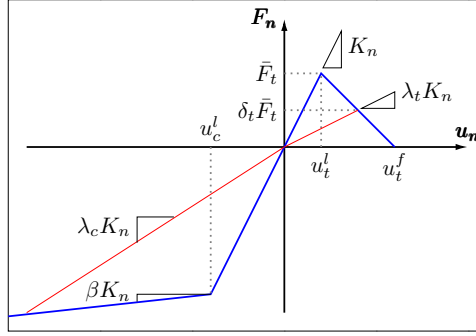
Figure 7.2: Force-deformation law in the normal direction (tensile and compressive).
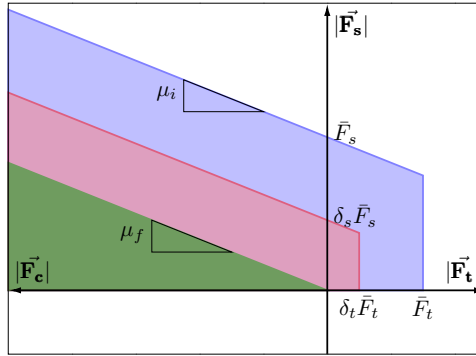
Figure 7.3: Mohr-coulomb law for admissible stress states. The blue and red areas represent the un-damaged and the damaged cohesive bond interaction, respectively. The green area represents friction interaction between two particles.

$$
\begin{cases}
\bar{F}_t = \eta_f f_t A_{ij} \\
\bar{F}_c = \eta_f f_c A_{ij} \\
\bar{F}_s = \eta_f f_s A_{ij} - \mu_i F_n
\end{cases}
\tag{7.12}
$$

In Eq. (7.12), f_t, f_c and f_s are tensile, compressive and shear strength values, respectively, and μ_i is the coefficient of internal friction (Fig. 7.3). Thermal degradation is considered through the strength-related damage parameter η_f. At the same time, the level of mechanical damage is incorporated into Eq. (7.11) through the parameters δ_t, δ_c and δ_s which respectively correspond to the tensile, compressive and shear strengths.

When force components reach the Mohr-Coloumb based limits, cohesive bond interactions begin to degrade, whereby strength and stiffness values need to be reduced using the *mechanical* damage parameters λ and δ in Eqs. (7.8) and (7.11). The damage mechanism is governed by the maximum deformation experienced in each

direction. For normal deformations in the tensile direction:

$$
\begin{cases}
\lambda_t = 1.0 & (u_t^d \le u_t^l) \\
\lambda_t = \left(\dfrac{u_t^f - u_t^d}{u_t^f - u_t^l} \right) \left(\dfrac{u_t^l}{u_t^d} \right) < 1.0 & (u_t^d > u_t^l)
\end{cases}
\tag{7.13}
$$

and

$$
\begin{cases}
\delta_t = 1.0 & (u_t^d \le u_t^l) \\
\delta_t = \dfrac{u_t^f - u_t^d}{u_t^f - u_t^l} < 1.0 & (u_t^d > u_t^l)
\end{cases}
\tag{7.14}
$$

and in compression:

$$
\begin{cases}
\delta_c = 1.0 & (u_t^d \le u_t^l) \\
\delta_c = 1.0 + \dfrac{\beta(u_c^d - u_c^l)}{u_c^l} > 1.0 & (u_c^d > u_c^l)
\end{cases}
\tag{7.15}
$$

where β determines the slope of the compressive response after the initial linear region as illustrated in Fig. 7.2. Moreover, u_t^d is the maximum normal deformation that has been experienced during the analysis, and u_t^f is the deformation at which the bond breaks.

The linear deformation limit u_t^l is equal to:

$$
u_t^l = f_t A_{ij} / K_n
\tag{7.16}
$$

The damage parameters δ_s and λ_c are defined similar to δ_t and λ_t, therefore, the formulation is not repeated here. A cohesive bond interaction is broken once the normal deformation in the tensile direction becomes greater than u_t^f. Once a cohesive bond breaks between two particles, the only interaction that can later appear between them is a contact interaction.

7.2.4 Contact interaction

In contrast to cohesive bond interactions, contact interactions are non-cohesive and can appear or disappear at any time during the analysis and between any two particles. Contact interactions appear whenever the distance between two particles, regardless of being of aggregate or mortar type, is less than the sum of their radii, or $|\vec{\mathbf{d}}_{ij}| \leq r_i + r_j$. These interactions are dynamically detected at the beginning of each time step.

While contact interactions are an integral part of a discrete element model, in comparison to cohesive bond interactions, they do not have a significant contribution towards the strength and the stiffness of the assembly. In this work, the formulation for contact interactions and cohesive bond interactions are similar. In fact both interactions use the same equations, except that contact interactions are simplified by setting $\bar{F}_c$ and $\bar{F}_s$ to zero and omitting any type damage. This can be seen as the green region depicted in Fig. 7.3.

7.2.5 Equations of motion and time integration

The 2D discrete element assembly used in this study consists of circular particles (cylindrical with unit thickness) governed by the equations of motion:

$$
\begin{cases}
\vec{\mathbf{F}}_i = m_i \ddot{\vec{\mathbf{x}}}_i \\
\vec{\mathbf{T}}_i = I_i \ddot{\vec{\boldsymbol{\theta}}}_i
\end{cases}
\tag{7.17}
$$

where $\vec{\mathbf{F}}_i$ is the resultant of all forces acting on particle i and $\ddot{\vec{\mathbf{x}}}_i$ is the acceleration of the particle. Similarly, $\vec{\mathbf{T}}_i$ is the net moment resulting from all the forces that act on particle i and $\ddot{\vec{\boldsymbol{\theta}}}_i$ represents the angular acceleration of the particle. In Eq. (7.17), m_i and I_i respectively denote the mass and the moment of inertia of particle i.

Eq. (7.17) is solved using the Verlet method of time integration with a constant time-step size of $\Delta t = 10^{-6}$ s. Each analysis takes around 5–7 hours of computation time to complete.

This study also incorporates different types of damping into the model. These are in
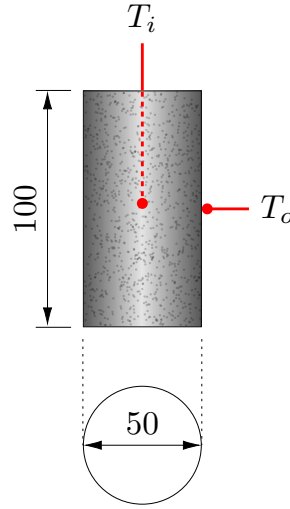
Figure 7.4: Concrete sample geometry (in mm) and thermocouple placement.

the form of global viscous damping and local damping between interacting particles. These are included in the model for the sole purpose of assisting in the stabilisation of the analysis. The values of the damping coefficients are chosen small enough to have negligible effects on the results of the analyses.

7.3 Experimental program

This section describes the experimental program used in this study to determine the *residual* properties of cylindrical concrete samples for two different temperatures of 200 and 400°C. Special care has been made in this program to create a uniform state of temperature-induced damage in each sample by avoiding large thermal gradients. The main steps taken for this purpose are the use of a small sample diameter (50 mm as opposed to the typical 150 mm diameter) and low heating rates.

7.3.1 Material

Samples of 50-mm diameter and 100-mm height are used in this program (Fig. 7.4). This sample size has shown to produce reliable results in terms of reproducibility of data (less scatter within the test results) under monotonic as well as cyclic loading [25]. At the same time, with the cross section being of cylindrical shape and the diameter of the sample being 50 mm, the process of attaining uniform temperature is simplified.

(a)   (b)
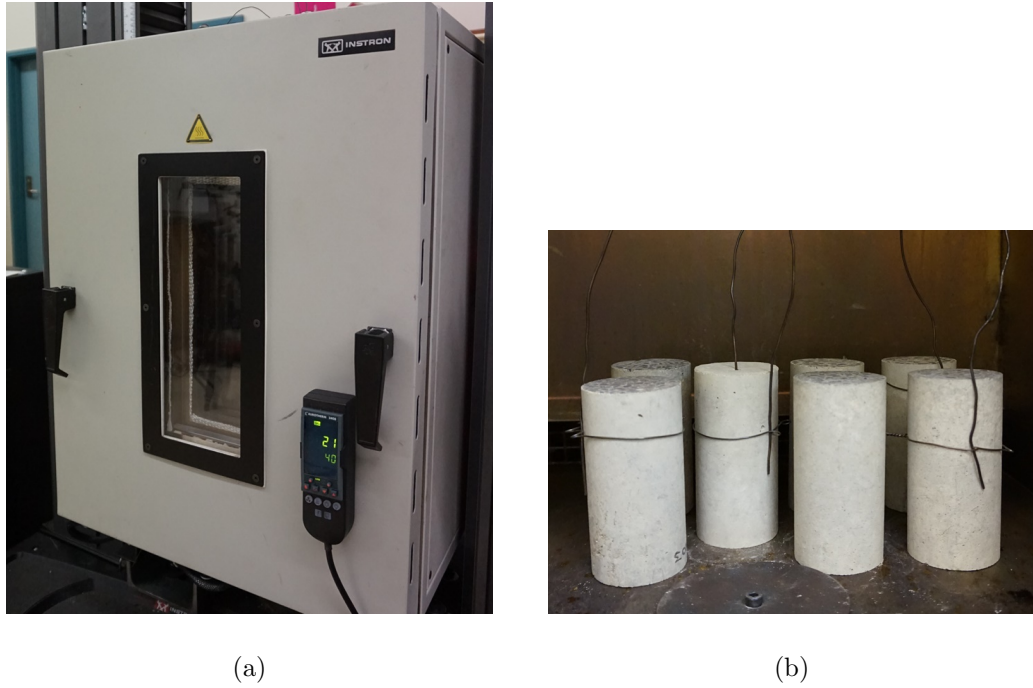
Figure 7.5: Laboratory setup for temperature exposure. (a) Environmental chamber and (b) placement of samples in groups of 7 inside the chamber.

All specimens are made using the same concrete mix with a 28-day target strength of 35 MPa. With a maximum diameter of $d_a = 8$ mm, the coarse aggregates used in this study are small enough to avoid the wall effect. The water/cement ratio is 0.55 and general purpose cement (type I Portland cement) is used as the only cementitious component of the concrete mix. After 24 hours of being cast, samples are removed from their molds and placed inside a curing tank where they rest in lime-saturated water at a temperature of approximately 23°C. On day-7, samples are removed from the tank and allowed to cure further in free air at room temperature until testing day. On approximately day-10, the two ends of the samples are ground for a smooth and parallel finish. All samples are tested after 90 days of age and each test is repeated 6 times.

7.3.2   Testing scheme

Samples are exposed to elevated temperatures using an Instron environmental chamber (model 3119-408, Fig. 7.5). Target temperatures are set to 200 and 400°C, while the heating rate is set to 10°C min^{-1}. Samples are placed inside the chamber in groups of 7, where one of the samples is used to monitor the inner and outer temperature.

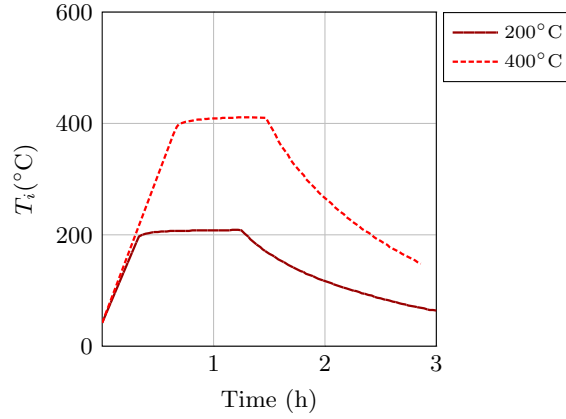Figure 7.6: Variation of temperature with time with heating and cooling phase.

Once the inner temperature of the sample (not the chamber) reaches the target value, the temperature is kept constant for 60 minutes (Fig. 7.6). This 1 hour duration is usually used by researchers as a lower limit for the exposure time [2]. On the other hand, it has been shown by Wu and Wu [2] that for normal strength concrete, exposure durations above 1 hour have negligible effect on strength reduction. During this time, the temperature of the sample is logged by thermocouples on the surface and the inside of the specimen (Fig. 7.4). It is worth noting that spalling has not been observed in any of the samples tested in this program. After the 60-minute period of constant temperature, the heater is turned off and to avoid any thermal shock, the samples are allowed to slowly cool down to room temperature before opening the chamber.

It is worth pointing to Fig. 7.7 which shows the variation of temperature with time recorded from the two thermocouples depicted in Fig. 7.4. One thermocouple measures the temperature on the surface of the sample, while the other is embedded inside the sample and measures the temperature at the centre.

Residual mechanical properties of cooled-down samples are determined by compression tests. The machine used for this is a Shimadzu AG-X with a load capacity of 300 kN, whereby samples are loaded at a constant cross-head displacement rate of 0.1 mm/min resulting in strain rates lower than $\dot{\epsilon} = 10^{-4}$ s^{-1}. Fig. 7.8 illustrates the schematics of the test setup. Forces are directly accumulated from the machine, while the overall longitudinal strain of the sample is determined using the relative displacement of the two end platens. This relative displacement is recorded by a non-contact MTS laser extensometer (model LX500) with reference to the two retro-reflective tapes that are attached to the front of the platens (Fig. 7.8). Loading as well as data accumulation is continued at a frequency of 4 Hz until failure.
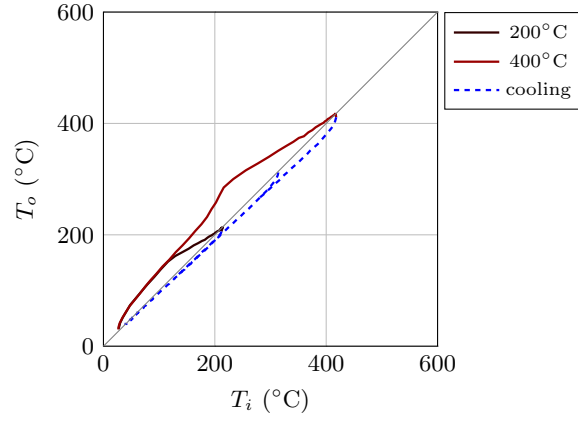
Figure 7.7: Center temperature against surface temperature recorded by the thermocouples placed inside (T_i) and on the surface (T_o) of the sample.
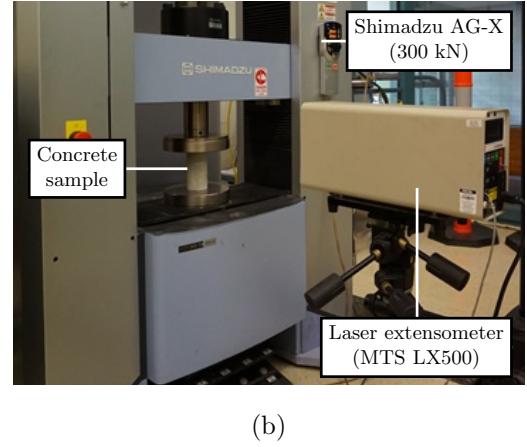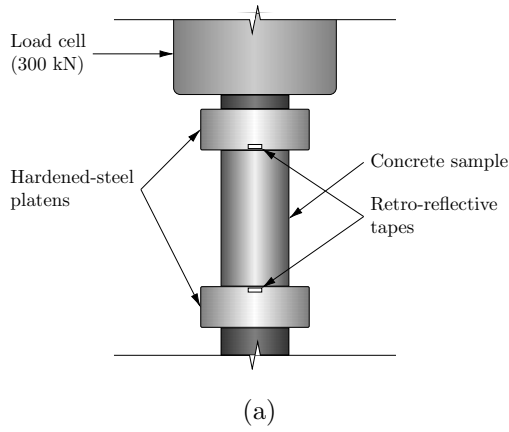
Figure 7.8: Test setup and the location of the retro-reflective tapes. (a) Schematics and (b) Laboratory setup.

With every test being repeated 6 times, the range of stress-strain curves obtained for exposure temperatures of 20, 200 and 400°C are shown in Fig. 7.9.

7.4   Numerical simulations

The setup for the of the numerical simulations is described in this section. The parameters considered in this study are the residual properties of the samples after they have slowly cooled down to room temperature. These are denoted by the superscript r and include the residual peak stress f_c^r, and initial modulus E_c^r. A 2D discrete element program has been developed to carry out the analyses.
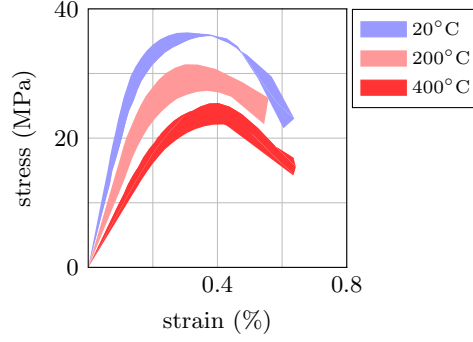
Figure 7.9: Experimental stress-strain curves for samples at room temperature and after cooldown from temperatures of 200 and 400°C.

7.4.1 Particle assembly

The particle assembly used in this study is depicted in Fig. 7.10. Note that in this figure, red particles represent the aggregates and blue particles represent the mortar matrix. This assembly consists of 816 aggregate particles with diameters ranging between 1-8 mm. This number is based on the mix proportion of the coarse aggregates used in casting the laboratory specimens. These aggregate particles are embedded between 2105 mortar particles with a diameter of 1 mm (Fig. 7.11a). The total number of cohesive bonds at the start of the analysis is 7578, where 3942 of them are aggregate-mortar (AM) bonds and 3636 are of mortar-mortar (MM) type. The distribution of the orientation of these bonds is graphically shown in Fig. 7.11b. There are no particle overlaps at the beginning of the analysis and all damage parameters are set to $\eta = 1.0$, $\delta = 1.0$ and $\lambda = 1.0$. Time step size is equal to $\Delta t = 1.0 \times 10^{-6}$ s and is constant throughout the analysis.

7.4.2 Micro-mechanical parameters

The base parameters of the model are calibrated against the stress-strain curve of a concrete sample at room temperature (20°C). These calibrated values are given in Tables 7.1 and 7.2. Note that Table 7.1 corresponds to the properties of the material (that is, aggregates and the mortar matrix), while Table 7.2 relates to the properties of the cohesive bond interactions. Fig. 7.12 illustrates the stress-strain curve resulting from using these parameters. This figure shows that the simulated curve properly falls within the range of curves obtained through experimentation.
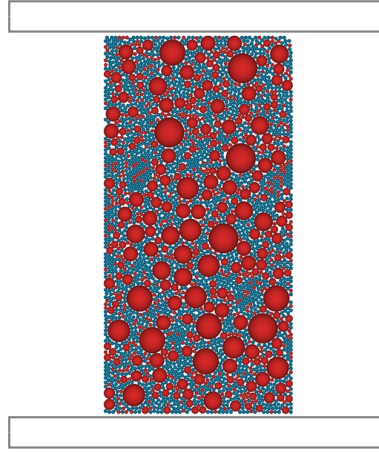
Figure 7.10: Particle assembly of the model used in this study. Red particles represent aggregates and blue particles represent the mortar matrix.

(a)   (b)
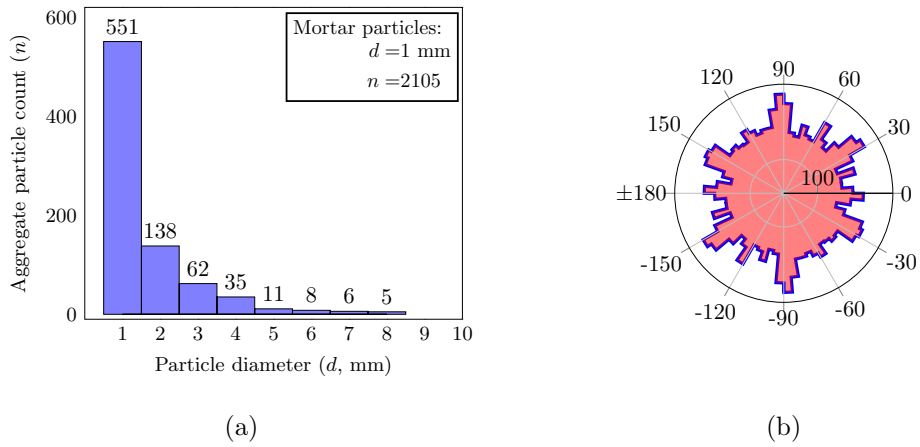
Figure 7.11: Characteristics of the particle assembly used in this study. (a) Particle count for the aggregate particles and mortar particles. (b) Number of cohesive bond interactions over different orientations.

Table 7.1: Mechanical properties of the constituent materials: aggregate (A) and mortar matrix (M).

category	A	M
E (GPa)	70.0	15.0
ν	0.2	0.2

Table 7.2: Micro-mechanical properties of the cohesive bonds: aggregate-mortar (AM) and mortar-mortar (MM).

category	AM	MM
K_n (Nm^{-1})	from Eq. (7.9) and Table 7.1	
$\xi = K_s/K_n$	0.40	0.40
f_t (MPa)	2.55	5.10
f_s/f_t	4.62	4.62
f_c/f_t	16.75	16.75
u_t^f/u_t^l	2.00	2.00
u_t^f/u_t^l	2.00	2.00
β	0.05	0.05
μ_i	$\tan 30°$	$\tan 30°$
μ_f	$\tan 25°$	$\tan 25°$
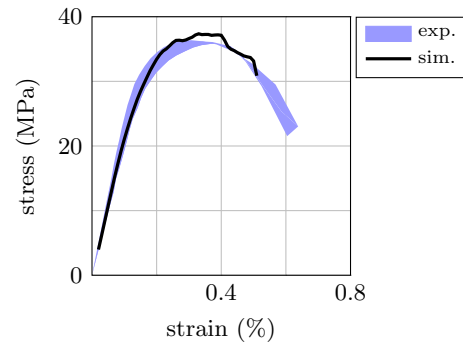
Figure 7.12: Simulated stress-strain curve produced by the discrete element model at room temperature against the curves found from experimentation.

7.4.3 Introducing temperature effects

The effect of temperature is introduced into the model in the form of two main effects:

- Thermal expansion of particles as a result of their coefficient of thermal expansion (CTE) denoted by α_a for aggregate particles and α_m for mortar particles.

- Thermal degradation of the cohesive bonds between the particles. This is applied through the damage parameters η_k and η_f for stiffness and strength degradation, respectively.

A global temperature variable T is incorporated into the analysis. This temperature variable is used to determine the diameter of the particles using the equation of linear thermal expansion $D_T = D_{20}(1.0 + \alpha(T - 20))$, where α is the coefficient of thermal expansion of the material, D_T is the particle diameter at temperature T and D_{20} is the particle diameter at room temperature. At the same time the stiffness and strength of the cohesive bonds are affected by the global temperature parameter T through the values of the thermal damage parameters η_k and η_f. The variation used in this study for these parameters is illustrated in Fig. 7.13. The values of η_k and η_f at $T = 200$ and $400°\text{C}$ are selected so that the model produces the curves shown in Fig. 7.14. Note that the simulated stress-strain curves given in this figure are attained without taking the effect of thermal incompatibility into account. These curves are presented here so that later on they can be used to demonstrate the additional damage caused by thermal incompatibility. Nevertheless, Figs. 7.12 and 7.14 show that the chosen parameters produce stress-strain curves that are in good agreement with experimental results.

7.4.4 Parametric analysis

The model is analysed under the loading scheme depicted in Fig. 7.15. Similar to the experimental program of Section 7.3, the loading scheme used in the numerical analysis involves a heating phase and a cooling phase. The rate of temperature change for both phases is set to $\dot{T} = 10°\text{C}\,\text{s}^{-1}$. The initial temperature is taken to be equal to $T = 20°\text{C}$ and it is assumed to be uniform throughout the entire body of the sample.
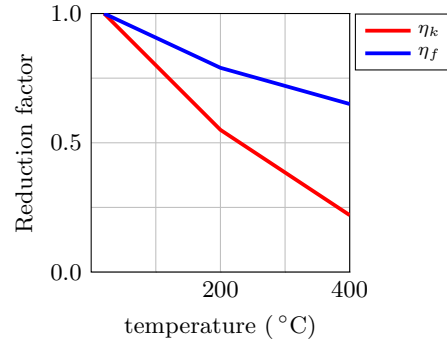
Figure 7.13: Variation of the thermal damage parameters η_k and η_f against temperature.

| (a) | (b) |
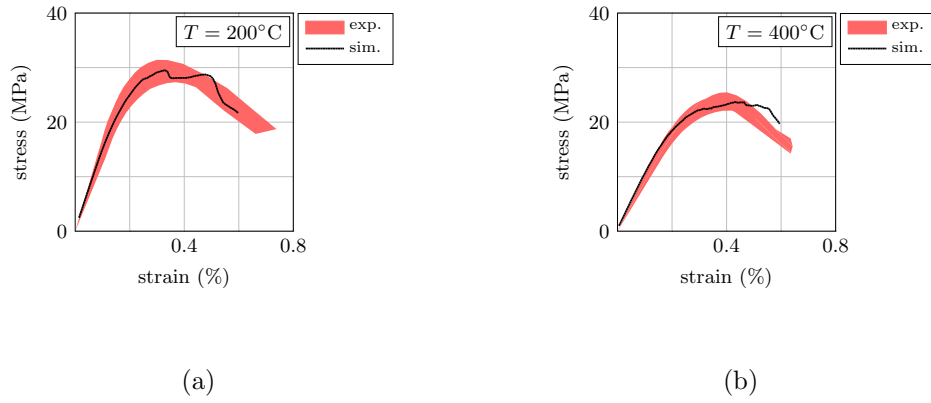
Figure 7.14: Simulated stress-strain curve produced by the discrete element model against the curves found from experimentation. (a) Simulation at 200°C and (b) simulation at 400°C
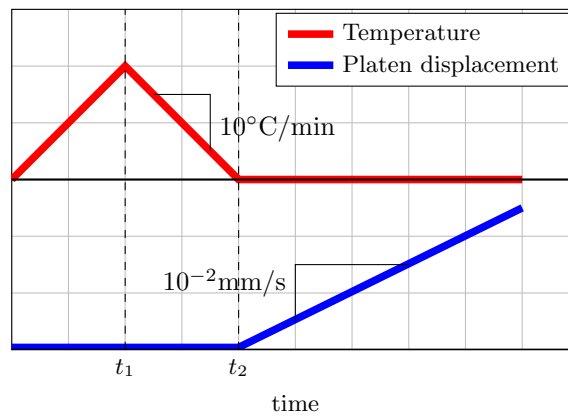
Figure 7.15: The loading scheme used in the analysis. This involves a global temperature variation in the first phase followed by displacement-controlled loading in the second phase.

As mentioned before, one effect of the global temperature parameter T is through thermal degradation of the bonds. This effect is taken to be irreversible, meaning that once the temperature reaches a certain value, thermal damage parameters are determined from that value and will not recover upon cooldown.

The global temperature parameter also affects the degradation of the samples through the expansion of the particles, and this is where the analysis takes the form of a parametric study. According to literature, the typical range of values of the coefficient of thermal expansion for aggregates and the mortar can range from $\alpha = 5.0$ to $10.0 \times 10^{-6}/\,^{\circ}\mathrm{C}$ [6, 26–29]. As a results, the model presented in this study is analysed under 72 different combinations of (α_a, α_m) where the coefficient of the aggregates and the mortar are set to $\alpha = 5.0, 6.0, ..., 10.0 \times 10^{-6}/\,^{\circ}\mathrm{C}$. These combinations are henceforth divided into cases where:

- $\alpha_a/\alpha_m > 1.0$, where the CTE of aggregates is greater than the mortar.

- $\alpha_a/\alpha_m < 1.0$, where the CTE of aggregates is less than the mortar.

These cases are observed to have different effects on the results. Fig. 7.16 shows the evolution of force-chains within the assembly as the temperature rises from 20°C to 400°C. In this figure, compressive forces are depicted by the blue colour, while tensile forces are in red. Fig. 7.16a corresponds to the case where $\alpha_a/\alpha_m = 2.0$. In this case, aggregates tend to expand at a higher rate that the mortar, leading to compression in the aggregates and tension in the mortar matrix. On the other hand, Fig. 7.16b corresponds to the case where $\alpha_a/\alpha_m = 0.5$. In this case, aggregates expand at a lower rate that the mortar, leading to tensile forces in the aggregates and compressive forces in the mortar matrix. Comparing Figs. 7.16a and b indicates that the internal forces which form when $\alpha_a/\alpha_m = 0.5$ are lower than the forces of $\alpha_a/\alpha_m = 2.0$. It is demonstrated later that aggregate-mortar (AM) bonds and mortar-mortar (MM) bonds tend to break at different rates depending on the α_a/α_m ratio. This in itself affects the extent of strength and stiffness degradation.

Fig. 7.17 illustrates the variation of residual strength (f_c^r) and residual stiffness (E_c^r) for all combinations of (α_a, α_m) analysed in this study. All residual parameters are observed to remain constant when α_a and α_m are equal. However, as the value of α_a and α_m diverge, residual strength and stiffness decline. Moreover, it is observed that the rate at which the residual properties decline depends on whether $\alpha_a/\alpha_m > 1.0$ or $\alpha_a/\alpha_m < 1.0$. In fact, residual properties tend to attain smaller values for cases where $\alpha_a/\alpha_m < 1.0$. Another point can be made when Figs. 7.17a and b
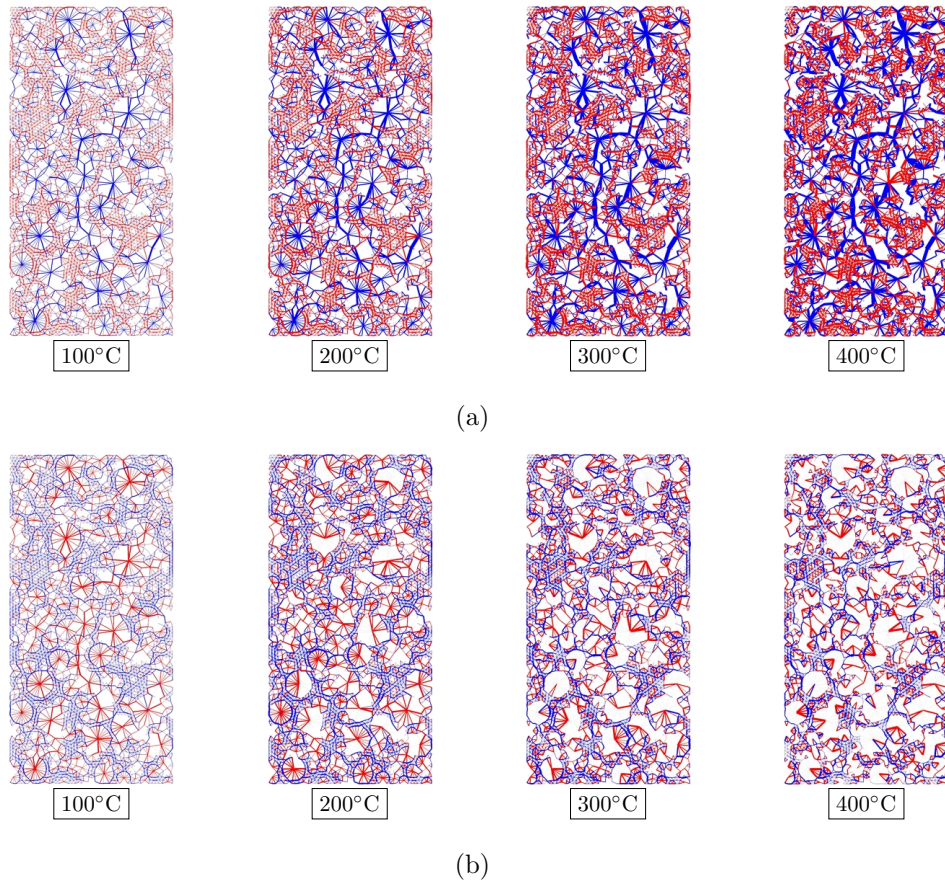
Figure 7.16: Evolution of force-chains with rising temperature. (a) For the case where $\alpha_a/\alpha_m = 2.0$ and (b) for the case where $\alpha_a/\alpha_m = 0.5$
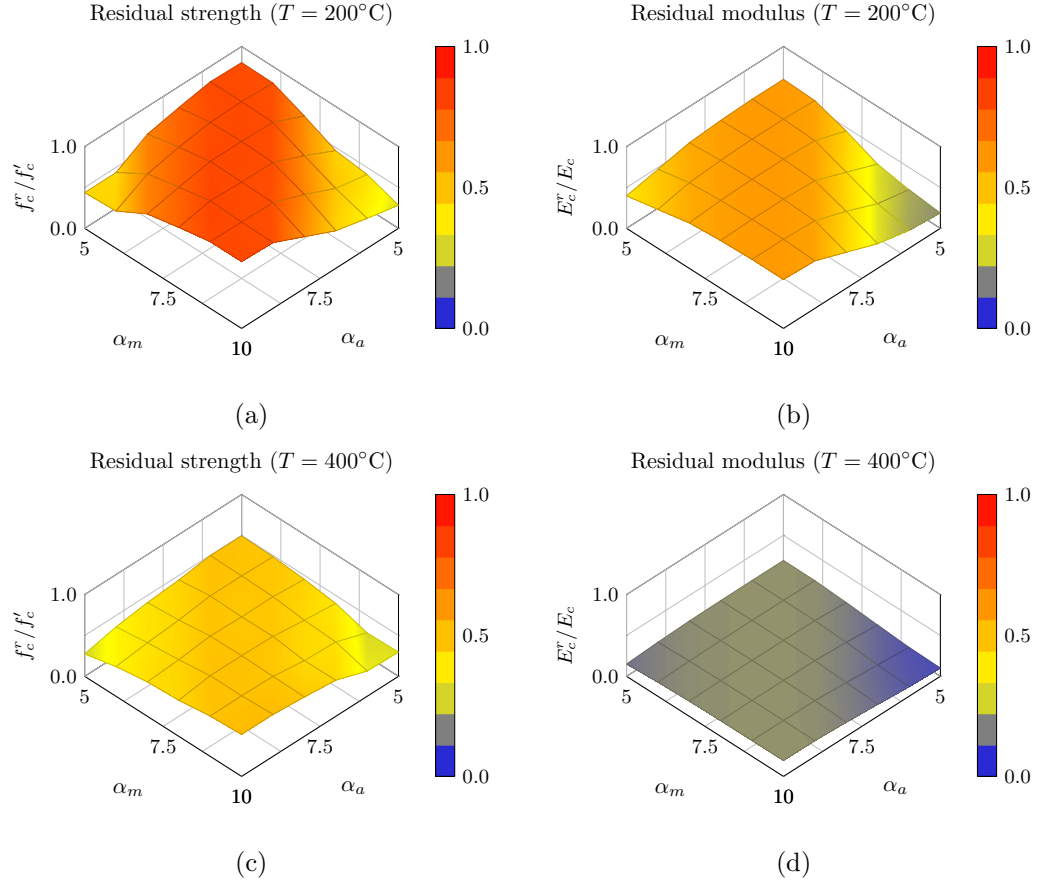
Figure 7.17: Variation of residual strength (f_c^r) and residual stiffness (E_c^r) against α_a and α_m for temperatures equal to (a,b) 200°C and (c,d) 400°C.

corresponding to $T = 200$°C are compared to Figs. 7.17c and d which correspond to $T = 400$°C. When comparing these figures, it is observed that the curvature of the surface decreases as the temperature rises. This reveals the fact that as higher temperatures are reached, the degradation caused by weakening of bonds overshadows the degradation caused by thermal incompatibility.

It is also important to analyse the variation of the residual stress-strain curves in terms of α_a and α_m. This is illustrated in Fig. 7.18 for $\alpha_a/\alpha_m > 1.0$ and $\alpha_a/\alpha_m < 1.0$ after exposure to $T = 200$ and 400°C. This figure clearly demonstrates the extent that the stress-strain curve can change as a result of different values of α_a and α_m. This figure alone shows the importance of thermal incompatibility when simulating the effect of high temperature on concrete material.

The final plots presented in this paper are those of Fig. 7.19 illustrating the progression of the breakage of bonds over the entire duration of the analysis. Note that similar to Fig.7.15, t_1 designates the end of heating, while t_2 simultaneously corresponds to the end of cooling and the onset of compressive loading. One observation
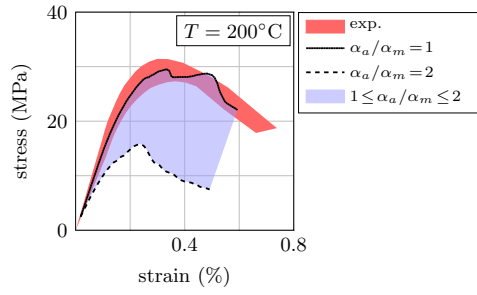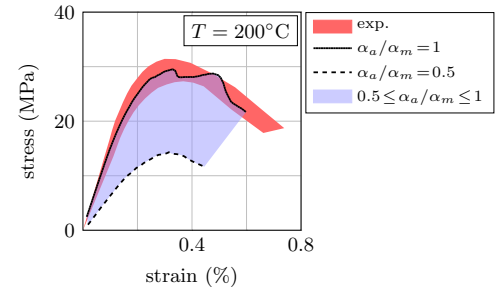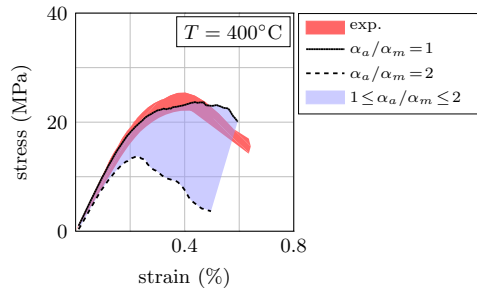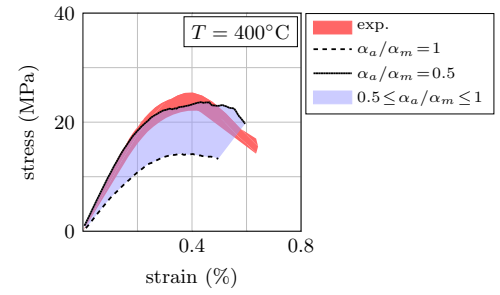
Figure 7.18: Variation of the residual stress-strain curve for different combinations of α_a and α_m. (a,b) Stress-strain curve after exposure to 200°C and (c,d) after exposure to 400°C
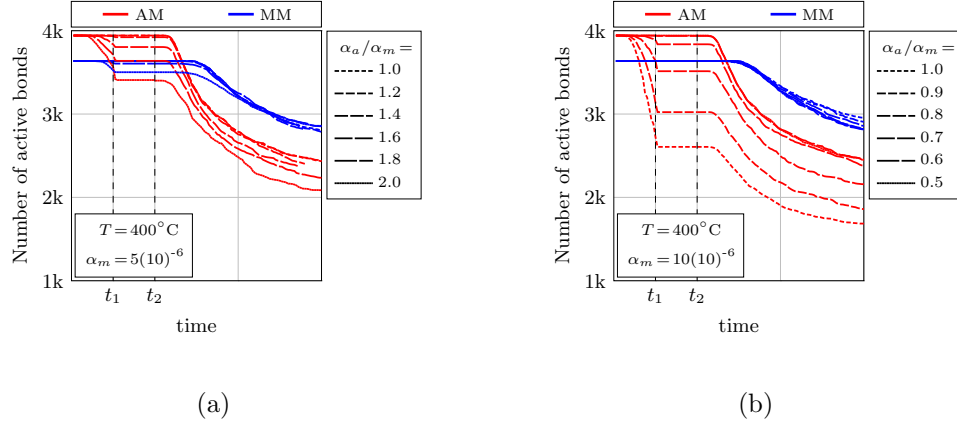
Figure 7.19: Number of cohesive bonds for aggregate-mortar (AM) and mortar-mortar (MM) interactions for target temperature of $T = 400°C$. (a) $\alpha_m = 5(10)^{-6}$ and (b) $\alpha_m = 10(10)^{-6}$

is that mortar-mortar (MM) bonds generally do not break over the heating region, except for cases where $\alpha_a/\alpha_m > 1.6$. Aggregate-mortar (AM) bonds are seen to break at a higher rate if $\alpha_a/\alpha_m < 1.0$ as opposed to $\alpha_a/\alpha_m > 1.0$. This explains why in Fig. 7.17 the values of residual strength and stiffness are generally lower when $\alpha_a/\alpha_m < 1.0$. The highest rate at which aggregate-mortar (AM) bonds break is the case where $\alpha_a/\alpha_m = 0.5$, which corresponds to lowest value of the residual strength and stiffness observed in Fig. 7.17.

7.5   Conclusions

This study aimed to simulate the degradation of concrete materials by utilisation of the discrete element method. This is accomplished by creating a 2-phase model which distinguishes between the thermo-mechanical properties of the aggregates and the mortar matrix. The damage induced by temperature is taken to be caused by two different phenomena: degradation of bonds and thermal incompatibility. A range of values are assumed for the coefficient of thermal expansion of the aggregates and the mortar matrix, and a parametric study is performed by analysing the model for different combinations of the CTE. The following conclusions can be drawn from the results:

1. The results show that thermal incompatibility can have a significant effect on the degradation of concrete when exposed to elevated temperatures.

2. It is shown that in general, residual strength and residual stiffness attain lower values when the CTE of the aggregates is less than the CTE of the mortar.

3. As the exposure temperature increases, the degradation caused by thermal incompatibility becomes less significant compared to the degradation caused by the weakening of the cohesive bonds.

4. The residual stress-strain curve can exhibit significant changes for different values of the CTE, however, the upper bound is $\alpha_a = \alpha_m$ and the lower bound is when α_a and α_m are far apart.

5. When cohesive bonds are divided into aggregate-mortar (AM) and mortar-mortar (MM) bonds, the progression of their breakage can be used to explain the variation of the residual parameters in terms of different values of the α_a/α_m ratio.

6. Although the results of this study have shown to be effective in simulating the effect of temperature on concrete, a more accurate model is bound to provide more insight into the degradation of concrete material. Higher accuracy can be reached by incorporating more damage parameters into the model (e.g. for the fracture strain). Moreover, including other physical phenomena, such as moisture diffusion, into the simulation can help to create a more general model and improve the results.

7. While researchers have emphasised the importance of the coefficient of thermal expansion on strength degradation of concrete exposed to high temperatures [4–6, 13], there still exists a lack of experimental data on the subject. The results of this research can be used for the design of a comprehensive experimental program dedicated to the effect of thermal incompatibility on strength degradation of concrete under high temperatures.

Acknowledgement

References

[1] Yue Zhai, Zichen Deng, Nan Li, and Rui Xu. Study on compressive mechanical capabilities of concrete after high temperature exposure and thermo-damage constitutive model. *Construction and Building Materials*, 68:777–782, 2014.

[2] Yaopeng Wu and Bo Wu. Residual compressive strength and freeze–thaw resistance of ordinary concrete after high temperature. *Construction and Building Materials*, 54:596–604, 2014.

[3] Ali Ergün, Gökhan Kürklü, Başpınar M Serhat, and Mohamad Y Mansour. The effect of cement dosage on mechanical properties of concrete exposed to high temperatures. *Fire Safety Journal*, 55:160–167, 2013.

[4] Omer Arioz. Effects of elevated temperatures on properties of concrete. *Fire Safety Journal*, 42(8):516–522, 2007.

[5] Kristian Dahl Hertz. Concrete strength for fire safety design. *Magazine of Concrete Research*, 57(8):445–453, 2005.

[6] Minho Yoon, Gyuyong Kim, Gyeong Choel Choe, Youngwook Lee, and Taegyu Lee. Effect of coarse aggregate type and loading level on the high temperature properties of concrete. *Construction and Building Materials*, 78:26–33, 2015.

[7] Yu-Fang Fu, Yuk-Lung Wong, Chi-Sun Poon, Chun-An Tang, and Peng Lin. Experimental study of micro/macro crack development and stress–strain relations of cement-based composite materials at elevated temperatures. *Cement and Concrete Research*, 34(5):789–797, 2004.

[8] Joshua B Odelson, Elizabeth A Kerr, and Wilasa Vichit-Vadakan. Young's modulus of cement paste at elevated temperatures. *Cement and Concrete Research*, 37(2):258–263, 2007.

[9] Rosen Tenchev and Phil Purnell. An application of a damage constitutive model to concrete at high temperature and prediction of spalling. *International Journal of Solids and Structures*, 42(26):6550–6565, 2005.

[10] Thomas Gernay, Alain Millard, and Jean-Marc Franssen. A multiaxial constitutive model for concrete in the fire situation: Theoretical formulation. *International Journal of Solids and Structures*, 50(22):3659–3673, 2013.

[11] Dariusz Gawin, Francesco Pesavento, and Bernhard A Schrefler. What physical phenomena can be neglected when modelling concrete at high temperature?

a comparative study. part 1: Physical phenomena and mathematical model. *International journal of solids and structures*, 48(13):1927–1944, 2011.

[12] Dariusz Gawin, Francesco Pesavento, and Bernhard A Schrefler. What physical phenomena can be neglected when modelling concrete at high temperature? a comparative study. part 2: Comparison between models. *International Journal of Solids and Structures*, 48(13):1945–1961, 2011.

[13] G Xotta, G Mazzucco, VA Salomoni, CE Majorana, and KJ Willam. Composite behavior of concrete materials under high temperatures. *International Journal of Solids and Structures*, 64:86–99, 2015.

[14] M Nitka and J Tejchman. Modelling of concrete behaviour in uniaxial compression and tension with dem. *Granular Matter*, 17(1):145–164, 2015.

[15] Fatemeh Javidan, Sharif Shahbeyk, and Mohammad Safarnejad. Lattice discrete particle modeling of compressive failure in hollow concrete blocks. *COMPUTERS AND CONCRETE*, 13(4):437–456, 2014.

[16] Eugenio Oñate, Francisco Zárate, Juan Miquel, Miquel Santasusana, Miguel Angel Celigueta, Ferran Arrufat, Raju Gandikota, Khaydar Valiullin, and Lev Ring. A local constitutive model for the discrete element method. application to geomaterials and concrete. *Computational Particle Mechanics*, pages 1–22, 2015.

[17] VT Tran, F-V Donzé, and P Marin. A discrete element model of concrete under high triaxial loading. *Cement and Concrete Composites*, 33(9):936–948, 2011.

[18] N Monteiro Azevedo, JV Lemos, and J Rocha de Almeida. Influence of aggregate deformation and contact behaviour on discrete particle modelling of fracture of concrete. *Engineering Fracture Mechanics*, 75(6):1569–1586, 2008.

[19] Jerzy Rojek, Carlos Labra, Okan Su, and Eugenio Oñate. Comparative study of different discrete element models and evaluation of equivalent micromechanical parameters. *International Journal of Solids and Structures*, 49(13):1497–1517, 2012.

[20] Sina Sinaie, Amin Heidarpour, and Xiao-Ling Zhao. Mechanical properties of cyclically-damaged structural mild steel at elevated temperatures. *Construction and Building Materials*, 52:465–472, 2014.

[21] Sina Sinaie, Amin Heidarpour, and Xiao-Ling Zhao. Stress–strain–temperature relation for cyclically-damaged structural mild steel. *Engineering Structures*, 77:84–94, 2014.

[22] Mahsa Mirmomeni, Amin Heidarpour, Xiao-Ling Zhao, Christopher R Hutchinson, Jeffrey A Packer, and Chengqing Wu. Mechanical properties of partially damaged structural steel induced by high strain rate loading at elevated temperatures–an experimental investigation. *International Journal of Impact Engineering*, 76:178–188, 2015.

[23] Sajjad Hosseini, Amin Heidarpour, Frank Collins, and Christopher R Hutchinson. Effect of strain ageing on the mechanical properties of partially damaged structural mild steel. *Construction and Building Materials*, 77:83–93, 2015.

[24] Fatemeh Azhari, Amin Heidarpour, Xiao-Ling Zhao, and Christopher R Hutchinson. Mechanical properties of ultra-high strength (grade 1200) steel tubes under cooling phase of a fire: An experimental investigation. *Construction and Building Materials*, 2015.

[25] Sina Sinaie, Amin Heidarpour, Xiao-Ling Zhao, and Jay G Sanjayan. Effect of size on the response of cylindrical concrete samples under cyclic loading. *Construction and Building Materials*, 84:399–408, 2015.

[26] Changjun Zhou, Xiang Shu, and Baoshan Huang. Predicting concrete coefficient of thermal expansion with an improved micromechanical model. *Construction and Building Materials*, 68:10–16, 2014.

[27] Md Sarwar Siddiqui and David W Fowler. A systematic optimization technique for the coefficient of thermal expansion of portland cement concrete. *Construction and Building Materials*, 88:204–211, 2015.

[28] Carlos R Cruz and M Gillen. Thermal expansion of portland cement paste, mortar and concrete at high temperatures. *Fire and materials*, 4(2):66–70, 1980.

[29] Zdenek P Bazant and Maurice F Kaplan. *Concrete at high temperatures: material properties and mathematical models*. Longman Group Limited, 1996.

CHAPTER 8

Conclusions and future work

Contents

8.1 Research outcomes

This section summaries the main conclusions drawn from this research. This includes knowledge gained from experimentation as well as numerical modelling. These are presented in two separate parts for steel and concrete materials.

8.1.1 Steel

The aim of carrying out experiments on steel was to gain a fundamental understanding of the effects that a prior history of cyclic loading has on the subsequent monotonic properties at elevated temperatures. For this purpose, steel specimens were initially subjected to a number of strain-controlled cycles, and then monotonically loaded in tension at different temperatures until failure. With the number of cycles and the strain amplitude serving as variables for the cyclic phase, and temperature being the variable for the monotonic phase, their combined influence on subsequent mechanical properties of structural steel at elevated temperatures was examined. Where admissible, the variations observed in this program were compared to the relationships given by design codes. The following conclusions can be drawn from the experimental and numerical results:

1. By comparing complete stress-strain curves attained at elevated temperatures without pre-damage to their counterparts that include cyclically-induced pre-damage, it is revealed that high temperature mainly contributes towards strength degradation and reduction in ductility. At the same time, the pre-induced damage mainly contributes towards the reduction in ductility. Moreover, both temperature and pre-damage have noticeable effects on stiffness.

2. Based on the experimental results, it is evident that within the range tested in this program, the effect of cycle amplitude is more significant than the number of cycles.

3. In view of the variations of the mechanical properties against temperature and cyclic loading, it appears that at 600°C, curves with cyclically-induced damage converge towards curves without damage. This implies that at this temperature, the effect of high temperature dominates over the effect of cyclic damage and hence, the effect of pre-induced damage on the response becomes

insignificant.

4. The proposed model based on Bézier curves is as effective as an explicit relationship in reproducing full-range stress-strain-temperature curves. Unlike explicit relations, all the parameters used to describe the proposed model are in the form of strain, stress or modulus and therefore, not only have a real physical meaning but can also be directly taken from experimental stress-strain plots. The introduction of a new parameter, representing level of damaged induced by the cyclic phase, into the relations and hence establishing a relation between stress, strain, temperature and the level of damage is very straightforward.

5. For a given state of temperature and damage level, the proposed Bézier -based model is not only capable of calculating stress as a function of strain, but at no additional cost, is also capable of calculating strain as a function of stress. Hence, the model is able to predict the strain-temperature response of the material for a constant stress value. This can be directly used to analyse the transient behaviour of structures under fire conditions.

6. When it comes to nonlinear plasticity models, an automated parameter determination technique was developed based on multi-objective optimisation. The results indicated that the calibrated model not only accurately traces the stress variation of the load history it was calibrated against, but is also capable of tracing other load histories. This is in addition to the fact that in a multi-objective problem, the operator has the power to enforce preferences into the solution. Hence, giving a multi-objective approach advantages that are not available through a single-objective method.

8.1.2   Concrete

This thesis investigated the effect of temperature exposure on concrete samples that have previously been subjected to cyclic loading. For this purpose, cylindrical samples were cast and tested over a 3-phase program. Phase 1 comprised of subjecting samples to cyclic loading. In phase 2, damaged samples were exposed to a target temperature for 60 minutes and then allowed to slowly cool down. Phase 3 was the final phase, where the residual properties of the damaged samples were attained through compression tests. The residual properties extracted from stress-

strain curves involved the strength, peak strain and the initial modulus. Bézier curves were utilised for the numerical representation of the residual properties as a function of temperature and damage level. These were then used as input parameters for the stress-strain relation to numerically reproduce the stress-strain curves over different values of temperature and damage level. The following conclusions can be drawn from the results:

1. Under cyclic loading alone, all residual properties decreased in value except for the post-peak response which remained quite constant. The variations were explained through the progression of cracks and micro-cracks under mechanical loading. Under temperature exposure alone, strength and stiffness deteriorated, while the peak strain increased in value. These variations were be explained by available knowledge on chemical degradation and thermal stresses caused by high temperature.

2. When the two events (cyclic loading and temperature exposure) were applied in sequence, the variation of the residual properties became a function of both events. However, these variations could still be explained in the context of each individual event.

3. Given the sequence of events (cyclic damage and then temperature exposure), once the level of damage was determined, under increasing temperature, strength and stiffness degraded, while the peak strain increased.

4. As the temperature attained higher values, its effect began to dominate over the effect of pre-induced damage.

5. Bézier formulations were demonstrated to be capable of evaluating residual properties in terms of the two independent variables of temperature and the damage level. The stress-strain equation when combined with Bézier formulations, was shown to produce accurate results for any given level of damage and temperature in the tested range.

6. The performance of the discrete element method in simulating the effect of high temperature on concrete was illustrated in this thesis. Using this approach, the influence of the thermal incompatibility of the aggregate particles and the mortar matrix was quantified through parametric study.

8.2   Future work

This section summaries recommendation and suggestions for potential future research work. These recommendations are based on current knowledge gaps. This includes both experimental and numerical studies and is divided into three parts for steel, concrete and composite research.

8.2.1   Steel

The following items are recommended for future studies on steel:

1. While both variables of the cyclic loading phase (amplitude and number of cycles) were observed to influence the subsequent tensile properties of steel, it is evident that within the range used in this program, the effect of the amplitude is more significant than the number of cycles. In order to generalise this conclusion, further experiments must be performed with higher number of cycles.

2. Regarding the variation of the yield stress with temperature, the difference between design code expressions and the values observed in this research seemingly imply that design code expressions are too conservative when it comes to the post-cyclic behaviour of structural steel. However, when coupled with the loss of ductility due to the decrease in the ultimate strain and the loss of stiffness due to the decrease in tangent moduli, the combined behaviour becomes much more complex, and not necessarily conservative. This calls for more elaborate design expressions that are not only a function of temperature, but are also a function of the intensity of the previously sustained cyclic loading.

3. With constitutive plasticity models showing to be effective in simulating the cyclic and monotonic responses of steel, implementing temperature and rate dependent properties can be rather useful for future simulations of structures and structural members under post-earthquake fire conditions.

4. Transient state tests reflect a more realistic response of the material under post-earthquake fire conditions, carrying out such experiments can lead to a

deeper insight on the subject. This would also allow the quantification of transient creep under elevated temperatures.

8.2.2   Concrete

Suggestions for future investigations on concrete are listed in the following:

1. The present study quantifies the residual properties of concrete after cooldown, carrying out experiments at elevated temperatures (without cooldown) will extend this understanding and is recommended for future research. Investigating the effect of higher temperatures (above 600°C) as well as heating and cooling rates can also give more insight into the subject. In addition, X-ray tomography and microscope images can also be useful for the interpretation of the underlying causes of strength degradation under multi-phase loading histories.

2. In addition to further experimental investigations, the authors also believe that a better understanding on the subject can be attained through numerical discrete element simulations. A deeper understanding of the underlying damage mechanisms which result in size related dependencies can be gained through models.

3. Carrying out transient state tests (similar to those common for steel) can reveal a more realistic behaviour of the material under post-earthquake fire conditions. In addition, transient creep (whether at high temperature or ambient temperature) is an important characteristic of concrete material. Investigating the rate of creep on partially damaged samples can lead to important implications regarding durability and long-term response.

4. In the tests carried out in this research, the time gap between the damage induction phase, the temperature exposure phase and strength determination phase was kept constant. However, carrying out experiments where this time gap is the variable can be useful for rehabilitation and restoration of seismically damaged structures.

5. The discrete element model prepared for this thesis is still in its early stages. However, it has shown to be effective in simulating the interaction between the different components of concrete. When combined with the effect of cyclic

loading, the model is capable of simulating the sequential degradation of concrete material under mechanical and thermal effects.

8.2.3 Steel-concrete composites

Based on the findings of this study, the following research problems are recommended for steel-concrete composite members:

1. It has been shown that the mechanical properties of steel and concrete are functions of temperature and the level of pre-induced damage. Combining these effects for the analysis of a steel-concrete composite member/structure is the next step in post-earthquake fire research.

2. The thermo-mechanical properties (thermal expansion, conductivity, etc.) of steel and concrete vary with temperature. Incorporating these variations into thermal analyses will allow for a more accurate representation of temperature distribution as a function of time and energy input. As a composite member is being heated, steel loses strength faster than concrete. Therefore, combined with the previous item, a complex relation between time and the strength of the member is expected. Carrying out such analyses will give a better evaluation of a members strength under post-earthquake fire conditions.

3. During cool down, concrete suffers additional strength loss, hence a concrete member is prone to what is know as 'delayed failure'. Combining this effect with the changes that steel experiences during cooling, is suggested for future research.